



LAWRENCE
LIVERMORE
NATIONAL
LABORATORY

Flight and Stability of a Laser Inertial Fusion Energy Target in the Drift Region between Injection and the Reaction Chamber with Computational Fluid Dynamics

T. Mitori

December 13, 2013

Disclaimer

This document was prepared as an account of work sponsored by an agency of the United States government. Neither the United States government nor Lawrence Livermore National Security, LLC, nor any of their employees makes any warranty, expressed or implied, or assumes any legal liability or responsibility for the accuracy, completeness, or usefulness of any information, apparatus, product, or process disclosed, or represents that its use would not infringe privately owned rights. Reference herein to any specific commercial product, process, or service by trade name, trademark, manufacturer, or otherwise does not necessarily constitute or imply its endorsement, recommendation, or favoring by the United States government or Lawrence Livermore National Security, LLC. The views and opinions of authors expressed herein do not necessarily state or reflect those of the United States government or Lawrence Livermore National Security, LLC, and shall not be used for advertising or product endorsement purposes.

This work performed under the auspices of the U.S. Department of Energy by Lawrence Livermore National Laboratory under Contract DE-AC52-07NA27344.

FLIGHT AND STABILITY OF A LASER INERTIAL FUSION ENERGY TARGET IN
THE DRIFT REGION BETWEEN INJECTION AND THE REACTION CHAMBER
WITH COMPUTATIONAL FLUID DYNAMICS

A Thesis
presented to
the Faculty of California Polytechnic State University,
San Luis Obispo

In Partial Fulfillment
of the Requirements for the Degree
Master of Science in Mechanical Engineering

By
Tiffany Leilani Mitori
December 2013

© 2013

Tiffany Leilani Mitori

ALL RIGHTS RESERVED

COMMITTEE MEMBERSHIP

TITLE: Flight and Stability of a Laser Inertial Fusion Energy
Target in the Drift Region between Injection and the
Reaction Chamber with Computational Fluid Dynamics

AUTHOR: Tiffany Leilani Mitori

DATE SUBMITTED: December 2013

COMMITTEE CHAIR: Dr. Kim Shollenberger, Mechanical Engineering Professor
at California Polytechnic State University

COMMITTEE MEMBER: Dr. Patrick Lemieux, Mechanical Engineering Professor at
California Polytechnic State University

COMMITTEE MEMBER: Dr. James Scott Patton, Mechanical Engineering Professor
at California Polytechnic State University

COMMITTEE MEMBER: Dr. Mark Havstad, Engineering at Lawrence Livermore
National Laboratory

ABSTRACT

Flight and Stability of a Laser Inertial Fusion Energy Target in the Drift Region between Injection and the Reaction Chamber with Computational Fluid Dynamics Software

Tiffany Leilani Mitori

A Laser Inertial Fusion Energy (LIFE) target's flight through a low Reynolds number and high Mach number regime was analyzed with computational fluid dynamics software. This regime consisted of xenon gas at 1,050 K and approximately 6,670 Pa. Simulations with similar flow conditions were performed with a sphere and compared with experimental data and published correlations for validation purposes. Transient considerations of the developing flow around the target were explored. Simulations of the target at different velocities were used to determine correlations for the drag coefficient and Nusselt number as functions of the Reynolds number. Simulations with different angles of attack were used to determine the aerodynamic coefficients of drag, lift, Magnus moment, and overturning moment as well as target stability. The drag force, lift force, and overturning moment changed minimally with spin. Above an angle of attack of 15° , the overturning moment would be destabilizing. At low angles of attack (less than 15°), the overturning moment would tend to decrease the target's angle of attack, indicating the lack of a need for spin for stability at small angles. This stabilizing moment would cause the target to move in a mildly damped oscillation about the axis parallel to the free-stream velocity vector through the target's center of gravity.

Keywords: CFD, low Reynolds number, high Mach number, drag coefficient correlation, Nusselt correlation, angle of attack, aerodynamic coefficients, flight stability.

ACKNOWLEDGMENTS

The author would like to thank Lawrence Livermore National Laboratory (LLNL) for sponsoring the thesis. The author would also like to thank ANSYS customer support for providing temporary high-performance-computing licenses and Don at Livermore Computing for installing ANSYS on the LLNL clusters. 3D simulations would have been impossible without their help. The author would also like to thank Paul and the rest of the Laser Inertial Fusion Energy (LIFE) team for their support and guidance. Finally, the author wishes to thank Dr. Kim Shollenberger and Dr. Mark Havstad for their mentorship, advice, and support over the duration of the project. Their help has been invaluable in the completion of this thesis.

TABLE OF CONTENTS

	Page
LIST OF TABLES.....	viii
LIST OF FIGURES	x
CHAPTER	
I. INTRODUCTION.....	1
The National Ignition Facility (NIF) and Laser Inertial Fusion Energy (LIFE).....	1
Target Flight.....	3
List of Terms.....	6
II. BACKGROUND.....	8
Xenon Properties.....	8
External Flow over a Sphere.....	12
Flight Stability.....	15
III. COMPUTATIONAL FLUID DYNAMICS (CFD).....	18
Sphere Validation: Fluent Setup.....	19
Sphere Validation: Domain Size and Mesh Refinement Studies.....	21
2D, Axisymmetric Drift Regime: Fluent Setup.....	28
2D, Axisymmetric Drift Regime: Domain Size, Mesh Refinement, and Transient Considerations.....	30
3D Drift Regime: Fluent Setup.....	37
IV. RESULTS.....	42
Sphere Validation: Results.....	42

2D, Axisymmetric Drift Regime: Results.....	54
3D Drift Regime: Results.....	67
V. CONCLUSIONS.....	88
BIBLIOGRAPHY.....	89
APPENDICES	
A. Fluent Setup.....	92
B. Additional Plots of 2D, Axisymmetric Swirl, Transient Simulation of Target in Drift Region.....	98
C. Additional Plots of 3D, Steady-State Simulation of Target in Drift Region.....	102
D. Angle of Attack MATLAB Code and Plots.....	128

LIST OF TABLES

Table	Page
1. Summary of LIFE Target Injection Regimes.....	5
2. Gaseous Xenon Viscosity and Thermal Conductivity at Selected Temperatures Determined by Kinetic Theory.....	11
3. Estimates for Target Mass and Moments of Inertia.....	17
4. Velocities and Mach Numbers corresponding to Sphere Validation Cases with Different Reynolds Numbers.....	20
5. Xenon Properties for Sphere Validation Simulations in Drift Region at 1050 K and 6,666 Pa.....	21
6. Sphere Domain Size Study.....	22
7. Sphere Mesh Refinement Study.....	25
8. Xenon Properties in Drift Region at 6,666 Pa for Target Simulation.....	29
9. Domain Study on 2D, Axisymmetric Swirl, Transient Drift Flow over Target.....	33
10. Mesh Refinement Study on 2D, Axisymmetric Swirl, Transient Drift Flow over Target.....	34
11. Time Step Size Study on 2D, Axisymmetric Swirl, Transient Drift Flow over Target.....	36
12. Velocities and Mach Numbers for 3D, Steady-State Target Simulations with Different Reynolds Numbers.....	40
13. 3D, Steady-State Target Spin Axis for Varying Angle of Attack Cases.....	41
14. Sphere Drag Coefficient Comparison.....	43

15. Sphere Separation Angles (from Front Stagnation Point to Separation Point) from Fluent Simulations and Clift Correlation at Different Reynolds Numbers.....	46
16. Drag Force and Heat Transfer on Target after 1 ms from 2D, Axisymmetric Swirl Model.....	62
17. Drag Force and Heat Transfer on Target from 3D, Steady-State Target Model.....	71
18. Drag and Heat Transfer Coefficient Percent Difference between Transient, 2D, Axisymmetric Swirl Model and 3D, Steady-State Model.....	73
19. Drag and Heat Transfer from 3D, Steady-State Target Simulations at Different Reynolds Numbers.....	77
20. Aerodynamic Coefficients and Static Stability of Target in Drift Region at Different Angles of Attack.....	85
21. Angle of Attack Oscillation and Exit Value Determined by MATLAB Code...	87
22. Detailed Fluent Case Setup for 2D, Axisymmetric Sphere in Drift Region.....	92
23. Detailed Fluent Case Setup for 2D, Axisymmetric Swirl Target in Drift Region.....	93
24. Detailed Fluent Case Setup for 3D, Steady-State Target in Drift Region.....	95

LIST OF FIGURES

Figure	Page
1. Picture of NIF Target; Credit: Lawrence Livermore National Laboratory [16].....	2
2. Simulated Image of Lasers Heating NIF Target Hohlraum; Credit: Lawrence Livermore National Laboratory [17].....	2
3. LIFE Target Chamber Depicting Lasers and Target Injection Path; Credit: Lawrence Livermore National Laboratory [15].....	3
4. LIFE Target Geometry with Dimensions (Not Drawn to Scale).....	4
5. Sphere Domain Size Study.....	23
6. Sphere Mesh Convergence Plot.....	26
7. Selected Mesh (Case 6 from Refinement Table) for Sphere Simulations.....	26
8. Inflation Layers of Selected Mesh (Case 6 from Refinement Table) for Sphere Simulations.....	27
9. 2D, Axisymmetric Swirl Target Mesh Convergence Plot.....	34
10. Entire View of 2D, Axisymmetric Target Mesh.....	35
11. Inflation Layer View of 2D, Axisymmetric Target Mesh.....	35
12. Overall View of 3D Target mesh Sliced at X-Y Plane.....	38
13. Zoomed-in View of Target in 3D Target Mesh Sliced at X-Y Plane.....	39
14. Inflation Layer View of 3D Target Mesh Sliced at X-Y Plane.....	39
15. Sphere Drag Coefficient versus Reynolds Number for Experimental Data, a Published Correlation, and Fluent Simulation Results.....	43

16. Graph of Percent Difference between Fluent Results and Experimental Data and a Published Correlation.....	44
17. Wall Shear Stress Plot on Sphere at Different Reynolds Numbers.....	45
18. Sphere Velocity Contour with Streamlines Overlaid at $Re=21.1$	47
19. Sphere Velocity Contour with Streamlines Overlaid at $Re=23.4$	47
20. Sphere Velocity Contour with Streamlines Overlaid at $Re=29.1$	48
21. Sphere Velocity Contour with Streamlines Overlaid at $Re=45$	48
22. Sphere Velocity Contour with Streamlines Overlaid at $Re=50.6$	48
23. Sphere Velocity Contour with Streamlines Overlaid at $Re=54.4$	49
24. Sphere Velocity Contour with Streamlines Overlaid at $Re=68.9$	49
25. Sphere Velocity Contour with Streamlines Overlaid at $Re=78.2$	49
26. Sphere Velocity Contour with Streamlines Overlaid at $Re=88.1$	50
27. Sphere Velocity Contour with Streamlines Overlaid at $Re=93.8$	50
28. Sphere Velocity Contour with Streamlines Overlaid at $Re=101$	50
29. Sphere Velocity Contour with Streamlines Overlaid at $Re=104$	51
30. Sphere Velocity Contour with Streamlines Overlaid at $Re=108$	51
31. Sphere Velocity Contour with Streamlines Overlaid at $Re=109$	51
32. Sphere Velocity Contour with Streamlines Overlaid at $Re=124$	52
33. Sphere Velocity Contour with Streamlines Overlaid at $Re=130$	52
34. Zoomed-in View of Sphere Velocity Contour with Streamlines Overlaid at $Re=21.1$	52
35. Zoomed-in View of Sphere Velocity Contour with Streamlines Overlaid at $Re=23.4$	53

36. Velocity Contour and Streamlines of 2D, Axisymmetric Swirl Flow over Target at 1.00E-4 s.....	55
37. Velocity Contour and Streamlines of 2D, Axisymmetric Swirl Flow over Target at 2.00E-4 s.....	55
38. Velocity Contour and Streamlines of 2D, Axisymmetric Swirl Flow over Target at 3.00E-4 s.....	56
39. Velocity Contour and Streamlines of 2D, Axisymmetric Swirl Flow over Target at 4.00E-4 s.....	56
40. Velocity Contour and Streamlines of 2D, Axisymmetric Swirl Flow over Target at 5.00E-4 s.....	57
41. Velocity Contour and Streamlines of 2D, Axisymmetric Swirl Flow over Target at 6.00E-4 s.....	57
42. Velocity Contour and Streamlines of 2D, Axisymmetric Swirl Flow over Target at 7.00E-4 s.....	58
43. Velocity Contour and Streamlines of 2D, Axisymmetric Swirl Flow over Target at 8.00E-4 s.....	58
44. Velocity Contour and Streamlines of 2D, Axisymmetric Swirl Flow over Target at 9.00E-4 s.....	59
45. Velocity Contour and Streamlines of 2D, Axisymmetric Swirl Flow over Target at 1.00E-3 s.....	59
46. Drag Force over Time on Target in Drift Region from 2D, Axisymmetric Swirl Model.....	60

47. Heat Transfer over Time on Target in Drift Region from 2D, Axisymmetric Swirl Model.....	61
48. Absolute Pressure on Target in Drift Region from 2D, Axisymmetric Swirl Model.....	63
49. Mach Number on Target in Drift Region from 2D, Axisymmetric Swirl Model.....	64
50. Density on Target in Drift Region from 2D, Axisymmetric Swirl Model.....	64
51. Turbulent Intensity on Target in Drift Region from 2D, Axisymmetric Swirl Model.....	65
52. Total Surface Heat Flux on Target in Drift Region from 2D, Axisymmetric Swirl Model.....	65
53. Velocity Contour and Streamline Plot for Target in 3D, Steady-State, Drift Simulation.....	67
54. Absolute Pressure around Target from 3D, Steady-State Simulation.....	68
55. Mach Number around Target from 3D, Steady-State Simulation.....	69
56. Density around Target from 3D, Steady-State Simulation.....	69
57. Turbulent Intensity around Target from 3D, Steady-State Simulation.....	70
58. Total Surface Heat Flux around Target from 3D, Steady-State Simulation.....	70
59. Drag Coefficient Comparison between Transient, 2D, Axisymmetric Swirl Model and 3D, Steady-State Model.....	72
60. Heat Transfer Comparison between Transient, 2D, Axisymmetric Swirl Model and 3D, Steady-State Model.....	72

61. Heat Flux from 3D, Steady-State Case Plotted with Published Heat Transfer Correlations.....	75
62. Drag Coefficient Plotted for 3D, Steady-State Target Simulations at Different Reynolds Numbers.....	78
63. Nusselt Number Plotted for 3D, Steady-State Target Simulations at Different Reynolds Numbers.....	78
64. Velocity Contour and Streamline Plot for Target in 3D, Steady-State, Drift Simulation with 1° Angle of Attack.....	80
65. Velocity Contour and Streamline Plot for Target in 3D, Steady-State, Drift Simulation with 2° Angle of Attack.....	80
66. Velocity Contour and Streamline Plot for Target in 3D, Steady-State, Drift Simulation with 5° Angle of Attack.....	81
67. Velocity Contour and Streamline Plot for Target in 3D, Steady-State, Drift Simulation with 10° Angle of Attack.....	81
68. Velocity Contour and Streamline Plot for Target in 3D, Steady-State, Drift Simulation with 15° Angle of Attack.....	82
69. Velocity Contour and Streamline Plot for Target in 3D, Steady-State, Drift Simulation with 20° Angle of Attack.....	82
70. Forces on Spinning and Non-Spinning Target in Drift Region at Different Angles of Attack from 3D, Steady-State Model.....	83
71. Moments on Spinning and Non-Spinning Target in Drift Region at Different Angles of Attack from 3D, Steady-State Model.....	84

72. Pressure Contour of 2D, Axisymmetric Swirl Flow over Target in Drift Region at 1.00E-3 s.....	98
73. Temperature Contour of 2D, Axisymmetric Swirl Flow over Target in Drift Region at 1.00E-3 s.....	98
74. Total Temperature around Target in Drift Region from 2D, Axisymmetric Swirl Model.....	99
75. Wall Shear Stress around Target in Drift Region from 2D, Axisymmetric Swirl Model.....	99
76. Turbulent Dissipation Rate around Target in Drift Region from 2D, Axisymmetric Swirl Model.....	100
77. Turbulent Kinetic Energy around Target in Drift Region from 2D, Axisymmetric Swirl Model.....	100
78. Y+ Values around Target in Drift Region from 2D, Axisymmetric Swirl Model.....	101
79. Pressure Contour on 3D, Steady-State Spinning Target in Drift Region.....	102
80. Temperature Contour on 3D, Steady-State Spinning Target in Drift Region.....	102
81. Total Temperature around Target in Drift Region from 3D, Steady-State Model.....	103
82. Wall Shear Stress around Target in Drift Region from 3D, Steady-State Model.....	103
83. Turbulent Dissipation Rate around Target in Drift Region from 3D, Steady-State Model.....	104

84. Turbulent Kinetic Energy around Target in Drift Region from 3D, Steady-State Model.....	104
85. Y+ Values around Target in Drift Region from 3D, Steady-State Model.....	105
86. Pressure Contour on 3D, Steady-State Spinning Target in Drift Region with a 1° Angle of Attack.....	105
87. Temperature Contour on 3D, Steady-State Spinning Target in Drift Region with a 1° Angle of Attack.....	106
88. Pressure Contour on 3D, Steady-State Spinning Target in Drift Region with a 2° Angle of Attack.....	106
89. Temperature Contour on 3D, Steady-State Spinning Target in Drift Region with a 2° Angle of Attack.....	106
90. Pressure Contour on 3D, Steady-State Spinning Target in Drift Region with a 5° Angle of Attack.....	107
91. Temperature Contour on 3D, Steady-State Spinning Target in Drift Region with a 5° Angle of Attack.....	107
92. Pressure Contour on 3D, Steady-State Spinning Target in Drift Region with a 10° Angle of Attack.....	107
93. Temperature Contour on 3D, Steady-State Spinning Target in Drift Region with a 10° Angle of Attack.....	108
94. Pressure Contour on 3D, Steady-State Spinning Target in Drift Region with a 15° Angle of Attack.....	108
95. Temperature Contour on 3D, Steady-State Spinning Target in Drift Region with a 15° Angle of Attack.....	108

96. Pressure Contour on 3D, Steady-State Spinning Target in Drift Region with a 20° Angle of Attack.....	109
97. Temperature Contour on 3D, Steady-State Spinning Target in Drift Region with a 20° Angle of Attack.....	109
98. Drag Force on Spinning Target in Drift Region at Different Angles of Attack from 3D, Steady-State Model.....	110
99. Lift Force on Spinning Target in Drift Region at Different Angles of Attack from 3D, Steady-State Model.....	110
100. Z-Axis Force on Spinning Target in Drift Region at Different Angles of Attack from 3D, Steady-State Model.....	111
101. Local X-Axis (Axial) Moment on Spinning Target in Drift Region at Different Angles of Attack from 3D, Steady-State Model.....	111
102. Local Y-Axis (negative Magnus) Moment on Spinning Target in Drift Region at Different Angles of Attack from 3D, Steady-State Model.....	112
103. Z-Axis (Overturning) Moment on Spinning Target in Drift Region at Different Angles of Attack from 3D, Steady-State Model.....	112
104. Drag Force on Non-Spinning Target in Drift Region at Different Angles of Attack from 3D, Steady-State Model.....	113
105. Lift Force on Non-Spinning Target in Drift Region at Different Angles of Attack from 3D, Steady-State Model.....	113
106. Z-Axis Force on Non-Spinning Target in Drift Region at Different Angles of Attack from 3D, Steady-State Model.....	114

107. Local X-Axis (Axial) Moment on Non-Spinning Target in Drift Region at Different Angles of Attack from 3D, Steady-State Model.....	114
108. Local Y-Axis (negative Magnus) Moment on Non-Spinning Target in Drift Region at Different Angles of Attack from 3D, Steady-State Model.....	115
109. Z-Axis (Overturning) Moment on Non-Spinning Target in Drift Region at Different Angles of Attack from 3D, Steady-State Model.....	115
110. Pressure Contour on 3D, Steady-State, Spinning Target in Drift Region at a Reynolds Number of 2400.....	116
111. Temperature Contour on 3D, Steady-State, Spinning Target in Drift Region at a Reynolds Number of 2400.....	116
112. Velocity Contour with Streamlines on 3D, Steady-State, Spinning Target in Drift Region at a Reynolds Number of 2400.....	117
113. Pressure Contour on 3D, Steady-State, Spinning Target in Drift Region at a Reynolds Number of 2800.....	117
114. Temperature Contour on 3D, Steady-State, Spinning Target in Drift Region at a Reynolds Number of 2800.....	118
115. Velocity Contour with Streamlines on 3D, Steady-State, Spinning Target in Drift Region at a Reynolds Number of 2800.....	118
116. Pressure Contour on 3D, Steady-State, Spinning Target in Drift Region at a Reynolds Number of 3200.....	119
117. Temperature Contour on 3D, Steady-State, Spinning Target in Drift Region at a Reynolds Number of 3200.....	119

118. Velocity Contour with Streamlines on 3D, Steady-State, Spinning Target in Drift Region at a Reynolds Number of 3200.....	120
119. Pressure Contour on 3D, Steady-State, Spinning Target in Drift Region at a Reynolds Number of 3600.....	120
120. Temperature Contour on 3D, Steady-State, Spinning Target in Drift Region at a Reynolds Number of 3600.....	121
121. Velocity Contour with Streamlines on 3D, Steady-State, Spinning Target in Drift Region at a Reynolds Number of 3600.....	121
122. Pressure Contour on 3D, Steady-State, Spinning Target in Drift Region at a Reynolds Number of 4400.....	122
123. Temperature Contour on 3D, Steady-State, Spinning Target in Drift Region at a Reynolds Number of 4400.....	122
124. Velocity Contour with Streamlines on 3D, Steady-State, Spinning Target in Drift Region at a Reynolds Number of 4400.....	123
125. Pressure Contour on 3D, Steady-State, Spinning Target in Drift Region at a Reynolds Number of 4800.....	123
126. Temperature Contour on 3D, Steady-State, Spinning Target in Drift Region at a Reynolds Number of 4800.....	124
127. Velocity Contour with Streamlines on 3D, Steady-State, Spinning Target in Drift Region at a Reynolds Number of 4800.....	124
128. Pressure Contour on 3D, Steady-State, Spinning Target in Drift Region at a Reynolds Number of 5200.....	125

129. Temperature Contour on 3D, Steady-State, Spinning Target in Drift Region at a Reynolds Number of 5200.....	125
130. Velocity Contour with Streamlines on 3D, Steady-State, Spinning Target in Drift Region at a Reynolds Number of 5200.....	126
131. Pressure Contour on 3D, Steady-State, Spinning Target in Drift Region at a Reynolds Number of 5600.....	126
132. Temperature Contour on 3D, Steady-State, Spinning Target in Drift Region at a Reynolds Number of 5600.....	127
133. Velocity Contour with Streamlines on 3D, Steady-State, Spinning Target in Drift Region at a Reynolds Number of 5600.....	127
134. Angle of Attack over Time for Target with Initial Angle of Attack of 1°.....	129
135. Angle of Attack over Time for Target with Initial Angle of Attack of 2°.....	129
136. Angle of Attack over Time for Target with Initial Angle of Attack of 5°.....	130
137. Angle of Attack over Time for Target with Initial Angle of Attack of 10°.....	130
138. Angle of Attack over Time for Target with Initial Angle of Attack of 15°.....	131

CHAPTER I: INTRODUCTION

The National Ignition Facility (NIF) and Laser Inertial Fusion Energy (LIFE)

The National Ignition Facility (NIF) at Lawrence Livermore National Laboratory (LLNL) contains one of the world's largest and most powerful laser systems. The 192 laser beams at the facility can produce almost 2 million joules of energy [7]. One of the main goals of the NIF is to achieve energy gain from thermonuclear fusion of deuterium and tritium [11]. Instead of directly targeting the lasers on the deuterium and tritium, an indirect drive approach has been used [9]. The NIF lasers have been targeted at a hohlraum (gold cylinder surrounding a spherical capsule of deuterium and tritium) [11]. Figure 1 is a picture of one of the NIF Targets. To achieve thermonuclear fusion burn, the lasers heat the inside of the hohlraum, creating hot plasma that bathes the capsule with X-rays [9]. See Figure 2 for a simulated image of the laser beams heating the hohlraum. The X-rays quickly heat the capsule, which causes an ablation of the outer surface of the capsule [9]. This ablation causes the deuterium and tritium in the capsule to compress to about 100 times the density of lead and reach a core temperature over 100 million K [11]. These extreme conditions are required to achieve inertial confinement fusion. The fusion of these 2 hydrogen isotopes can theoretically produce 10 to 100 times more energy than the amount required to power the lasers [9].

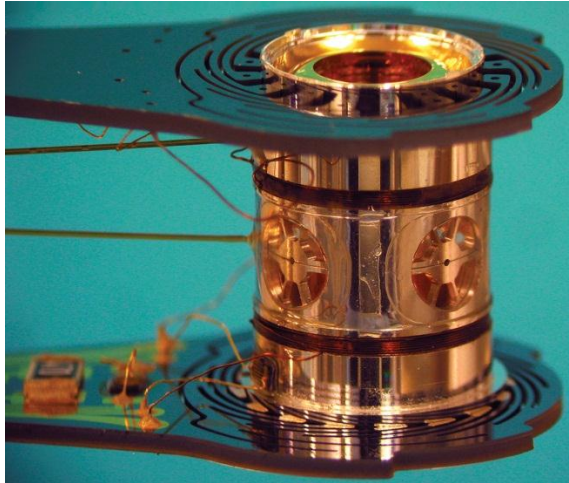


Figure 1. Picture of NIF Target; Credit: Lawrence Livermore National Laboratory [16]

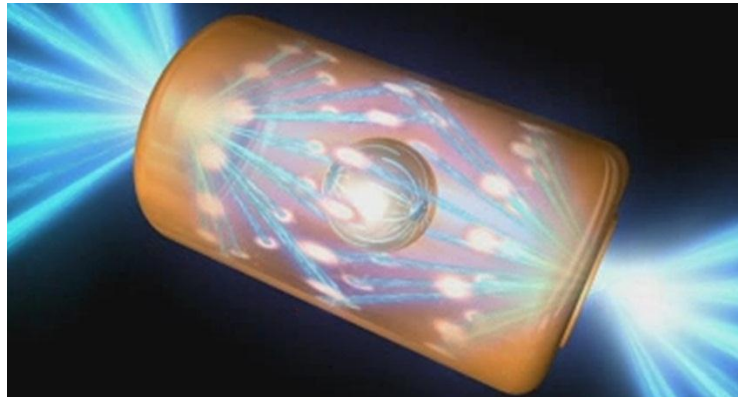


Figure 2. Simulated Image of Lasers Heating NIF Target Hohlraum; Credit: Lawrence Livermore National Laboratory [17]

The Laser Inertial Fusion Energy (LIFE) project was developed to create a power plant from the fusion technology developed at the NIF. Energy from the fusion reaction can be used to heat water and generate electricity through steam-turbine generators [7]. The advantages of a LIFE facility include: no harmful emissions, no nuclear waste, and an abundant fuel supply [7]. A LIFE facility would require a target injection system to launch targets into the reaction chamber at approximately 15 Hz [7]. Note that the LIFE target will be different than the NIF target because of this change from a stationary to an injected target. The first fleet of LIFE plants could each produce 1.5 GW of electricity [7]. The first demonstration plant could be constructed by the late 2020's [7].

Target Flight

The current design for the LIFE target injection requires the target to travel approximately 9 m through the injector, 4 m through a drift region ending with a neutron and gamma radiation shielding shutter, and finally 6 m to the center of the spherical target chamber to reach the point of laser contact. See Figure 3 below for the injection path. Note that the injector is directly above the spherical reaction chamber.

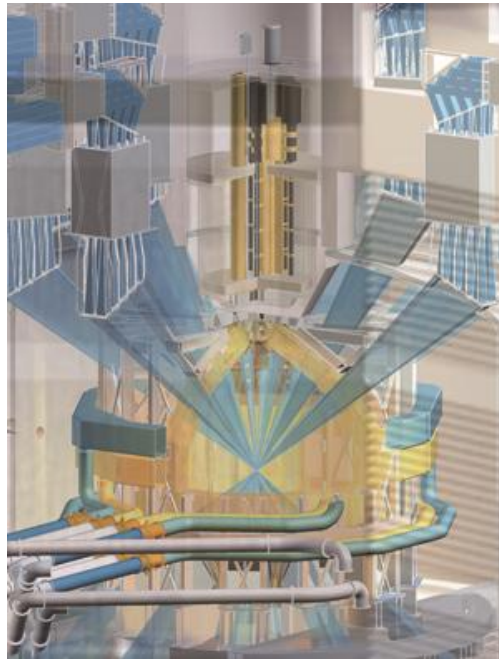


Figure 3. LIFE Target Chamber Depicting Lasers and Target Injection Path; Credit: Lawrence Livermore National Laboratory [15]

The target is modeled as a beveled cylinder with an outer diameter of 10.5 mm and a total length of 13.8 mm. The outer dimensions of the target geometry can be seen in Figure 4. The target is assumed to travel at a constant 250 m/s, while spinning at 1 revolution per meter of travel, and at a constant temperature of 20 K. The variation in target speed is expected to be no more than 1% and the heat transfer to the target during this short flight is expected to be minimal, making these modeling assumptions reasonable for this analysis.

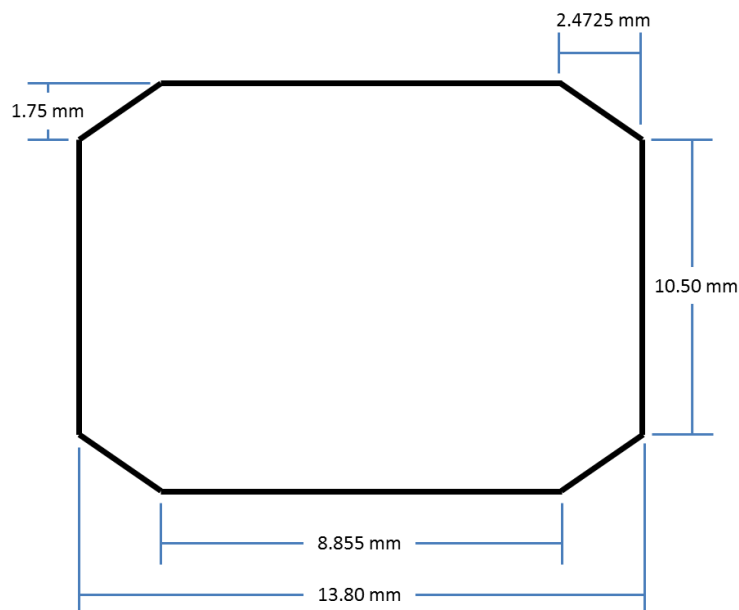


Figure 4. LIFE Target Geometry with Dimensions (Not Drawn to Scale)

The 9 m-long injector environment consists of xenon gas at approximately 1,050 K and 3,000 Pa. The Mach number of this regime (with a target speed of 250 m/s) is 0.75 and the Reynolds number (using the target's outer diameter as the characteristic length) is 1,768.

After the injector, the target enters a 4 m-long, cylindrical drift region 0.5 m in diameter. The region is filled with xenon gas at approximately 6,670 Pa. The temperature of this region will be 1,050 K. Using the same target speed and characteristic length as before, the Mach number and Reynolds number are 0.75 and 3,937 respectively. The neutron and gamma radiation shielding shutter located at the end of the drift region is a rotating cement disk approximately 0.5 m in diameter and 1 m thick. It spins at 4 revolutions per second, and contains a spiral-cut hole 0.2 m off the axis of rotation for the target to pass through. The target launch will be timed to ensure the target passes through the spiral-cut opening in the shutter.

After the target passes through the shutter, it enters the spherical reaction chamber, which is filled with xenon gas at approximately 6,000 K and 3,070 Pa. It travels 6 m to the point of laser contact at the center of the spherical chamber. Using the same target speed and characteristic length as before, the Mach number and Reynolds number in this chamber are 0.31 and 100.5, respectively. See Table 1 below for a summary of the region specifications. Note the extreme combination of low Reynolds numbers and high Mach numbers in the injection and drift regions.

Table 1. Summary of LIFE Target Injection Regimes

Region	Length of Flight (m)	Temperature (K)	Pressure (Pa)	Mach Number	Reynolds Number
Injection	9	1050	3000	0.75	1768
Drift	4	1050	6666	0.75	3937
Chamber	6	6000	3066	0.31	100.5

The goal of this project is to simulate the target's flight in the drift region using computational fluid dynamics software to highlight key features of the flow, estimate drag and heat transfer as a functions of the Reynolds number, and determine the target's stability. The coefficients of drag, lift, Magnus moment, and overturning moment will be used to determine the target's stability. Phase changes of xenon gas will be considered negligible. The any solidification of xenon is expected to be brief and have a minimal effect on target flight. Gravity will also be neglected. Similar fluid conditions, assumptions, fluid properties, and methods of mesh generation will be used with a sphere projectile and compared to experimental data and published correlations for validation purposes.

List of Terms

ε/k_B =Energy parameter used in kinetic theory of gases.

k_B =Boltzmann constant equal to 1.381E-23 J/K [10]

σ =Characteristic length used in kinetic theory of gases; often reported in angstroms (\AA)
where $\text{\AA}=10^{-10}\text{m}$

b^* =First virial coefficient

B^* =Second virial coefficient

β, Ω'_{22} =Universal functional

Ω_{22}, Ω_{11} =Collision Integrals

T =Temperature in Kelvin

T^* =Non-dimensionalized form of the temperature

μ =Dynamic viscosity in units of Pa-s or kg/(m-s)

k =Thermal conductivity in units of W/(m-K)

M =Molecular weight in g/mol

M' =Molecular weight in kg/mol

R =Universal gas constant equal to 8.3144621 J/(mol-K) [5]

\bar{c}_p =Molar specific heat at constant pressure in J/(mol-K)

c_p =Specific heat at constant pressure in J/(kg-K)

Re_d = Reynolds number with characteristic length equal to the diameter d

d =diameter in m

ρ =fluid density in kg/m^3

V =velocity in m/s

C_D =Drag coefficient

θ_s =Separation angle (in degrees) measured from the front stagnation point to the point of separation (in flow over a sphere)

m =mass in kg

S =reference area in m^2

I_y = transverse moment of inertia through an axis through the projectile's center of mass (in kgm^2)

C_{M_α} =overturning moment coefficient

M_α =overturning moment in Nm

α_t = total yaw angle in radians

β = angle of sideslip in radians

α = angle of attack in radians

S_d =dynamic stability factor

C_{L_α} =lift force coefficient

$C_{M_{p\alpha}}$ =magnus moment coefficient

C_{M_q} =pitch damping moment coefficient due to transverse angular velocity

q_t =transverse angular velocity in rad/s

$C_{M_{\dot{\alpha}}}$ =pitch damping moment coefficient due to the angle of attack's rate of change

$\dot{\alpha}_t$ =angle of attack's rate of change in rad/s

I_x =axial moment of inertia

L_α =lift force in N

$M_{p\alpha}$ =magnus moment in Nm

p =axial spin in rad/s

D = drag force in N

M_{pd} =pitch damping moment in Nm

St = Strouhal number with characteristic length equal to diameter d

f =frequency of oscillation in Hz

a =acceleration in m/s^2

Pr =Prandtl number

CHAPTER 2: BACKGROUND

Xenon Properties

As mentioned in the target flight section of the introduction, xenon phase changes were ignored. Note that at the drift region pressure of 6,666 Pa, gaseous xenon would undergo deposition at approximately 135 K according to the xenon phase diagram [30]. Knowing that the region at the front stagnation point of the target would see a larger pressure, gaseous xenon could even change to a solid at about 150 K. However, the build-up of xenon ice on the target is expected to be brief and thin. Therefore, xenon property correlations were determined for the gas phase and extended to these lower temperatures as well.

“Most of the better [fluid property] estimation methods use equations based on the form of an incomplete theory with empirical correlations of the constants that are not provided by that theory” [23]. Therefore, the xenon property correlations used in the simulations were a product of an extension of basic kinetic molecular theory with experimentally determined scaling factors. Kestin, Ro, and Wakeham [14] developed these equilibrium and transport property correlations for noble gases for a wide range of temperatures and moderate range of pressures.

Kestin *et al.* [14] used the Chapman-Enskog theory to include the effects of intermolecular forces in the basic kinetic molecular theory. Kestin *et al.* [14] assumed that xenon, argon, krypton, and neon “obey the same intermolecular force potential” but had different numerical values for the 2 experimentally determined scaling constants: the energy parameter, ϵ/k_B , and the characteristic length, σ . (Note that k_B is the Boltzmann constant; ϵ (in units of energy) is the experimentally determined part of the energy parameter.) Viscosity, binary diffusion coefficient, and virial coefficient data over a

large temperature range (60 K - 2100 K) was used with universal functions for the first and second virial coefficients (b^* and B^*), universal functionals β and Ω'_{22} , and collision integrals Ω_{22} and Ω_{11} from Hirschfelder *et al.* [8] to approximate the parameters. These estimations provided an energy parameter of 285.27 K and a characteristic length of 3.858 Å.

With the energy parameter and characteristic length estimated, Kestin *et al.* used the universal functions Hirschfelder *et al.* [8] provided to evaluate B^* , b^* , Ω_{22} , Ω_{11} , Ω'_{22} , and β at several temperatures and determine correlations for each in terms of normalized temperature, T^* . Kestin *et al.* [14] estimated the correlation for the collision integral Ω_{22} as:

$$\ln \Omega_{22} = 0.4394 - 0.4764(\ln T^*) + 0.1235(\ln T^*)^2 - 0.0156(\ln T^*)^3 \quad (1)$$

where T^* is the non-dimensionalized form of T (the temperature in Kelvin):

$$T^* = \frac{T}{\frac{\epsilon}{k}} \quad (2)$$

Note that correlations depicting the collision integral are typically applicable between T^* of 0.3 and 100 [23].

The temperature, kinetic theory parameters, and collision integral can be used to determine the viscosity and thermal conductivity of the gas. The following equations for dynamic viscosity (μ) in units of kg/(m-s) and thermal conductivity (k) in units of W/(m-K) have been adapted from Reid *et al.* [23]:

$$\mu = 2.669 * 10^{-26} \frac{\sqrt{MT}}{\sigma^2 \Omega_{22}} \quad (3)$$

$$k = 2.63 * 10^{-23} \frac{\sqrt{T/M'}}{\sigma^2 \Omega_{22}} \quad (4)$$

where M is the molecular weight in g/mol and M' is the molecular weight in kg/mol. According to the Thomas Jefferson National Accelerator Facility [28], the molecular weight of xenon is 131.293 g/mol.

The preceding equations only account for fluid temperature, not pressure. However, the Chapman-Enskog theory used by Kestin *et al.* [14] is valid for low-pressure, non-polar gases with only 0.5% to 1.5% error [23]. Since the pressure in the drift region is only approximately 6,666 Pa, this theory is adequate in this regime. Additionally, the density of xenon at 1050 K and 6,666 Pa is only 0.10025 kg/m³; therefore, no high-density adjustments need to be considered for a reasonable approximation of viscosity. Similarly, although the thermal conductivity increases as pressure increases, the effect is negligible at low and moderate pressures [23]. Between 100 and 1,000,000 Pa, thermal conductivity only increases about 1% per 100,000 Pa [23]. Therefore, the effect of pressure on viscosity and thermal conductivity has been neglected.

Using equations 3 and 4 from Reid *et al.* [23] with the Kestin *et al.* [14] kinetic theory parameters and collision integral correlation, the viscosity and thermal conductivity for gaseous xenon were evaluated from 86 K (the first whole-integer temperature where T^* is above 0.3) to 1050 K in 1 K increments. Table 2 shows the viscosity and thermal conductivity of gaseous xenon evaluated at selected temperatures in this region. Best-fit polynomials were determined for the entire set of dynamic viscosity values in units of kg/(m-s) and thermal conductivity values in units of W/(m-K):

$$\mu = (-2.243 * 10^{-11})T^2 + (8.796 * 10^{-8})T - 1.167 * 10^{-6} \quad (5)$$

$$k = (-5.323 * 10^{-9})T^2 + (2.088 * 10^{-5})T - 2.769 * 10^{-4} \quad (6)$$

Note that the R^2 value for both correlations was 0.9998, indicating a great curve fit.

Table 2. Gaseous Xenon Viscosity and Thermal Conductivity at Selected Temperatures Determined by Kinetic Theory

Temperature, T (K)	Non-Dimensionalized Temperature, T*	Collision Integral Ω_{22}	Viscosity, μ (kg/(m-s))	Thermal Conductivity, k (W/(m-K))
100	0.351	2.982	6.891E-06	1.636E-03
150	0.526	2.227	1.130E-05	2.681E-03
200	0.701	1.868	1.556E-05	3.692E-03
250	0.876	1.656	1.962E-05	4.656E-03
300	1.052	1.515	2.348E-05	5.573E-03
350	1.227	1.415	2.717E-05	6.448E-03
400	1.402	1.339	3.069E-05	7.284E-03
450	1.577	1.279	3.407E-05	8.085E-03
500	1.753	1.231	3.731E-05	8.855E-03
550	1.928	1.192	4.043E-05	9.596E-03
600	2.103	1.158	4.345E-05	1.031E-02
650	2.279	1.130	4.636E-05	1.100E-02
700	2.454	1.105	4.919E-05	1.167E-02
750	2.629	1.084	5.193E-05	1.233E-02
800	2.804	1.064	5.460E-05	1.296E-02
850	2.980	1.047	5.720E-05	1.358E-02
900	3.155	1.032	5.973E-05	1.418E-02
950	3.330	1.018	6.221E-05	1.476E-02
1000	3.505	1.005	6.463E-05	1.534E-02
1050	3.681	0.994	6.699E-05	1.590E-02

For a monatomic gas, the specific heat at constant pressure can be approximated with kinetic theory with the following equation from Moran *et al.* [20]:

$$\bar{c}_p = \frac{5}{2} R \quad (7)$$

where R is the universal gas constant approximated as 8.3144 J/(mol-K) [5] and \bar{c}_p is the molar specific heat at constant pressure. Therefore, for xenon with a molecular weight of 0.131293 kg/mol [28], the specific heat at constant pressure (c_p) is estimated as 158.32 J/(kg-K).

External Flow over a Sphere

External flow over a sphere can be categorized into several regimes according to its Reynolds number. Reynolds number (Re_d) is defined [21] as

$$Re_d = \frac{\rho V d}{\mu} \quad (8)$$

where ρ is the fluid density, V is the fluid velocity, d is the sphere diameter. Between a Reynolds number of 0 and 20, the flow over a sphere is unseparated, but the streamlines and vorticity contours are not symmetric due to the fluid's viscosity [4, 21]. At a Reynolds number of 20, flow separation occurs due to an adverse pressure gradient, which is indicated by a change in the sign of the vorticity [4] as well as no wall shear stresses or velocity gradients at the separation point [21]. Recirculation, or the forming of a wake region behind the sphere, also occurs near a Reynolds number of 20 [4, 22]. Between a Reynolds number of 20 and 130, the flow is steady, axisymmetric, and has an attached wake region [4, 22]. As the Reynolds number increases, the separation point, which began at the rear stagnation point, moves towards the point where the tangent to the sphere is parallel with the free-stream flow [4]. As the separation point extends along the curve of the sphere from the rear stagnation point, the wake region behind the sphere becomes wider and longer and changes from a concave shape to a convex shape [4, 22]. The transition point between concave and convex wake shapes occurs near a Reynolds number of 35 [22]. A periodic oscillation of the vortex wake behind the sphere begins between a Reynolds number of 130 and 190 [27, 22]. From a Reynolds number of 210 to 270, the vortices behind the sphere appear as a “two streamwise vortical tails of equal strength and opposite sign” [12]. Although the flow is no longer axisymmetric, the vortices are still planar-symmetric [12]. Between a Reynolds of 270 and 400, the flow

becomes unsteady, but still planar-symmetric. Between a Reynolds of 400 and 1000, the flow is no longer planar-symmetric. Above a Reynolds number of 1000, the flow becomes turbulent.

For validation purposes, the 20 to 130 Reynolds range was selected. Since the flow is steady and symmetric in this range, a 2D, steady-state, axisymmetric model could effectively capture the flow structure. Furthermore, the experimental drag data taken in the steady flow field was more reliable than measurements taken during vortex shedding at higher Reynolds numbers [24]. Additionally, the drag coefficient correlation used for comparison was valid for incompressible flows (at low Mach numbers), which required low velocities (and, therefore, low Reynolds numbers) [2]. The drag coefficient, separation angle, and wake structure from the Fluent simulations were analyzed within this Reynolds number range and compared to experimental data and published correlations.

A strong relationship between Reynolds number and drag coefficient exists for a sphere with wall temperature equal to the free-stream temperature and where the free-stream is laminar and has a low Mach number [2]. This is typically referred to as the “standard” drag curve [2]. If the sphere wall temperature is greater than the free-stream temperature, the drag coefficient is greater than would be predicted by the “standard” drag curve [2]. Figure 4 in “Sphere Drag Coefficient for a Broad Range of Mach and Reynolds Numbers” shows the drag coefficient increases with Mach number; however, it appears relatively steady below Mach 0.25 [2]. Clift *et al.* [4] presented this “standard” correlation in the 20 to 260 Reynolds range:

$$C_D = \frac{24}{Re_d} (1 + 0.1935 Re_d^{0.6305}) \quad (9)$$

Additionally, some of the experimental data from Roos and Willmarth [24] falls within the 20 to 130 Reynolds range. The drag fluctuation during the experiment was estimated to be no more than about 5% of the average value [24]. This experimental data along with the correlation by Clift *et al.* [4] served as points of comparison with the drag results from Fluent sphere simulations.

As mentioned previously, the separation point extends from the rear stagnation point along the curve of the sphere as the Reynolds number increases in this range. Clift *et al.* [4] provided an equation estimating the separation angle (in degrees) measured from the front stagnation point to the point of separation as a function of the Reynolds number:

$$\theta_s = 180 - 42.5 \left[\ln \frac{Re_d}{20} \right]^{0.483} \quad (10)$$

The separation point coincides with the point of zero shear stress on the wall [21]. The separation angle was estimated by approximating the separation point from the Fluent simulation wall shear stress plots at a variety of Reynolds numbers in this range and were compared to Clift's [4] relationship above.

Finally, the changes in wake structure with Reynolds number was observed by Nakamura [22]. As mentioned previously, in the 20-130 Reynolds range, the wake increases with Reynolds number and the wake changes from concave to convex at approximately a Reynolds number of 35. The Fluent simulation streamline plots will be analyzed to see if this wake structure criterion is met.

Flight Stability

Robert McCoy provided stability criteria for a rigid-body, axisymmetric projectile traveling with a small yaw angle along a flat-fire trajectory with negligible wind effects in *Modern Exterior Ballistics* [18]. Since the flight of the LIFE target satisfies all of these assumptions, McCoy's stability criteria was used to determine the stability of the target in the drift region. The remainder of this flight stability section serves as a summary of McCoy's flight stability criteria.

The variable M was used to differentiate between 2 stability categories: statically stable and statically unstable. M is defined as:

$$M = k_y^{-2} C_{M_\alpha}^* \quad (11)$$

where

$$k_y^{-2} = \frac{md^2}{I_y} \quad (12)$$

$$C_{M_\alpha}^* = \frac{\rho S d}{2m} C_{M_\alpha} \quad (13)$$

where m is the projectile mass, d is the reference diameter, ρ is the fluid density, S is the reference area defined as $S = \frac{\pi d^2}{4}$, I_y is the transverse moment of inertia through an axis through the projectile's center of mass, and C_{M_α} is the overturning moment coefficient defined by:

$$M_\alpha = \frac{1}{2} \rho V^2 S d C_{M_\alpha} \sin \alpha_t \quad (14)$$

where M_α is the overturning moment associated with the lift or normal force on the projectile, V is the projectile velocity, and α_t is the total yaw angle due to the angle of sideslip (β) and angle of attack (α). For small yaw angles (less than 15°), $\alpha_t \cong \sqrt{\alpha^2 + \beta^2}$.

A statically stable projectile is defined as satisfying $M < 0$. Static stability indicates the projectile is stable without spin. Note that too much spin on a statically stable projectile could be destabilizing. If the dynamic stability factor is between 0 and 2, the statically stable projectile is also dynamically stable. The dynamic stability factor, S_d , defined as:

$$S_d = \frac{2(C_{L\alpha} + k_x^{-2} C_{M_{p\alpha}})}{C_{L\alpha} - C_d - k_y^{-2} (C_{M_q} + C_{M_{\dot{\alpha}}})} \quad (15)$$

where $C_{L\alpha}$ is the lift force coefficient, $C_{M_{p\alpha}}$ is the magnus moment coefficient, C_d is the drag force coefficient, C_{M_q} is the pitch damping moment coefficient due to transverse angular velocity (q_t), $C_{M_{\dot{\alpha}}}$ is the pitch damping moment coefficient due to the angle of attack's rate of change ($\dot{\alpha}_t$), and k_x^{-2} is given by

$$k_x^{-2} = \frac{md^2}{I_x} \quad (16)$$

where I_x is the axial moment of inertia.

The coefficients used in the definition of the dynamic stability factor are determined from the following equations:

$$L_\alpha = \frac{1}{2} \rho V^2 S C_{L\alpha} \sin \alpha_t \quad (17)$$

$$M_{p\alpha} = \frac{1}{2} \rho V^2 S d \left(\frac{p d}{V} \right) C_{M_{p\alpha}} \sin \alpha_t \quad (18)$$

$$D = -\frac{1}{2} \rho V^2 S C_d \quad (19)$$

$$M_{pd} = \frac{1}{2} \rho V^2 S d \left(\frac{q_t d}{V} \right) (C_{M_q} + C_{M_{\dot{\alpha}}}) \quad (20)$$

where L_α is the lift force (perpendicular to the projectile's trajectory), $M_{p\alpha}$ is the magnus moment due to the force created by unequal pressures on opposite sides of a spinning projectile, p is the axial spin in rad/s, D is the drag force (opposing the projectile's

motion), and M_{pd} is the pitch damping moment due to the fluid's resistance of the projectile's pitching motion. If S_d is between 0 and 2, a statically stable projectile will also be dynamically stable.

A statically unstable projectile is defined as satisfying $M > 0$. Unlike statically stable projectiles, a statically unstable projectile must meet both gyroscopic and dynamic stability criteria to be stable. Gyroscopic stability is defined as satisfying the following:

$$P^2 - 4M > 0 \quad (21)$$

where M is defined in equation 11 and P is defined as:

$$P = \frac{I_x}{I_y} \left(\frac{pd}{V} \right) \quad (22)$$

As with statically stable projectiles, statically unstable projectiles must also satisfy the dynamic stability criteria: $0 < S_d < 2$ where S_d is defined in equation 15. If the statically unstable projectile satisfies the gyroscopic and dynamic stability criteria, it can be spin-stabilized. The following inequality can be used to determine the appropriate axial spin rate:

$$P^2 > \frac{4M}{S_d(2-S_d)} \quad (23)$$

Estimates for the mass and moments of inertia for the target were provided and can be seen below in Table 3.

Table 3. Estimates for Target Mass and Moments of Inertia

Target Mass (kg)	3.033E-3
Axial Moment of Inertia, I_x (kgm²)	5.72E-8
Transverse Moment of Inertia, I_y (kgm²)	8.6E-8

CHAPTER 3: COMPUTATIONAL FLUID DYNAMICS (CFD)

A collection of programs within ANSYS workbench version 14.5.7 was used to create, run, and post-process all simulations. ANSYS mesh was used to create all meshes (both 2D and 3D). ANSYS Fluent was used to create and run the CFD simulations. ANSYS CFD-Post was used for visual post-processing.

As described in the “ANSYS Fluent User’s Guide: Release 14.5” [1], Fluent uses the finite volume method to numerically approximate partial differential equations in fluid dynamic theory (continuity, conservation of momentum, and in the case of compressible flow or heat transfer, conservation of energy). Fluent provides 2 types of solvers to evaluate these equations. The density-based solver was developed for compressible flows and uses continuity to solve for density and an equation of state (i.e. ideal gas law) to solve for pressure. The pressure-based solver was developed for incompressible flows. The pressure-based solver calculates pressure with a pressure-correction equation (created from the combination of continuity and conservation of momentum). Both the density-based and pressure-based solvers calculate velocity with conservation of momentum.

This chapter discusses Fluent case setup as well as mesh refinement, domain size, and transient considerations (for unsteady cases).

Sphere Validation: Fluent Setup

Drift conditions were applied to the simulations of flow around a sphere. The external flow was xenon at 1,050 K and 6,666 Pa. The sphere diameter was 0.01 m. As discussed in the sphere background section, the simulations were done in the Reynolds number range of 20-130 to ensure a steady-state solution and low Mach numbers (less than 0.03) and with no heat flux applied at the sphere wall to avoid discrepancy with the Clift *et al.* [4] drag coefficient correlation.

Since the flow in this regime is steady and axisymmetric, a 2D, steady, axisymmetric model was used in the Fluent simulations replicating this flow. The axis was the sphere's centerline (parallel to the free-stream flow). The outer boundary was treated as a wall with no shear and no heat flux. The sphere wall was specified as a no-slip wall with zero heat flux. The inlet was specified as a mass-flow inlet, and the outlet was a pressure outlet. To achieve different Reynolds numbers, the velocity was allowed to change. Velocity and inlet size were used to calculate the flow rate, which was an input for the mass-flow inlet boundary condition. Total (or stagnation) temperature (which was specified in both the inlet and outlet) is also function of velocity and given by [21],

$$T_0 = T + \frac{V^2}{2c_p} \quad (24)$$

The Reynolds number, velocity, total temperature, and Mach number for each case are provided in Table 4.

Table 4. Velocities and Mach Numbers corresponding to Sphere Validation Cases with Different Reynolds Numbers

Re_d	Velocity (m/s)	Mach Number	Total Temperature (K)
21.1	1.4102	0.00424	1050.01
23.4	1.5639	0.00470	1050.01
29.1	1.9448	0.00584	1050.01
45	3.0074	0.00903	1050.03
50.6	3.3817	0.01016	1050.04
54.4	3.6357	0.01092	1050.04
68.9	4.6047	0.01383	1050.07
78.2	5.2263	0.01570	1050.09
88.1	5.8879	0.01769	1050.11
93.8	6.2688	0.01883	1050.12
101	6.7500	0.02028	1050.14
104	6.9505	0.02088	1050.15
108	7.2178	0.02168	1050.16
109	7.2847	0.02188	1050.17
124	8.2871	0.02489	1050.22
130	8.6881	0.02610	1050.24

The pressure-based solver was selected due to the incompressibility indicated by the low Mach numbers of the simulations. The density was treated as an ideal gas due to the high temperature and low pressure. The coupled solver was used with 2nd order upwinding schemes, 2nd order pressure discretization, and Green Gauss node-based gradient discretization for improved accuracy. Constant properties were used. Viscosity and thermal conductivity were approximated at 1,050 K from Table 2 in the xenon properties section. See Table 5 for a complete list of property values for the sphere simulations. The pseudo transient option was selected to improve the efficiency of the calculations. Default settings for the relaxation factors and solution limits were used. The solution was initialized from the inlet conditions. See Table 22 in Appendix A for a detailed list of the complete setup. All simulations discussed in the sphere validation

sections were run on a single processor on a Windows PC, and all resulting residuals were less than 1E-9.

Table 5. Xenon Properties for Sphere Validation Simulations in Drift Region at 1050 K and 6,666 Pa

Properties	Value
Dynamic Viscosity, μ	6.70e-5 kg/(m-s)
Thermal Conductivity, k	0.0159 W/(m-K)
Specific Heat at Constant Pressure, c_p	158.32 J/(kg-K)
Molecular Weight, M	131.293 g/mol

Before running the Fluent simulations at the different Reynolds numbers, the size of the domain and mesh refinement were studied. These were analyzed for the setup at a Reynolds number of 101 (with a velocity of approximately 6.75 m/s).

Sphere Validation: Domain Size and Mesh Refinement Studies

The first domain considered consisted of 10 body lengths before the sphere, 15 body lengths above the sphere, and 20 body lengths behind the sphere (where the body length is the sphere's diameter). Each mesh was made with a 1.02 overall growth rate (which has been determined sufficiently refined in the next section), 12 inflation layers surrounding the sphere wall with a 1.10 growth rate and a default transition ratio of 0.272, edge sizing along the sphere wall of 1E-4 m, and a triangle-dominated method. All simulations had the same Fluent case setup with a Reynolds number of 101. See Table 6 and Figure 5 for the results from the different domain sizes.

Table 6. Sphere Domain Size Study

Case	Body Lengths Before	Body Lengths Above	Body Lengths Behind	Nodes	Drag Force (N)	Drag Coefficient
1	10	15	20	28496	1.9480E-04	1.08597
2	5	15	20	26616	1.9581E-04	1.09161
3	20	15	20	29391	1.9457E-04	1.08473
4	30	15	20	29944	1.9455E-04	1.08460
5	10	7	20	24334	1.9511E-04	1.08770
6	10	25	20	29680	1.9475E-04	1.08569
7	10	15	5	25652	1.9474E-04	1.08566
8	10	15	10	26642	1.9475E-04	1.08569
9	10	15	30	28738	1.9475E-04	1.08570
10	20	15	5	26962	1.9455E-04	1.08462

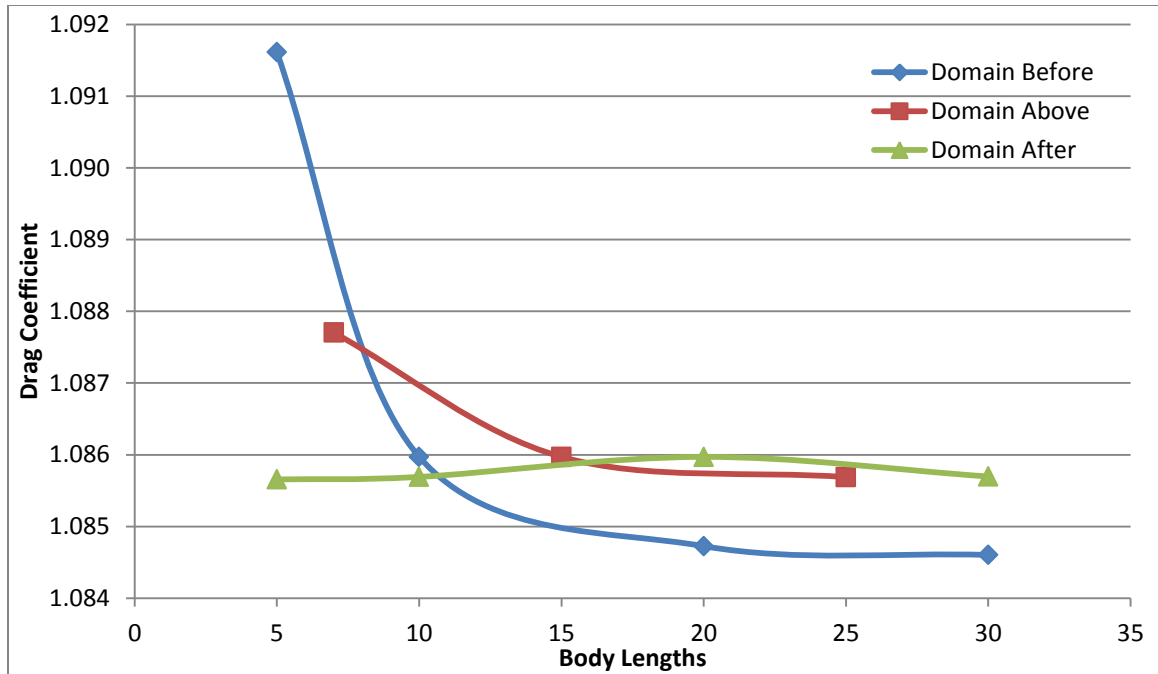


Figure 5. Sphere Domain Size Study

As can be seen in the mesh refinement section, the converged drag coefficient value appears to be close to 1.084. Therefore, cases 2 (with only 5 body lengths before the sphere) and 5 (with only 7 body lengths above the sphere) appear to produce the greatest error. Typically, as the domain increases in any direction, the drag coefficient decreases towards 1.084. When analyzing the distance before the sphere, note that there is only a 0.012% difference in the drag coefficient when changing the domain from 30 body lengths before to 20 body lengths before. The case with 10 body lengths before has 10 times this percent difference compared to the case with 30 body lengths before. The case with 5 body lengths before is even worse with 50 times the percent difference. Therefore, 20 body lengths before the sphere appears adequate to model the flow properly. When analyzing the domain above the sphere, cases with 25 and 15 body lengths above the sphere have only a 0.026% difference. Cases with 25 and 7 body lengths above the sphere have over 7 times this percent difference. Therefore, a distance

of 15 body lengths was chosen as the size of the domain above the sphere to sufficiently capture the flow. Very little percent difference in drag occurred between the cases with different domain sizes behind the sphere. Therefore, the smallest domain size simulated behind the sphere appeared acceptable. However, as the distance behind the sphere decreases, the domain will encroach upon the wake region, thus inaccurately predicting the drag coefficient. As a check, Taneda's [27] wake length plot was used to approximate the maximum wake length in this Reynolds number range. Taneda's wake length plot predicted an upper wake-length limit of 1.5 body lengths. Therefore, including 5 body lengths behind the sphere would safely avoid inaccuracies due to encroachment on the wake. Based on these results, 20 body lengths before, 15 body lengths above, and 5 body lengths behind the sphere seems to provide the most efficient and yet accurate results. The drag results with the final domain selected can be seen in case 9. Note that the drag coefficient from case 9 is almost the same as the drag coefficient closest to the converged value in Table 6 (found in case 4). Note that case 4 had one of the largest domain sizes and the most nodes. Compared to case 4, case 9 provided almost the same drag coefficient with almost 3,000 less nodes.

The mesh refinement study has been done with the chosen domain size: 20 body lengths before, 15 body lengths above, and 5 body lengths behind the sphere. As in the domain size study, 12 inflation layers with a 1.10 growth rate and default transition ratio of 0.272 were used around the sphere wall to accurately model the boundary layer.

The results from the mesh refinement study can be seen in Table 7. The first 7 cases were made with an edge size of $1\text{E-}4$ m along the sphere wall. A plot of the drag coefficient from these first 7 meshes can be seen in Figure 6. Based on the exceedingly

low percent difference between the 1.01 and 1.02 growth rate cases (0.006%) and yet large difference in the number of nodes, the 1.02 growth rate case has sufficient refinement. The last 2 cases in Table 7 explore changing the sphere edge size. Note that changing the edge size by a factor of 10 while keeping the growth rate at 1.02 has minimal effect on the results despite a large change in the number of nodes. This minimal drag coefficient change with changing edge size can also be seen in Figure 6. Therefore, the mesh from case 6 with the 1.02 growth rate, 1E-4 m edge size around the sphere, and 12 inflation layers with 1.10 growth rate and default transition ratio of 0.272 is sufficiently refined for these simulations. See Figures 7 and 8 for images of the selected mesh.

Table 7. Sphere Mesh Refinement Study

Case	Mesh Type		Nodes	Drag Force (N)	Drag Coefficient	% Difference of Drag Correlation		
	Edge Size (m)	Overall Growth Rate				Between Steps	with Correlation	with Experiment
1	1.0E-04	1.20	5158	1.98048E-04	1.10410		3.3607	2.2314
2	1.0E-04	1.15	5562	1.95884E-04	1.09204	-1.0922	2.2318	1.1149
3	1.0E-04	1.10	6423	1.95267E-04	1.08860	-0.3153	1.9095	0.7961
4	1.0E-04	1.05	9867	1.94745E-04	1.08569	-0.2674	1.6370	0.5265
5	1.0E-04	1.03	16271	1.94627E-04	1.08503	-0.0606	1.5754	0.4656
6	1.0E-04	1.02	26962	1.94554E-04	1.08462	-0.0375	1.5373	0.4279
7	1.0E-04	1.01	66847	1.94542E-04	1.08456	-0.0060	1.5312	0.4219
8	5.0E-05	1.02	40973	1.94548E-04	1.08459	0.0030	1.5343	0.4250
9	1.0E-05	1.02	65660	1.94520E-04	1.08443	-0.0144	1.5197	0.4105

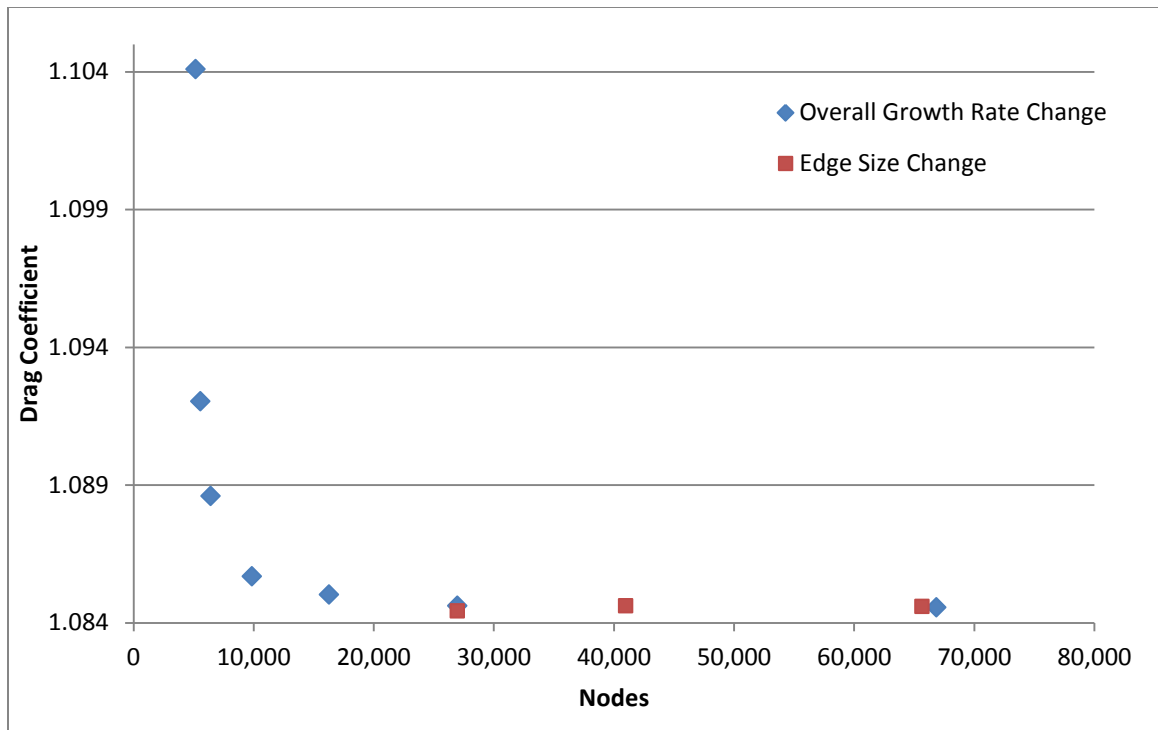


Figure 6. Sphere Mesh Convergence Plot

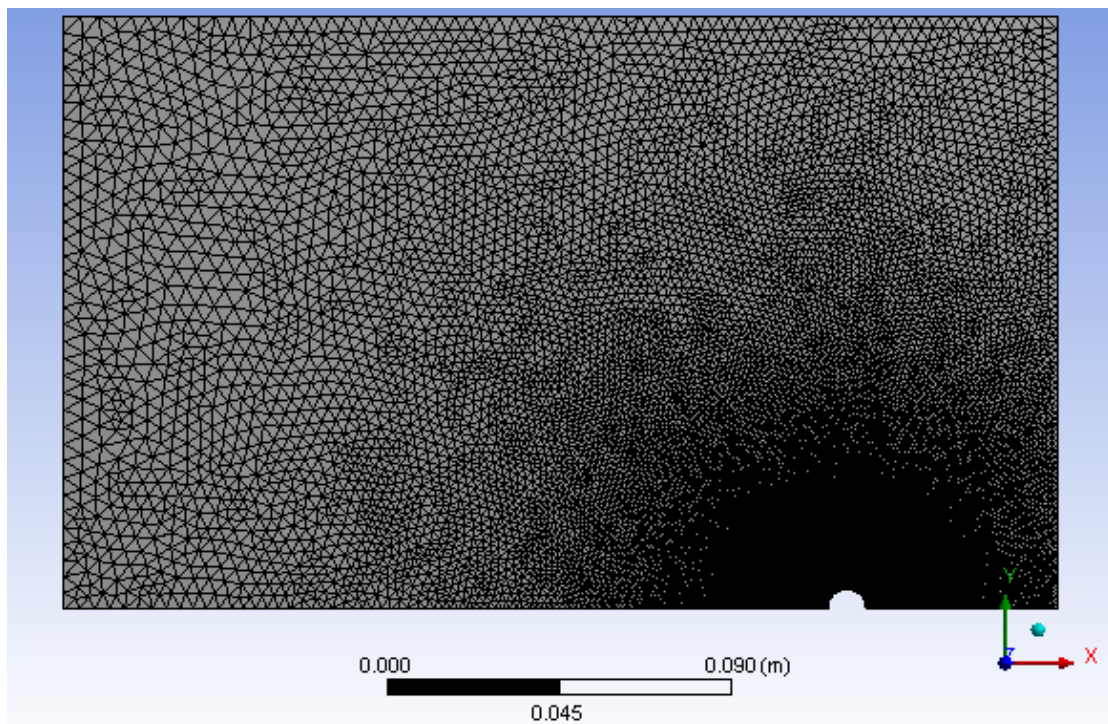


Figure 7. Selected Mesh (Case 6 from Refinement Table) for Sphere Simulations

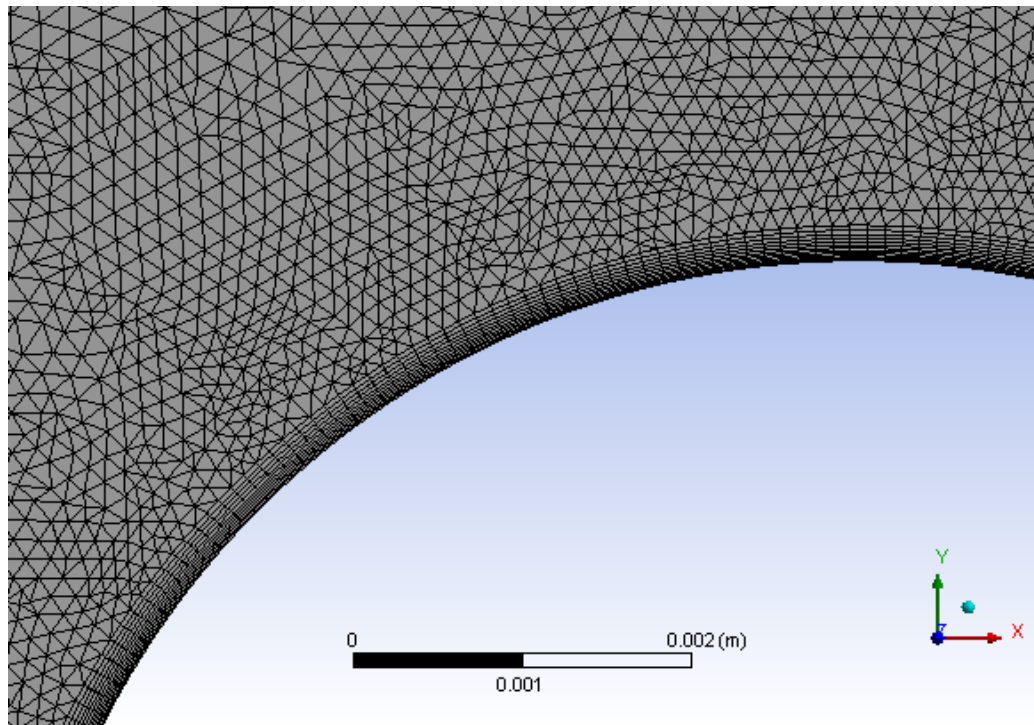


Figure 8. Inflation Layers of Selected Mesh (Case 6 from Refinement Table) for Sphere Simulations

2D, Axisymmetric Drift Regime: Fluent Setup

As mentioned in the introduction, the drift region consists of xenon gas at 1,050 K and 6,666 Pa. The target has a forward velocity of 250 m/s, spin of 1 revolution per meter traveled, and wall temperature of 20 K. A 2D, axisymmetric swirl model of this flow was utilized first. A 3D model was also done (see sections pertaining to the 3D drift regime) to examine if the flow around the target could adequately be simulated with a 2D model and calculate moments needed to determine flight stability. The remainder of this section discusses the setup for the 2D, axisymmetric swirl model.

The axis of symmetry was the target's centerline (parallel to the free-stream flow). A far-field pressure boundary condition was specified for the inlet with a Mach number of approximately 0.75 in the axial direction and a static temperature 1,050K. The outlet was specified as a pressure outlet with backflow total temperature of approximately 1,250 K. (The total temperature was calculated with equation 24 from the sphere fluent setup section.) The outer boundary of the domain was treated as a wall with no shear and no heat flux. Each target wall was specified with no slip and given an absolute rotational speed of approximately 1,571 rad/s and a wall temperature of 20 K. The operating pressure of the flow was approximately 6,666 Pa.

Since the Mach number in the drift region indicates compressible flow, the density-based solver was selected over the pressure-based solver. Due to the high temperature and low pressure of the drift region, the ideal gas assumption was reasonable and used for the density calculations. The generally recommended implicit solver and Roe-FDS convective flux were used [1]. Green Gauss node-based gradient discretization was used for improved accuracy, but only 1st order upwinding schemes for flow, turbulent kinetic energy, and specific dissipation rate were used to ensure convergence.

Due to the varying temperature from the wall to the free-stream, property correlations (functions of temperature) were used from the xenon properties section. See Table 8 for a summary of the xenon properties.

Table 8. Xenon Properties in Drift Region at 6,666 Pa for Target Simulation

Properties	Value	Units
Dynamic Viscosity, μ	$(-2.243\text{E-}11)\text{T}^2 + (8.796\text{E-}8)\text{T} - 1.167\text{E-}6$	kg/(m-s)
Thermal Conductivity, k	$(-5.323\text{E-}9)\text{T}^2 + (2.088\text{E-}5)\text{T} - 2.769\text{E-}4$	W/(m-K)
Specific Heat at Constant Pressure, c_p	158.32	J/(kg-K)
Molecular Weight, M	131.293	g/mol

As mentioned in the introduction, the Reynolds number in the drift region is 3,937. For pipe flows, the transition between laminar and turbulent flow occurs between a Reynolds number of 2,100 and 4,000 (where the characteristic length is the pipe diameter) [21]. However, this transition is more difficult to identify for external flows due to the complexity introduced by object curvature [21], the somewhat arbitrary selection of the characteristic length, and other parameters. Typically, the transition from laminar to turbulent for external flow occurs with a Reynolds number on the order of 10^5 [21]. However, the only way to accurately determine whether the flow is laminar or turbulent is through physical observation. Assuming the flow was laminar, several 2D, axisymmetric swirl, laminar target simulations were created and run. However, after performing domain size, mesh refinement, and transient studies, a converged solution could not be obtained. Therefore, a weak turbulence model was implemented instead. Although the k-epsilon models are the most widely used turbulence models, they tend to not fully take adverse pressure gradients into account and predict delayed or reduced boundary layer separation [1]. The k-omega SST model was designed to “accurately

compute flow separation from smooth surfaces” and has become the “most widely used...for aerodynamic flows” [1]. Therefore, the k-omega SST turbulence model with a weak turbulent intensity of 1% and small turbulent viscosity ratio of 1 at the inlet (and for any backflow at the outlet) has been used in each simulation presented in the drift regime sections.

A converged, steady-state solution for the 2D, axisymmetric swirl model could not be obtained for the spinning target in the drift region. Therefore, a transient model was employed. See the following section for details on how the time step size was selected. The time step used was 5.0E-7 s. Absolute convergence criteria set for all residuals was 1E-8. The maximum number of iterations per time step was 150. The residuals at the end of each time step never exceeded 10^{-3} . The transient formulation was first order implicit.

The default courant number and under-relaxation factors were used. The solution was initialized from the inlet conditions. The energy equation was automatically turned on. See these and other specific input parameters in Table 23 in Appendix A.

2D, Axisymmetric Drift Regime: Domain Size, Mesh Refinement, and Transient Considerations

For the sphere validation section, several cases were run to determine not only a converged solution, but also an optimal and computationally efficient case. Since these cases were steady-state simulations, these additional runs took less than 10 minutes. As explained in the previous section, simulating the spinning target in the drift region required transient simulations. Since transient cases must calculate a solution at each time step instead of one solution at steady state, transient simulations take much longer to complete. On a single processor, these simulations typically took 2-3 days to finish a calculation with 2,000 time steps. (The time to run a simulation varied depending on the number of nodes.) Therefore, simple convergence studies were performed to identify a 2D, axisymmetric target case that produced a reasonably converged solution. Computational efficiency was not explored.

An initial guess was made for an adequate domain size and mesh refinement for the 2D target simulations based on the mesh refinement and domain size studies on the sphere simulations. The initial domain extended 20 body lengths in front of the target, 15 body lengths above the target, and 20 body lengths behind the target. Although a distance of only 5 body lengths behind the sphere was acceptable in the sphere simulations, this domain was extended due to the larger Reynolds number of the flow around the target. The mesh of this domain was given 12 inflation layers with a growth rate of 1.10 and default transition ratio of 0.272, an overall growth rate of 1.02, and a target edge size of $5\text{E-}5$ m. Although an edge size of $1\text{E-}4$ m was sufficient in the sphere validation case, this was reduced due to the angularity of the target's geometry.

An initial guess for an adequate time step was also determined based on results from a sphere. Sakamoto and Haniu [25] measured the frequencies of wake fluctuation behind a sphere and plotted the non-dimensional form of this frequency (low-mode Strouhal number) as a function of Reynolds number in the Reynolds number range of 3,000-40,000. All Strouhal numbers (St) in this range were less than 0.26. Using the definition of the Strouhal number [25],

$$St = \frac{fd}{v} \quad (25)$$

the maximum frequency of wake fluctuation (f) for a sphere with the same diameter as the target can be calculated as approximately 6,190 Hz. Therefore, an oscillation would occur at least every 1.6E-4 s. Dividing this oscillation period into 150 time steps should allow Fluent to effectively capture the flow oscillation. This would be a time step of approximately 1.0E-6 s. Since this is an approximation for a sphere, the initial time step used in the drift target simulations was half of this value or 5.0E-7 s.

This initial case (with domain, mesh refinement, and time step described previously) was run and compared to cases with larger domains in each direction to determine if the domain of the initial test case (20 body lengths before, 15 body lengths above, and 20 body lengths behind) was adequate. The drag coefficient and heat transfer after 1 ms were used as points of comparison. The results can be seen in Table 9. Note that this is a transient flow, and some of the variance between cases is due to its dynamic nature. Less than a 4% difference in drag and a 2% difference in heat transfer between cases for a 2D, axisymmetric swirl model of a 3D flow after only 1 ms is reasonable. Therefore the initial domain of 20 body lengths before, 15 body lengths above, and 20 body lengths behind was accepted as adequately encompassing the flow field.

Table 9. Domain Study on 2D, Axisymmetric Swirl, Transient Drift Flow over Target

Case	Body Lengths Before	Body Lengths Above	Body Lengths Behind	Nodes	Drag Force (N) at 1 ms	Drag Coefficient at 1 ms	Drag % Difference with Case 1	Heat Transfer (W) at 1 ms	Heat Transfer % Difference with Case 1
1	20	15	20	47285	0.1512	0.5572		25.13	
2	30	15	20	48232	0.1559	0.5746	-3.036	25.45	1.254
3	20	25	20	49607	0.1514	0.5580	-0.149	25.44	1.223
4	20	15	30	48190	0.1533	0.5653	-1.428	25.58	1.775

The initial case's mesh was then compared to more refined and coarser meshes to determine adequate refinement of the domain. As previously mentioned, the initial test case's mesh had 12 inflation layers with a 1.10 growth rate and a default transition ratio of 0.272, an overall growth rate of 1.02, and a target edge size of 5E-5 m. The more refined mesh was made by reducing the edge size to 2.5E-5 m and lowering the overall growth rate to 1.015. One of the coarser meshes had an increased edge size of 1E-4 m and overall growth rate of 1.06. The coarsest mesh had an edge size of 2.5E-4 m and overall growth rate of 1.08. Table 10 and Figure 9 show the comparison between these 4 levels of refinement based on the drag coefficient and heat transfer after 1 ms. Note that almost doubling the nodes in the mesh from the initial case results in only a 0.75% difference in drag and only a -0.04% difference in heat transfer. Therefore, the initial case is sufficiently refined. Figures 10 and 11 show the final domain and mesh used for the 2D, axisymmetric swirl simulations.

Table 10. Mesh Refinement Study on 2D, Axisymmetric Swirl, Transient Drift Flow over Target

Case	Nodes	Drag Force (N) at 1 ms	Drag Coefficient at 1 ms	Drag % Difference with Case 1	Heat Transfer (W) at 1 ms	Heat Transfer % Difference with Case1
1	47285	0.1512	0.5572	NA	25.13	
2	80114	0.1523	0.5614	0.753	25.12	-0.0426
3	10312	0.1585	0.5841	4.830	25.17	0.1423
4	4851	0.1734	0.6391	14.58	28.87	14.86

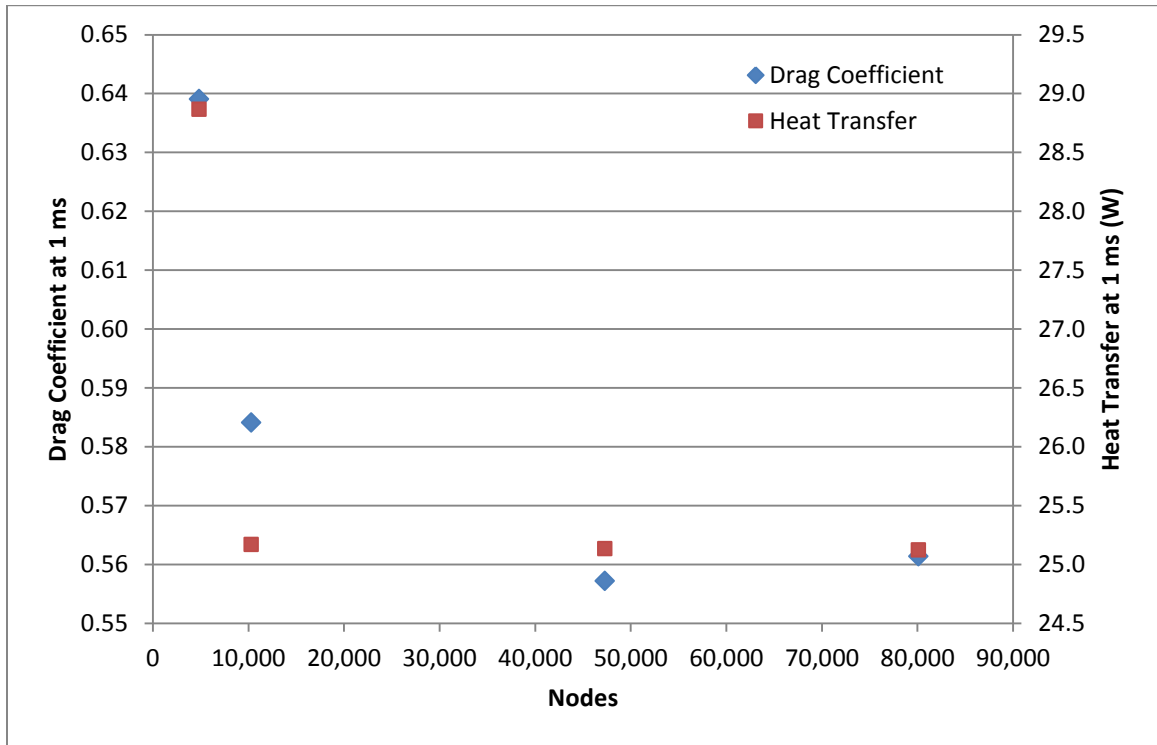


Figure 9. 2D, Axisymmetric Swirl Target Mesh Convergence Plot

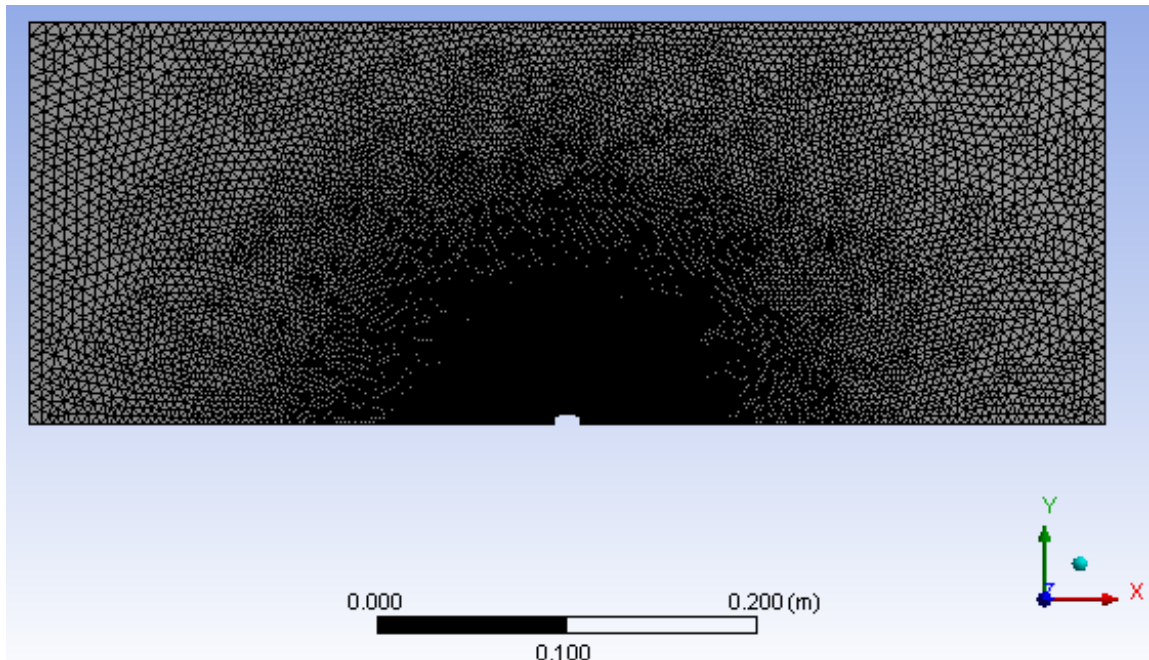


Figure 10. Entire View of 2D, Axisymmetric Target Mesh

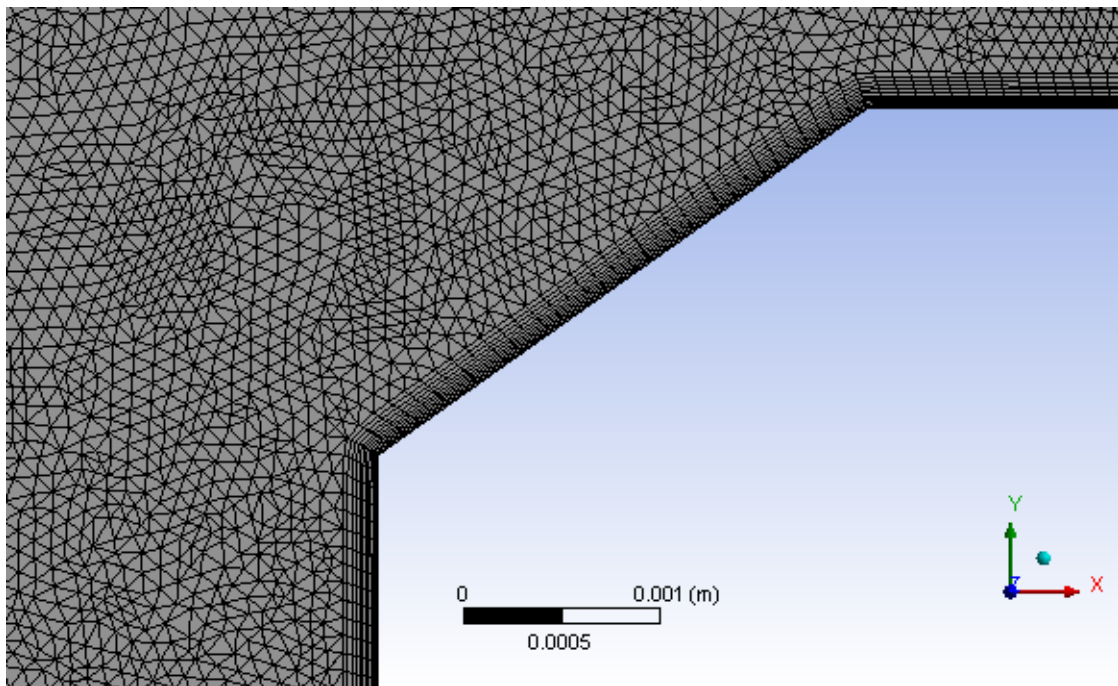


Figure 11. Inflation Layer View of 2D, Axisymmetric Target Mesh

Finally, the initial guess for the time step size, $5.0\text{E-}7$ s, was evaluated. The drag coefficient and heat transfer results from a case with the same domain and mesh but with a smaller time step ($2.0\text{E-}7$ s) were compared to those from the initial case. Table 11 shows the minimal effect of time step size on both drag and heat transfer at 1 ms. Reducing the original time step by more than half the original value changed the drag coefficient and heat transfer at 1 ms by approximately 0.7%. Therefore, the original time step, $5.0\text{E-}7$ s, is sufficient for modeling the flow.

Table 11. Time Step Size Study on 2D, Axisymmetric Swirl, Transient Drift Flow over Target

Case	Time Step (s)	Drag Force (N) at 1 ms	Drag Coefficient at 1 ms	Drag % Difference with Case 1	Heat Transfer (W) at 1 ms	Heat Transfer % Difference with Case 1
1	5.00E-07	0.1512	0.5572		24.97	
2	2.00E-07	0.1522	0.5610	0.672	25.13	0.673

The domain size, mesh refinement, and time step studies have shown the initial case is capable of providing relatively precise (within 5%) drag and heat transfer values after simulating only 1 ms. Steady-state results (like those provided in the 3D target simulations) should provide even higher levels of precision. The results presented in the 2D, axisymmetric swirl section are the results from this initial transient, 2D, axisymmetric swirl case.

3D Drift Regime: Fluent Setup

It was necessary to develop a 3D model of the flow around the target in the drift region. Comparison of the results from the 3D model and the 2D, axisymmetric swirl model discussed in the previous sections would determine if the flow over the target in the drift region can adequately be modeled as axisymmetric. Additionally, analyzing the target's flight stability by varying the angle of attack could only be accomplished with a 3D model. Due to the large number of nodes, the 3D simulations were run across 120 parallel processors on LLNL clusters. All simulations presented in the 3D drift regime sections had residual drops of over 4 orders of magnitude unless otherwise specified.

Much of the setup discussed in the Fluent setup section for 2D, axisymmetric swirl models applies to the 3D case setup as well. Since the 2D, axisymmetric swirl model indicated the flow reaches a steady state after roughly 1 ms and the flight through the drift region is approximately 16 ms (see 2D, axisymmetric drift results section), the 3D cases were setup as steady-state. Note that a 3D laminar case was also attempted, but the continuity residual grew to unusable values. Like with the 2D, axisymmetric swirl cases, a k-omega SST turbulence model was used instead. Table 24 in Appendix A summarizes the Fluent input parameters for the 3D target case in the drift region.

Due to limited access to high performance computing licenses, only 1 3D simulation could run at any given time. Keeping the deadline in mind, it was recommended to base mesh refinement, domain size, and time step size on results from the 2D, axisymmetric swirl studies in the previous section. Therefore, the domain size from the 2D, axisymmetric swirl model was adopted: 20 body lengths before, 15 body lengths above, and 20 body lengths behind the target. The fluid region was created by sketching the 2D, axisymmetric domain in the x-y plane and revolving it 360° about the

x-axis. The refinement of this domain was limited by the 8GB of memory available on the computer used for meshing. The most refined mesh created consisted of 12 inflation layers with a 1.10 growth rate and default transition ratio of 0.272, overall growth rate of 1.03, target face size of 1E-4 m, and advanced size function on proximity and curvature. This mesh provided 5,450,161 nodes, and it is pictured in Figures 12-14.

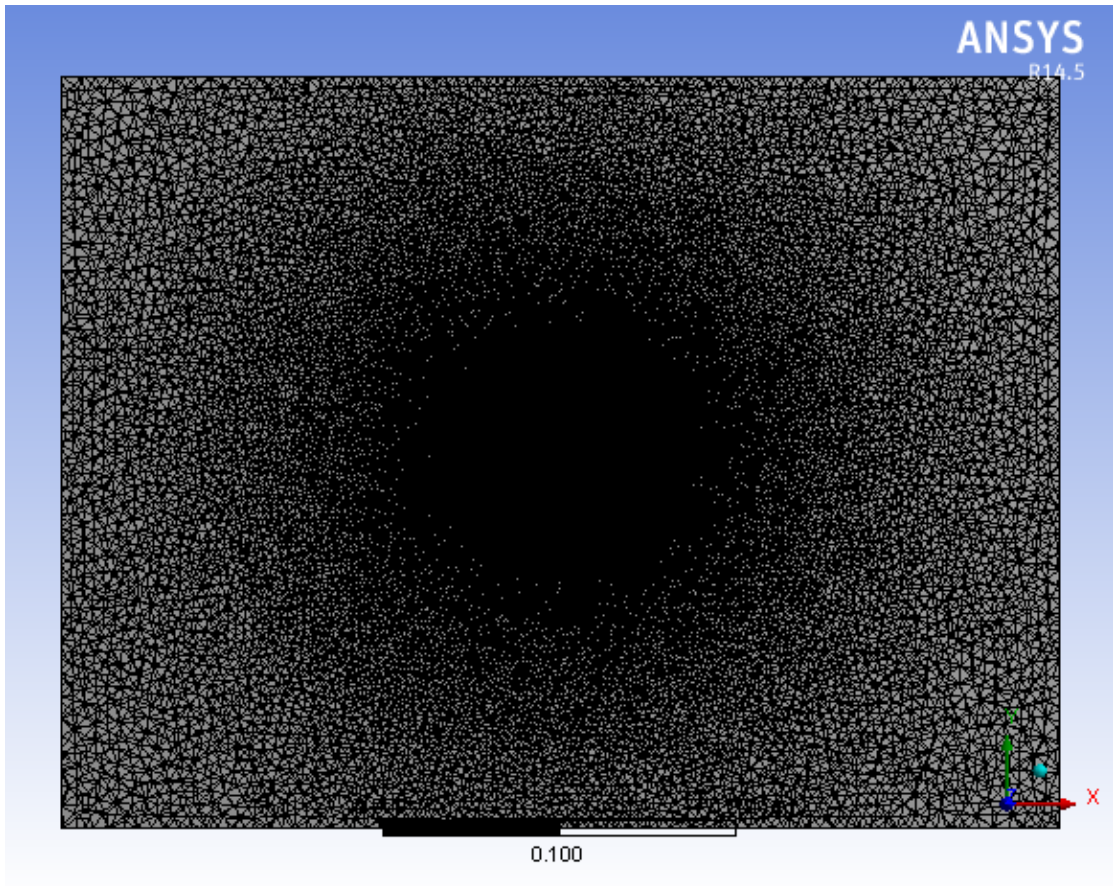


Figure 12. Overall View of 3D Target Mesh Sliced at X-Y Plane

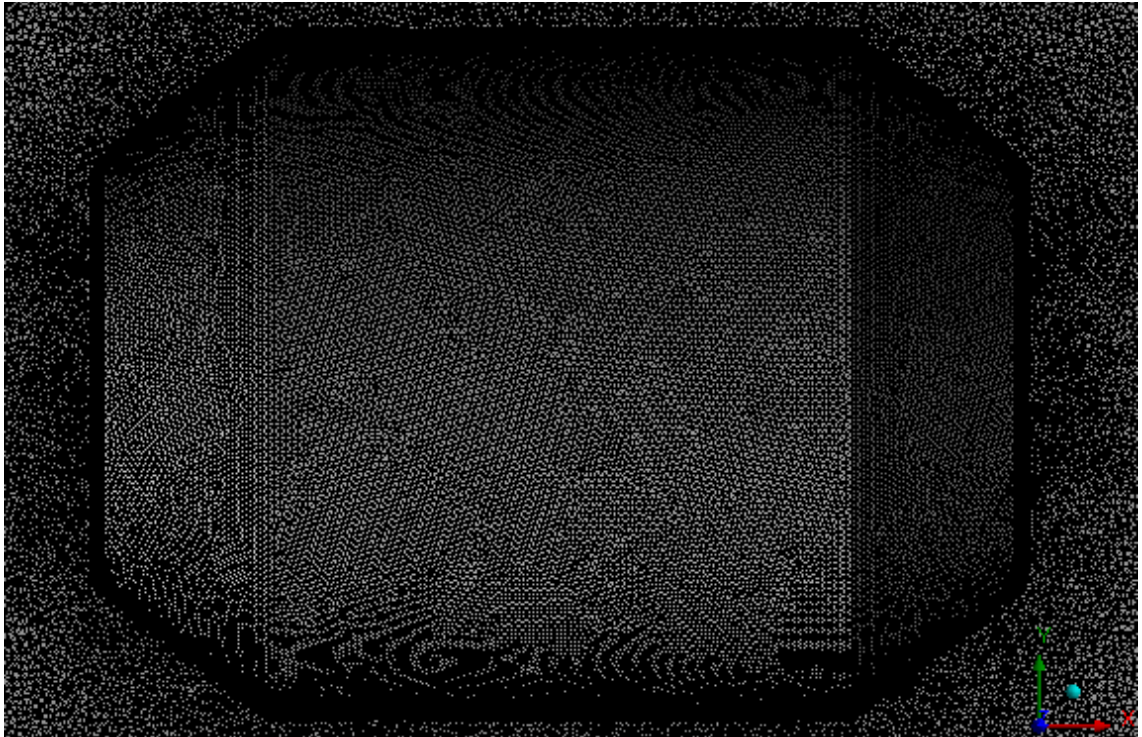


Figure 13. Zoomed-in View of Target in 3D Target Mesh Sliced at X-Y Plane

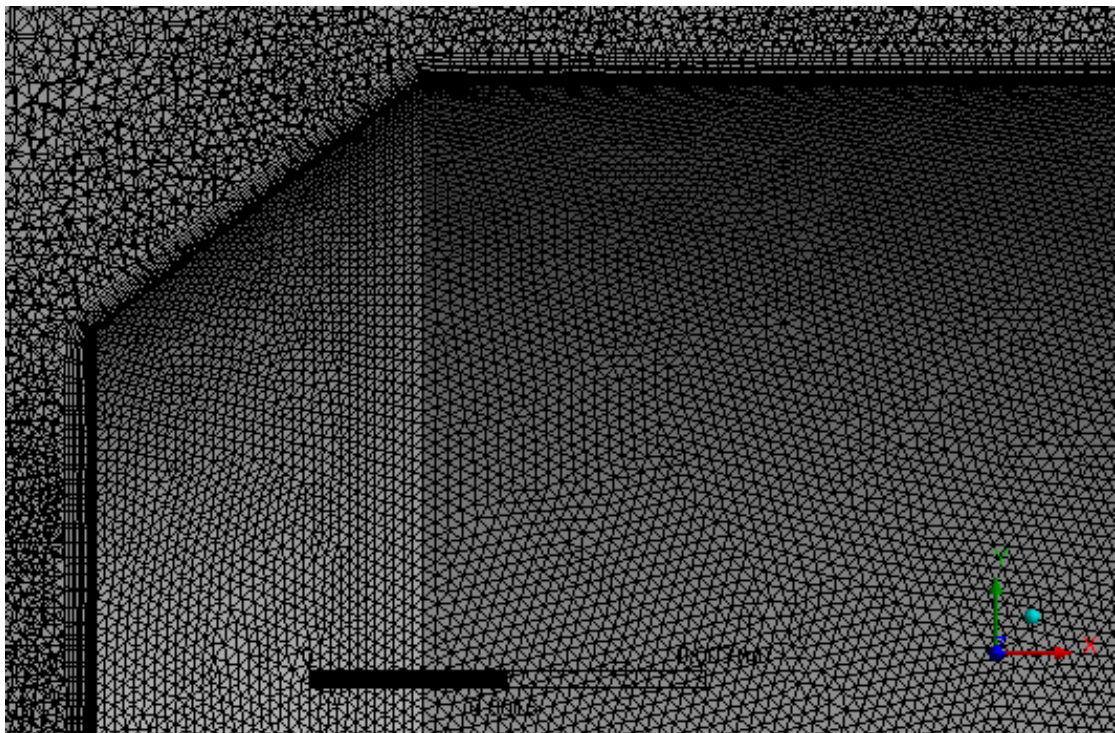


Figure 14. Inflation Layer View of 3D Target Mesh Sliced at X-Y Plane

To achieve the different Reynolds numbers in the drift region, the velocity was allowed to change. Velocity was used to calculate the inlet Mach number, which was an input for the far-field pressure inlet boundary condition. The total temperature was also calculated for each velocity using equation 24 and used as the backflow total temperature in the pressure outlet boundary condition. See Table 12 below for the velocity, Mach number, and total temperature for each case.

Table 12. Velocities and Mach Numbers for 3D, Steady-State Target Simulations with Different Reynolds Numbers

Case	Reynolds Number	Velocity (m/s)	Mach Number	Total Temperature (K)
1	3937	250.0	0.75097	1247.4
2	2400	152.74	0.45883	1123.7
3	2800	178.2	0.53530	1150.3
4	3200	212.6	0.63863	1192.7
5	3600	229.12	0.688244	1215.8
6	4400	280.03	0.841187	1297.7
7	4800	305.49	0.917659	1344.7
8	5200	330.95	0.99413	1395.9
9	5600	356.4	1.0706	1451.2

The flight stability of the target was analyzed by examining the forces and moments on the target at different angles of attack. The target was rotated at 1°, 2°, 5°, 10°, 15°, and 20° from the horizontal axis. To create these simulations, an axisymmetric, rectangular sketch of the overall domain was created in the x-y plane and revolved 360° about the x-axis. Then, an axisymmetric sketch of the angled target was drawn in the x-y plane. This target sketch was rotated 360° about its own axis of symmetry and cut from the original domain. Due to the target rotation, a new centerline for the spin axis needed to be defined for each angle of attack case. These axes can be seen in Table 13. Each of these cases had the same meshing parameters as the original 0° angle of attack case with

5,450,161 nodes. A second set of simulations were run at these same angles without spin to show the effect of spin on aerodynamic forces and moments.

Table 13. 3D, Steady-State Target Spin Axis for Varying Angle of Attack Cases

Case	Angle of Attack (degrees)	Spin Axis Defined from (0, 0, 0)
1	1	(0.00689895, -0.000120422, 0)
2	2	(0.0068958, -0.00024081, 0)
3	5	(0.0068737, -0.000601375, 0)
4	10	(0.0067952, -0.0011982, 0)
5	15	(0.0066649, -0.0017859, 0)
6	20	(0.0064839, -0.0023599, 0)

CHAPTER 4: RESULTS

Sphere Validation: Results

Since the Roos and Willmarth [24] experiment results were one of the sources of comparison for the sphere drag coefficient, the velocities used in the Fluent simulations were calculated to result in the same Reynolds numbers from their experiments in the 20-130 Reynolds range. Table 14 and Figure 15 show the Fluent drag coefficients, Roos and Willmarth [24] drag coefficients, and Clift *et al.* [4] correlation drag coefficients at these Reynolds numbers. The percent difference between the Fluent drag coefficients and the 2 other publish results can also be seen in Table 14. The Fluent drag coefficients had less than 0.5% difference when compared to the Clift correlation. When compared to the Roos and Willmarth experimental data, the Fluent simulations had a maximum and minimum percent differences of 9.37% and -6.68%. However, the average percent difference was only -0.21%, indicating a random scattering. Recall that Roos and Willmarth predicted a maximum of 5% error in their drag calculations due to experimental fluctuations. It would appear that the experimental data lacks a high level of precision. A figure displaying the spread of the percent difference with the 2 published sources can be seen in Figure 16. Based on the close alignment with the Clift *et al.* correlation [4] and low average percent difference with the Roos and Willmarth experimental data [24], the Fluent simulations are very successful at modeling the drag on a sphere with drift flow conditions.

Table 14. Sphere Drag Coefficient Comparison

Re	Drag Coefficient			% Difference	
	Roos and Willmarth Experiment	Clift Correlation 20<Re<260	Fluent	with Experiment	with Clift Correlation
21.1	2.82	2.643	2.632	-6.680	-0.414
23.4	2.48	2.474	2.467	-0.518	-0.289
29.1	2.28	2.161	2.160	-5.268	-0.065
45	1.79	1.671	1.675	-6.441	0.219
50.6	1.58	1.564	1.568	-0.769	0.262
54.4	1.52	1.502	1.506	-0.916	0.281
68.9	1.34	1.320	1.324	-1.157	0.315
78.2	1.27	1.234	1.238	-2.489	0.316
88.1	1.12	1.160	1.164	3.891	0.306
93.8	1.03	1.123	1.126	9.367	0.296
101	1.08	1.082	1.085	0.424	0.282
104	1.05	1.066	1.069	1.764	0.275
108	1.02	1.045	1.048	2.770	0.264
109	1.03	1.041	1.043	1.299	0.262
124	0.994	0.976	0.978	-1.619	0.211
130	0.927	0.953	0.955	3.036	0.186

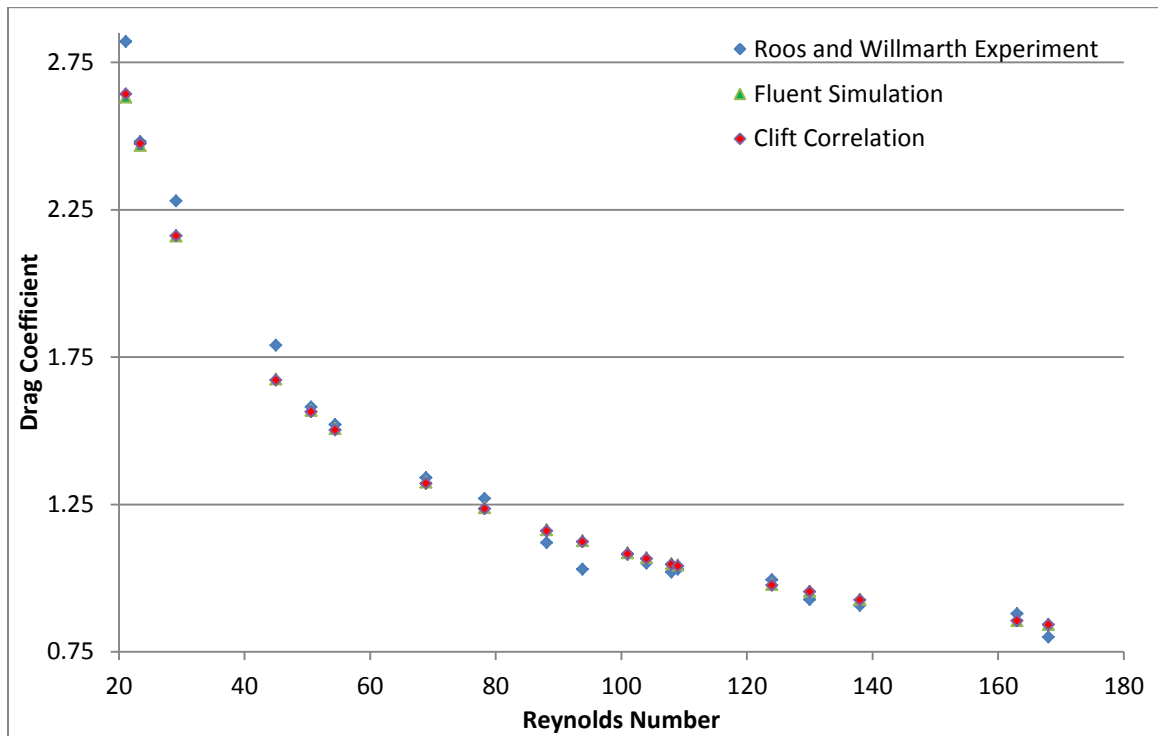


Figure 15. Sphere Drag Coefficient versus Reynolds Number for Experimental Data, a Published Correlation, and Fluent Simulation Results

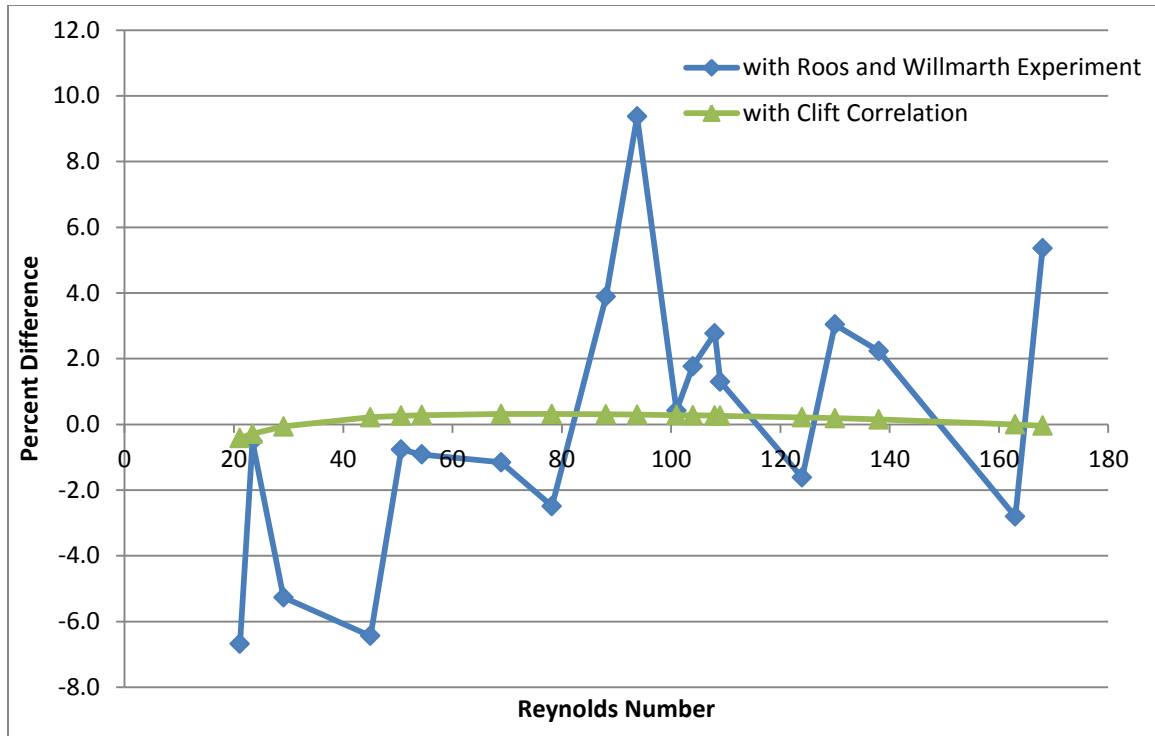


Figure 16. Graph of Percent Difference between Fluent Results and Experimental Data and a Published Correlation

The separation angle (measured from the front stagnation point to the separation point) in the Fluent simulation was determined by using the approximated location of zero wall shear stress as the separation point. To more closely approximate the location of separation, more nodes along the sphere wall were desired. Therefore, case 8 from the mesh refinement study (which had an edge size of $5\text{E-}5$ m, an overall growth rate of 1.02, and approximately 40,980 nodes) was used to produce the wall shear stress data. Figure 17 shows plots of the wall shear stress on the sphere from the front stagnation point to the back stagnation point for cases with different Reynolds numbers. The zero wall shear stress location for each case was estimated to be at the node closest to the smallest wall shear stress. (Note that the front and rear stagnation points were omitted from this minimum wall shear stress determination.) Since the nodes along the curved sphere wall were approximately $5.0\text{E-}5$ m apart, the separation angle had a maximum error of +/-

0.29° due to node spacing. The Fluent separation angles at different Reynolds numbers were compared to those determined by the Clift *et al.* [4] equation reproduced in the background section in Table 15. Notice that the Fluent separation angles are within 2.5% of the expected angles predicted by the correlation. Most of the separation angles are within 0.5%. The largest discrepancy occurred with the cases with the lowest Reynolds numbers. Considering over half of the 0.5% difference can be attributed to node spacing alone, Fluent’s ability to determine the separation in this flow field is satisfactory.

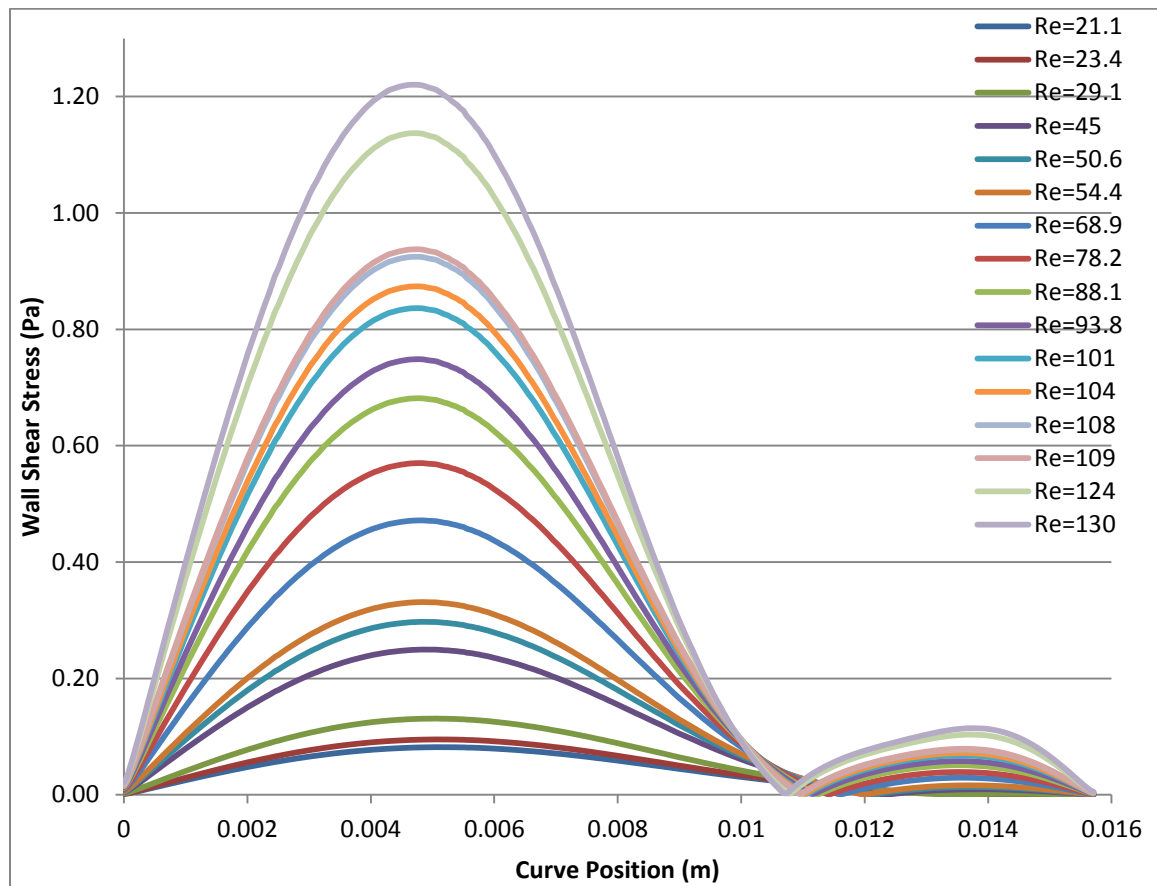


Figure 17. Wall Shear Stress Plot on Sphere at Different Reynolds Numbers

Table 15. Sphere Separation Angles (from Front Stagnation Point to Separation Point) from Fluent Simulations and Clift Correlation at Different Reynolds Numbers

Re	Separation Angle (degrees)		% Difference with Correlation
	Fluent	Clift's [4] Correlation	
21.1	173.70	169.66	2.376
23.4	163.95	162.62	0.818
29.1	153.63	153.54	0.064
45	141.60	141.59	0.003
50.6	138.73	139.00	-0.198
54.4	137.58	137.49	0.068
68.9	132.99	132.90	0.068
78.2	131.27	130.63	0.491
88.1	128.98	128.59	0.300
93.8	127.83	127.56	0.216
101	126.68	126.36	0.259
104	126.11	125.89	0.175
108	125.54	125.30	0.193
109	125.54	125.15	0.308
124	123.25	123.18	0.056
130	122.67	122.47	0.165

The flow around the sphere was also analyzed by viewing the Fluent velocity contours and streamlines. Figures 18-33 show the velocity contour plots overlaid with streamlines for the different Reynolds number cases. Notice that the velocity of the fluid increases as it passes over the front of the sphere. This occurs because the sphere does not have a negligible thickness (like a flat plate) [21], and the incompressible flow is forced to flow through a smaller cross-sectional area. By continuity, this would require an increased fluid velocity [21]. Also note that the wake is concave for the first 3 figures (where the Reynolds number is below 35) and convex for the remaining 13 figures (where the Reynolds number is above 35). This agrees well with Nakamura's [22] observations that the wake structure changes from concave to convex as the Reynolds number increases, and the transition occurs near a Reynolds number of 35. Note that the

separation is not apparent in the first 2 cases ($Re=21.1$ and $Re=23.4$) in Figures 18 and 19. This is due to the low speed near the rear stagnation point and coarse selection of streamline points. By adding more streamlines and zooming in on the region behind the sphere, small wake regions are visible at both Reynolds numbers (21.1 and 23.4) (see Figures 34 and 35). It is clear that out of these 16 cases, the case with the lowest Reynolds number ($Re=21.1$) has the smallest separation region. In the separation angle study, this case had the largest separation angle (173.7°), indicating a separation point only 6.3° from the rear stagnation point. This aligns well with Clift's [4] estimation that separation appears near a Reynolds number of 20.

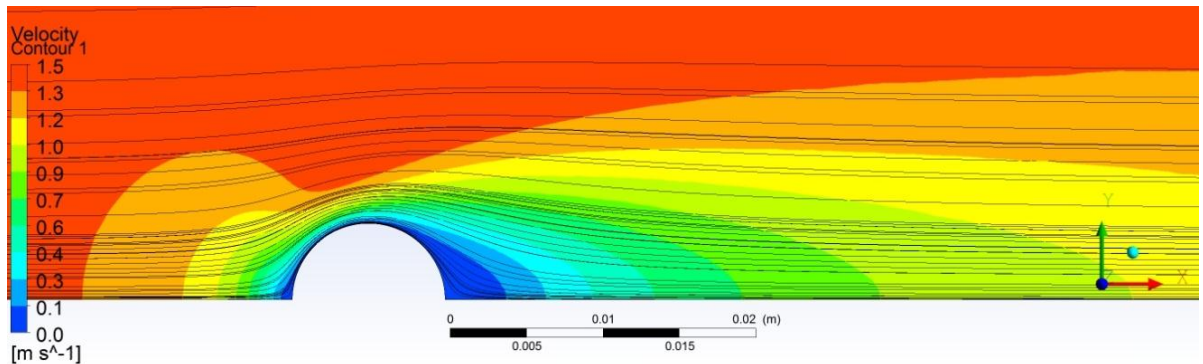


Figure 18. Sphere Velocity Contour with Streamlines Overlaid at $Re=21.1$

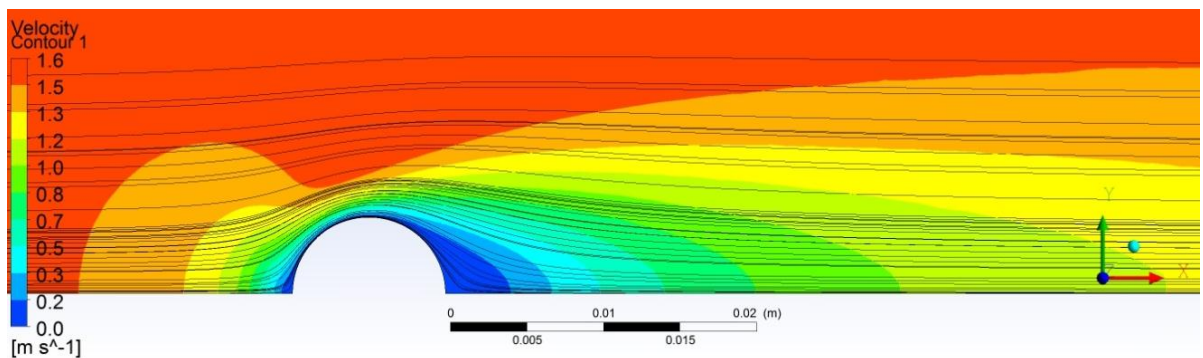


Figure 19. Sphere Velocity Contour with Streamlines Overlaid at $Re=23.4$

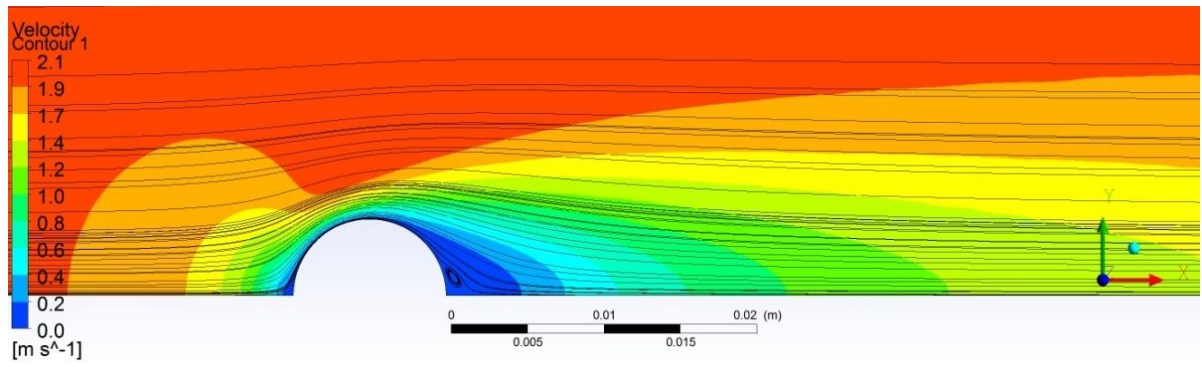


Figure 20. Sphere Velocity Contour with Streamlines Overlaid at $Re=29.1$

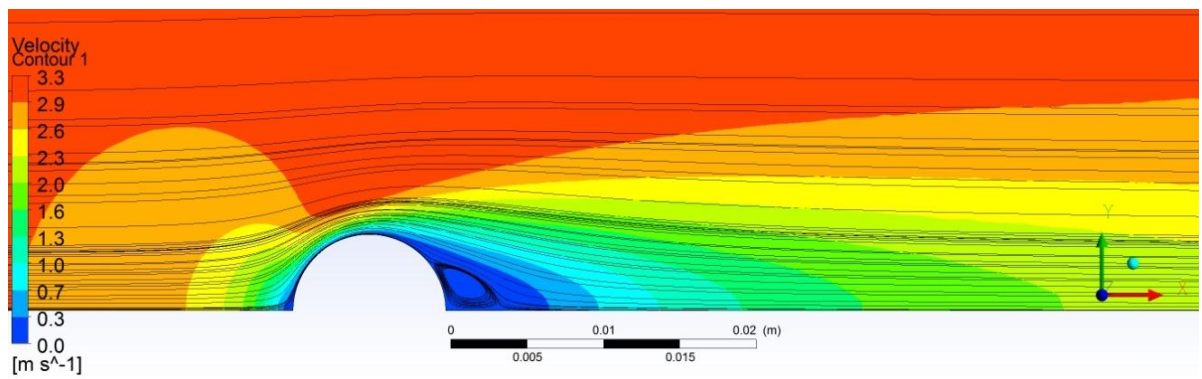


Figure 21. Sphere Velocity Contour with Streamlines Overlaid at $Re=45$

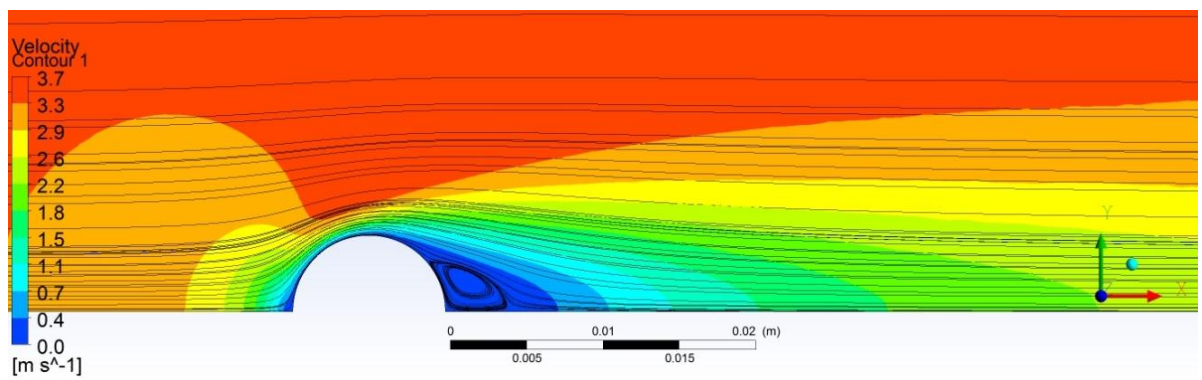


Figure 22. Sphere Velocity Contour with Streamlines Overlaid at $Re=50.6$

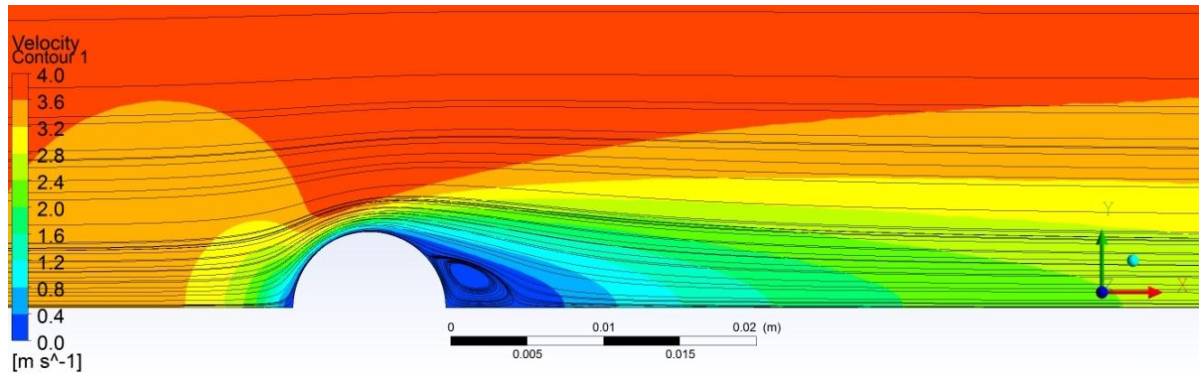


Figure 23. Sphere Velocity Contour with Streamlines Overlaid at $Re=54.4$

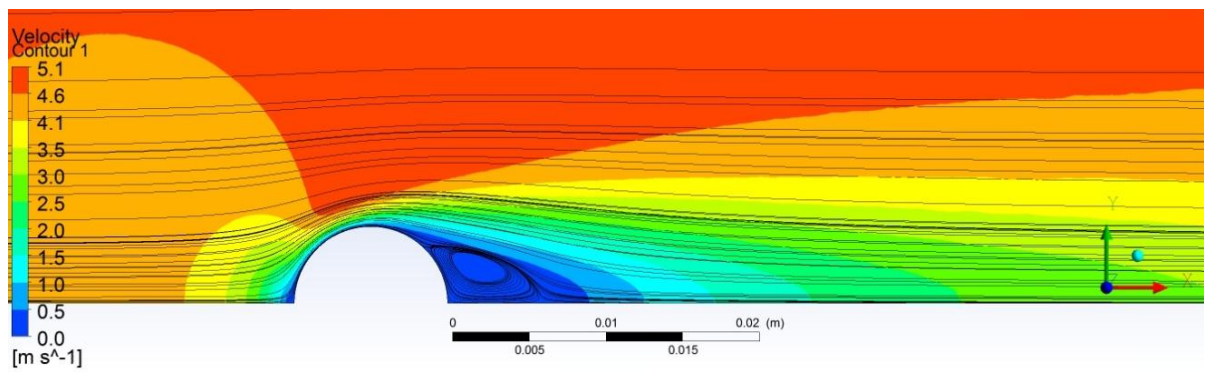


Figure 24. Sphere Velocity Contour with Streamlines Overlaid at $Re=68.9$

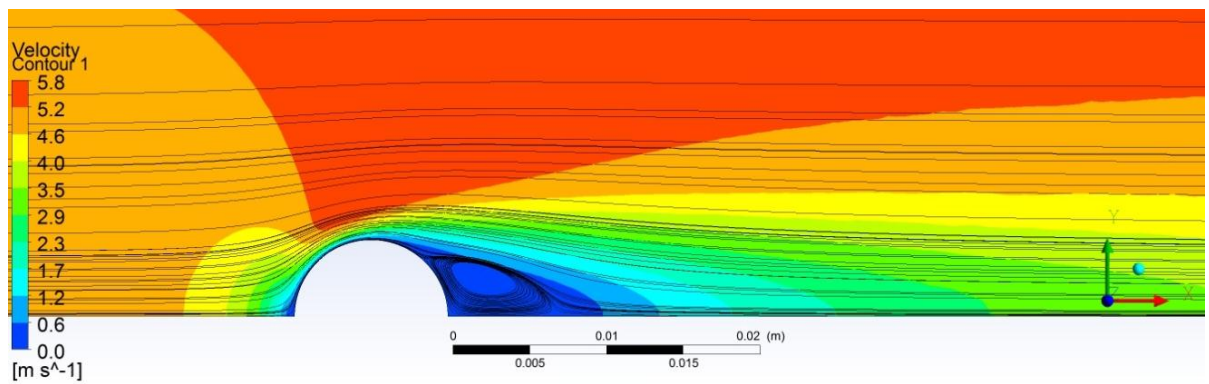


Figure 25. Sphere Velocity Contour with Streamlines Overlaid at $Re=78.2$

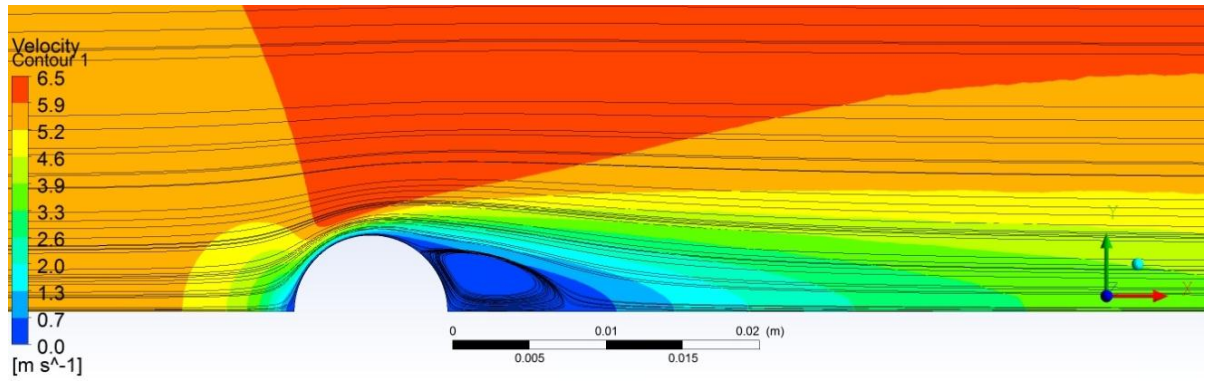


Figure 26. Sphere Velocity Contour with Streamlines Overlaid at Re=88.1

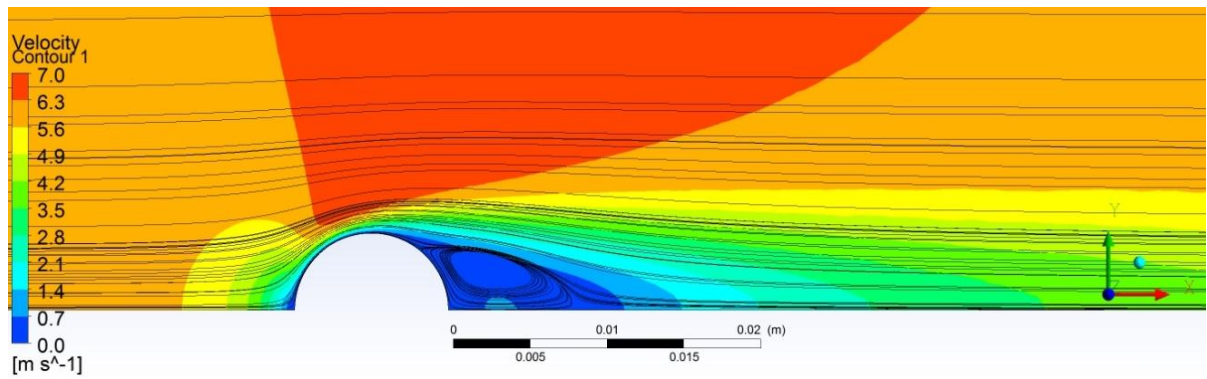


Figure 27. Sphere Velocity Contour with Streamlines Overlaid at Re=93.8

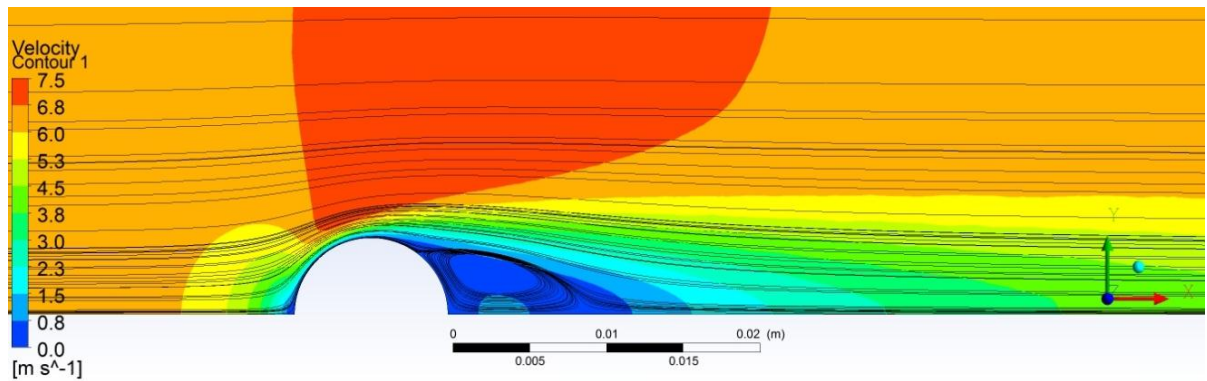


Figure 28. Sphere Velocity Contour with Streamlines Overlaid at Re=101

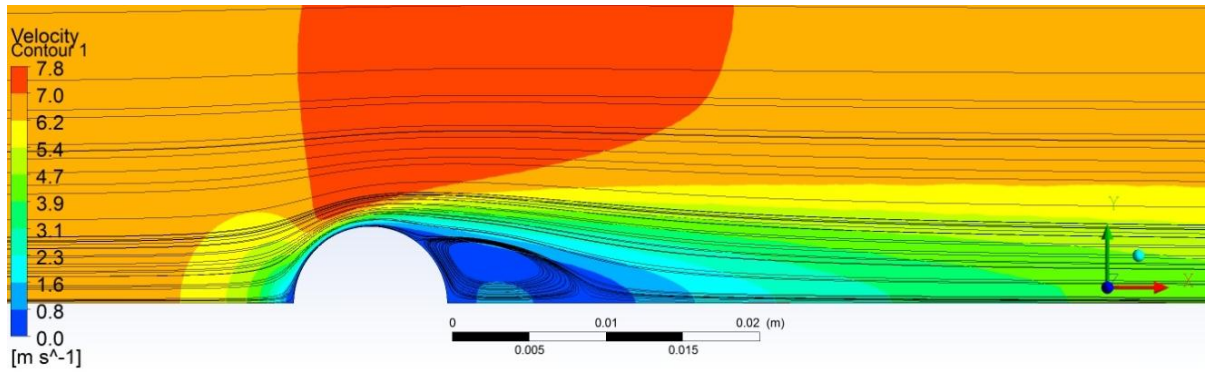


Figure 29. Sphere Velocity Contour with Streamlines Overlaid at $Re=104$

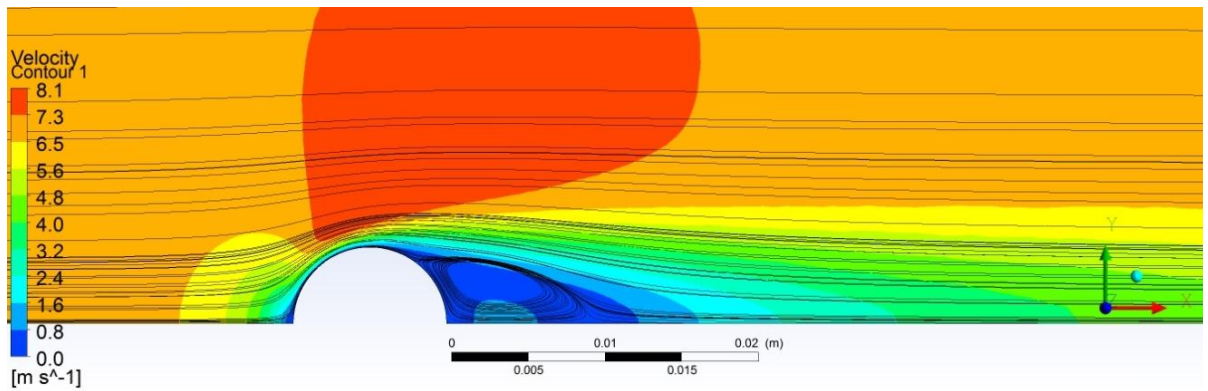


Figure 30. Sphere Velocity Contour with Streamlines Overlaid at $Re=108$

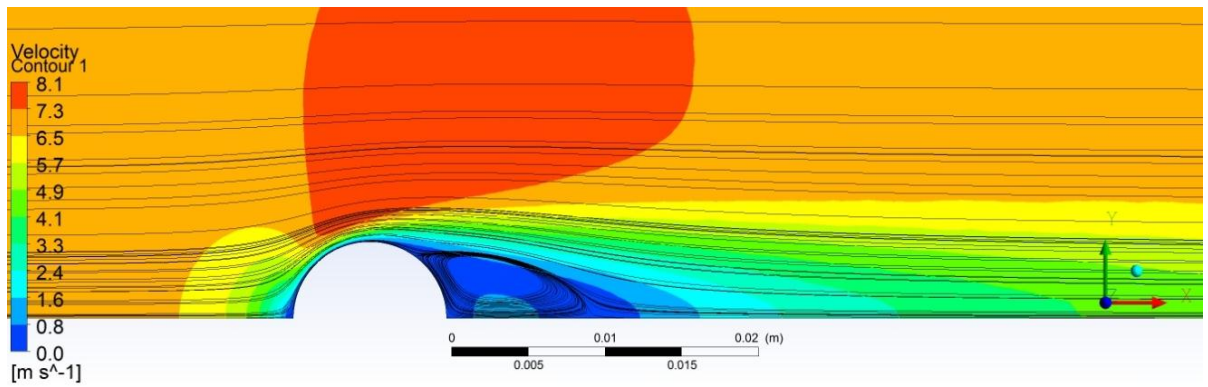


Figure 31. Sphere Velocity Contour with Streamlines Overlaid at $Re=109$

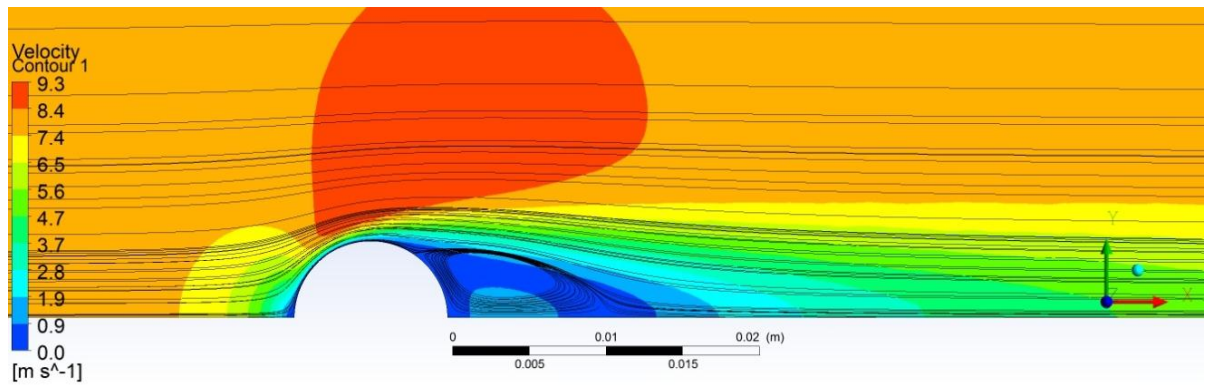


Figure 32. Sphere Velocity Contour with Streamlines Overlaid at $Re = 124$

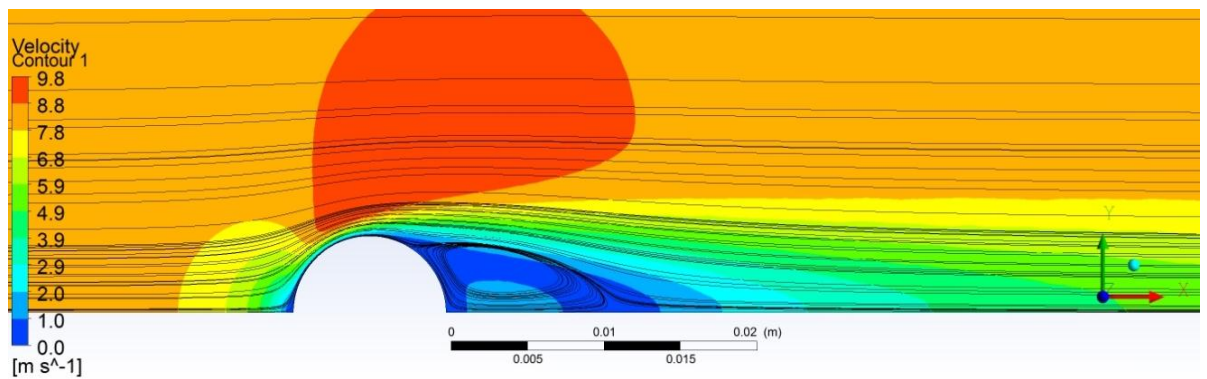


Figure 33. Sphere Velocity Contour with Streamlines Overlaid at $Re=130$

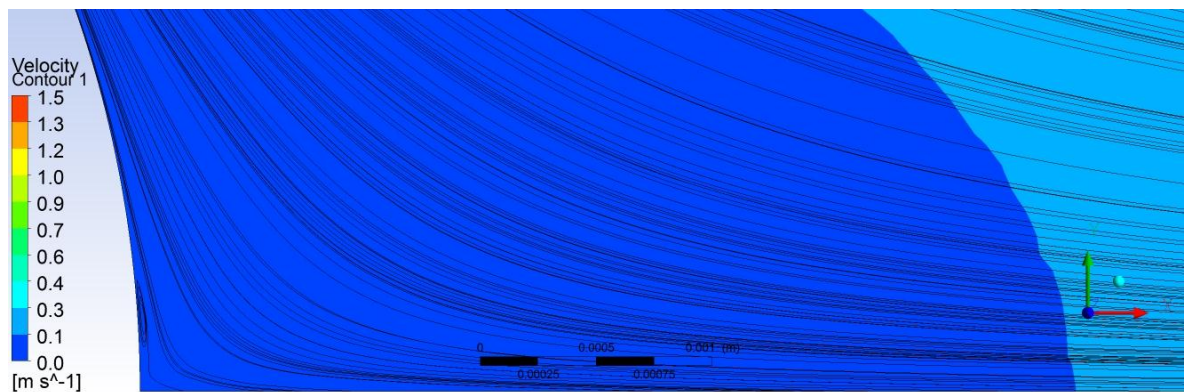


Figure 34. Zoomed-in View of Sphere Velocity Contour with Streamlines Overlaid at $Re = 21.1$

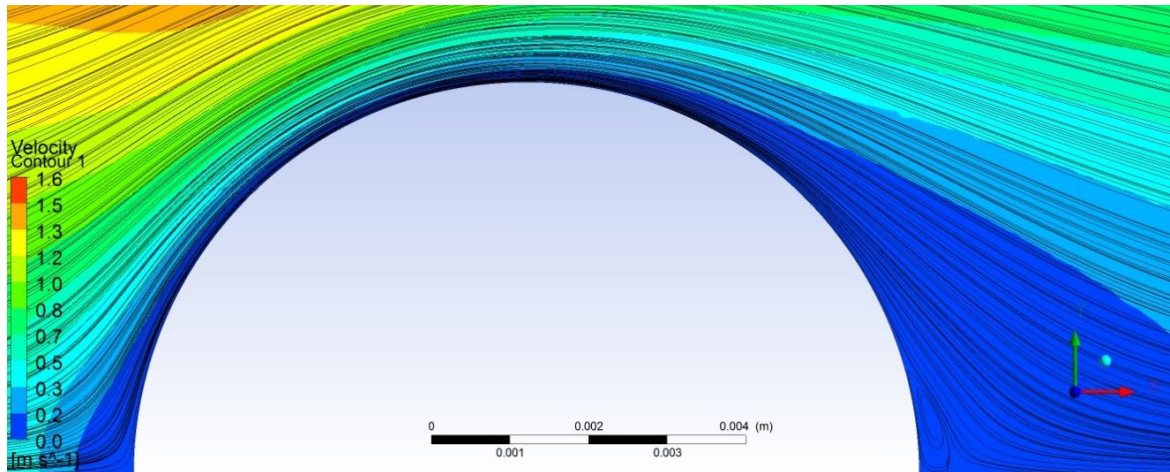


Figure 35. Zoomed-in View of Sphere Velocity Contour with Streamlines Overlaid at $Re = 23.4$

Based on the previously discussed sphere results and their fair alignment with published results for the drag coefficient, separation angle, and wake structure, the Fluent sphere simulations provided a high-level of accuracy. Since the flow conditions, mesh generation method, fluid properties, and assumptions are similar between the sphere and target simulations, it would be reasonable to assume similar levels of accuracy.

2D, Axisymmetric Drift Regime: Results

This section presents the results of the transient, 2D, axisymmetric swirl model of a target in the drift region as described in the 2D, axisymmetric drift regime sections in the CFD chapter. A 47,285-node mesh consisting of 12 inflation layers with a 1.10 growth rate and a default transition ratio of 0.272, an overall growth rate of 1.02, and a target edge size of 5E-5 m was created from an axisymmetric domain spanning 20 body lengths before, 15 body lengths above, and 20 body lengths behind. The Fluent case setup can be seen in Table 23 in Appendix A.

The velocity contours and streamlines were plotted at several times to visualize the flow and determine the existence of a steady-state solution. Figures 36-45 show the flow's development. Notice that the fluid velocity increases as it flows around the front of the target. Much like with the sphere, this is due to the fact that the target is not of negligible thickness, which forces the flow through a smaller cross-sectional area. Assuming the density remains relatively unchanged, the velocity must increase to satisfy continuity [21]. (The density assumption will be addressed later in this section.) The increase in velocity causes a favorable pressure gradient (decreasing pressure) along the front of the target by Bernoulli's equation [21]. However, just like flow over a sphere, the adverse pressure gradient that occurs after the front of the obstacle combined with the fluid's viscosity causes a separation point [21]. Notice that the flow separates from target near the beginning of the 3rd target wall (the wall parallel with the free-stream flow). A small thin vortex appears after this separation point along the horizontal face. The wake behind the target appears to grow as time elapses. The wake appears to reach a steady state after approximately 0.8 ms. The pressure and temperature contours at 1 ms can be seen in Figures 72 and 73 in Appendix B.

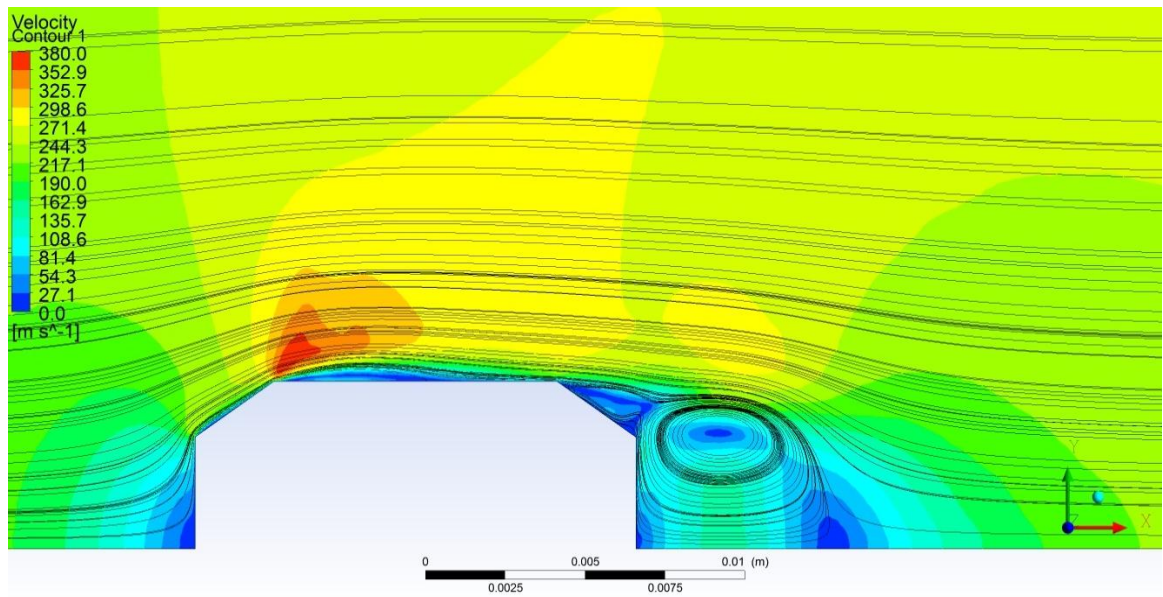


Figure 36. Velocity Contour and Streamlines of 2D, Axisymmetric Swirl Flow over Target at 1.00E-4 s

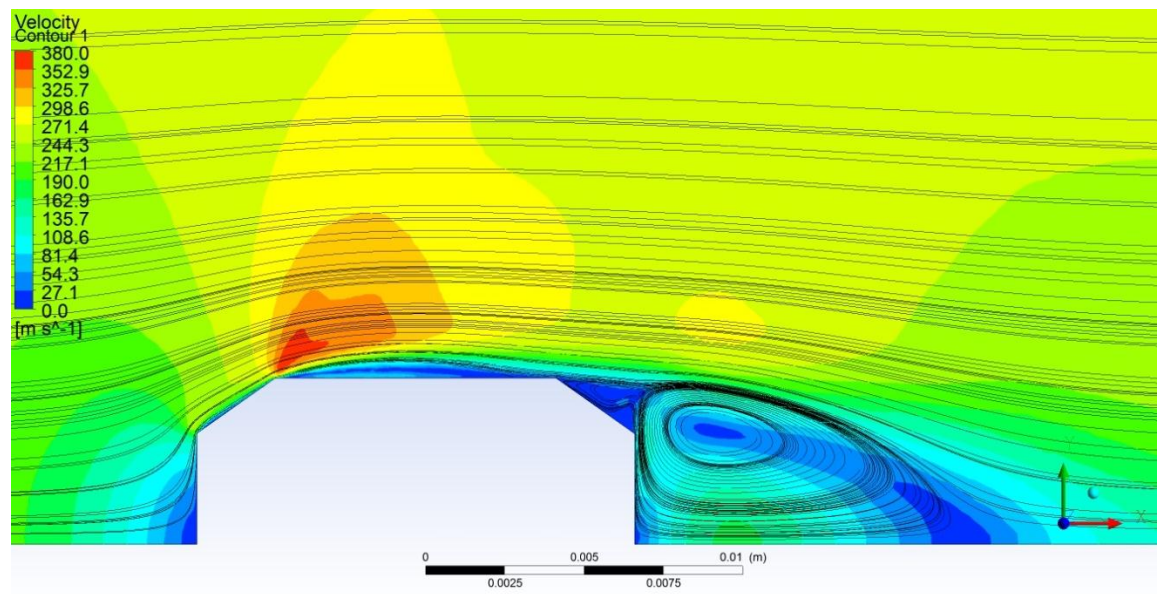


Figure 37. Velocity Contour and Streamlines of 2D, Axisymmetric Swirl Flow over Target at 2.00E-4 s

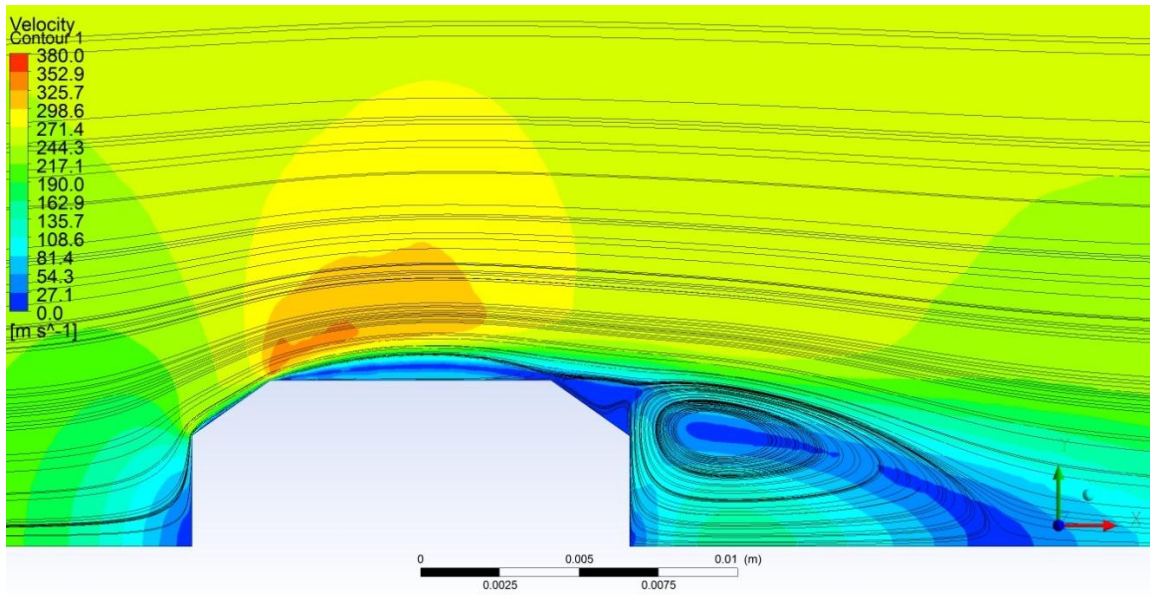


Figure 38. Velocity Contour and Streamlines of 2D, Axisymmetric Swirl Flow over Target at 3.00E-4 s

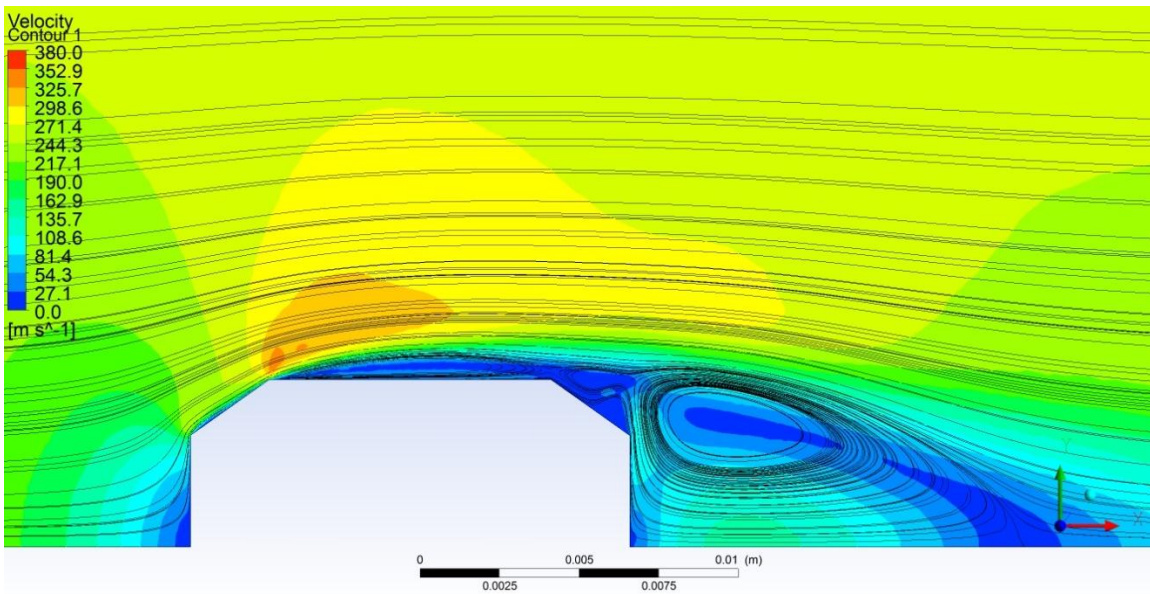


Figure 39. Velocity Contour and Streamlines of 2D, Axisymmetric Swirl Flow over Target at 4.00E-4 s

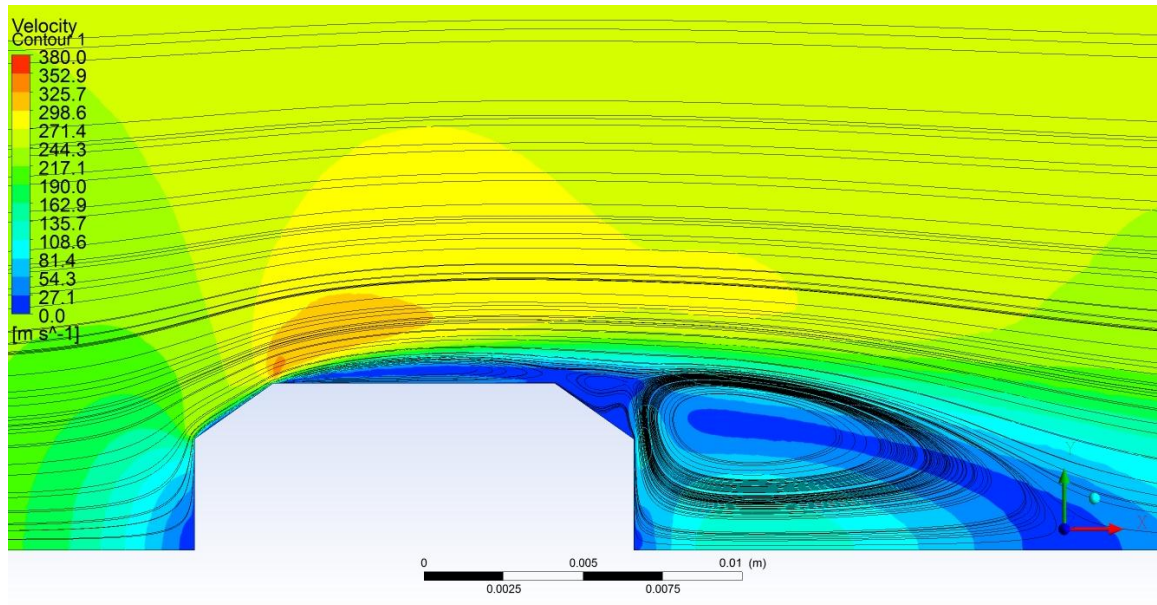


Figure 40. Velocity Contour and Streamlines of 2D, Axisymmetric Swirl Flow over Target at 5.00E-4 s

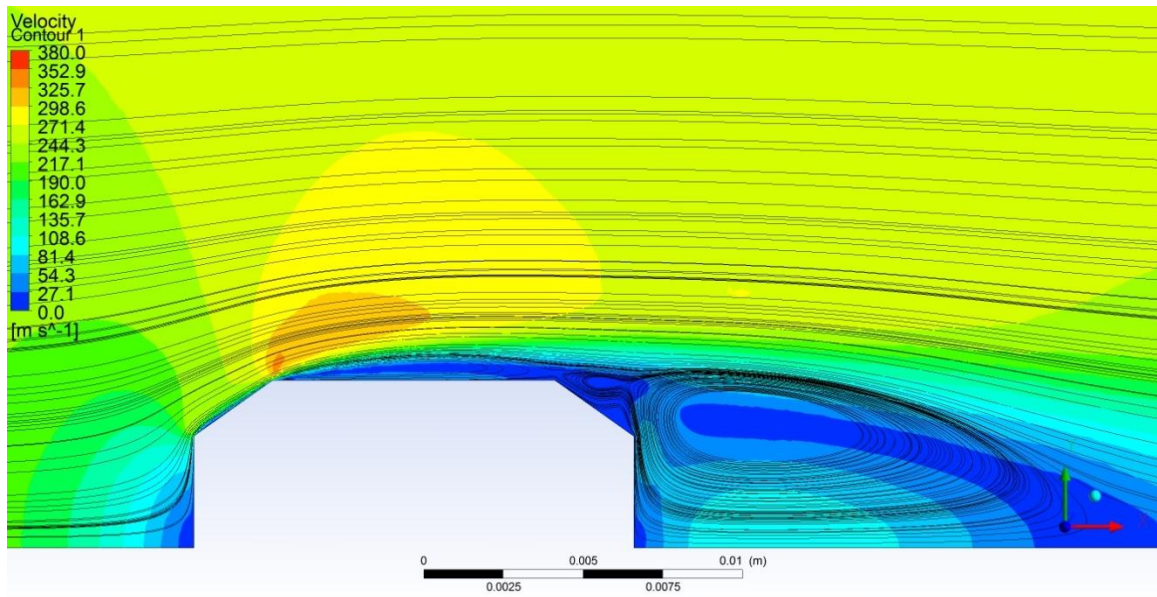


Figure 41. Velocity Contour and Streamlines of 2D, Axisymmetric Swirl Flow over Target at 6.00E-4 s

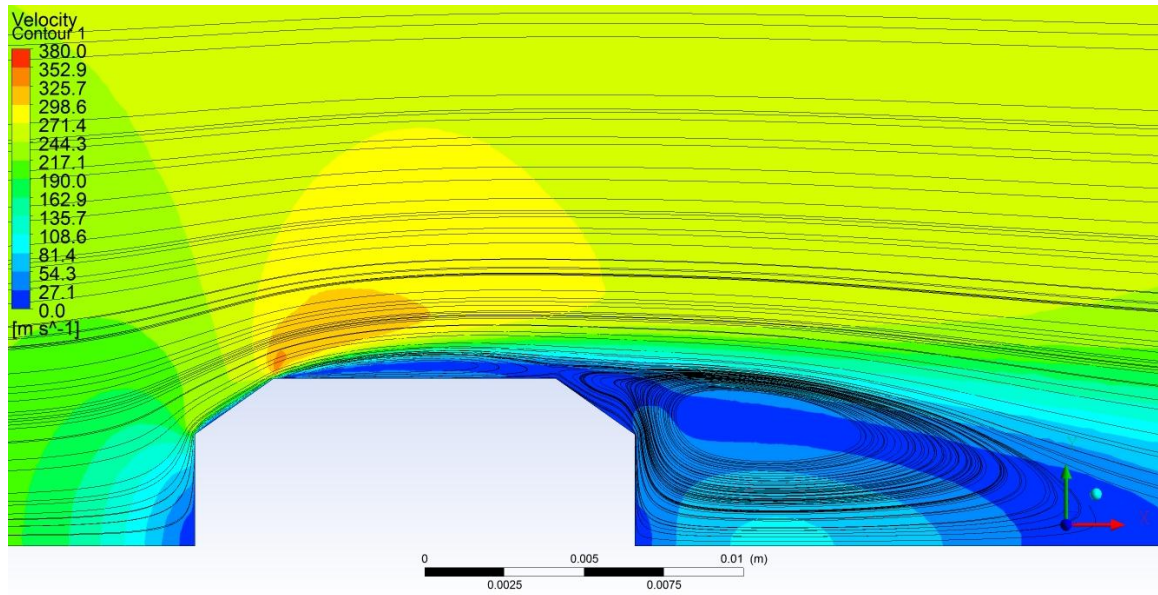


Figure 42. Velocity Contour and Streamlines of 2D, Axisymmetric Swirl Flow over Target at 7.00E-4 s

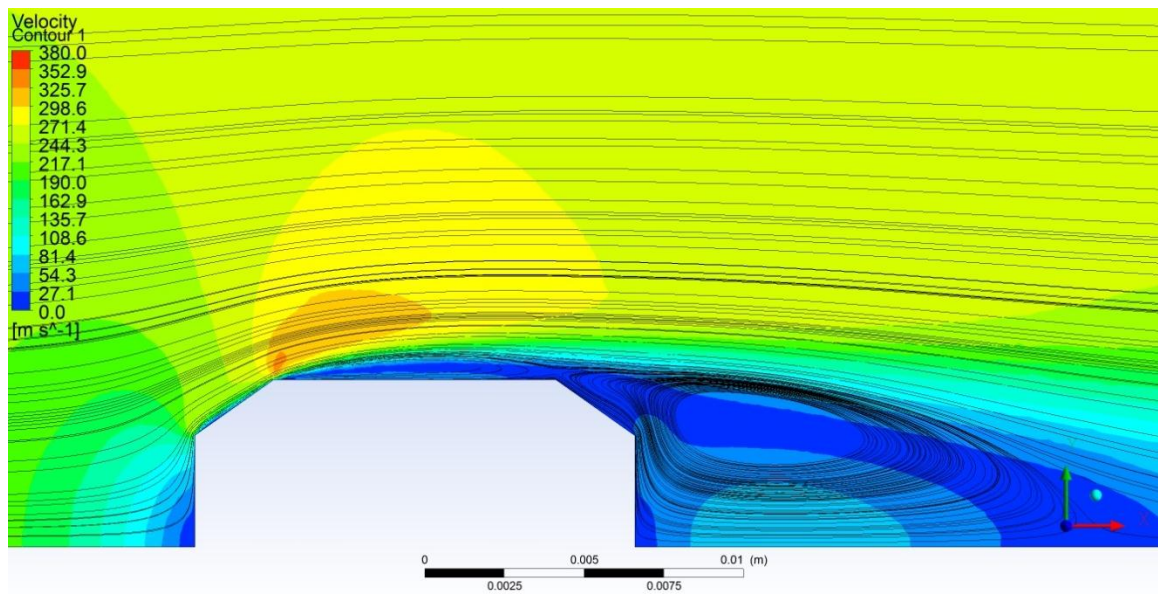


Figure 43. Velocity Contour and Streamlines of 2D, Axisymmetric Swirl Flow over Target at 8.00E-4 s

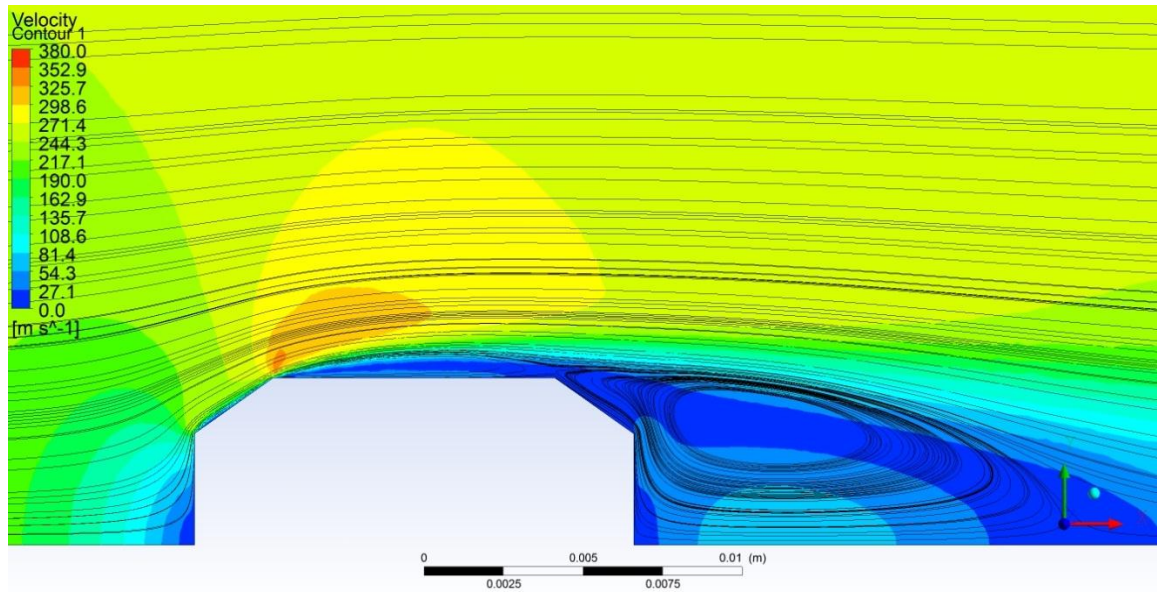


Figure 44. Velocity Contour and Streamlines of 2D, Axisymmetric Swirl Flow over Target at 9.00×10^{-4} s

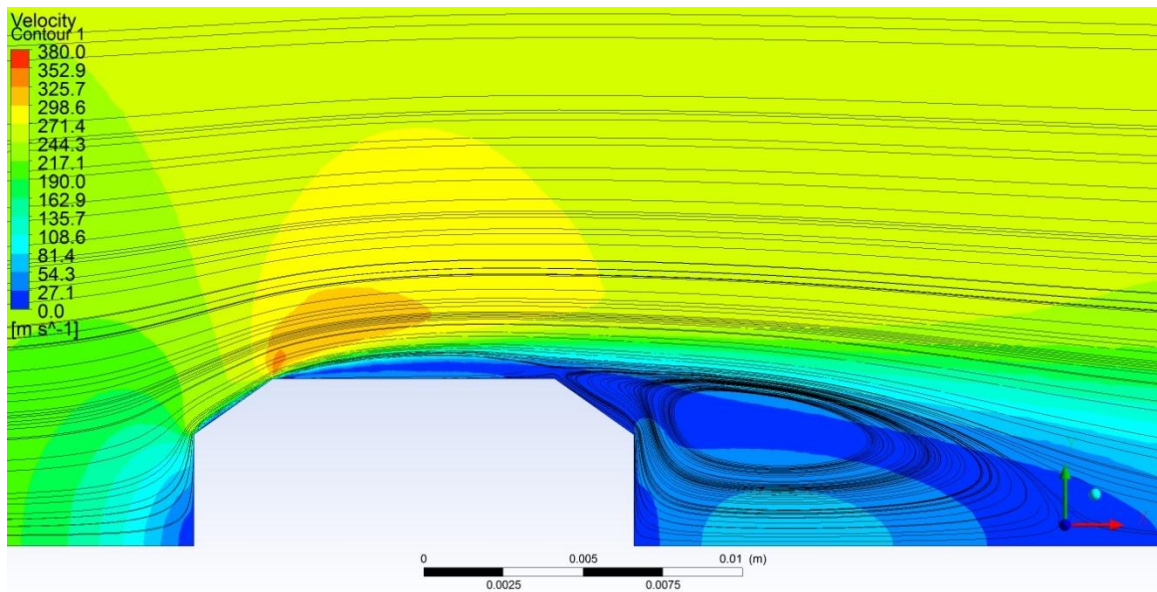


Figure 45. Velocity Contour and Streamlines of 2D, Axisymmetric Swirl Flow over Target at 1.00×10^{-3} s

Although the velocity contour and streamline plots indicate the flow reaches a steady state, the changes in a couple key variables, drag force and heat transfer, were also examined over time. Figures 46 and 47 depict the relationship between drag force and

heat transfer with time. (Note that the target walls are labeled in order from front to back.) It appears that both the drag force and heat transfer reach steady values after 8.0×10^{-4} s.

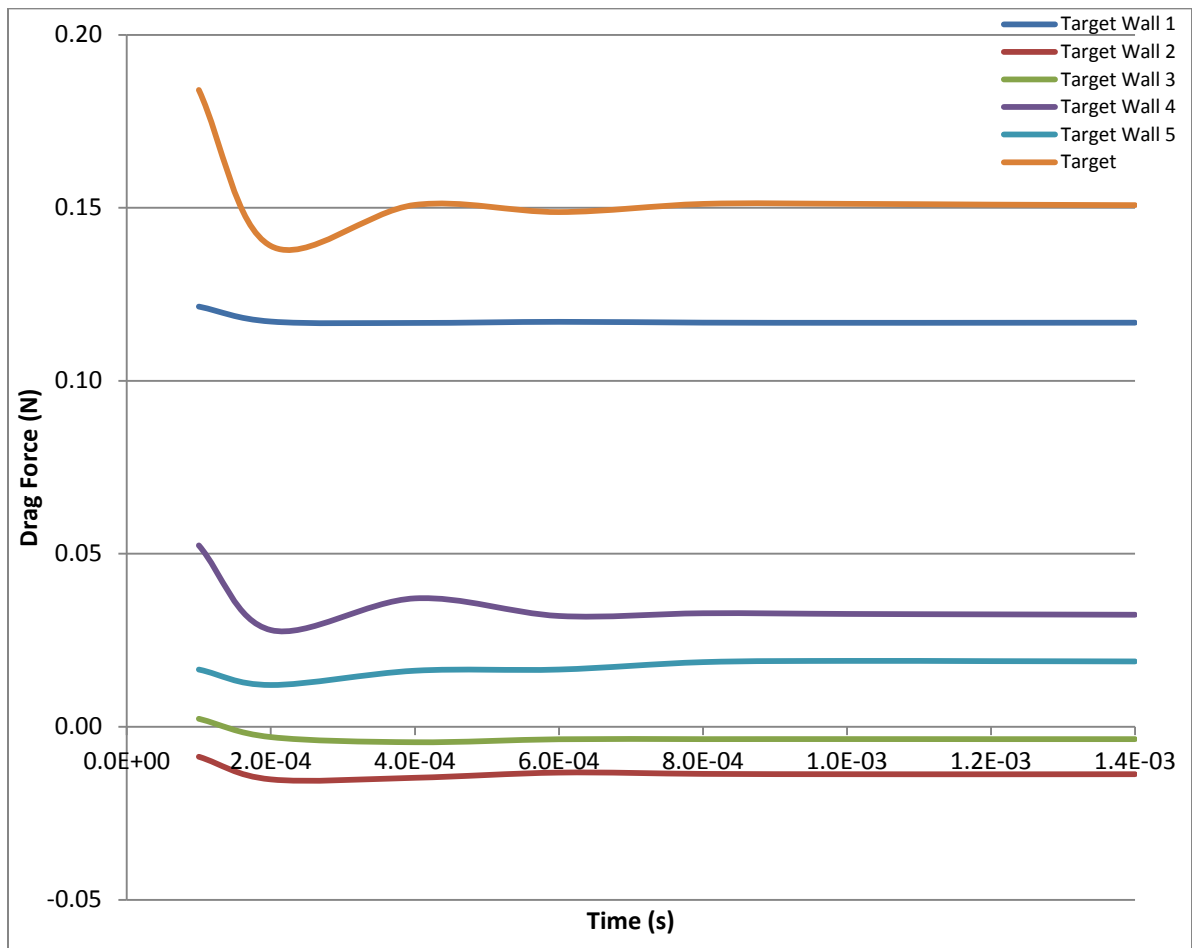


Figure 46. Drag Force over Time on Target in Drift Region from 2D, Axisymmetric Swirl Model

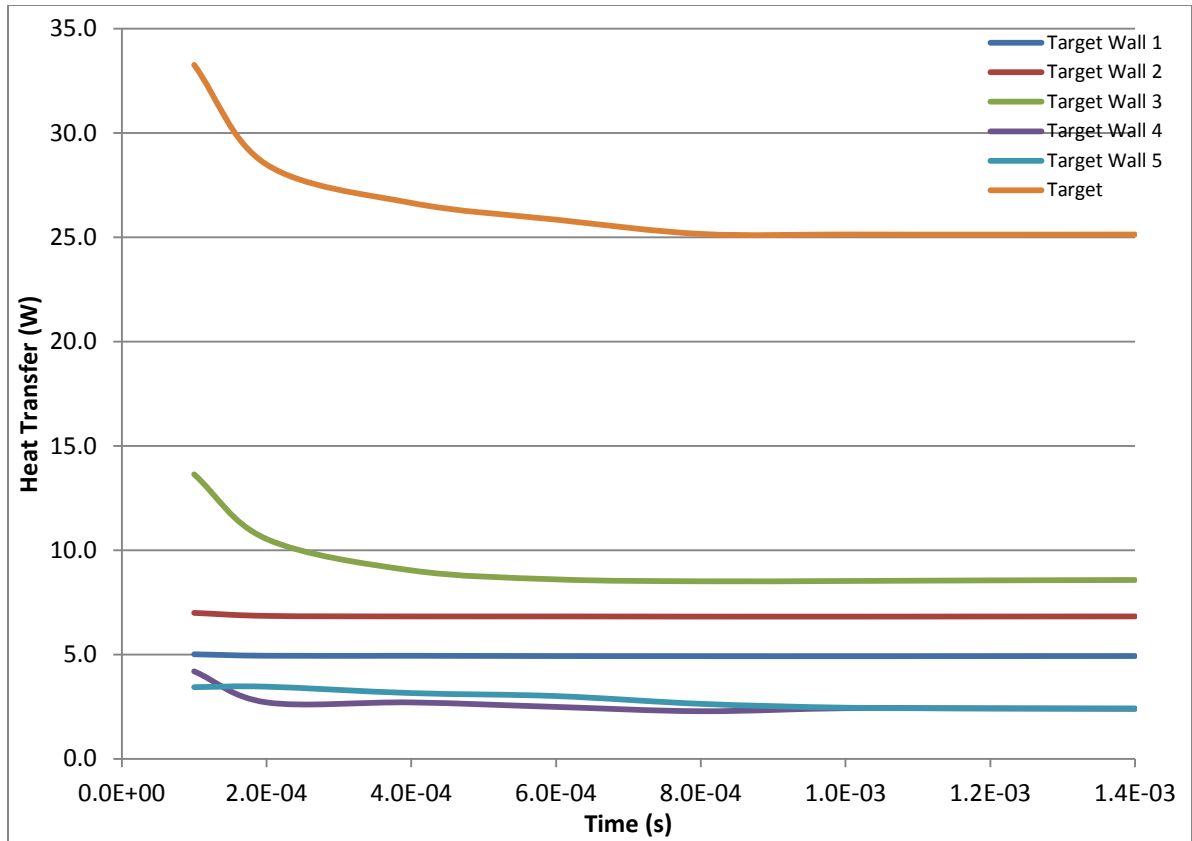


Figure 47. Heat Transfer over Time on Target in Drift Region from 2D, Axisymmetric Swirl Model

The largest contribution to the total drag force is from the front wall. Since this wall acts like a blunt object perpendicular to the flow, a relatively large drag force is to be expected. Also for this reason, the majority of the drag force on wall 1 should come from pressure drag. Wall 5 also acts as a blunt surface in the flow, and the pressure drag should comprise most of the drag on this face. Table 16 (which shows the drag force values on each wall due to both pressure and viscous forces) confirms these assumptions. The flow over wall 3, which lies horizontal to the flow, should act like flow over a flat plate parallel to free-stream flow. The drag force should be due to the viscous forces acting on the surface. Table 16 verifies this as well. Note that the viscous drag is negative along this wall. As can be seen in the streamlines in the velocity contour figures

discussed previously, a recirculation vortex occurs along this wall. Therefore, the flow directly above wall 3 is in the opposite direction of the free-stream flow, thereby giving the drag force a negative value along this wall. Note that the viscous drag force on wall 4, which also sees a recirculation vortex with reversed flow, also has a negative viscous drag force. However, the pressure drag force on wall 4 is positive and greater in magnitude than the viscous drag force, thereby making the overall drag force along wall 4 positive. The flow over wall 2 is not recirculated and therefore wall 2 has a positive viscous drag force. But the positive viscous drag is outweighed by the negative pressure drag force.

Table 16. Drag Force and Heat Transfer on Target after 1 ms from 2D, Axisymmetric Swirl Model

	Pressure Drag Force (N)	Viscous Drag Force (N)	Total Drag Force (N)	Drag Coefficient	Heat Transfer (W)	Heat Transfer Coefficient (W/(m²-K))
Target Wall 1	0.1168	1.12E-17	0.1168		4.9179	
Target Wall 2	-0.0179	0.0042	-0.0137		6.8164	
Target Wall 3	0.0	-0.0036	-0.0036		8.5235	
Target Wall 4	0.0329	-0.0003	0.0326		2.4259	
Target Wall 5	0.0190	8.65E-25	0.0190		2.4501	
Total Target	0.1508	0.0004	0.1512	0.5572	25.134	45.56

As another test of reaching steady state, the absolute pressure, Mach number, density, turbulent intensity, and heat flux were also plotted around the target at different times. Notice that as time progresses, the plots become more aligned, indicating the flow is reaching a steady state. As mentioned previously, there should be a decreasing (favorable) pressure gradient along the front wall and increasing (adverse) pressure gradient on the back of the target. This aligns well with the absolute pressure plot in Figure 48. Also, note that the greatest pressure occurs at the front stagnation point, which is also physically reasonable. In Figure 49, the increase in Mach number along

walls 1 and 2 is largely due to the increase in velocity mentioned earlier. Although spikes in the plots naturally occur at points of sharp geometry changes, the density remains relatively unchanged around the target in Figure 50. This confirms the assumption mentioned earlier regarding the change in velocity around the target. Finally, note the low turbulent intensity in Figure 51. This aligns well with the low Reynolds number (approximately 4,000) in the drift region. Other variables were plotted at these times and placed in Appendix B. See Figures 74-78.

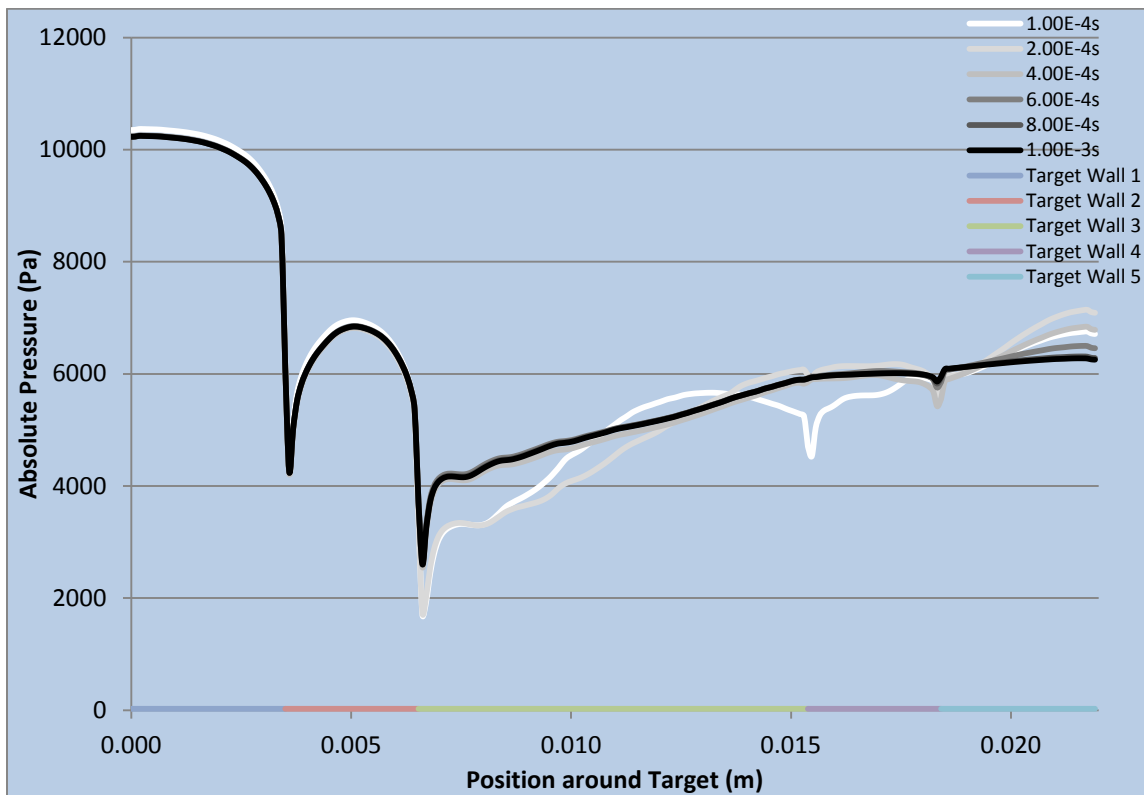


Figure 48. Absolute Pressure on Target in Drift Region from 2D, Axisymmetric Swirl Model

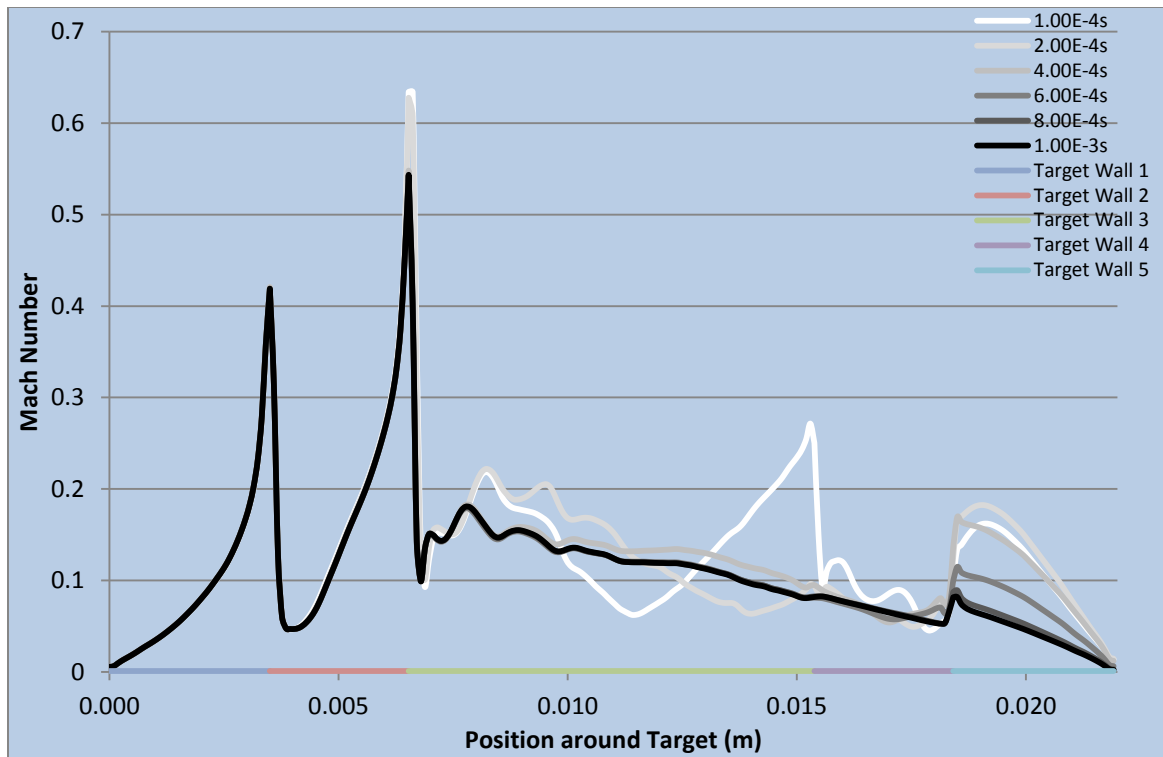


Figure 49. Mach Number around Target in Drift Region from 2D, Axisymmetric Swirl Model



Figure 50. Density around Target in Drift Region from 2D, Axisymmetric Swirl Model

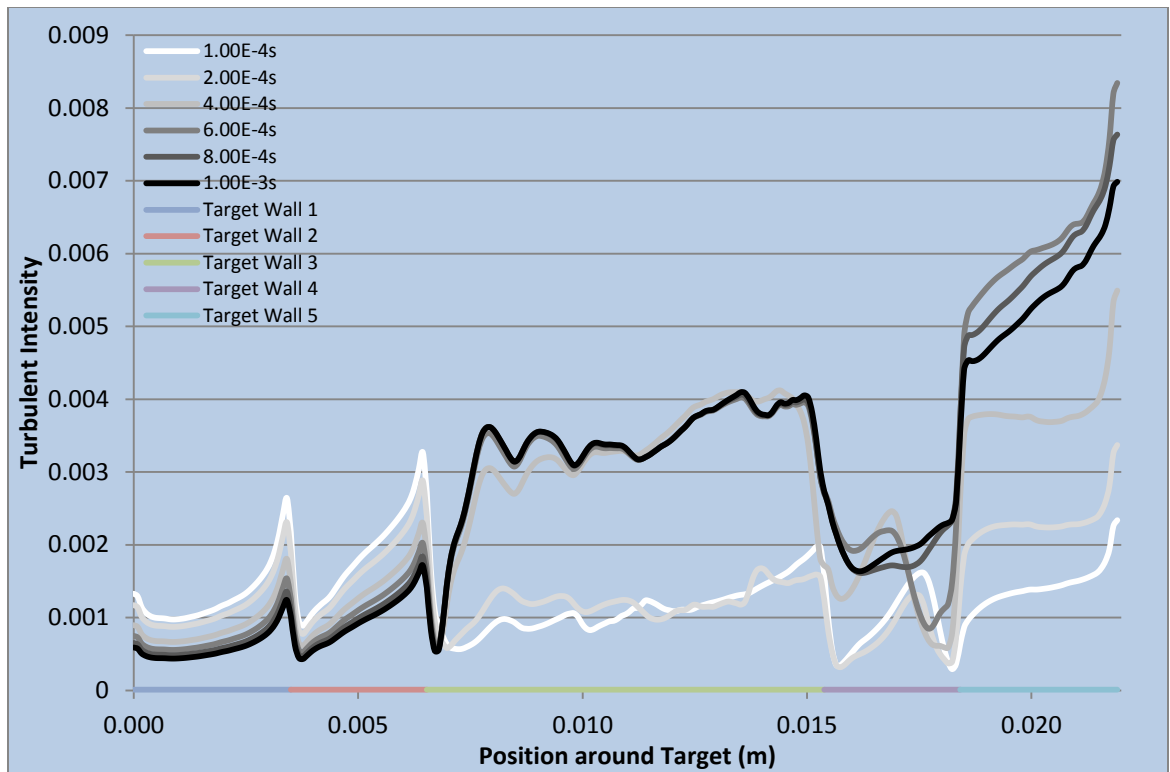


Figure 51. Turbulent Intensity on Target in Drift Region from 2D, Axisymmetric Swirl Model

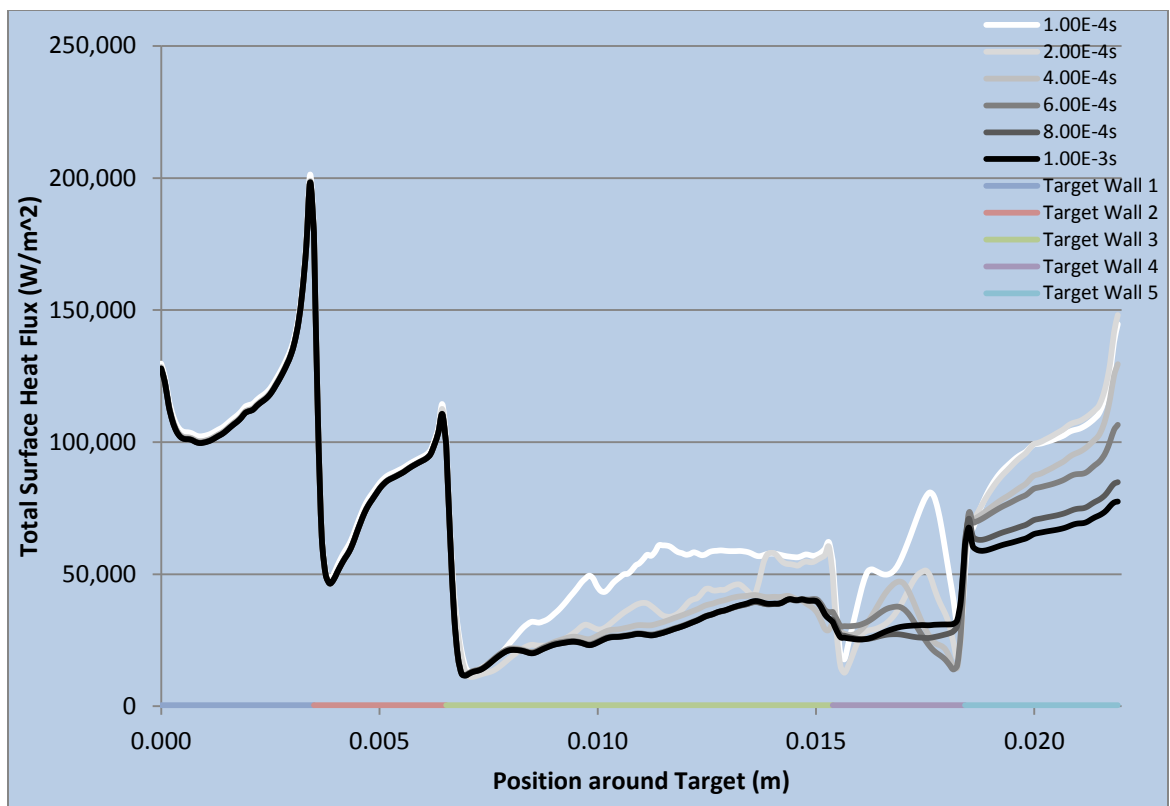


Figure 52. Total Surface Heat Flux on Target in Drift Region from 2D, Axisymmetric Swirl Model

Note that the y^+ values for the 2D, axisymmetric swirl simulation were approximately between 0.5 and 3.25. (See Figure 78 in Appendix B for the y^+ plot.) The SST k- ω turbulence model uses enhanced wall treatment as a default, which is relatively insensitive to y^+ values [1]. However, for greatest accuracy, y^+ values should be on the order of 1. This confirms reasonable mesh refinement at the target wall.

3D Drift Regime: Results

Since the 2D, axisymmetric swirl model of the flow around the target in the drift region indicated the existence of a steady-state solution, the 3D model was set up as a steady-state simulation. The results of the 3D, steady-state model of a target in the drift region as described in the 3D drift regime section in the CFD chapter are presented in this section. A 5,450,161-node mesh consisting of 12 inflation layers with a 1.10 growth rate and a default transition ratio of 0.272, an overall growth rate of 1.03, and a target edge size of 1E-4 m was created from an axisymmetric domain spanning 20 body lengths before, 15 body lengths above, and 20 body lengths behind. The Fluent case setup can be seen in Table 24 in Appendix A.

A velocity contour and streamline plot was made on the x-y plane with the 3D results. It can be seen in Figure 53. Notice that this looks very similar to the velocity contour and streamline plot from the 2D, axisymmetric swirl model at 1 ms in Figure 45. This serves as a confirmation of the 2D, axisymmetric swirl model of the flow around the target. The pressure and temperature contours also look similar to those of the 2D, axisymmetric swirl model and can be seen in Appendix C in Figures 79 and 80.

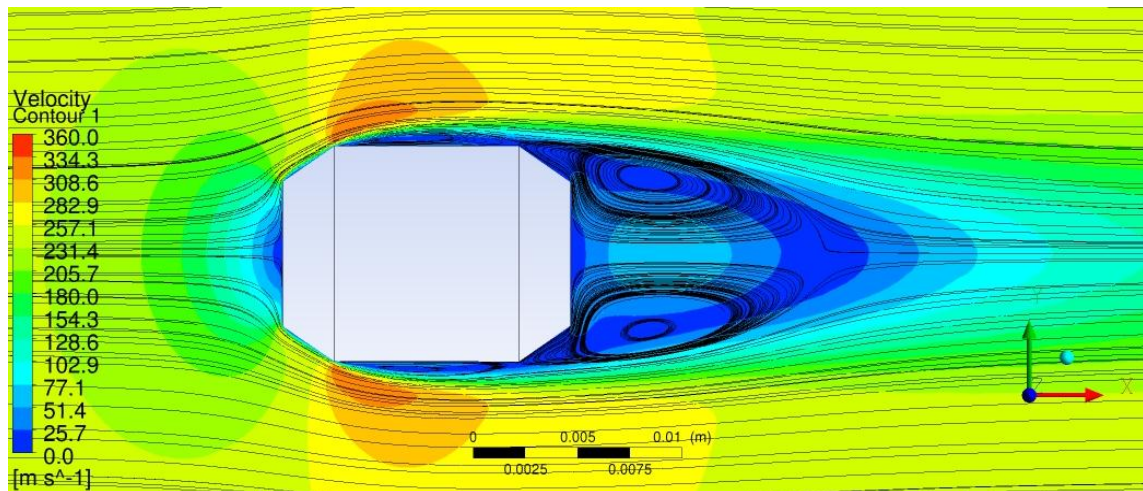


Figure 53. Velocity Contour and Streamline Plot for Target in 3D, Steady-State, Drift Simulation

As with the 2D, axisymmetric swirl simulation, several variables were plotted around the target. The absolute pressure, Mach number, density, turbulent intensity, and heat flux can be seen in Figures 54-58. Others can be seen in Figures 81-85 in Appendix C. Comparison between these plots and the 2D, axisymmetric swirl model plots at 1 ms are quite close. This serves as another confirmation of the 2D, axisymmetric swirl model of the flow around the target.

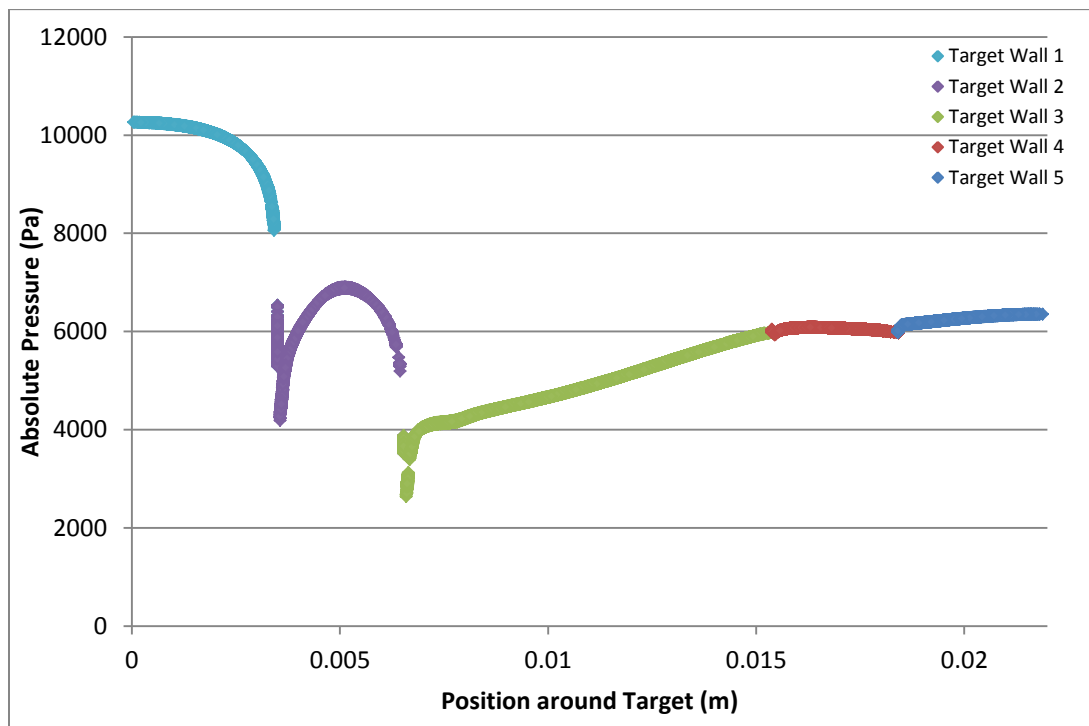


Figure 54. Absolute Pressure around Target from 3D, Steady-State Simulation

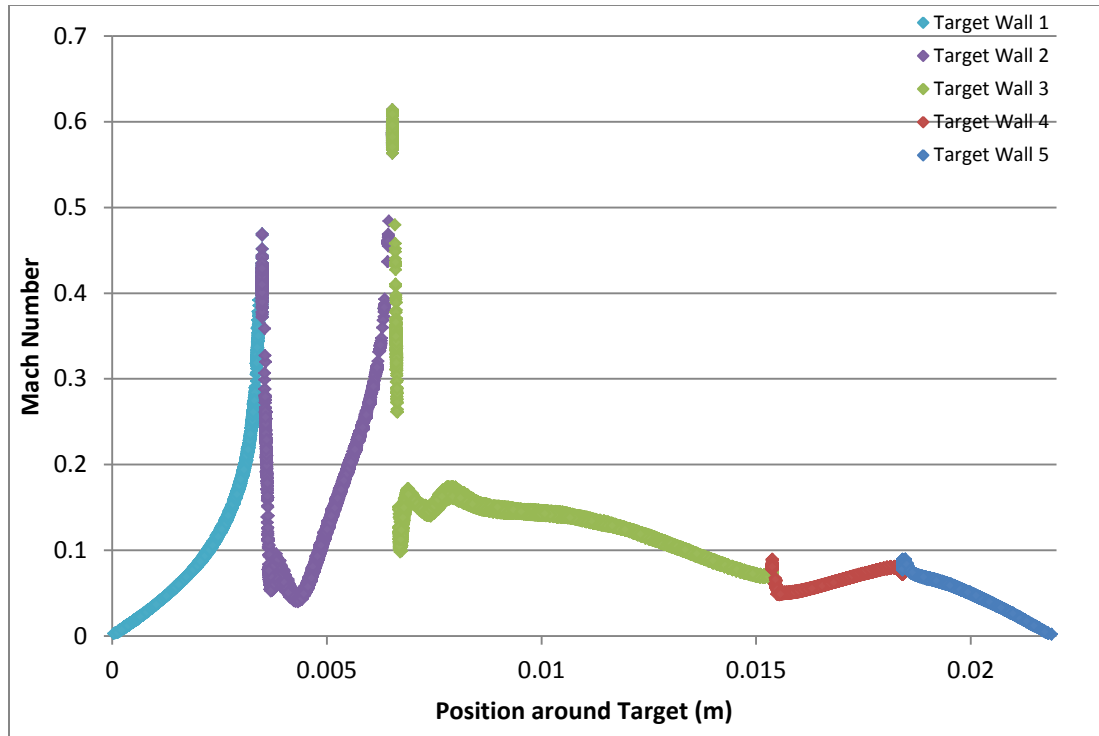


Figure 55. Mach Number around Target from 3D, Steady-State Simulation

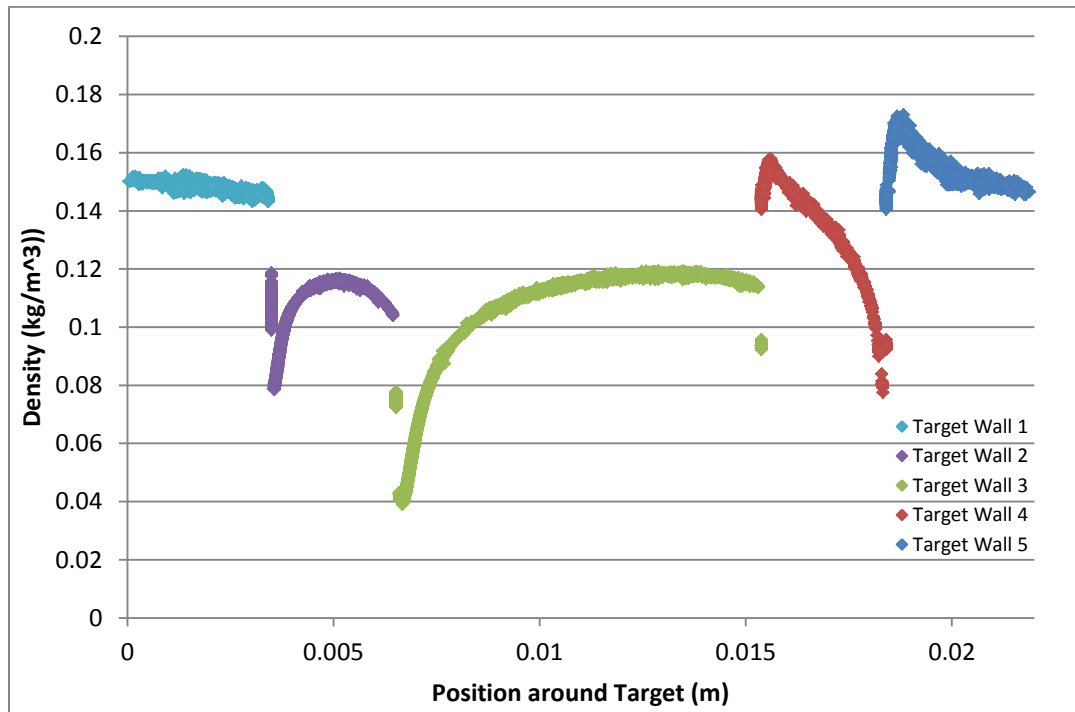


Figure 56. Density around Target in Drift Region from 3D, Steady-State Simulation

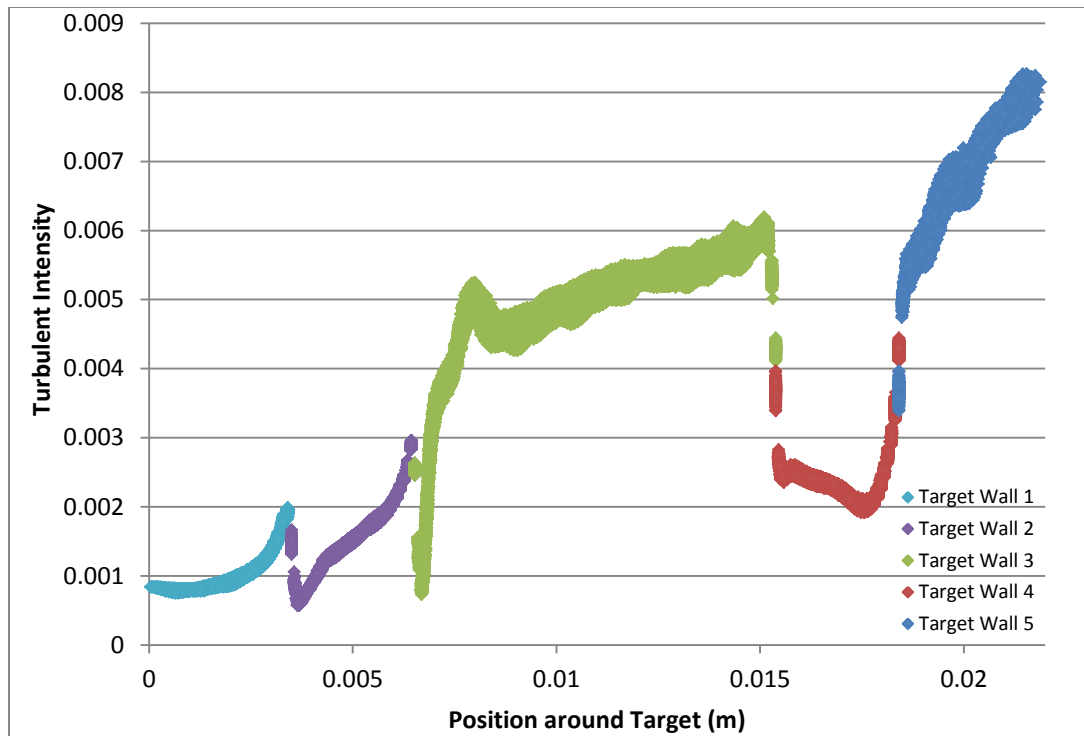


Figure 57. Turbulent Intensity around Target from 3D, Steady-State Simulation

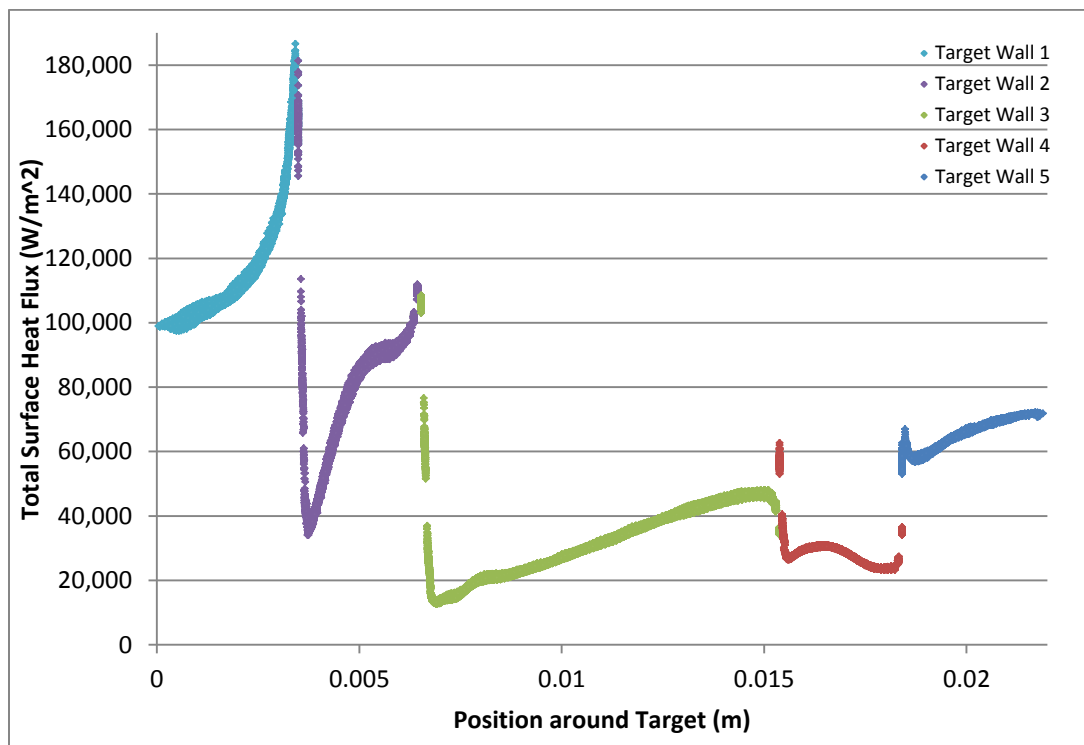


Figure 58. Total Surface Heat Flux around Target from 3D, Steady-State Simulation

The drag force and heat transfer table from the 2D, axisymmetric swirl results section was also created for the 3D, steady-state results. See Table 17. Notice the same general trends regarding the 2D, axisymmetric swirl drag force and heat transfer table are present here. The viscous drag force on the blunt surfaces (walls 1 and 5) and pressure drag force on the horizontal surface (wall 3) are practically zero. The viscous drag force on wall 2 is positive, while the viscous drag force on walls 3 and 4 (where the flow adjacent to the walls is in the reverse direction) is negative. The pressure drag forces outweigh the viscous drag forces on walls 2 and 4.

Table 17. Drag Force and Heat Transfer on Target from 3D, Steady-State Target Model

	Pressure Drag Force (N)	Viscous Drag Force (N)	Total Drag Force (N)	Drag Coefficient	Heat Transfer (W)	Heat Transfer Coefficient (W/(m²-K))
Target Wall 1	0.11562	-4.321E-17	0.11562		4.8120	
Target Wall 2	-0.01709	0.00388	-0.01321		6.7545	
Target Wall 3	-7.161E-06	-0.00374	-0.00375		9.4758	
Target Wall 4	0.02995	-0.00026	0.02969		2.3011	
Target Wall 5	0.01688	7.872E-18	0.01688		2.4449	
Total Target	0.14535	-0.00012	0.14523	0.5354	25.788	46.75

Figures 59 and 60 plot the drag coefficient and heat transfer coefficient from both the transient, 2D, axisymmetric swirl and the 3D, steady-state models over time. Good agreement can be seen after 8.0E-4 s. Table 18 shows the percent difference between the 3D, steady-state value and the transient, 2D, axisymmetric swirl values. After 8.0E-4s, the drag and heat transfer coefficients from both models are within 5% of each other, providing further validation of the 2D, axisymmetric swirl model.

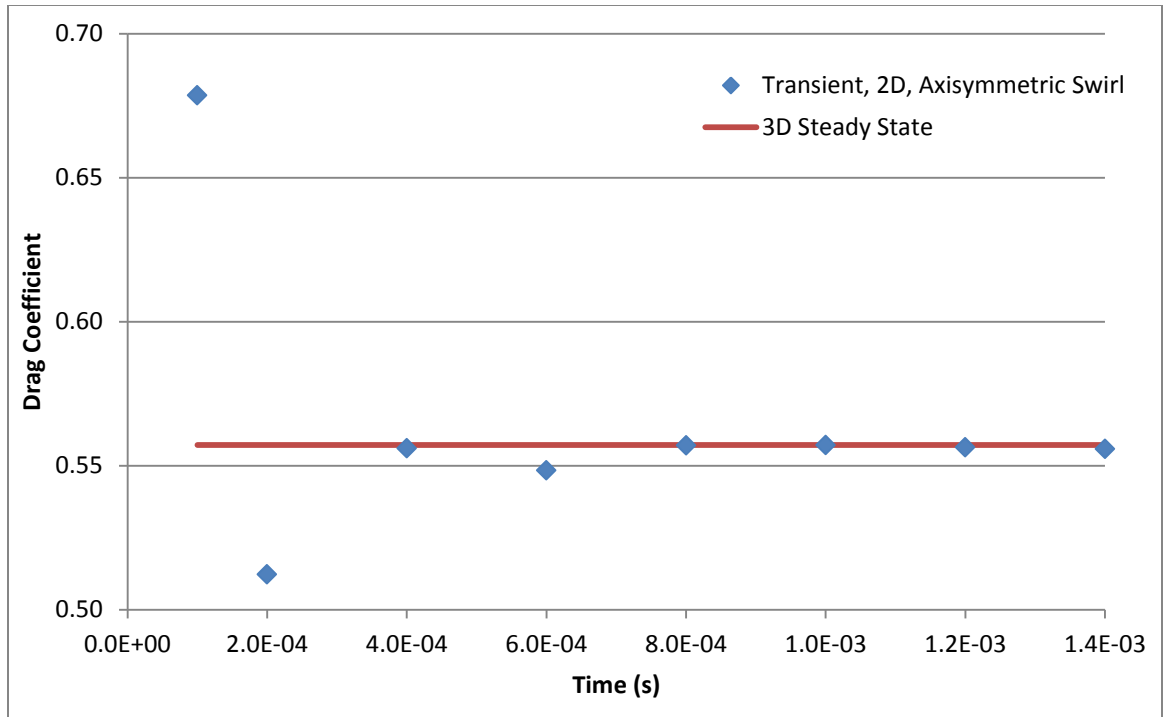


Figure 59. Drag Coefficient Comparison between Transient, 2D, Axisymmetric Swirl Model and 3D, Steady-State Model

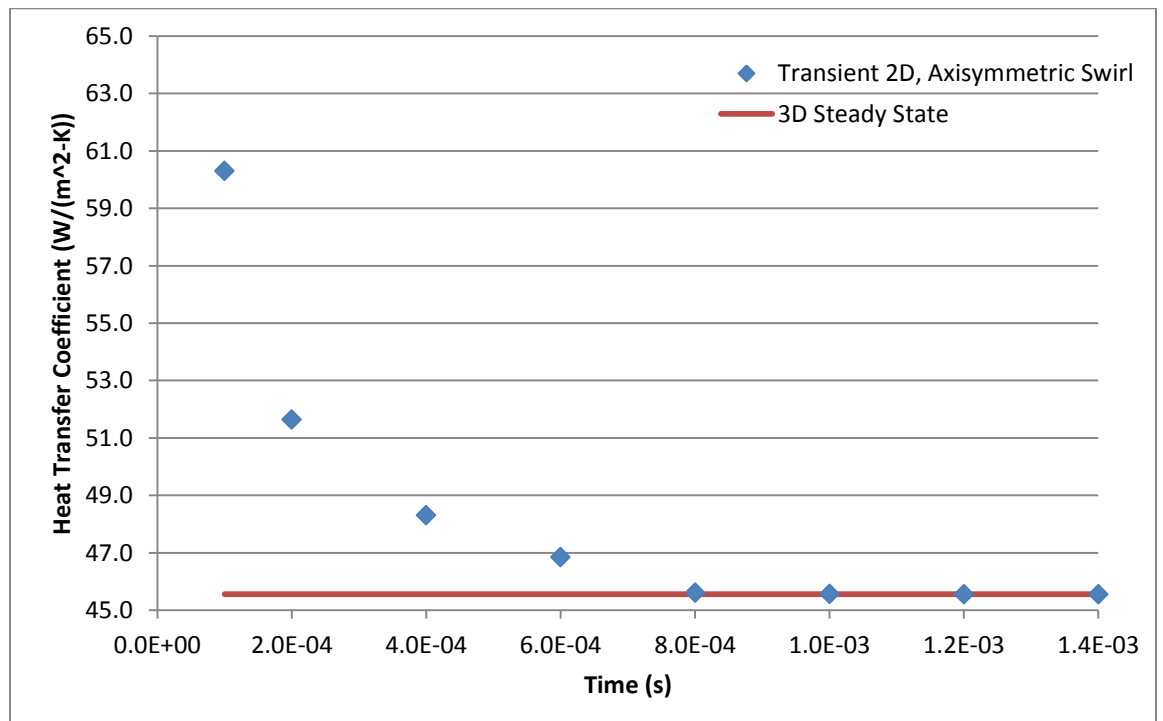


Figure 60. Heat Transfer Coefficient Comparison between Transient, 2D, Axisymmetric Swirl Model and 3D, Steady-State Model

Table 18. Drag and Heat Transfer Coefficient Percent Difference between Transient, 2D, Axisymmetric Swirl Model and 3D, Steady-State Model

Time (s)	Drag Coefficient	Drag % Difference with 3D Steady-State	Heat Transfer Coefficient (W/(m ² -K))	Heat Transfer Coefficient % Difference with 3D Steady-State
1.00E-04	0.679	26.74	60.30	28.99
2.00E-04	0.512	-4.32	51.64	10.47
4.00E-04	0.556	3.86	48.30	3.33
6.00E-04	0.548	2.44	46.85	0.22
8.00E-04	0.557	4.06	45.61	-2.44
1.00E-03	0.557	4.08	45.56	-2.54
1.20E-03	0.556	3.92	45.55	-2.56
1.40E-03	0.556	3.82	45.55	-2.55

To put the heat flux on the target in perspective, published heat transfer correlations were plotted along with the 3D, steady-state heat flux plot in Figure 61. Below and Terpigor'ev [3] developed a correlation predicting the Nusselt number at the stagnation point of a jet of fluid interacting with a blunt object. At stagnation, the correlation simplifies to

$$Nu = 0.763 * Pr^{0.4} * \sqrt{Re} \quad (26)$$

where Pr is the Prandtl number, and the Nusselt and Reynolds numbers are calculated with characteristic length equal to the diameter of the jet nozzle. For this application, it seemed reasonable to make this length equal to the diameter of the front wall. This correlation was adapted to predict heat flux on the front target wall. Hadad and Jafarpur [6] semi-analytically determined the average Nusselt number as a function of the Reynolds and Prandtl numbers for several objects in external flow. Their cylinder correlation was given as

$$Nu_d = 1.5828 + 0.5506 * Re_d^{1/2} * Pr^{1/3} \quad (27)$$

Note that this correlation is valid in the range $1 < Re_d < 100$, and the Reynolds number in the drift region is approximately 4,000. Nevertheless, the correlation was adjusted to predict an average heat flux over a cylinder with diameter equal to the target's outer diameter. Kang and Sparrow [13] experimentally determined a correlation between the Nusselt number as a function of Reynolds number for flow around a cylinder. However, they developed the correlation not as an overall average, but as the Nusselt number changes along the cylinder's axial direction. The correlation is approximated as

$$Nu_x = 0.0426 * Re_x^{0.767} \quad (28)$$

where x is the axial distance from the front of the cylinder. This correlation was adapted to predict heat flux along a cylinder with characteristic length equal to the axial distance from the front of the cylinder. Sogin [26] measured the heat transfer from the rear of bluff bodies in external flow and developed a correlation to predict the Nusselt number as a function of the Reynolds number:

$$Nu_L = 0.20 * Re_L^{2/3} \quad (29)$$

where L is the chord length of the flat plate strip. This correlation was adapted to predict the heat flux on the rear wall of an object with a flat plate chord length equal to the diameter of the target's rear wall. Note that the correlation is valid in the range of $10,000 < Re_L < 40,000$. The Reynolds number with characteristic length equal to the target's rear wall diameter is 2,620. The heat flux plot from the 3D, steady-state simulation can be seen in Figure 61 along with these 4 correlations. Note that the higher-than-average heat flux on the front and back walls aligns with the predictions by Belov and Terpigorev and Sogin.

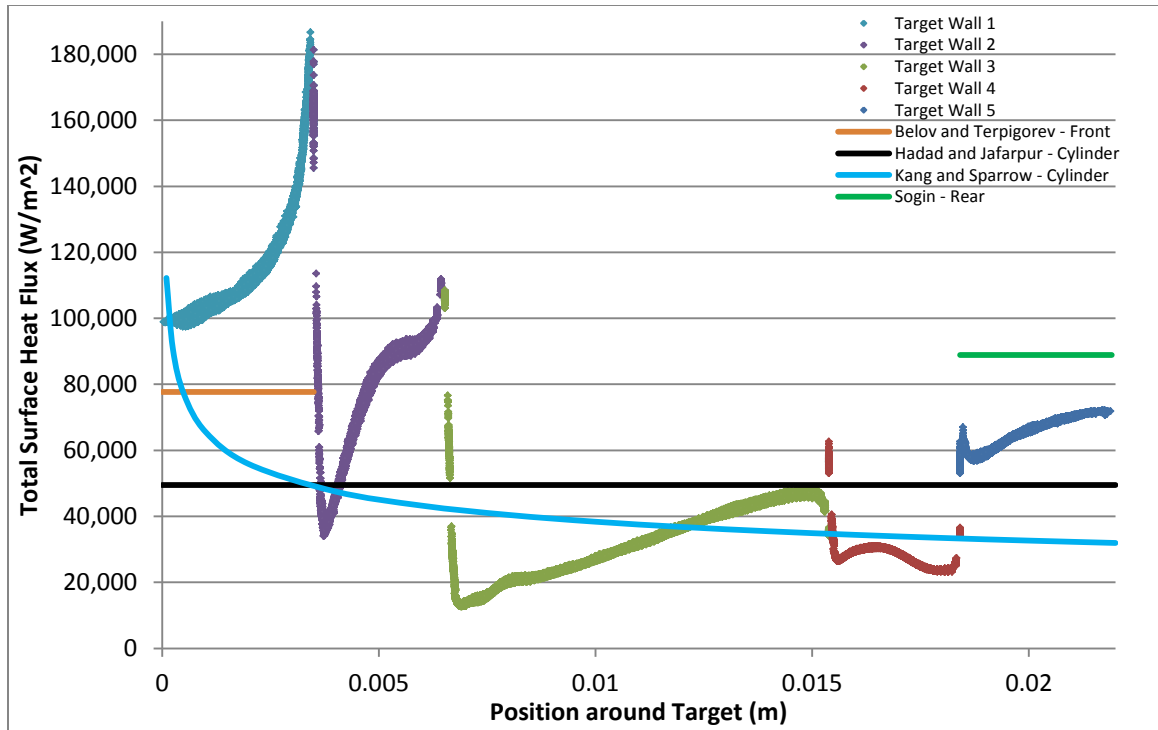


Figure 61. Heat Flux from 3D, Steady-State Case Plotted with Published Heat Transfer Correlations

Furthermore, the average heat coefficient can be calculated from the correlations and compared to the total heat coefficient from the 3D, steady-state simulation of 46.75 W/(m²-K) (found in Table 17). From the Nusselt correlation from Hadad and Jafarpur [6], the heat transfer coefficient is approximately 48.11 W/(m²-K), only 5.59% different than the total 3D, steady-state simulation value. The Nusselt correlation from Sogin [26] estimates a heat transfer coefficient of 57.56 W/(m²-K) on the rear wall. The heat transfer on wall 5 from the 3D, steady-state simulation was 2.4449 W (see Table 17), which translates to a heat transfer coefficient of 61.68 W/(m²-K) on the rear wall. This is only a 7.16% difference. Considering all properties used to evaluate Reynolds and Nusselt numbers for the published correlations were constants at the free-stream temperature and the obvious difference in shape, these published correlations align very

closely to the heat transfer results from the 3D, steady-state simulation, making it reasonable to assume the 3D, steady-state results could predict the actual target heat transfer quite closely.

Similarly, the value of the drag coefficient on the target from the 3D, steady-state simulations can be compared to the drag coefficient on a sphere predicted by Clift *et al.* [4]. Recall the Clift *et al.* correlation is valid for incompressible flow at a constant temperature. In the Reynolds number range of 1,500 to 12,000, the correlation was given as

$$\log_{10} C_D = -2.4571 + 2.5558 * \log_{10} Re_d - 0.9295 * (\log_{10} Re_d)^2 + 0.1049 * (\log_{10} Re_d)^3 \quad (30)$$

At a Reynolds number of 3,937 (the Reynolds number in the drift region), the predicted sphere drag coefficient is 0.3908. This is a 27.0% difference. Hadad and Jafarpur [6], determined a Nusselt correlation for flow over a sphere valid over a wide Reynolds number range of $1 < Re < 100,000$:

$$Nu_d = 2 + 0.5918 * Re_d^{1/2} * Pr^{1/3} \quad (31)$$

which would give the heat transfer coefficient in the drift region as 52.16 W/(m²-K).

Compared to the results from the 3D, steady-state simulation, this sphere heat transfer prediction has a 14.5% difference. For the same geometry, the predicted heat transfer coefficient has half as much percent difference as the predicted drag coefficient. This indicates the heat transfer predicted by the 3D, steady-state simulation would most likely have a greater accuracy than the drag prediction.

The total drag force and mass can be used to calculate acceleration using Newton's second law [19],

$$D = ma \quad (32)$$

The acceleration due to the drag force is approximately 47.9 m/s^2 against the direction of the flow. Using the velocity-acceleration equation [19],

$$V = \sqrt{V_0^2 + 2as} \quad (33)$$

(where the subscript 0 indicates the initial state and s is displacement in meters)

the velocity after traveling 4 m through the drift region would be approximately 250.8 m/s, resulting in only a 0.32% change in velocity. Therefore the initial assumption of a constant-velocity target is reasonable.

As described in the CFD chapter, the drag and heat transfer on the 3D target were analyzed at different target velocities. Table 19 summarizes the results of the simulations, and Figures 62 and 63 plot the dimensionless drag coefficient and Nusselt number as versus the Reynolds number.

Table 19. Drag and Heat Transfer from 3D, Steady-State Target Simulations at Different Reynolds Numbers

Re	2400	2800	3200	3600	3937	4400	4800	5200	5600
Drag Force (N)	0.0416	0.0571	0.0859	0.1052	0.1452	0.2290	0.3020	0.4774	0.5859
Drag Coefficient	0.4106	0.4145	0.4379	0.4618	0.5354	0.6729	0.7456	1.0042	1.0628
Heat Transfer (W)	20.290	21.933	24.349	25.149	25.788	28.576	30.981	32.183	35.803
Nusselt Number	24.288	26.255	29.148	30.106	30.871	34.208	37.087	38.526	42.860

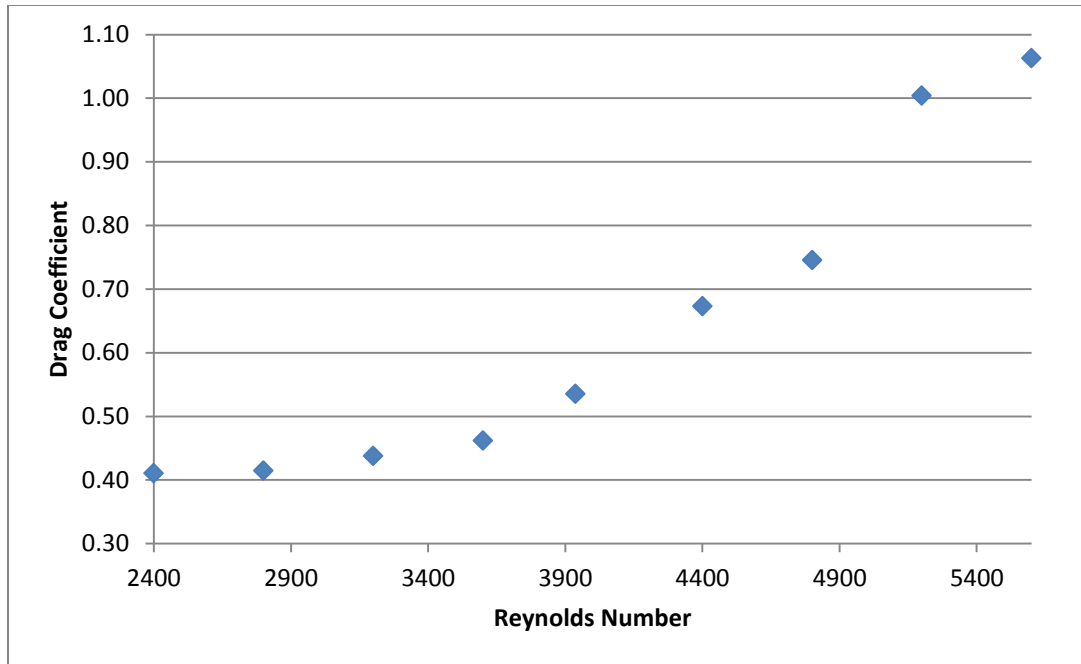


Figure 62. Drag Coefficient Plotted for 3D, Steady-State Target Simulations at Different Reynolds Numbers

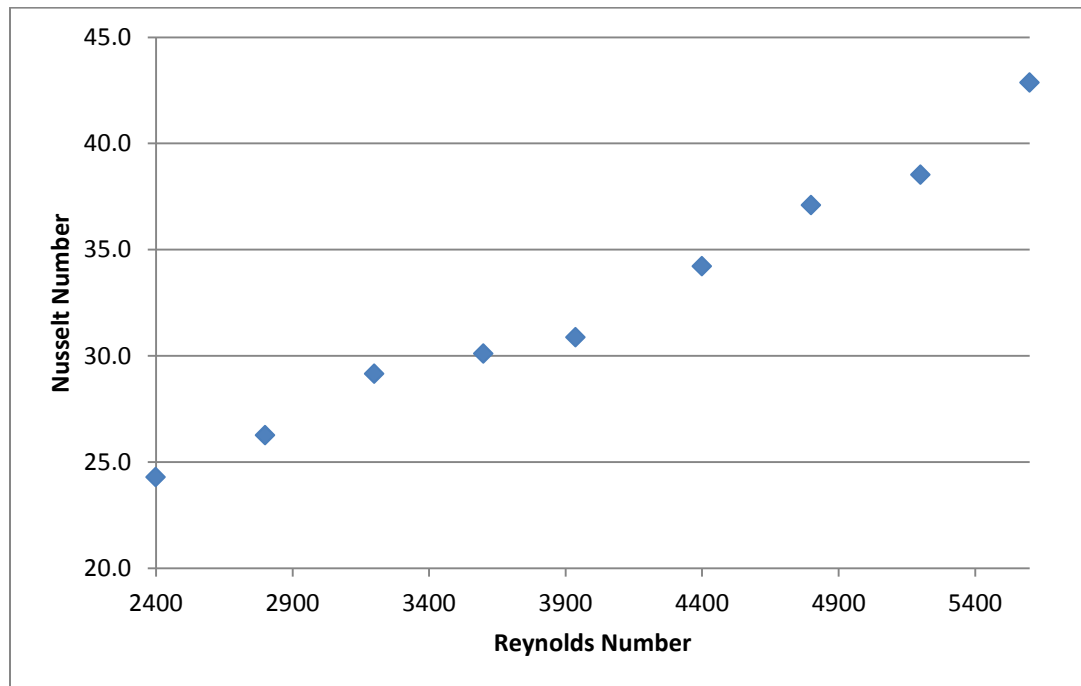


Figure 63. Nusselt Number Plotted for 3D, Steady-State Target Simulations at Different Reynolds Numbers

Excel was used to determine best-fit correlations for the drag coefficient and Nusselt number as functions of the Reynolds number in the Reynolds number range 2,400-5,600. The best-fit, 2nd order polynomial of the drag coefficient is

$$C_D = (7.7468E - 8)(Re_d^2) - (4.0284E - 4)Re_d + 0.92913 \quad (34)$$

And the best-fit power law for the Nusselt number is

$$Nu_d = 0.1681 * Re_d^{0.6361} \quad (35)$$

The R^2 value for each is 0.9818 and 0.9733, respectively, indicating a reasonable curve fit. Note that the published Nusselt-Reynolds correlations used as points of comparison regarding the target heat transfer have power-law exponents ranging from 0.5 to 0.767. The best-fit Nusselt number correlation for the target has a power-law exponent of 0.6361, which is within this range and, therefore, reasonable. Pressure, temperature, and velocity contours with streamlines were plotted for each Reynolds number case. They can be seen in Figures 110-133 in Appendix C.

Note the residuals in the simulation at a Reynolds number of 2,400 (velocity of 152.74 m/s) leveled off before dropping 4 orders of magnitude. All cases done with varying Reynolds number used the SST k-omega turbulence model. However, at this low Reynolds number, this model may not be as accurate as a laminar model. The residuals from this simulation only dropped 3 orders of magnitude. However, a popular criterion to determine convergence is requiring the residuals to drop 3 orders of magnitude [1]. Therefore, the results have been included and presented in the section.

As discussed in the CFD chapter, the target's angle of attack was altered to provide insight into the target's flight stability. Velocity contours with streamlines are shown at different angles of attack in Figures 64-69. Notice as the angle of attack

increases, the symmetry of the flow around the target decreases and eventually one asymmetric wake region forms. The pressure and temperature contours for each angle of attack can be found in Figures 83-94 in Appendix C.

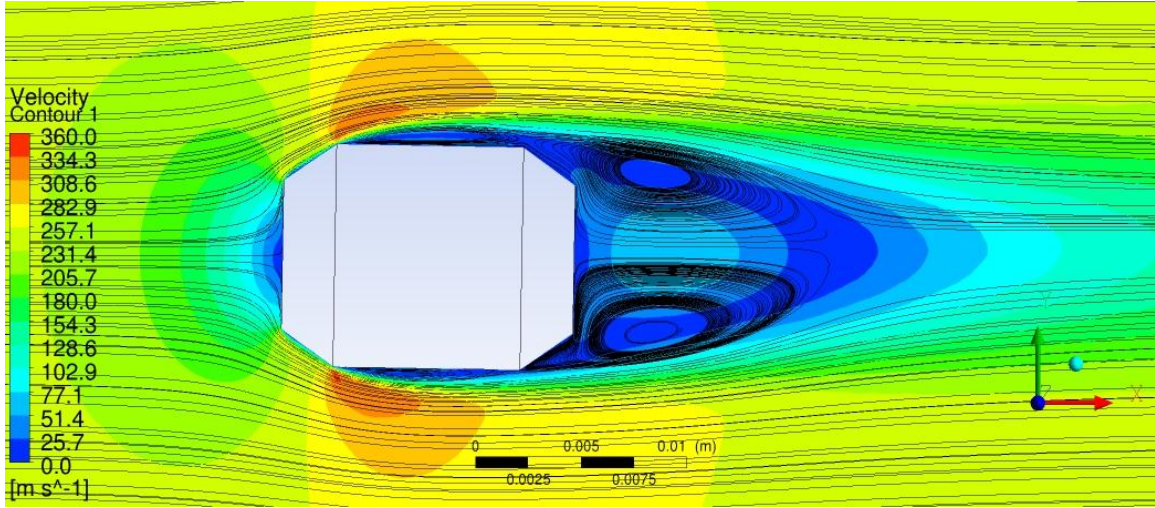


Figure 64. Velocity Contour and Streamline Plot for Target in 3D, Steady-State, Drift Simulation with 1° Angle of Attack

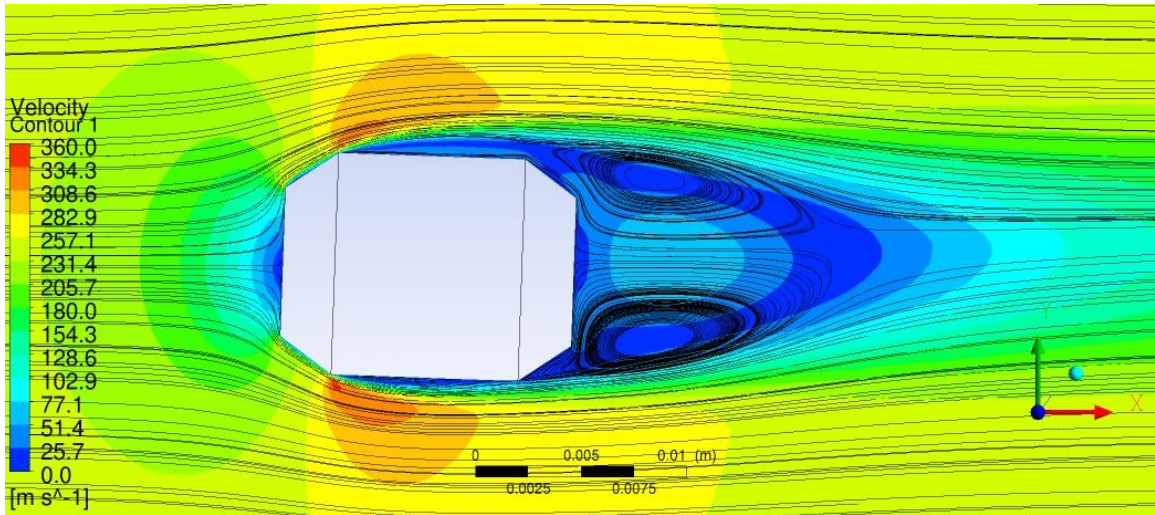


Figure 65. Velocity Contour and Streamline Plot for Target in 3D, Steady-State, Drift Simulation with 2° Angle of Attack

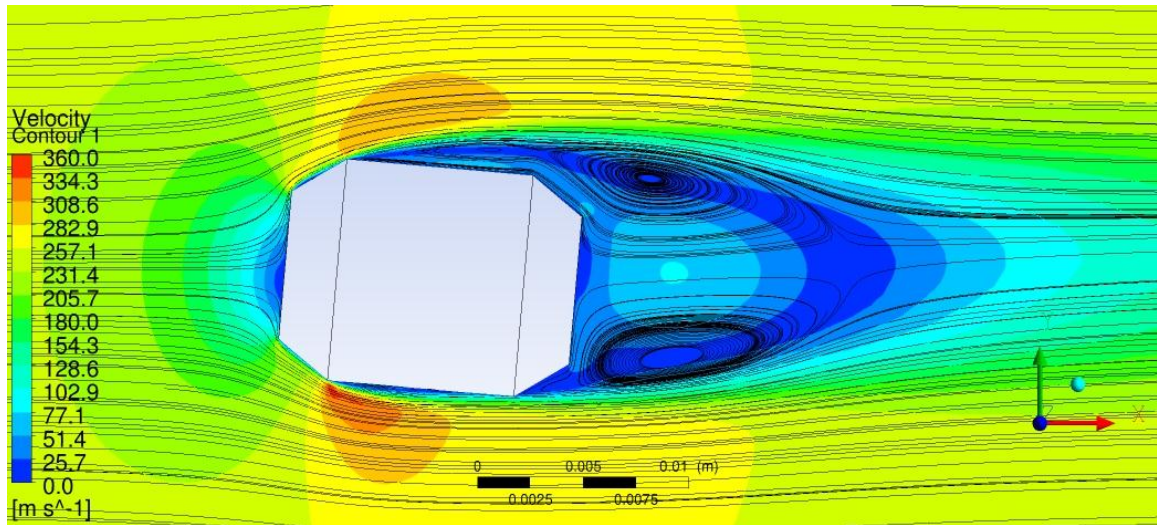


Figure 66. Velocity Contour and Streamline Plot for Target in 3D, Steady-State, Drift Simulation with 5° Angle of Attack

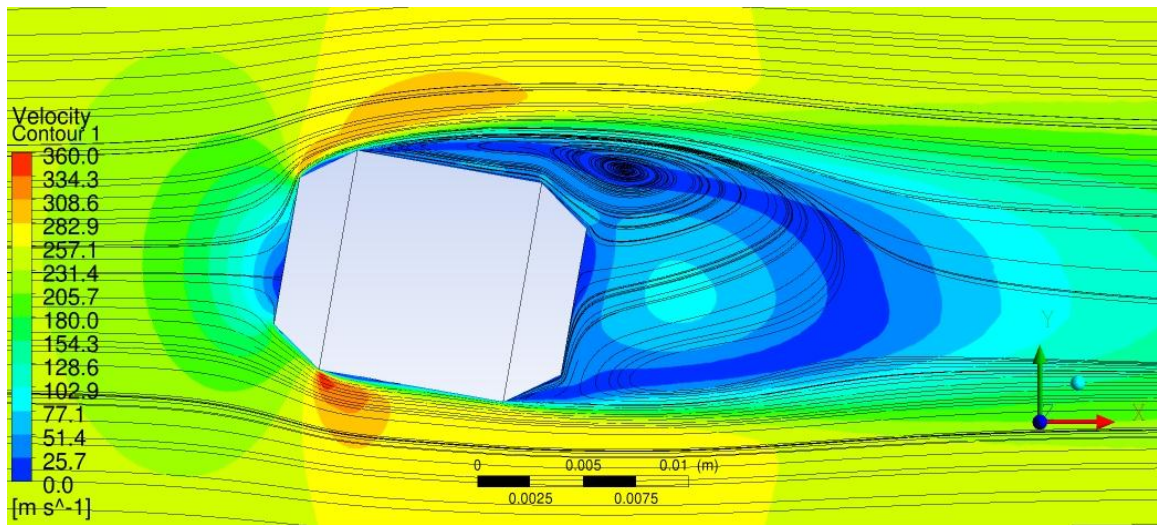


Figure 67. Velocity Contour and Streamline Plot for Target in 3D, Steady-State, Drift Simulation with 10° Angle of Attack

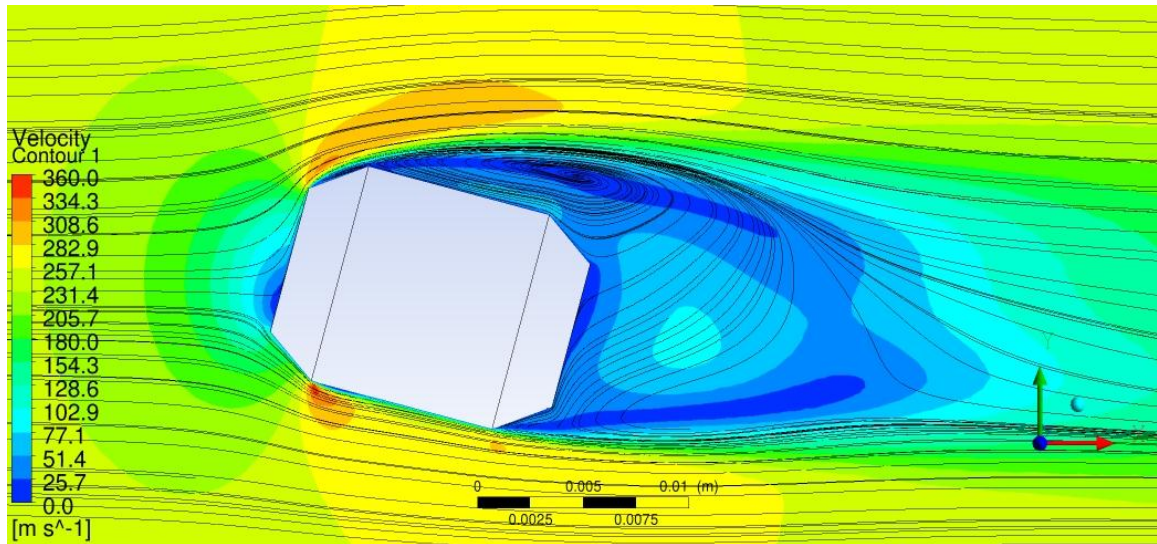


Figure 68. Velocity Contour and Streamline Plot for Target in 3D, Steady-State, Drift Simulation with 15° Angle of Attack

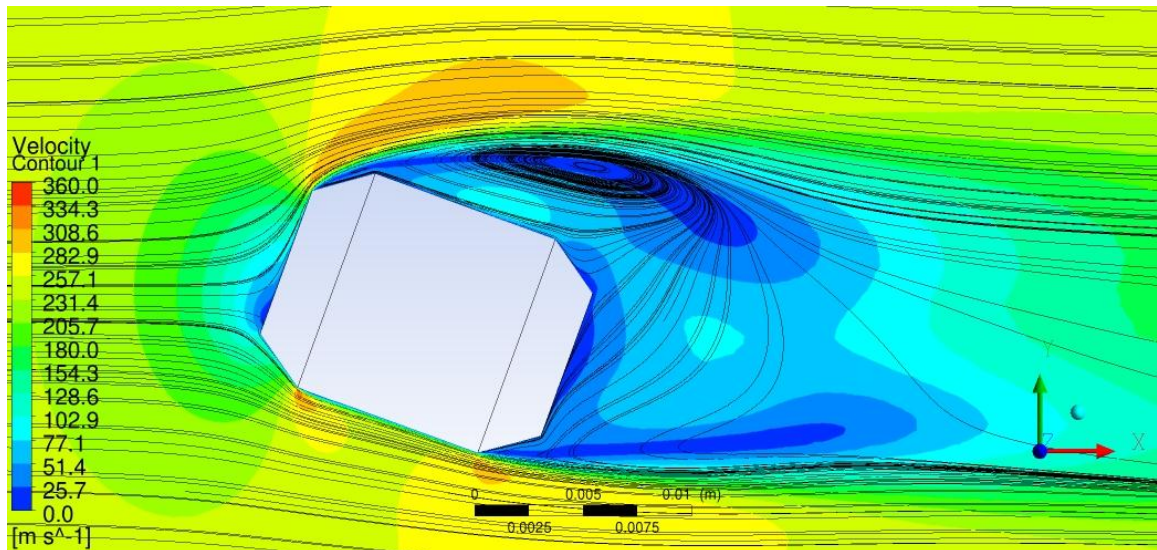


Figure 69. Velocity Contour and Streamline Plot for Target in 3D, Steady-State, Drift Simulation with 20° Angle of Attack

The forces and moments on the target at the different angles of attack were plotted and can be seen in Figures 70 and 71. Individual plots can be seen in Figures 98-109 in Appendix C. Simulations were done with the target spinning and not spinning. Note that the drag force, lift force, and z-axis (or overturning) moment changed minimally with

spin. This is to be expected, as “static aerodynamics [such as the drag force, lift force, and overturning moment] for spinning axisymmetric bodies are generally invariant with spin rate” [29]. Since the forces act at the center of pressure [18], local x-axis and local y-axis forces act through the local y-axis and local x-axis moment arms (distance from the center of gravity to the center of pressure in the local y-axis and local x-axis directions) to create the z-axis moment. Therefore, it is logical that minimal change due to spin in the drag and lift forces (which are simple transformations of the local x-axis and local y-axis forces) would create minimal change in the overturning moment.

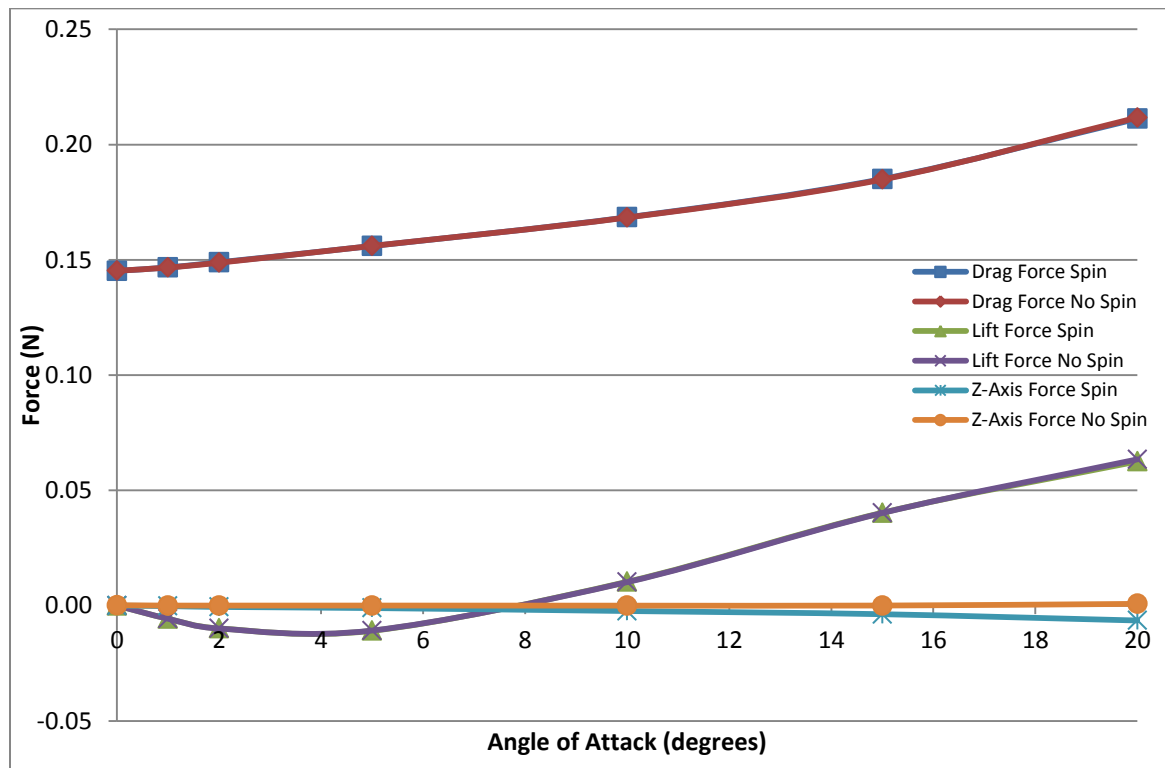


Figure 70. Forces on Spinning and Non-Spinning Target in Drift Region at Different Angles of Attack from 3D, Steady-State Model

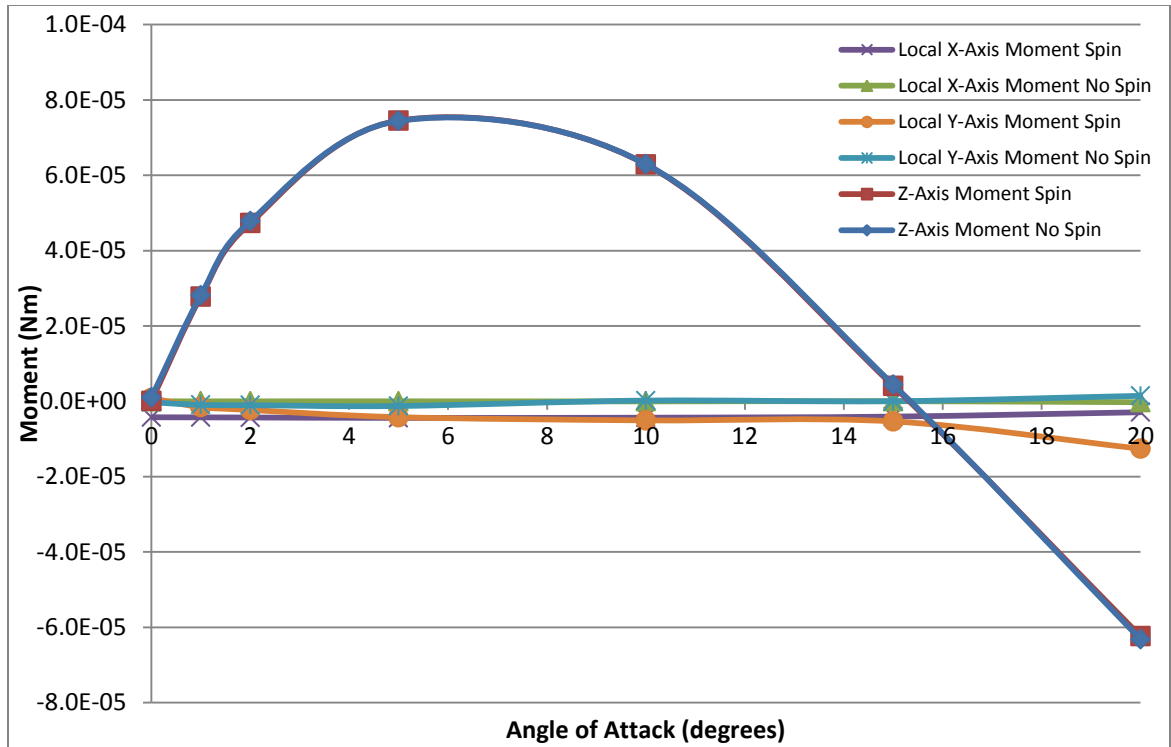


Figure 71. Moments on Spinning and Non-Spinning Target in Drift Region at Different Angles of Attack from 3D, Steady-State Model

In Figure 70, the drag force increases as the angle of attack increases. Since the frontal projected area increases as the angle of attack increases, an increase in drag seems physically reasonable. Also note that the lift force reaches a minimum point at approximately 4° and then appears to increase as the angle of attack increases. From the velocity contour and streamline plots above, it appears that only walls 1 and 2 interact with the frontal incoming jet at small angles of attack. As the angle of attack increases, the recirculation region around wall 3 decreases and wall 3 eventually joins walls 1 and 2 in interacting with the frontal jet. This frontal jet of fluid that interacts with wall 3 is forced downward around the target. This causes an equal and opposite force (upward lift) on the target by Newton's third law [19].

As can be seen in the velocity contour and streamline plots, the angle of attack simulations were created by rotating the target about the negative z-axis. From Figure

71, the z-axis (or overturning) moment above approximately 15° is negative and would increase the angle of attack, indicating a destabilizing moment. However, at small angles of attack, the overturning moment is positive, which would tend to decrease the angle of attack and tend to stabilize the target.

The static aerodynamic forces and moments (drag force, lift force, and overturning moment) were determined from the non-spinning target simulations and the Magnus moment (a dynamic moment) was determined from the spinning target simulations. This approach was recommended as aeroballistic “standard practice” [29]. Using these and the equations provided (and reproduced in the background chapter) by McCoy [18], the aerodynamic coefficients of drag, lift, Magnus moment, and overturning moment were calculated and used to determine static stability at different angles of attack. See Table 20 below. Note that the target is statically stable at or below an angle of attack of 15° . Note that this indicates the target does not need spin to be stabilized at low angles of attack. However, if the target’s angle of attack is greater than 15° , spin would be required to gyroscopically stabilize the target.

Table 20. Aerodynamic Coefficients and Static Stability of Target in Drift Region at Different Angles of Attack

Angle of Attack (degrees)	1	2	5	10	15	20
Drag Coefficient, C_D	0.5406	0.5484	0.5752	0.6207	0.6815	0.7805
Lift Coefficient, C_L	-1.1948	-1.0476	-0.4557	0.2170	0.5726	0.6841
Magnus Moment Coefficient, $C_{M_{p\alpha}}$	5.200E-05	3.851E-05	2.832E-05	1.708E-05	1.211E-05	2.156E-05
Overturning Moment Coefficient, C_{M_α}	-0.56632	-0.48095	-0.29985	-0.12727	-0.00599	0.06483
Starred Overturning Moment Coefficient, $C_{M_\alpha}^*$	-8.509E-06	-7.226E-06	-4.505E-06	-1.912E-06	-9.005E-08	9.741E-07
M	-3.309E-17	-2.811E-17	-1.752E-17	-7.437E-18	-3.502E-19	3.789E-18
Statically Stable?	Yes	Yes	Yes	Yes	Yes	No

If injected with an angle of attack less than 15° , the target would oscillate between positive and negative angles of attack (of decreasing magnitude) about the axis parallel to the free-stream flow. Since the overturning moment is typically calculated from non-spinning simulations, Excel was used to determine the best-fit polynomial for the overturning moment on the non-spinning target as a function of the angle of attack:

$$M_\alpha = (5.265E - 8) \left(\alpha_t \frac{180}{\pi} \right)^3 - (2.510E - 6) \left(\alpha_t \frac{180}{\pi} \right)^2 + (2.584E - 5) \alpha_t \frac{180}{\pi} + 3.290E - 6 \quad (36)$$

where M_α is the moment about the z-axis (overturning moment) in Nm and α_t is the total yaw angle (which is the angle of attack for these simulations) in radians. Using rotational kinematic equations of motion from Meriam [19] and the best-fit polynomial equation for the overturning moment, the angle of attack was plotted over time with MATLAB with different initial angles of attack. (Note that this motion is for a non-spinning target.)

However, since the duration of the flight through the drift region is only approximately 0.16 ms and the aspect ratio of the target is short, dynamic effects such as pitch damping would be minimal. Therefore, the oscillatory motion can be viewed as an approximation for a spinning target about a coordinate system that rotates at the target spin rate. See Appendix D for the MATLAB code including the equations used. Figures 134-138 in Appendix D show the plots of the angle of attack versus time for different initial angles of attack. Table 21 includes the period of oscillation for each initial angle of attack case. Since the flight in the drift region is only approximately 0.016 s, the target wouldn't complete an oscillation with any of the initial angle of attacks modeled. Also, the change in amplitude of the oscillations is presented in Table 21, indicating the effect of damping due to the overturning moment during short flight is negligible. The exiting angle of attack after 0.016 s for each initial case is also included in Table 21.

Table 21. Angle of Attack Oscillation and Exit Value Determined by MATLAB Code

Angle of Attack	1	2	5	10	15
Period of Oscillation (s)	0.0461	0.0499	0.0574	0.0832	0.2061
Peak Amplitude After 25 Periods (°)	0.9994	1.999	4.998	9.995	14.94
Change in Amplitude After 25 Periods (°)	0.0006	0.001	0.002	0.005	0.06
Angle of Attack after 0.016s (°)	-0.585	-0.882	-0.684	4.115	14.600
Change in Angle of Attack (°)	1.585	2.882	5.684	5.885	0.400

Further investigation of target flight stability could include simulating steady coning motion to determine the pitch damping moment at different angles of attack. The pitch damping moment coefficient can be used with the other aerodynamic coefficients presented above to determine the dynamic stability factor. This would allow the calculation of a spin rate limit for the low angle of attack flight as well as determine if the target could be spin-stabilized above an angle of attack of 15°.

CONCLUSIONS

In conclusion, the flow over the target in the drift region experiences many of the same trends in velocity, pressure, separation, and wake symmetry that flow over a sphere would. For the majority of the flight, the target would have a steady wake region. Only approximately 0.8 ms of its 16 ms flight through the drift regime would experience transient effects.

The target would be statically stable if injected at low angles of attack (less than 15°). Target spin would not be required for stability at these low angles. These results can have significant implications on the requirements and design of the target injection system. The drag and Nusselt correlations provided in the results chapter could further assist with design changes (i.e. target velocity change).

The simulations predictions of heat transfer aligned well with those predicted by experimentally and analytically determined correlations for similar conditions. Close alignment of the simulated and predicted drag coefficients was less successful. Therefore, the 3D, steady-state simulation's heat transfer estimation would most likely have greater accuracy than its drag coefficient approximation.

Future work could consist of determining the pitch damping moment through steady coning motion simulations. The pitch damping moment coefficient along with the other aerodynamics coefficients presented in the results section could be used to solve the simultaneous differential equations of motion presented in McCoy's 6-degrees-of-freedom section [18]. A 6-degree-of-freedom Fluent simulation could be created and run, and the results could be compared to the predictions given by McCoy's equations of motion. Additionally, the transition from the injector to the drift region and from the drift region to the chamber could be explored with transient simulations.

BIBLIOGRAPHY

- [1] ANSYS, Inc. “ANSYS Fluent User’s Guide: Release 14.5.” Pennsylvania, 2012.
- [2] Bailey, A. B., J. Hiatt. “Sphere Drag Coefficients for a Broad Range of Mach and Reynolds Numbers.” *AIAA Journal* 10 (1972): 1436-1440.
- [3] Belov, A., V. S. Terpigor’ev. “Turbulence in Calculations of Heat Transfer at the Stagnation Point of a Jet Interacting Normally with a Planar Obstacle.” New York: Plenum Publishing Corporation, 1972.
- [4] Clift, R., J. R. Grace, M. E. Weber. *Bubbles, Drops, and Particles*. New York: Academic Press, Inc, 1978.
- [5] “Fundamental Physical Constants.” *The NIST Reference on Constants, Units, and Uncertainty*. NIST Physical Measurement Laboratory, 2010. Web. 15 July 2013.
- [6] Hadad, Yaser, Khosrow Jafarpur. (2008, August). “Laminar Forced Convection Heat Transfer from Isothermal Bodies with Unit Aspect Ratio.” Paper presented at the 6th IASME/WSEAS International Conference on Heat Transfer, Thermal Engineering, and Environment, Rhodes, Greece.
- [7] Heller, Arnie. “Igniting our Energy Future.” *Science and Technology Review* July/August 2011: 4-12.
- [8] Hirschfelder, J. O., C. F. Curtiss, R. B. Bird. *The Molecular Theory of Gases and Liquids*. New York: Wiley, 1964.
- [9] “How ICF Works.” *NIF*. Lawrence Livermore National Laboratory, n.d. Web. 30 July 2013.
- [10] Incropera, Frank P., David P. Dewitt, Theodore L. Bergman, Adrienne S. Lavine. *Introduction to Heat Transfer*. 5th ed. John Wiley & Sons, Inc, 2007.

- [11] “Inertial Confinement Fusion: How to Make a Star.” *NIF*. Lawrence Livermore National Laboratory, n.d. Web. 30 July 2013.
- [12] Jones, D. A., D. B. Clarke. “Simulation of Flow Past a Sphere using the Fluent Code.” Victoria, Australia: Maritime Platforms Division, 2008.
- [13] Kang, S. S., E. M. Sparrow. “Heat Transfer from an Open- or Closed- Bore Cylinder Situated Longitudinal to a Freestream.” *Transactions of the ASME: Journal of Heat Transfer* 109 (1987): 314-320.
- [14] Kestin, J., S. T. Ro, W. Wakeham. “An Extended Law of Corresponding State for the Equilibrium and Transport Properties of the Noble Gases.” *Physica* 58 (1972): 165-211.
- [15] Lawrence Livermore National Laboratory. “LIFE Inside and Out.” Illustration. NIF Multimedia Photo Gallery: LIFE. Web. 09 Dec. 2013.
- [16] Lawrence Livermore National Laboratory. “NIF Hohlraum.” Photograph. NIF Multimedia Photo Gallery: Target Area. Web. 09 Dec. 2013.
- [17] Lawrence Livermore National Laboratory. “The Power of Light.” Simulation. NIF Multimedia Video Gallery. Web. 09 Dec. 2013.
- [18] McCoy, Robert L. *Modern Exterior Ballistics: The Launch and Flight Dynamics of Symmetric Projectiles*. Pennsylvania: Schiffer Publishing Ltd., 1999.
- [19] Meriam, J. L., L. G. Kraige. *Engineering Mechanics: Dynamics* 6th ed. John Wiley & Sons, Inc, 2007.
- [20] Moran, Michael J., Howard N. Shapiro. *Fundamentals of Engineering Thermodynamics*. 6th ed. John Wiley & Sons, Inc., 2008

- [21] Munson, Bruce R., Donald R. Young, Theodore H. Okiishi, Wade W. Huebsch. *Fundamentals of Fluid Mechanics*. 6th ed. John Wiley & Sons, Inc, 2009.
- [22] Nakamura, Isao. “Steady Wake Behind a Sphere.” *The Physics of Fluids* 19 (1976): 5-8.
- [23] Reid, Robert C., John M. Prausnitz, Bruce E. Poling. *The Properties of Gases & Liquids*. 4th ed. McGraw-Hill, 1987.
- [24] Roos, Frederick W., William W. Willmarth. “Some Experimental Results on Sphere and Disk Drag.” *AIAA Journal* 9 (1971): 285-291.
- [25] Sakamoto, H., H. Haniu. “A Study on Vortex Shedding from Spheres in a Uniform Flow.” *Transactions of the ASME: Journal of Fluids Engineering* 112 (1990): 386-392.
- [26] Sogin, H. H. “A Summary of Experiments on Local Heat Transfer from the Rear of Bluff Obstacles to a Low Speed Airstream.” *Transactions of the ASME: Journal of Heat Transfer* 86 (1964): 200-202.
- [27] Taneda, Sadatoshi. “Experimental Investigation of the Wake behind a Sphere at Low Reynolds Numbers.” *Journal of the Physical Society of Japan* 11 (1956): 1104-1108.
- [28] “The Element Xenon.” Thomas Jefferson National Accelerator Facility – Office of Science Education, n.d. Web. 16 July 2013.
- [29] Weinacht, Paul. “Prediction of Projectile Performance, Stability, and Free-Flight Motion Using Computational Fluid Dynamics.” Maryland: Army Research Laboratory, 2003.
- [30] Wolfram | Alpha. Wolfram Alpha LLC, 2013. Web. 16 July 2013.

APPENDICES

Appendix A: Fluent Setup

Table 22. Detailed Fluent Case Setup for 2D, Axisymmetric Sphere in Drift Region

Version		2D, double precision
Space Model		Axisymmetric
Time Model		Steady
Velocity Formulation		Absolute
Viscous Model		Laminar
Heat Transfer Model		Enabled
Xenon Density		Ideal gas
Xenon Specific Heat (J/(kg-K))		158.32
Xenon Thermal Conductivity (W/(m-K))		0.0159
Xenon Viscosity (kg/(m-s))		6.7E-5
Xenon Molecular Weight (kg/kgmol)		131.293
Aluminum Density (kg/m ³)		2719
Aluminum Specific Heat (J/(kg-K))		871
Aluminum Thermal Conductivity (W/(m-K))		202.4
Inlet	Mass Flow Inlet	
	Reference Frame	Absolute
	Mass Flow Specification Method	Mass Flow Rate
	Mass Flow Rate	Case dependent - see Table 4
	Supersonic/Initial Gauge Pressure	0 Pa
	Axial-component of flow direction	1
	Radial-component of flow direction	0
	Total temperature	Case dependent - see Table 4
Sphere	Stationary wall	
	No slip	
	Heat Flux	0 W/m ²
	Heat generation rate	0 W/m ³
	Material	Aluminum
Outer Wall	Stationary wall	
	Specified shear x-component	0 Pa
	Specified shear y-component	0 Pa
	Heat flux	0 W/m ²
	Heat generation rate	0 W/m ³
	Material	Aluminum
Outlet	Pressure outlet	
	Gauge pressure	0 Pa
	Backflow direction specification method	Normal to boundary
	Backflow total temperature	Case dependent - see Table 4

Axis	Axis	
Operating pressure	6666.118 Pa	
Solver	Pressure-based, Coupled	
Discretization Scheme	Gradient	Green-Gauss Node Based
	Pressure	Second order
	Density	Second order upwind
	Momentum	Second order upwind
	Energy	Second order upwind
Pseudo Transient	Enabled	
	Time Step Method	Automatic
	Timescale Factor	1
	Length Scale Method	Conservative
	Verbosity	0
Pressure Relaxation Factor	0.5	
Momentum Relaxation Factor	0.5	
Density Relaxation Factor	1	
Body Forces Relaxation Factor	1	
Energy Relaxation Factor	0.75	
Solution Limits	Default	
Residual Monitor	Absolute convergence criteria (all)	1e-9
	Iterations to store	1000
Solution Initialization	Standard, absolute	Compute from inlet
Initial Values	Gauge Pressure	0 Pa
	Axial Velocity	Case dependent – see Table 4
	Radial Velocity	0 m/s
	Temperature	1050 K
Number of iterations	500	

Table 23. Detailed Fluent Case Setup for 2D, Axisymmetric Swirl Target in Drift Region

Version	2D, double precision
Space Model	Axisymmetric swirl
Time Model	Unsteady, 1 st order implicit
Velocity Formulation	Absolute
Viscous Model	SST k-omega turbulence
Heat Transfer Model	Enabled
Xenon Density	Ideal gas
Xenon Specific Heat (J/(kg-K))	158.32
Xenon Thermal Conductivity (W/(m-K))	$-0.0002769 + 2.088\text{E-}5T - 5.323\text{E-}9T^2$
Xenon Viscosity (kg/(m-s))	$-1.167\text{E-}6 + 8.796\text{E-}8T - 2.243\text{E-}11T^2$

Xenon Molecular Weight (kg/kgmol)		131.293
Aluminum Density (kg/m ³)		2719
Aluminum Specific Heat (J/(kg-K))		871
Aluminum Thermal Conductivity (W/(m-K))		202.4
Inlet	Far-field pressure	
	Gauge pressure	0 Pa
	Mach number	0.7509739
	Temperature	1050 K
	Axial-component of flow direction	1
	Radial-component of flow direction	0
	Tangential-component of flow direction	0
	Turbulent intensity	1%
	Turbulent viscosity ratio	1%
Target 1-5	Moving wall with absolute, rotational motion	1570.796 rad/s
	No slip	
	Roughness height	0 m
	Roughness constant	0.5
	Temperature	20 K
	Heat generation rate	0 W/m ³
	Material	Aluminum
Outer Wall	Stationary wall	
	Specified shear x-component	0 Pa
	Specified shear y-component	0 Pa
	Specified shear z-component	0 Pa
	Roughness height	0 m
	Roughness constant	0.5
	Heat flux	0 W/m ²
	Heat generation rate	0 W/m ³
	Material	Aluminum
Outlet	Pressure outlet	
	Gauge pressure	0 Pa
	Backflow direction specification method	Normal to boundary
	Backflow turbulent intensity	1%
	Backflow turbulent viscosity ratio	1
	Backflow total temperature	1247.39 K
Axis	Axis	
Operating pressure	6666.118 Pa	
Solver	Density-based, Implicit	
Flux Type	Roe-FDS	
Discretization Scheme	Gradient	Green-Gauss Node Based
	Flow	First order upwind
	Turbulent Kinetic Energy	First order upwind
	Specified Dissipation Rate	First order upwind

Turbulent Kinetic Energy Relaxation Factor		0.8
Specified Dissipation Rate Relaxation Factor		0.8
Turbulent Viscosity Relaxation Factor		1
Solid Relaxation Factor		1
Courant Number		5
Solution Limits		Default
Residual Monitor	Absolute convergence criteria (all)	1e-4
	Iterations to store	10000
Solution Initialization	Standard, absolute	Compute from inlet
Initial Values	Gauge Pressure	0 Pa
	Axial Velocity	250 m/s
	Radial Velocity	0 m/s
	Swirl Velocity	0 m/s
	Turbulent Kinetic Energy	$9.37473 \text{ m}^2/\text{s}^2$
	Specific Dissipation Rate	52213.61 1/s
	Temperature	1050 K
Time step		5E-7 s
Number of time steps		2000
Max Iterations per time step		150

Table 24. Detailed Fluent Case Setup for 3D, Steady-State Target in Drift Region

Version		3D, double precision
Time Model		Steady
Velocity Formulation		Absolute
Viscous Model		SST k-omega turbulence
Heat Transfer Model		Enabled
Xenon Density		Ideal gas
Xenon Specific Heat (J/(kg-K))		158.32
Xenon Thermal Conductivity (W/(m-K))		$-0.0002769 + 2.088\text{E-}5T - 5.323\text{E-}9T^2$
Xenon Viscosity (kg/(m-s))		$-1.167\text{E-}6 + 8.796\text{E-}8T - 2.243\text{E-}11T^2$
Xenon Molecular Weight (kg/kgmol)		131.293
Aluminum Density (kg/m ³)		2719
Aluminum Specific Heat (J/(kg-K))		871
Aluminum Thermal Conductivity (W/(m-K))		202.4
Inlet	Far-field pressure	
	Gauge pressure	0 Pa
	Mach number	0.7509739
	Temperature	1050 K
	Axial-component of flow direction	1
	Radial-component of flow direction	0

	Tangential-component of flow direction	0
	Turbulent intensity	1%
	Turbulent viscosity ratio	1%
Target 1-5	Moving wall with absolute, rotational motion	
	Rotation-Axis Origin	(0, 0, 0)
	Rotation-Axis Direction	(1, 0, 0)
	Rotational Speed	1570.796 rad/s
	No slip	
	Roughness height	0 m
	Roughness constant	0.5
	Temperature	20 K
	Heat generation rate	0 W/m ³
	Material	Aluminum
Outer Wall	Stationary wall	
	Specified shear x-component	0 Pa
	Specified shear y-component	0 Pa
	Specified shear z-component	0 Pa
	Roughness height	0 m
	Roughness constant	0.5
	Heat flux	0 W/m ²
	Heat generation rate	0 W/m ³
	Material	Aluminum
Outlet	Pressure outlet	
	Gauge pressure	0 Pa
	Backflow direction specification method	Normal to boundary
	Backflow turbulent intensity	1%
	Backflow turbulent viscosity ratio	1
	Backflow total temperature	1247.39 K
Operating pressure	6666.118 Pa	
Solver	Density-based, Implicit	
Flux Type	Roe-FDS	
Discretization Scheme	Gradient	Green-Gauss Node Based
	Flow	First order upwind
	Turbulent Kinetic Energy	First order upwind
	Specified Dissipation Rate	First order upwind
Turbulent Kinetic Energy Relaxation Factor		0.8
Specified Dissipation Rate Relaxation Factor		0.8
Turbulent Viscosity Relaxation Factor		1
Solid Relaxation Factor		1
Courant Number		5
Solution Limits		Default
Residual Monitor	Absolute convergence criteria (all)	1e-4
	Iterations to store	10000

Solution Initialization	Standard, absolute	Compute from inlet
Initial Values	Gauge Pressure	0 Pa
	X Velocity	250 m/s
	Y Velocity	0 m/s
	Z Velocity	0 m/s
	Turbulent Kinetic Energy	9.37473 m ² /s ²
	Specific Dissipation Rate	52213.61 1/s
	Temperature	1050 K
Number of iterations		30000

Appendix B: Additional Plots of 2D, Axisymmetric Swirl, Transient Simulation of Target in Drift Region

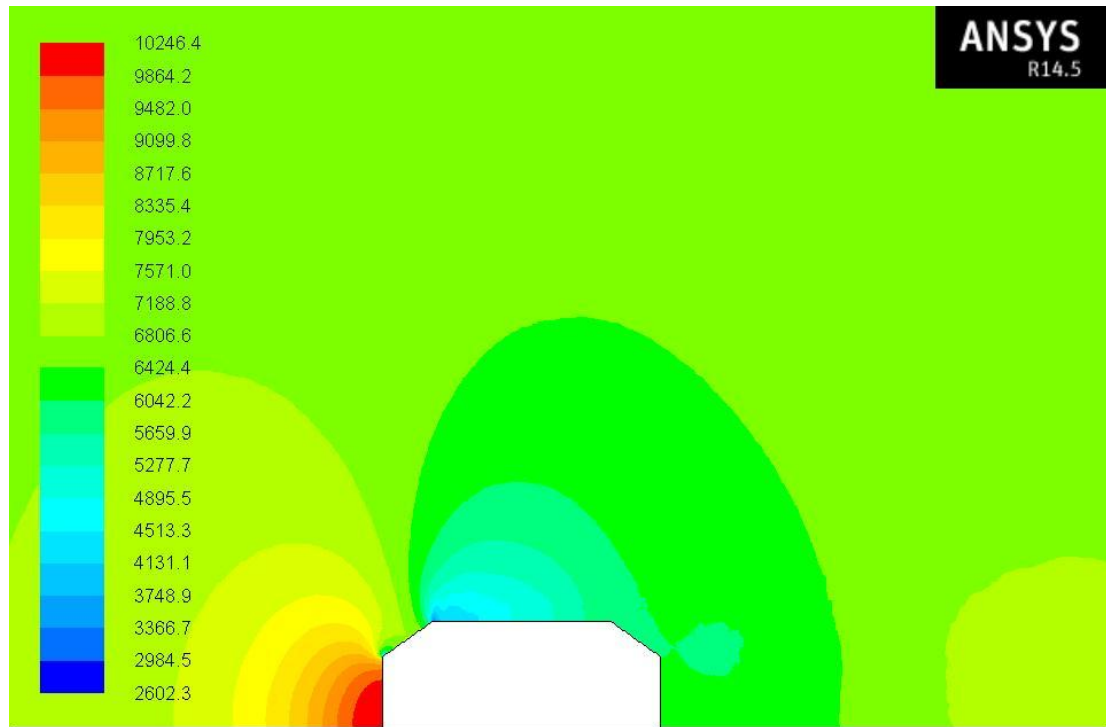


Figure 72. Pressure Contour of 2D, Axisymmetric Swirl Flow over Target in Drift Region at 1.00E-3 s

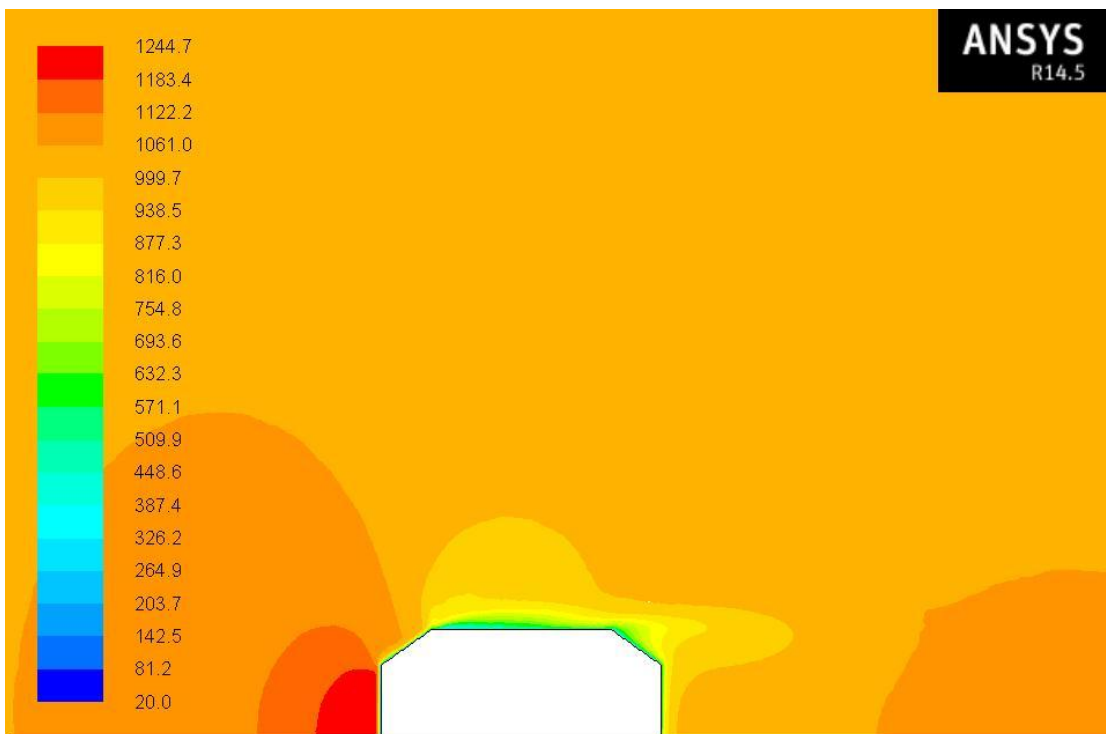


Figure 73. Temperature Contour of 2D, Axisymmetric Swirl Flow over Target in Drift Region at 1.00E-3 s

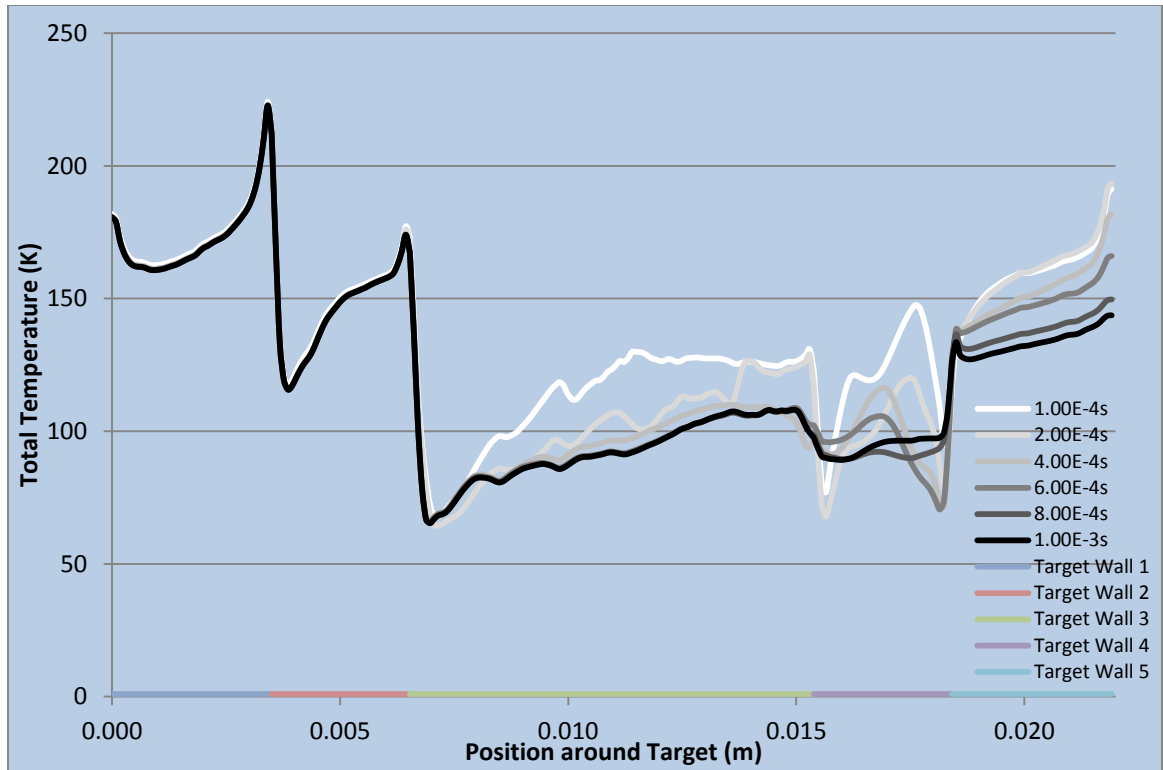


Figure 74. Total Temperature around Target in Drift Region from 2D, Axisymmetric Swirl Model

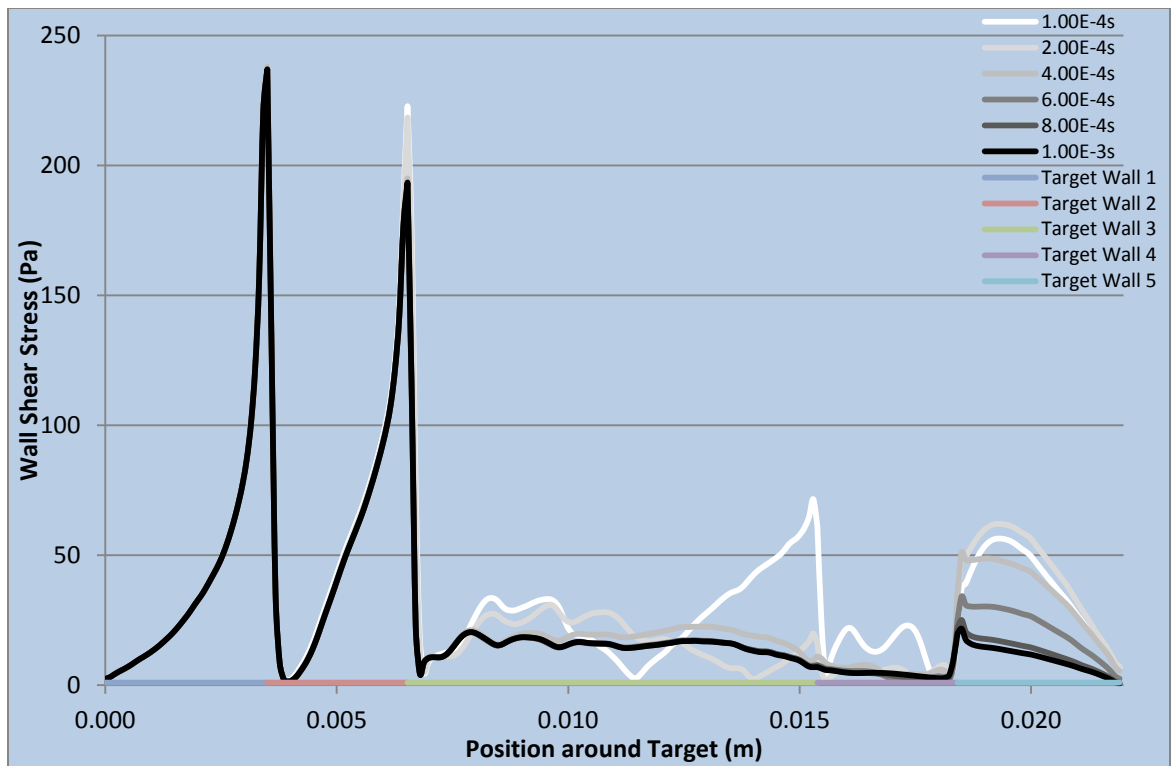


Figure 75. Wall Shear Stress around Target in Drift Region from 2D, Axisymmetric Swirl Model

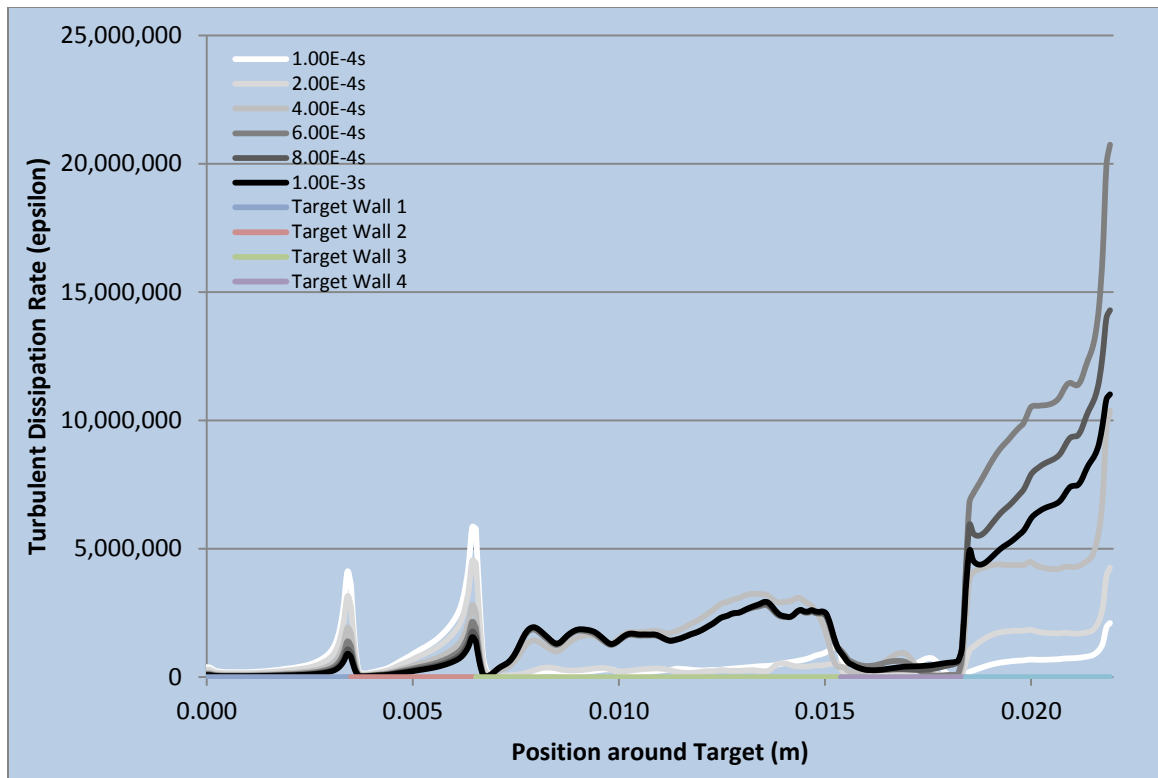


Figure 76. Turbulent Dissipation Rate around Target in Drift Region from 2D, Axisymmetric Swirl Model

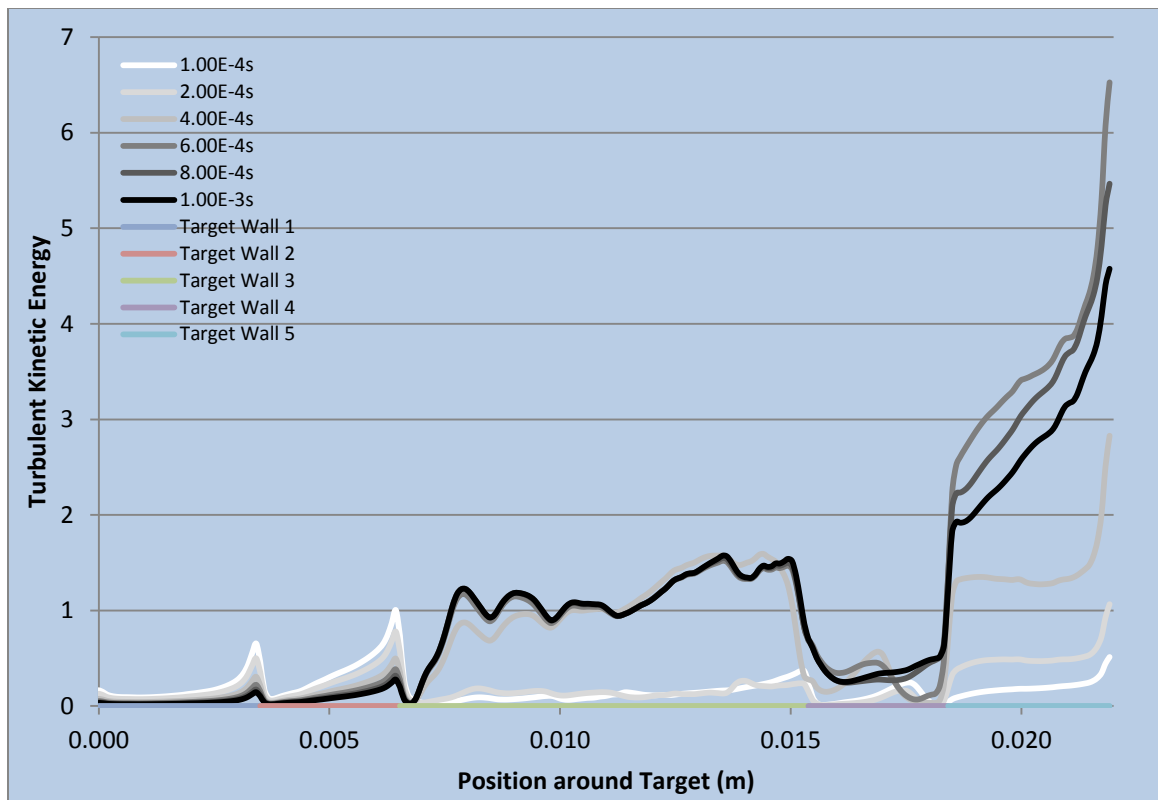


Figure 77. Turbulent Kinetic Energy around Target in Drift Region from 2D, Axisymmetric Swirl Model

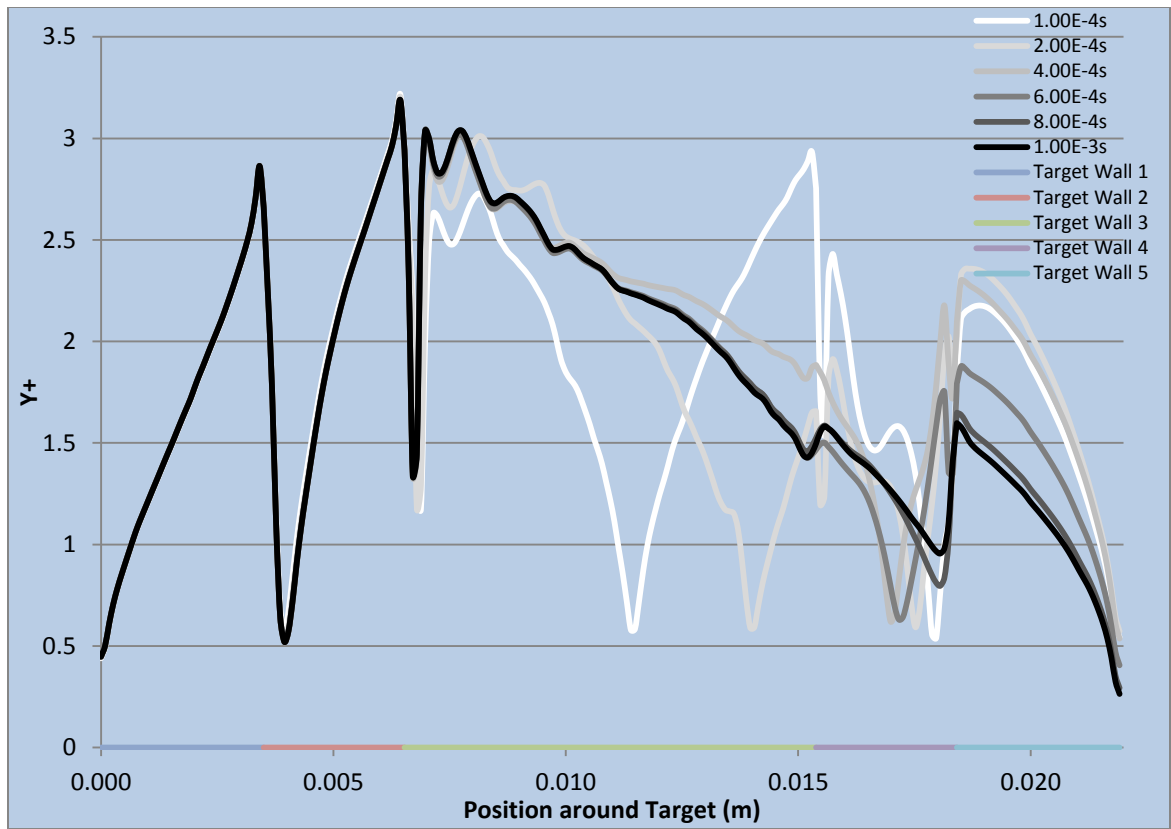


Figure 78. Y+ Values around Target in Drift Region from 2D, Axisymmetric Swirl Model

Appendix C: Additional Plots of 3D, Steady-State Simulation of Target in Drift Region

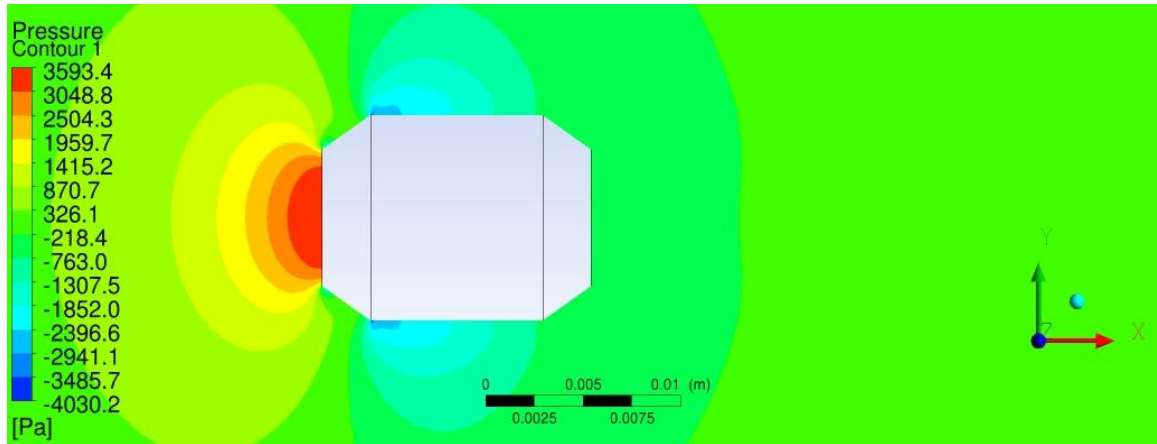


Figure 79. Pressure Contour on 3D, Steady-State Spinning Target in Drift Region

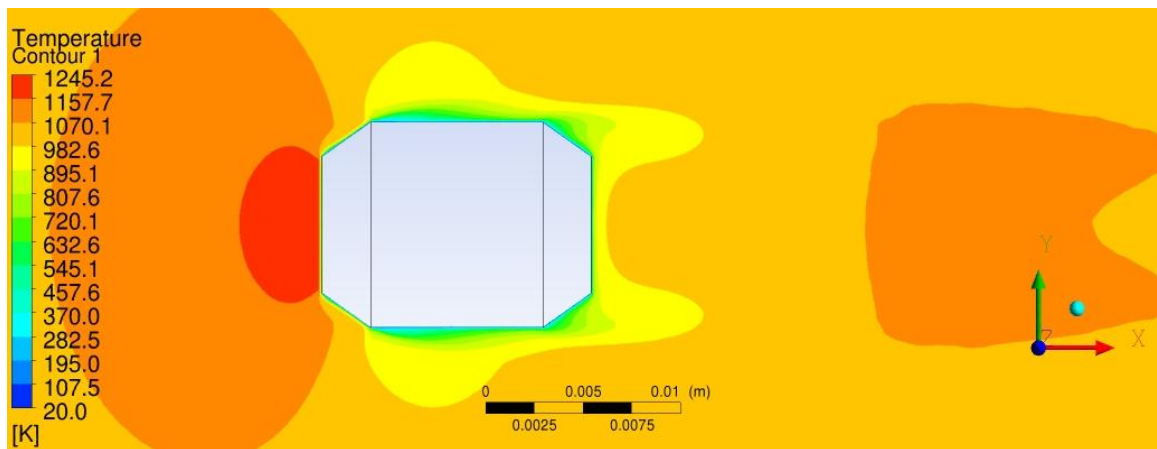


Figure 80. Temperature Contour on 3D, Steady-State Spinning Target in Drift Region

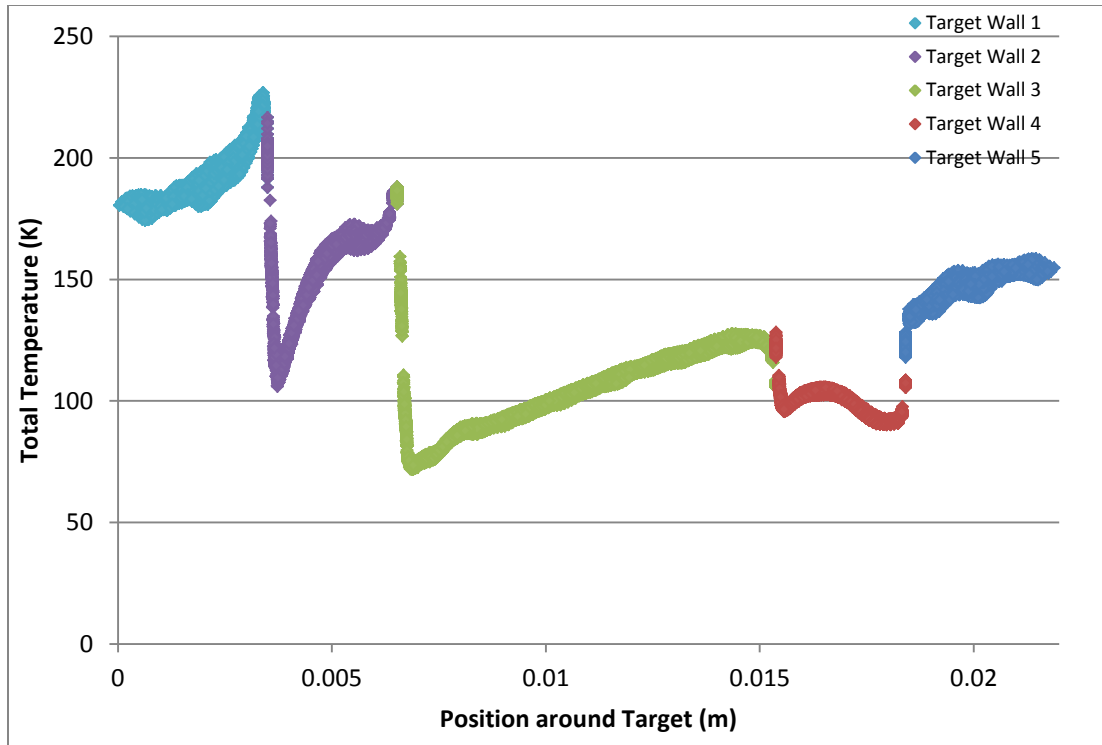


Figure 81. Total Temperature around Target in Drift Region from 3D, Steady-State Simulation

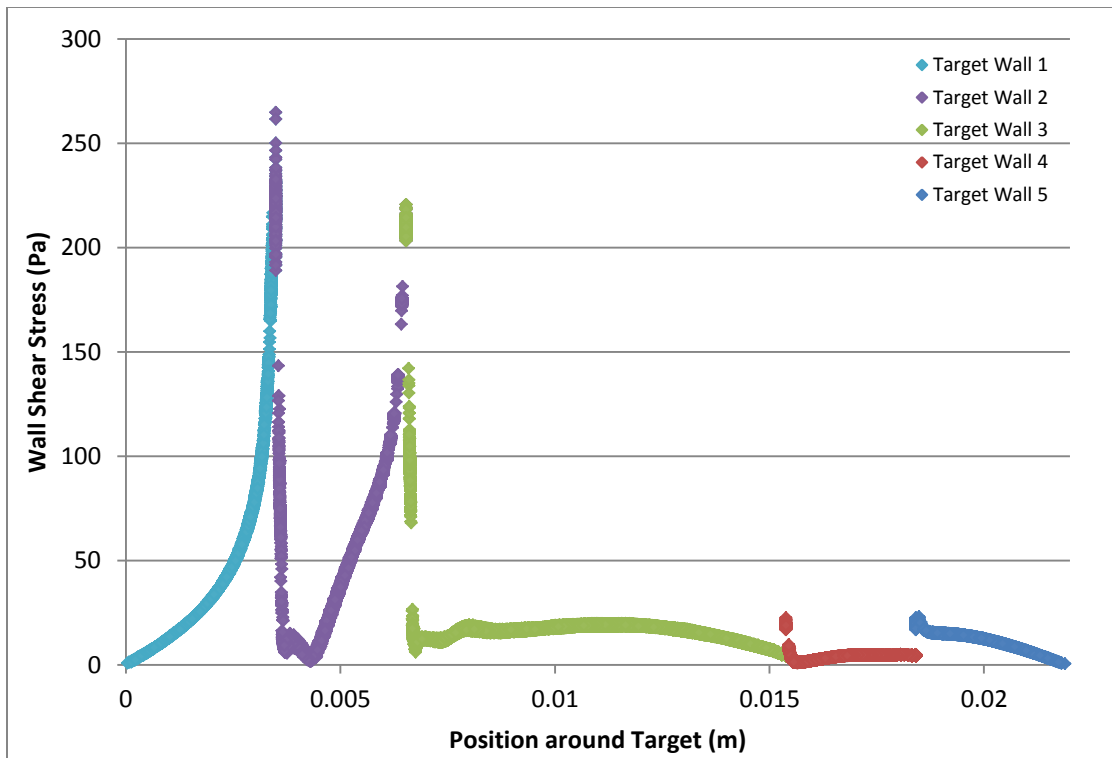


Figure 82. Wall Shear Stress around Target in Drift Region from 3D, Steady-State Simulation

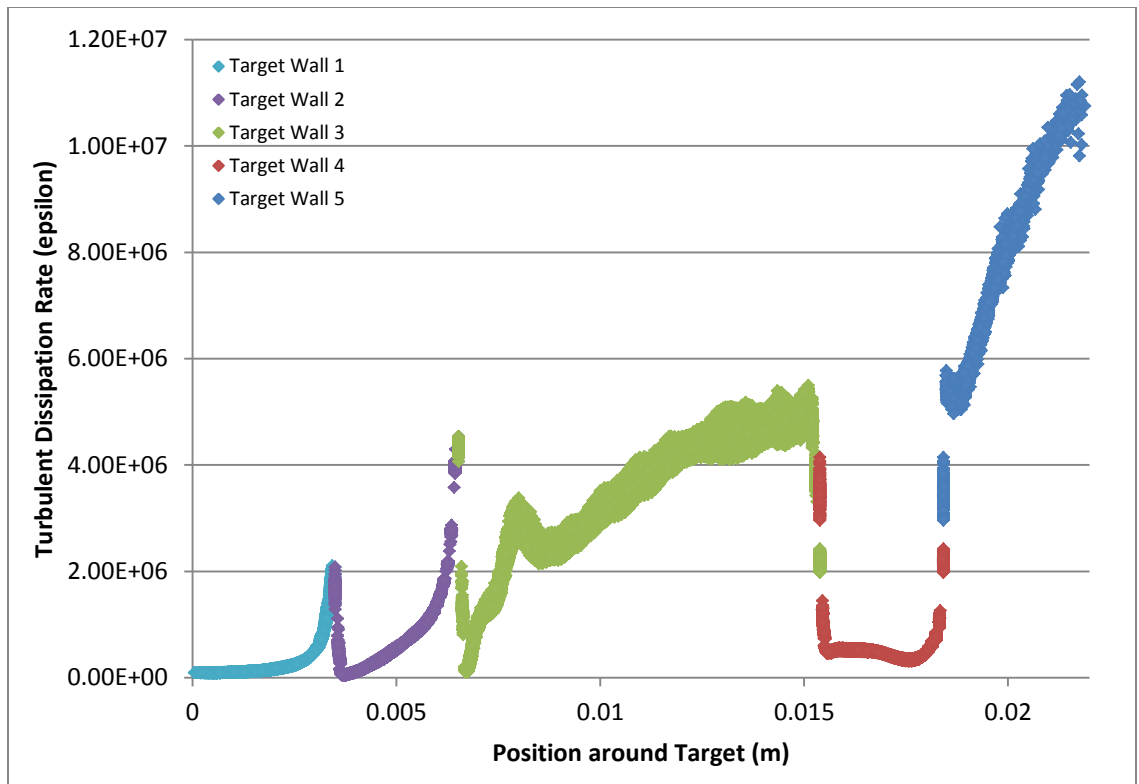


Figure 83. Turbulent Dissipation Rate around Target in Drift Region from 3D, Steady-State Simulation

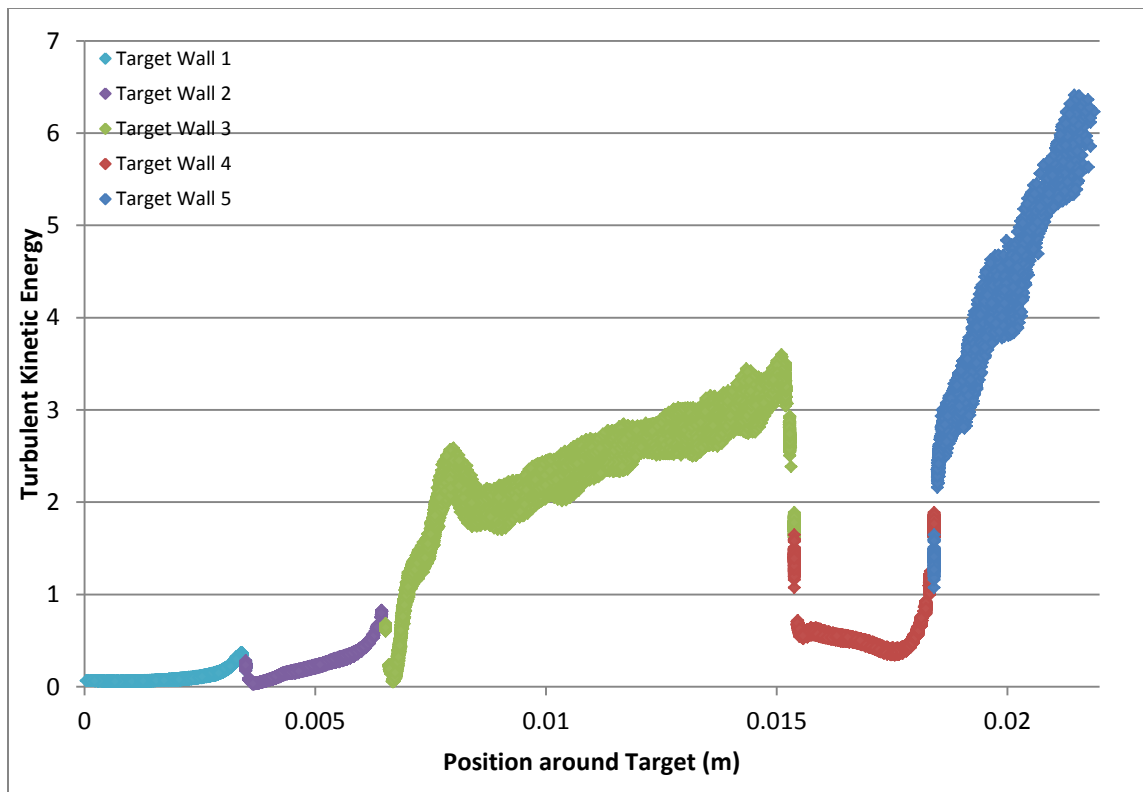


Figure 84. Turbulent Kinetic Energy around Target in Drift Region from 3D, Steady-State Simulation

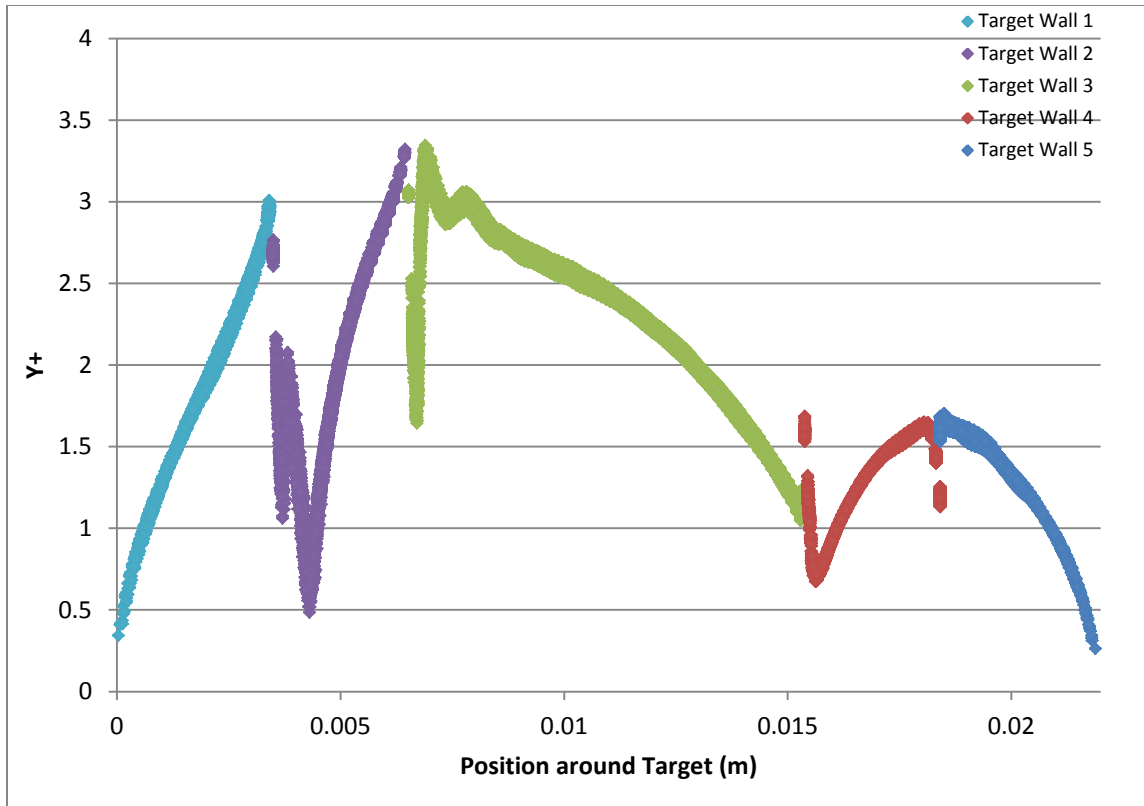


Figure 85. Y+ Values around Target in Drift Region from 3D, Steady-State Simulation

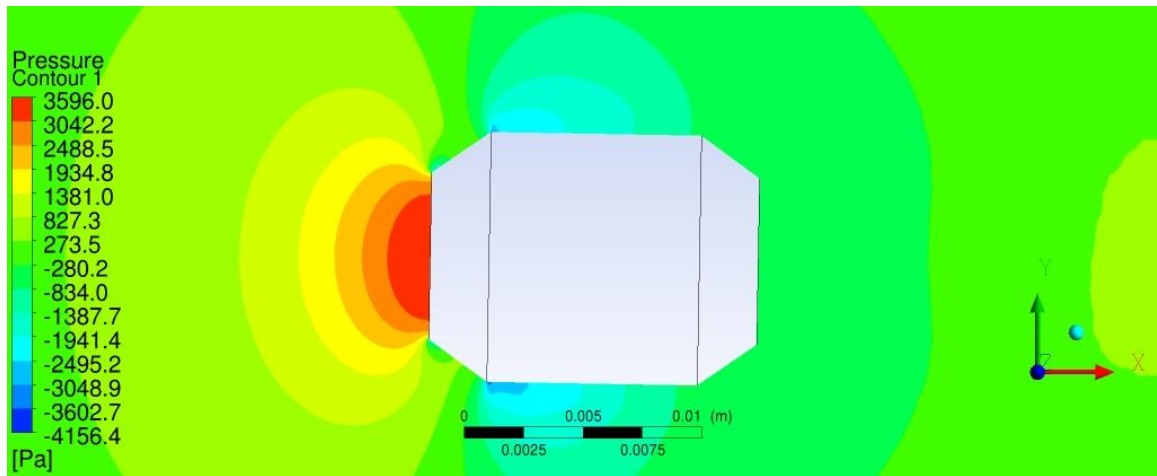


Figure 86. Pressure Contour on 3D, Steady-State Spinning Target in Drift Region with a 1° Angle of Attack

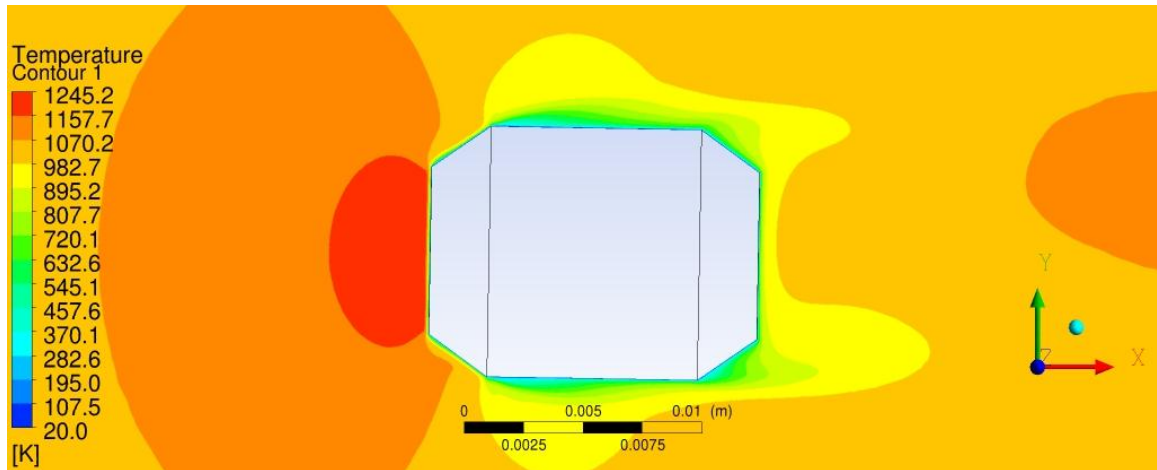


Figure 87. Temperature Contour on 3D, Steady-State Spinning Target in Drift Region with a 1° Angle of Attack

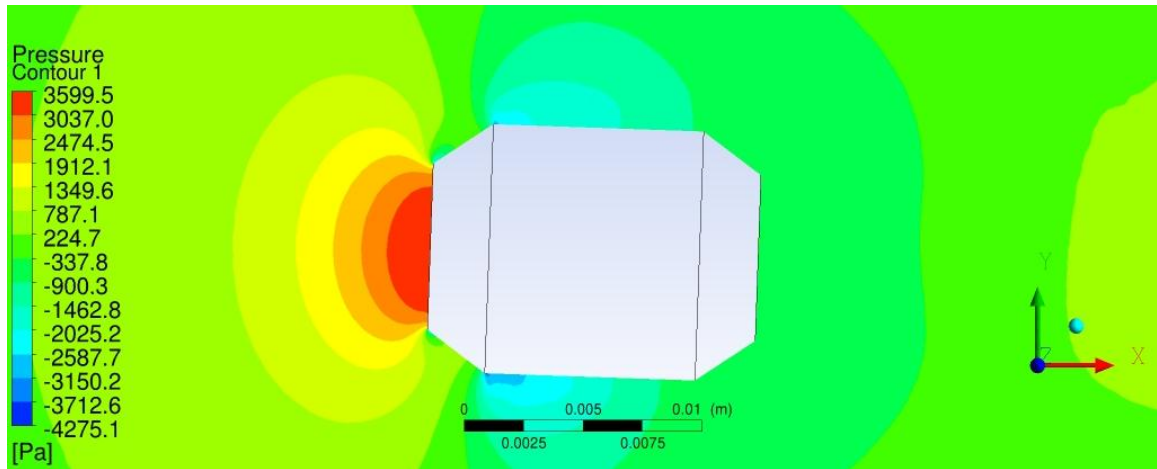


Figure 88. Pressure Contour on 3D, Steady-State Spinning Target in Drift Region with a 2° Angle of Attack

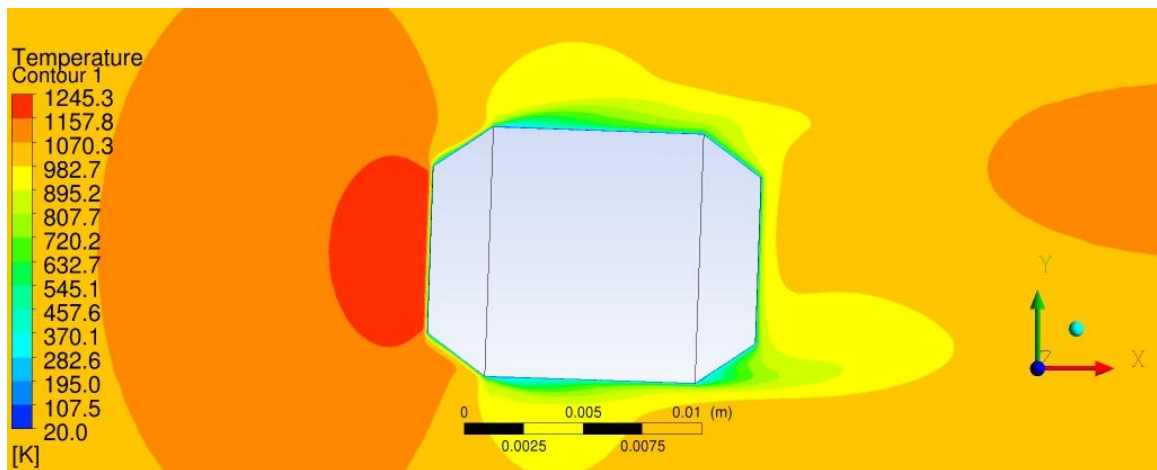


Figure 89. Temperature Contour on 3D, Steady-State Spinning Target in Drift Region with a 2° Angle of Attack

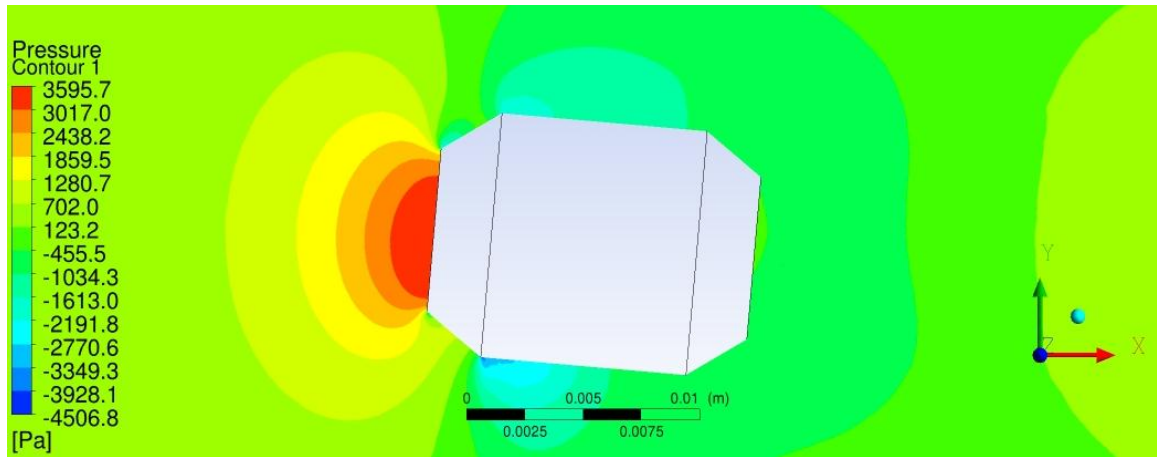


Figure 90. Pressure Contour on 3D, Steady-State Spinning Target in Drift Region with a 5° Angle of Attack

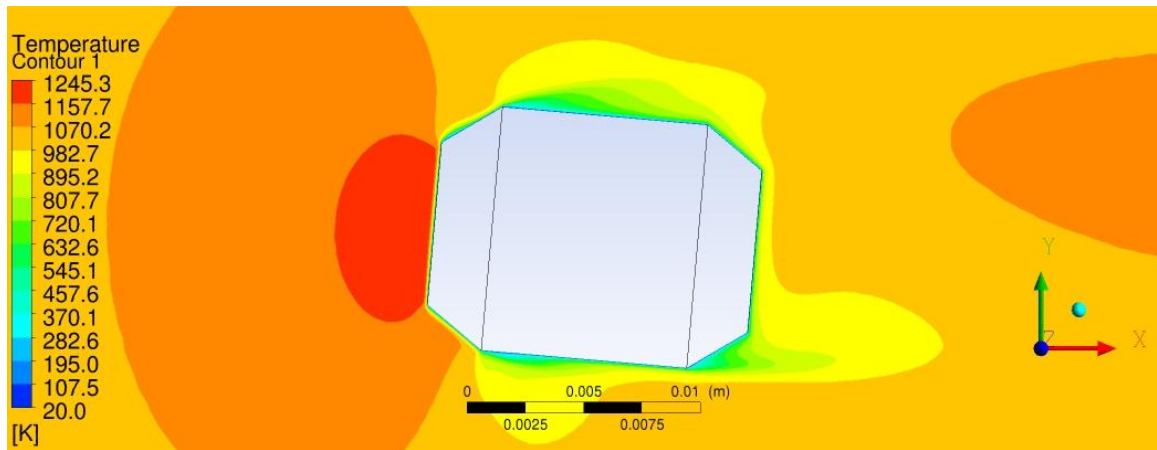


Figure 91. Temperature Contour on 3D, Steady-State Spinning Target in Drift Region with a 5° Angle of Attack

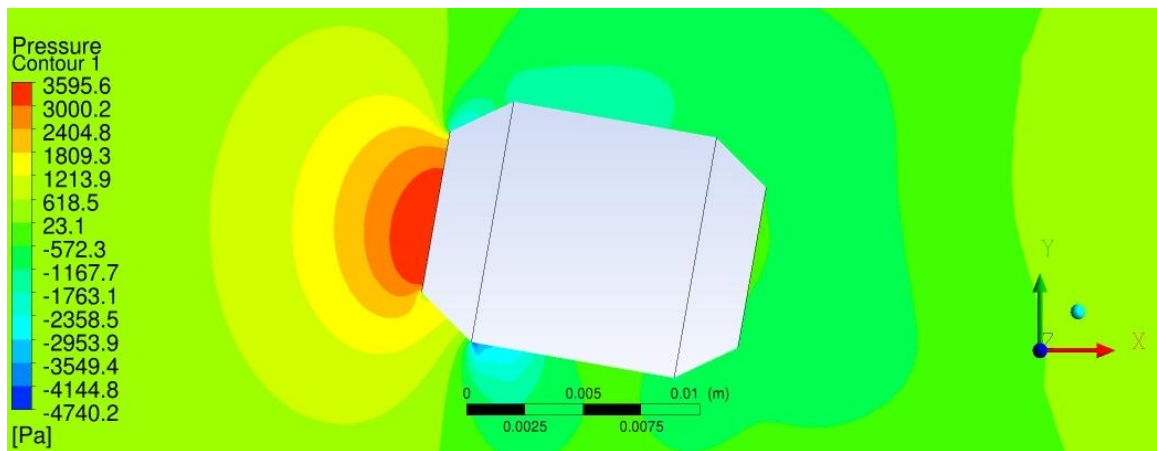


Figure 92. Pressure Contour on 3D, Steady-State Spinning Target in Drift Region with a 10° Angle of Attack

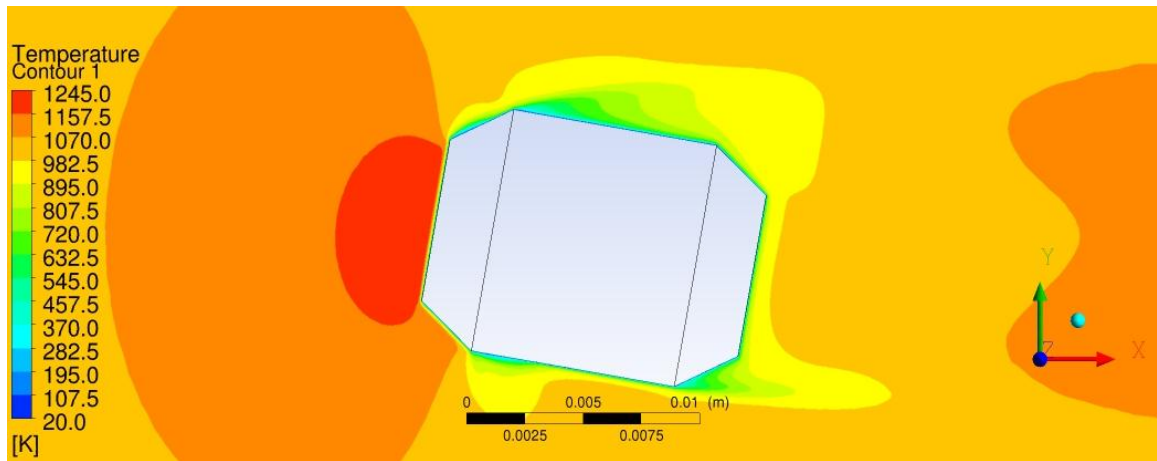


Figure 93. Temperature Contour on 3D, Steady-State Spinning Target in Drift Region with a 10° Angle of Attack

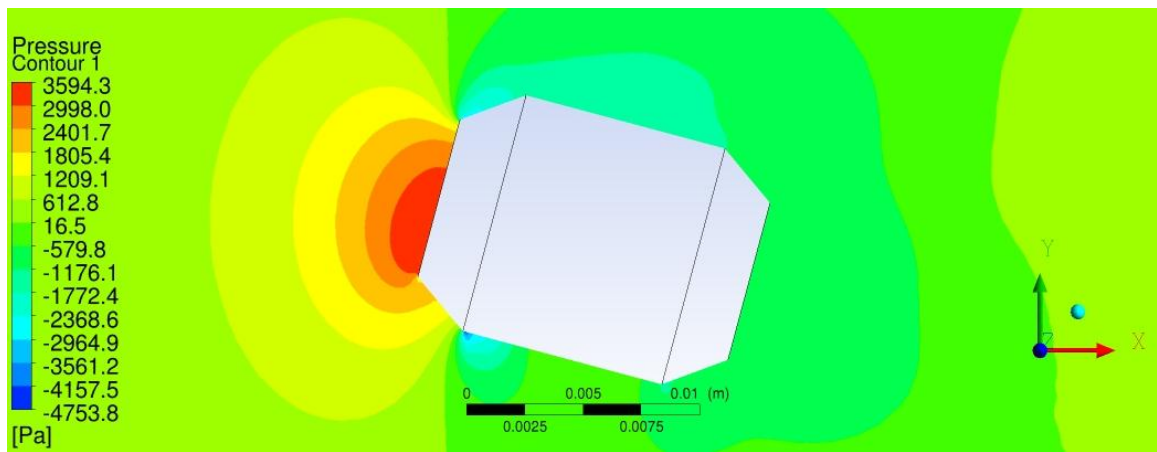


Figure 94. Pressure Contour on 3D, Steady-State Spinning Target in Drift Region with a 15° Angle of Attack

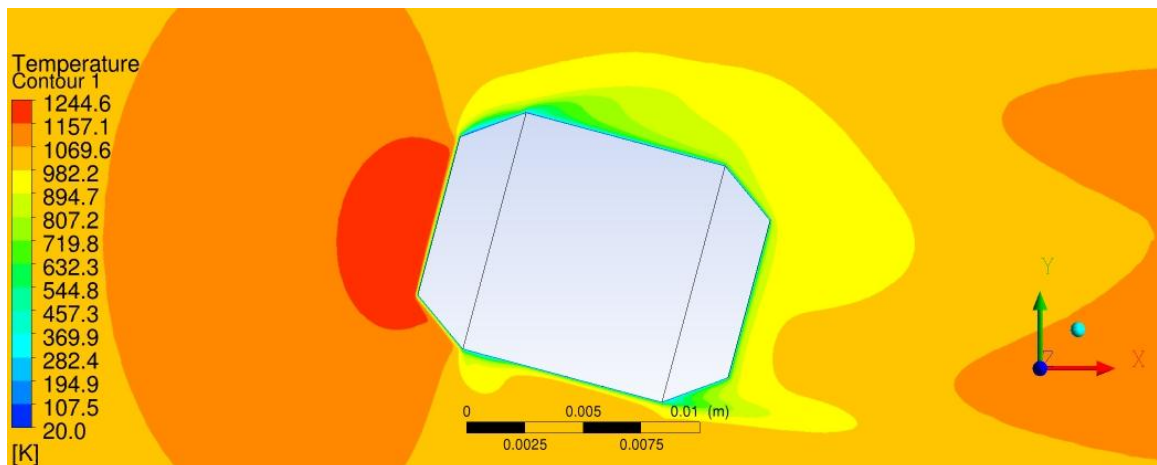


Figure 95. Temperature Contour on 3D, Steady-State Spinning Target in Drift Region with a 15° Angle of Attack

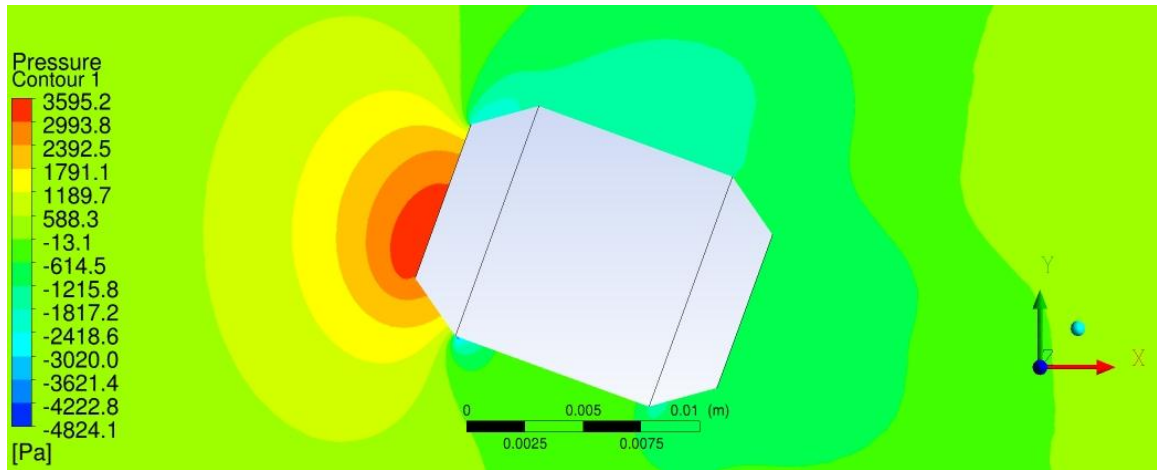


Figure 96. Pressure Contour on 3D, Steady-State Spinning Target in Drift Region with a 20° Angle of Attack

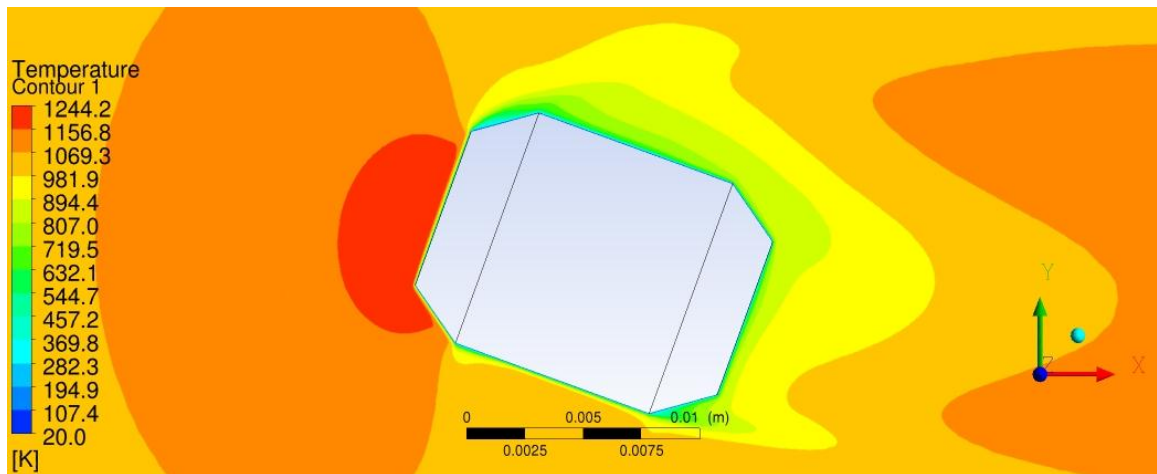


Figure 97. Temperature Contour on 3D, Steady-State Spinning Target in Drift Region with a 20° Angle of Attack

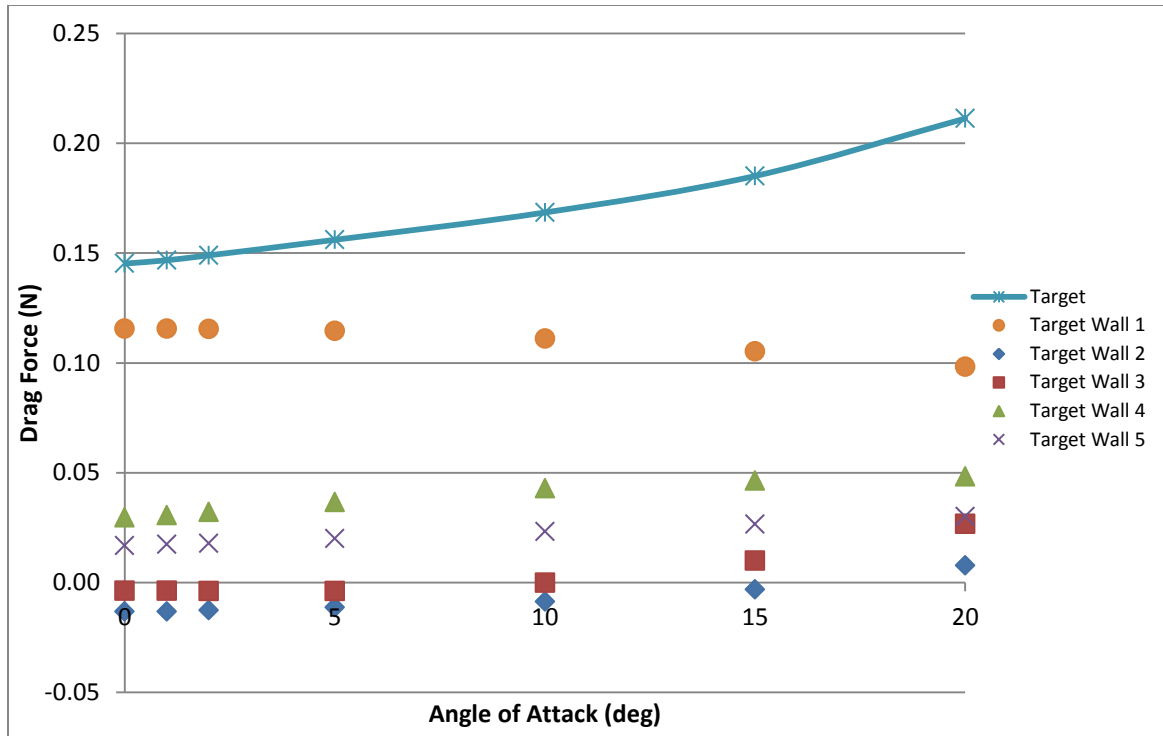


Figure 98. Drag Force on Spinning Target in Drift Region at Different Angles of Attack from 3D, Steady-State Model

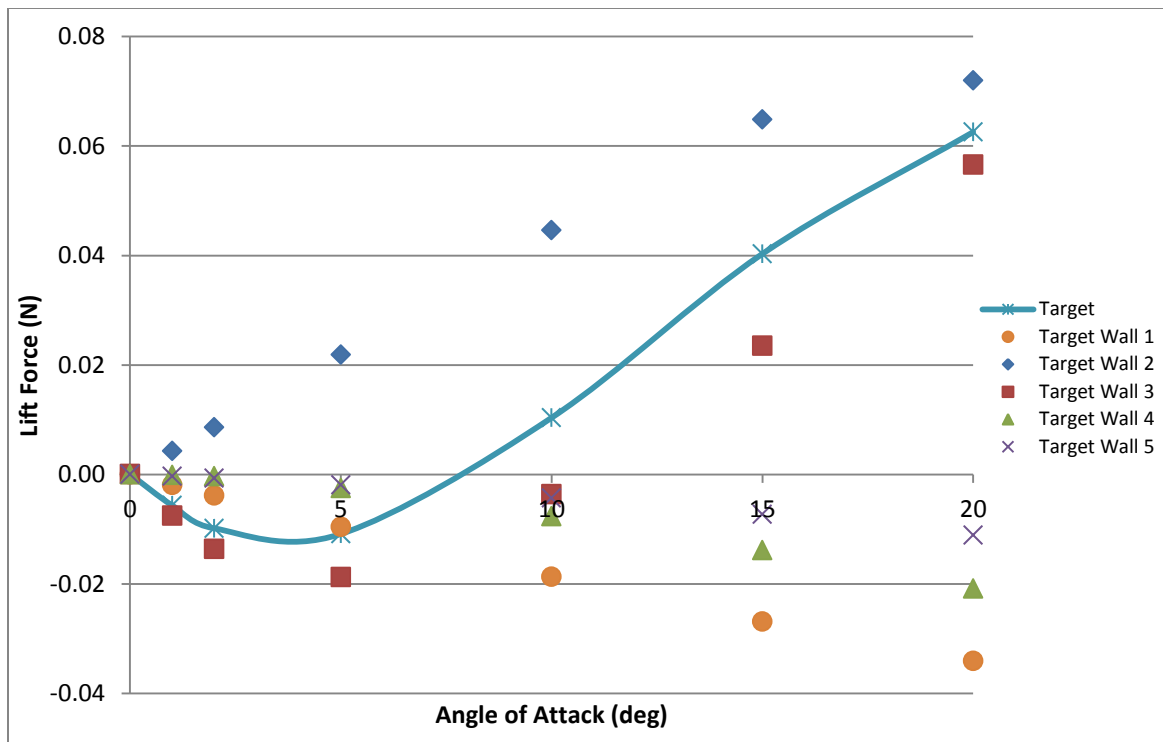


Figure 99. Lift Force on Spinning Target in Drift Region at Different Angles of Attack from 3D, Steady-State Model

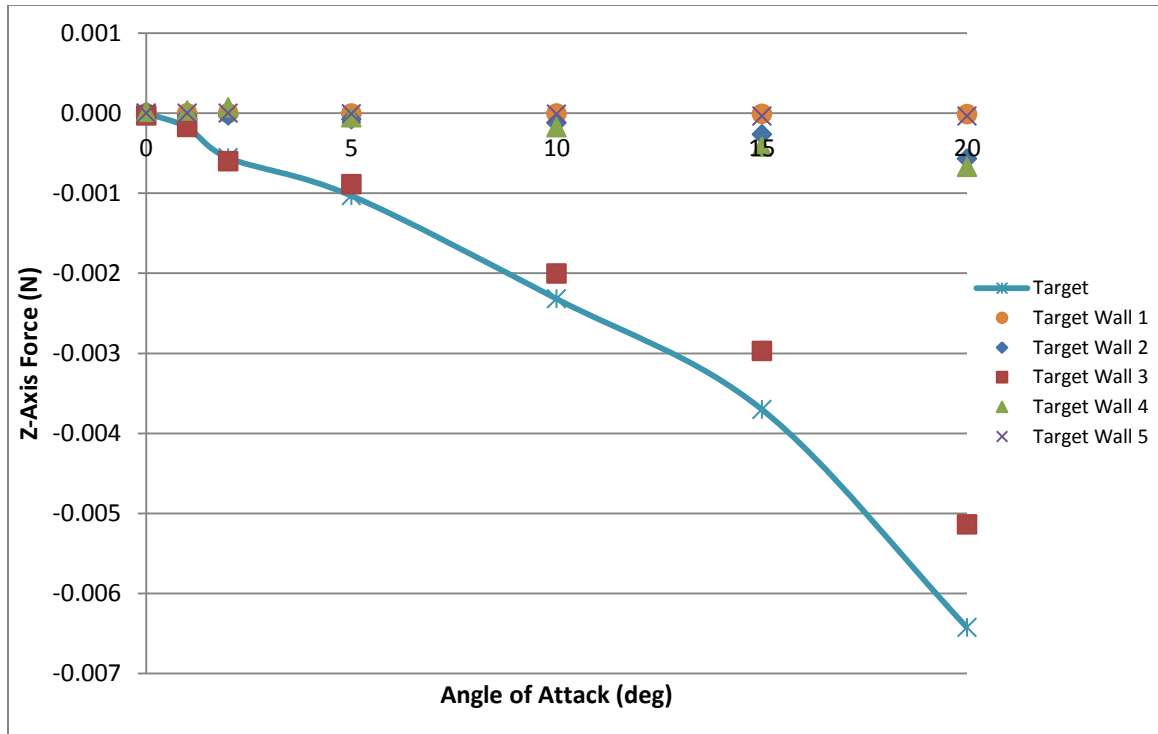


Figure 100. Z-Axis Force on Spinning Target in Drift Region at Different Angles of Attack from 3D, Steady-State Model

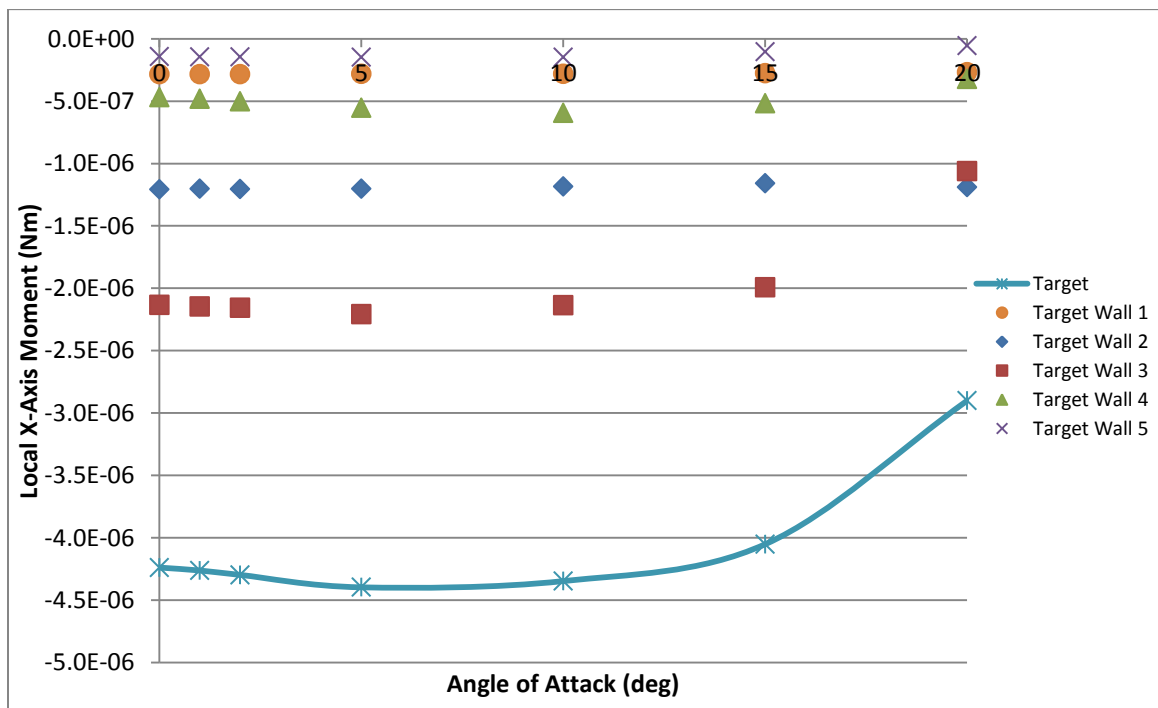


Figure 101. Local X-Axis (Axial) Moment on Spinning Target in Drift Region at Different Angles of Attack from 3D, Steady-State Model

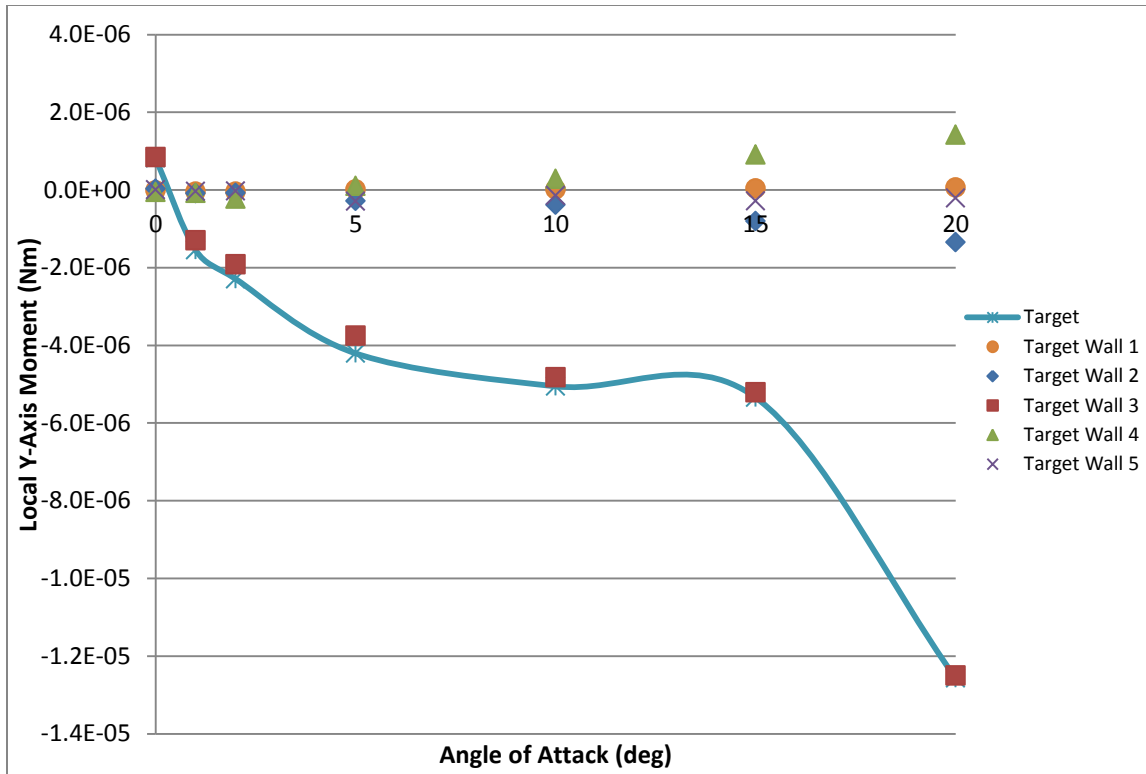


Figure 102. Local Y-Axis (negative Magnus) Moment on Spinning Target in Drift Region at Different Angles of Attack from 3D, Steady-State Model

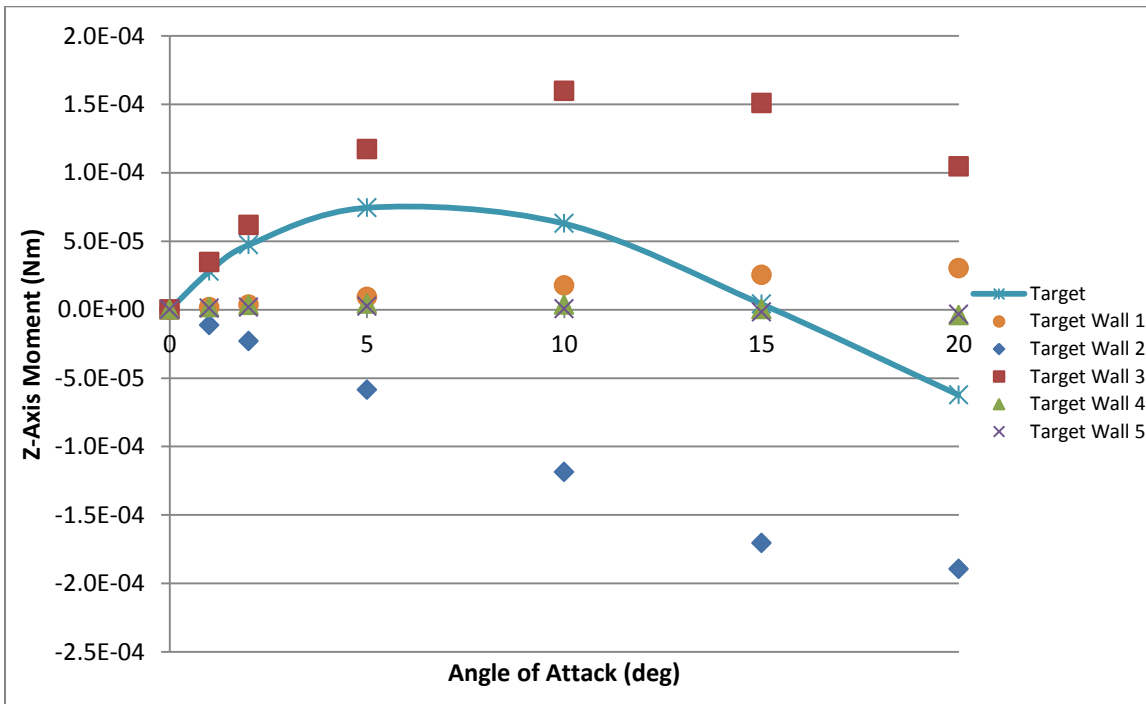


Figure 103. Z-Axis (Overturning) Moment on Spinning Target in Drift Region at Different Angles of Attack from 3D, Steady-State Model

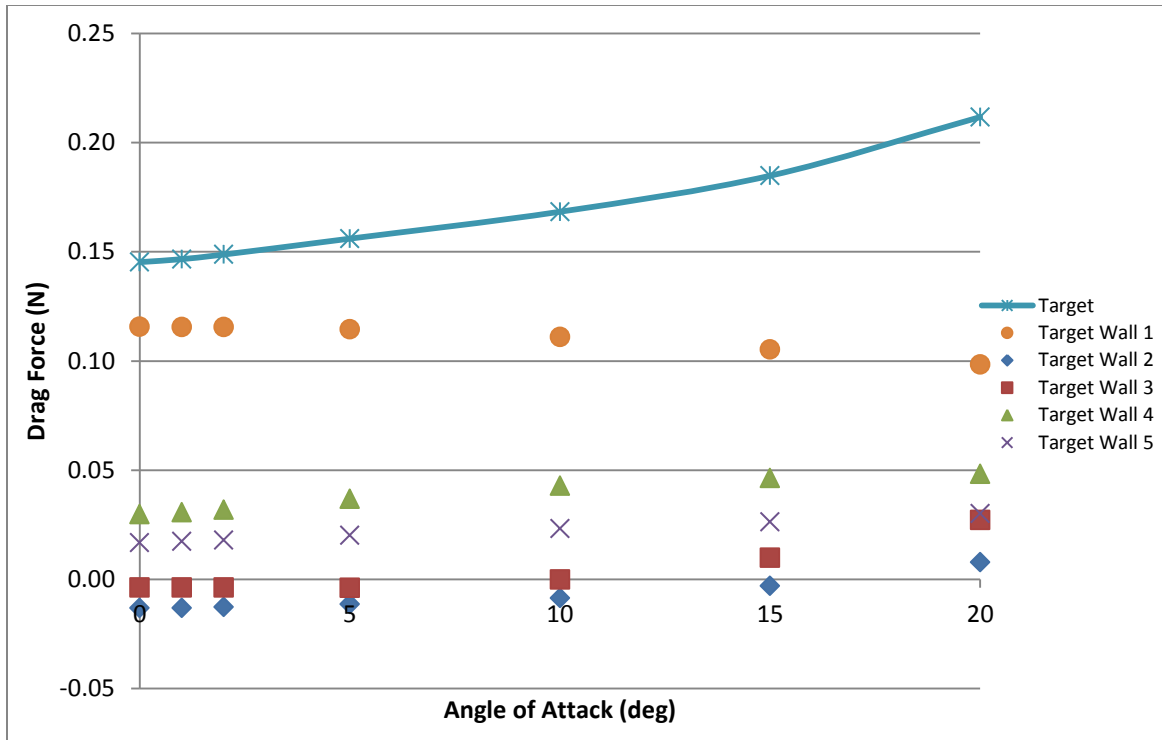


Figure 104. Drag Force on Non-Spinning Target in Drift Region at Different Angles of Attack from 3D, Steady-State Model

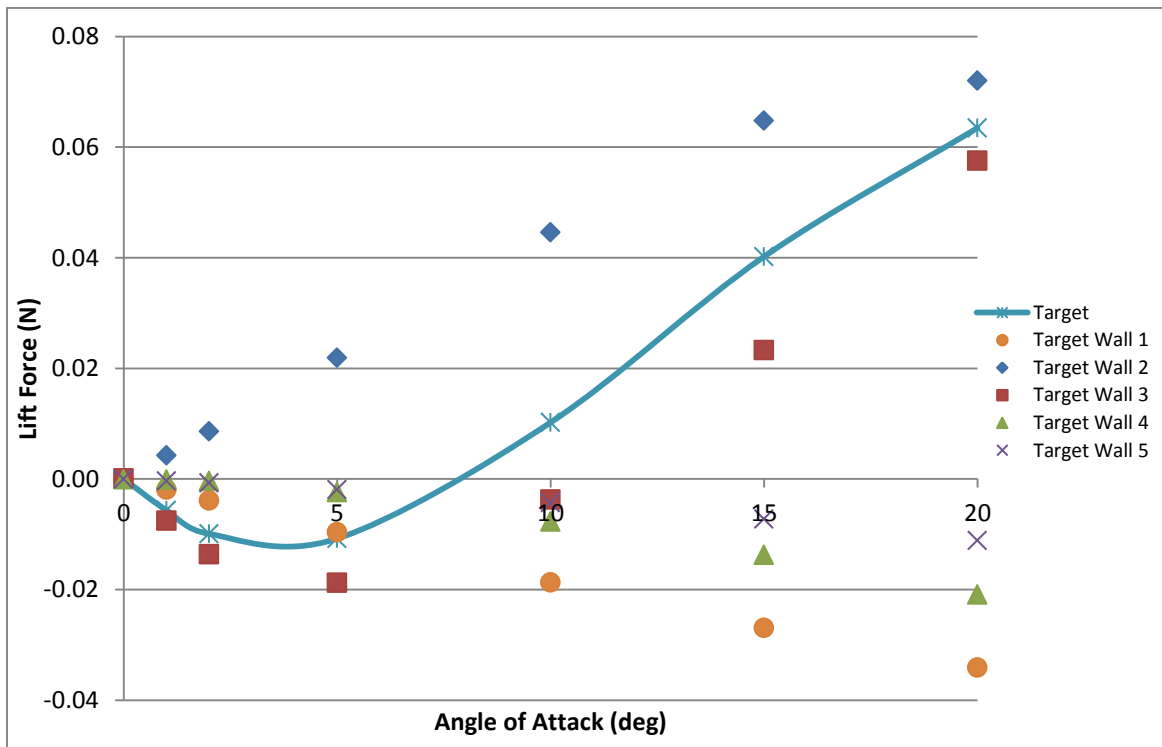


Figure 105. Lift Force on Non-Spinning Target in Drift Region at Different Angles of Attack from 3D, Steady-State Model

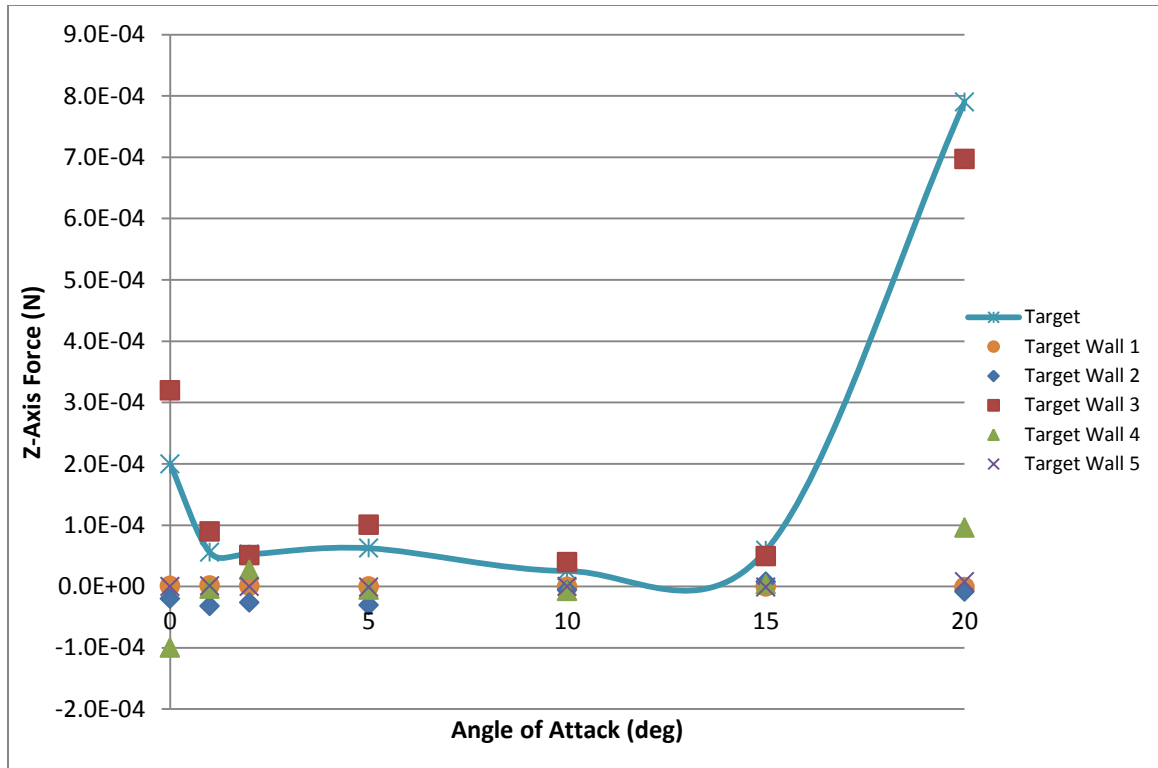


Figure 106. Z-Axis Force on Non-Spinning Target in Drift Region at Different Angles of Attack from 3D, Steady-State Model

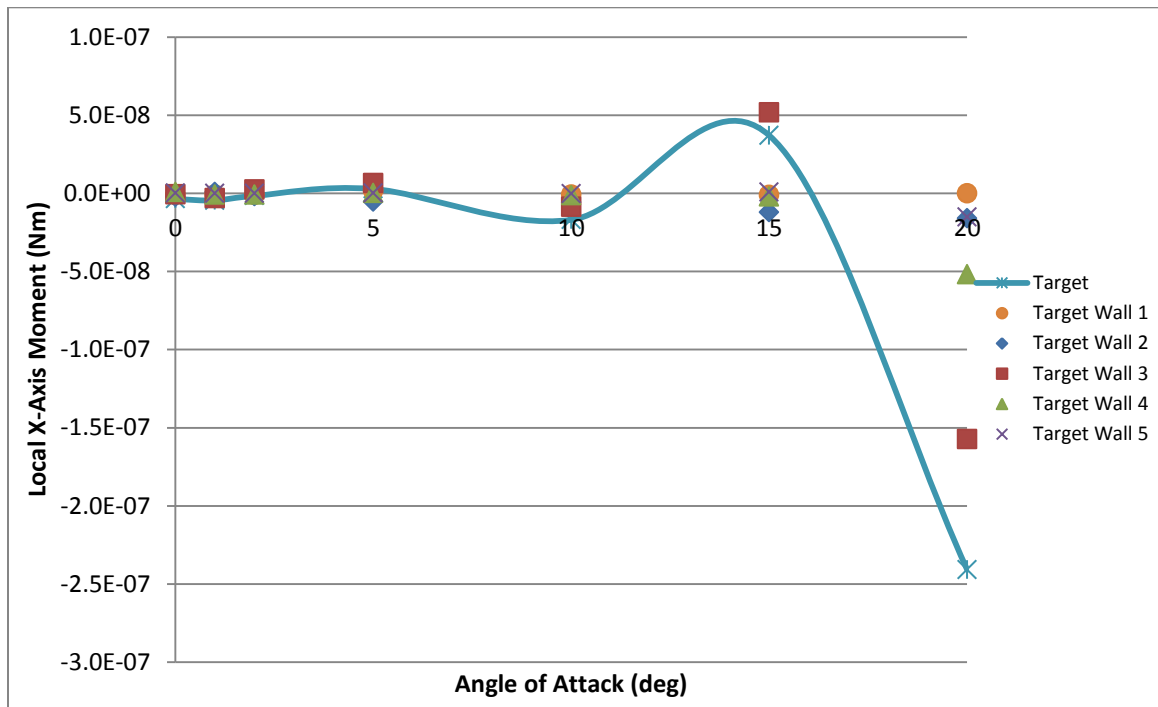


Figure 107. Local X-Axis (Axial) Moment on Non-Spinning Target in Drift Region at Different Angles of Attack from 3D, Steady-State Model

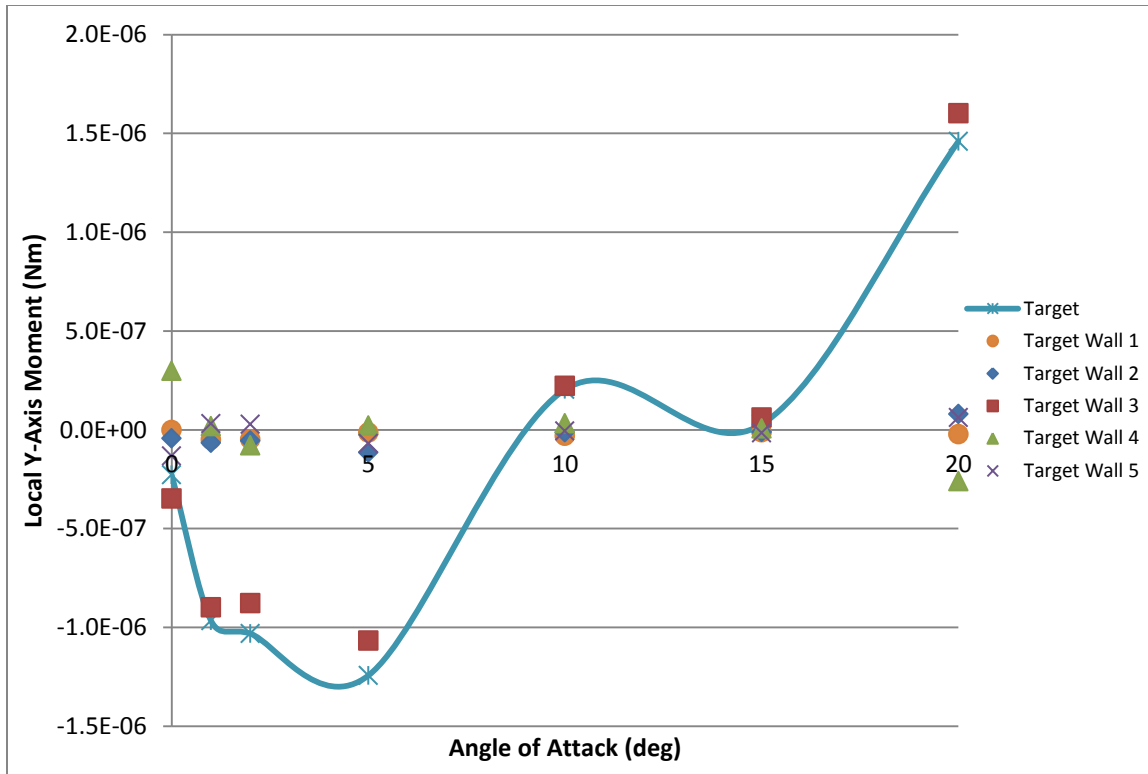


Figure 108. Local Y-Axis (negative Magnus) Moment on Non-Spinning Target in Drift Region at Different Angles of Attack from 3D, Steady-State Model

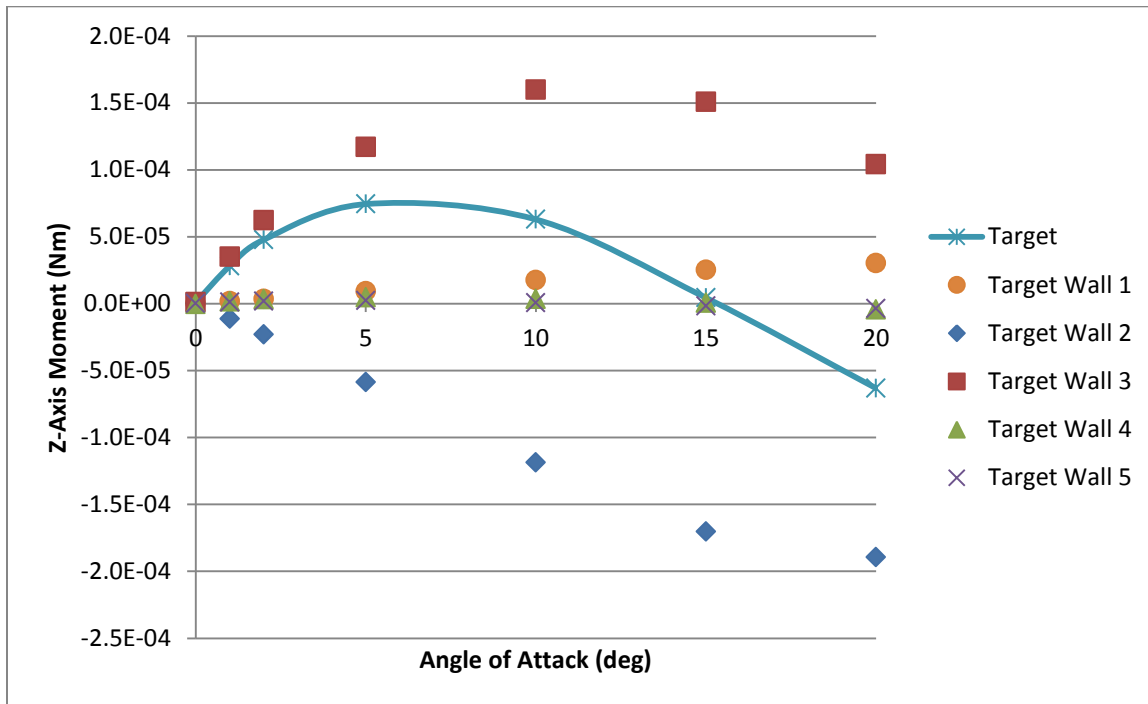


Figure 109. Z-Axis (Overturning) Moment on Non-Spinning Target in Drift Region at Different Angles of Attack from 3D, Steady-State Model

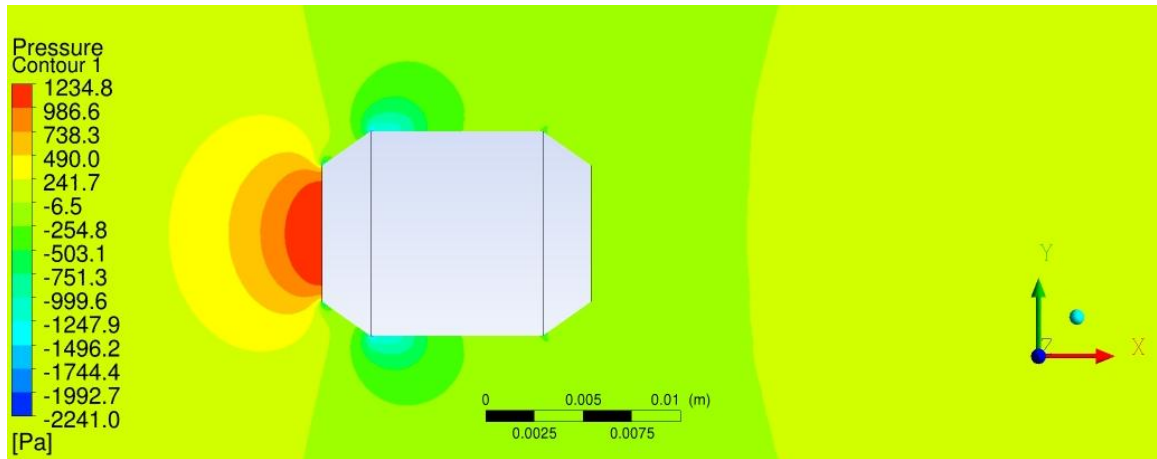


Figure 110. Pressure Contour on 3D, Steady-State Spinning Target in Drift Region at a Reynolds Number of 2400

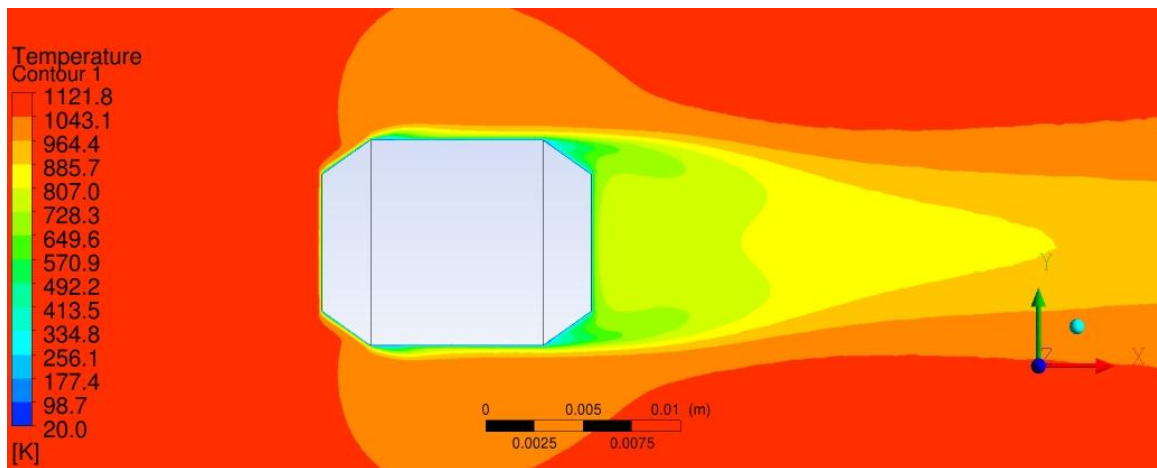


Figure 111. Temperature Contour on 3D, Steady-State Spinning Target in Drift Region at a Reynolds Number of 2400

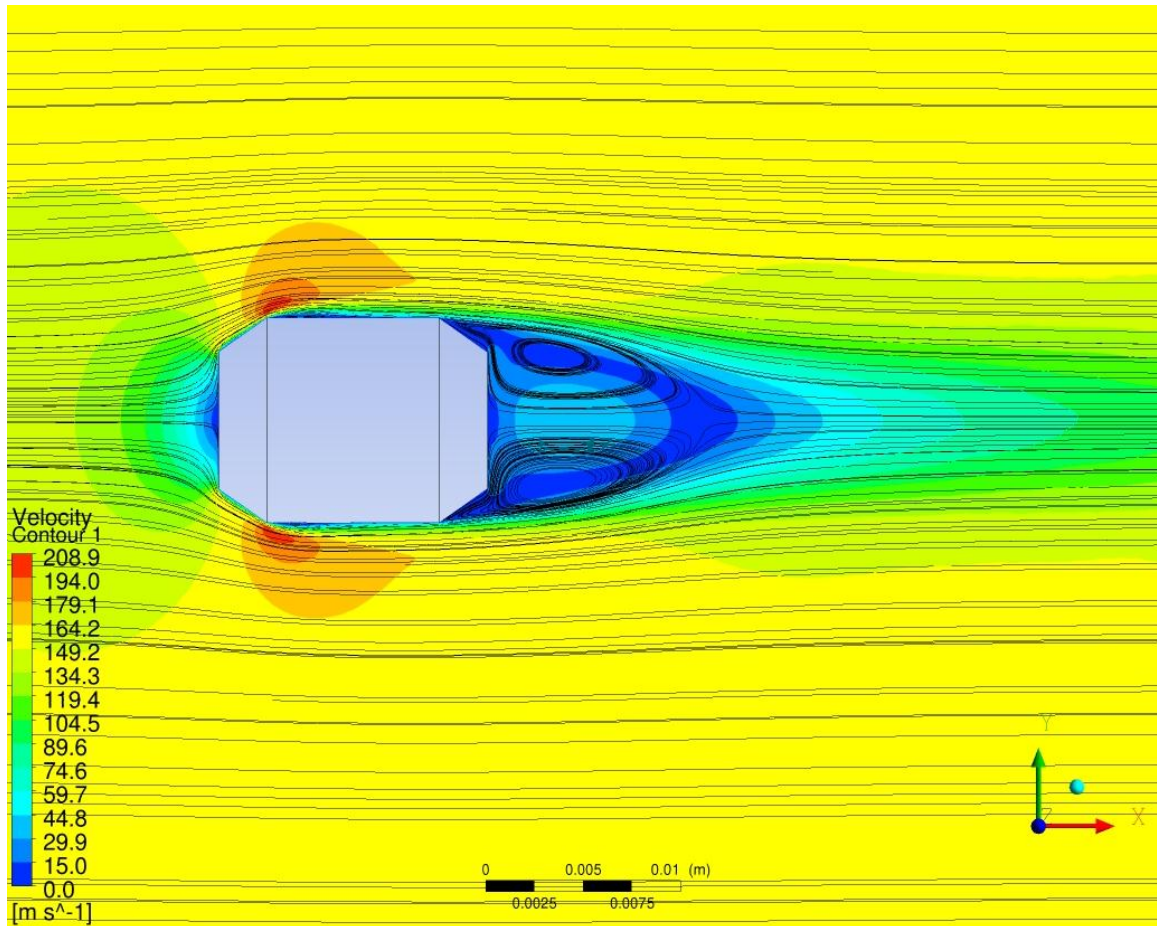


Figure 112. Velocity Contour with Streamlines on 3D, Steady-State Spinning Target in Drift Region at a Reynolds Number of 2400

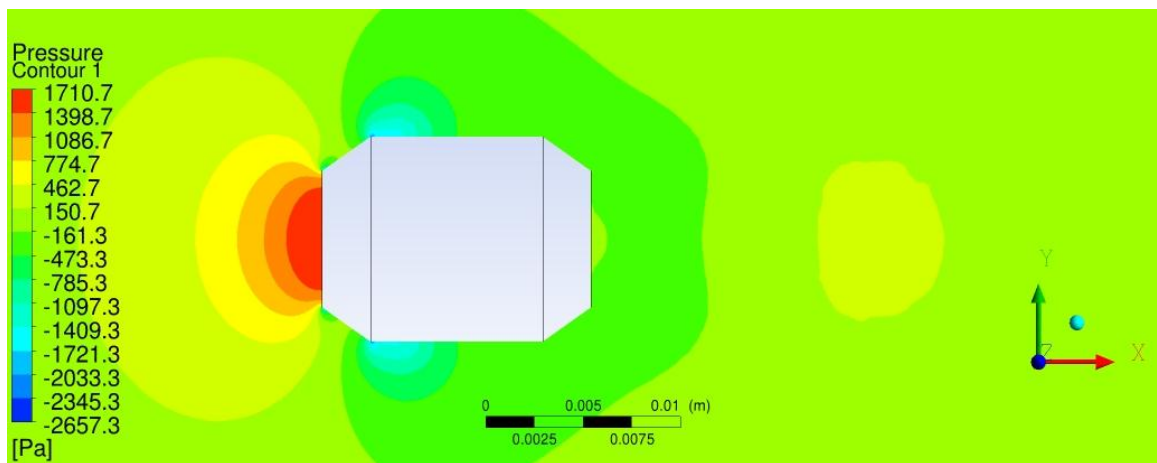


Figure 113. Pressure Contour on 3D, Steady-State Spinning Target in Drift Region at a Reynolds Number of 2800

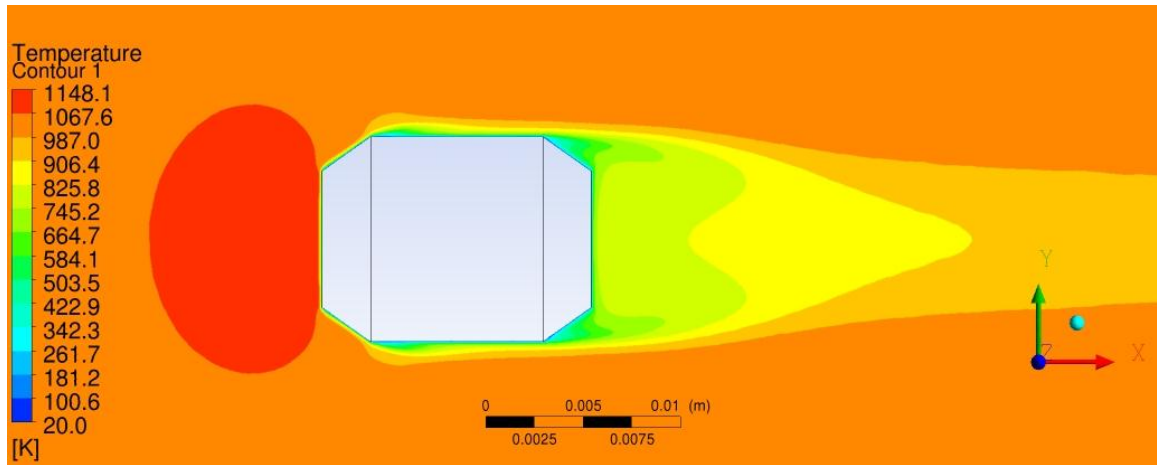


Figure 114. Temperature Contour on 3D, Steady-State Spinning Target in Drift Region at a Reynolds Number of 2800

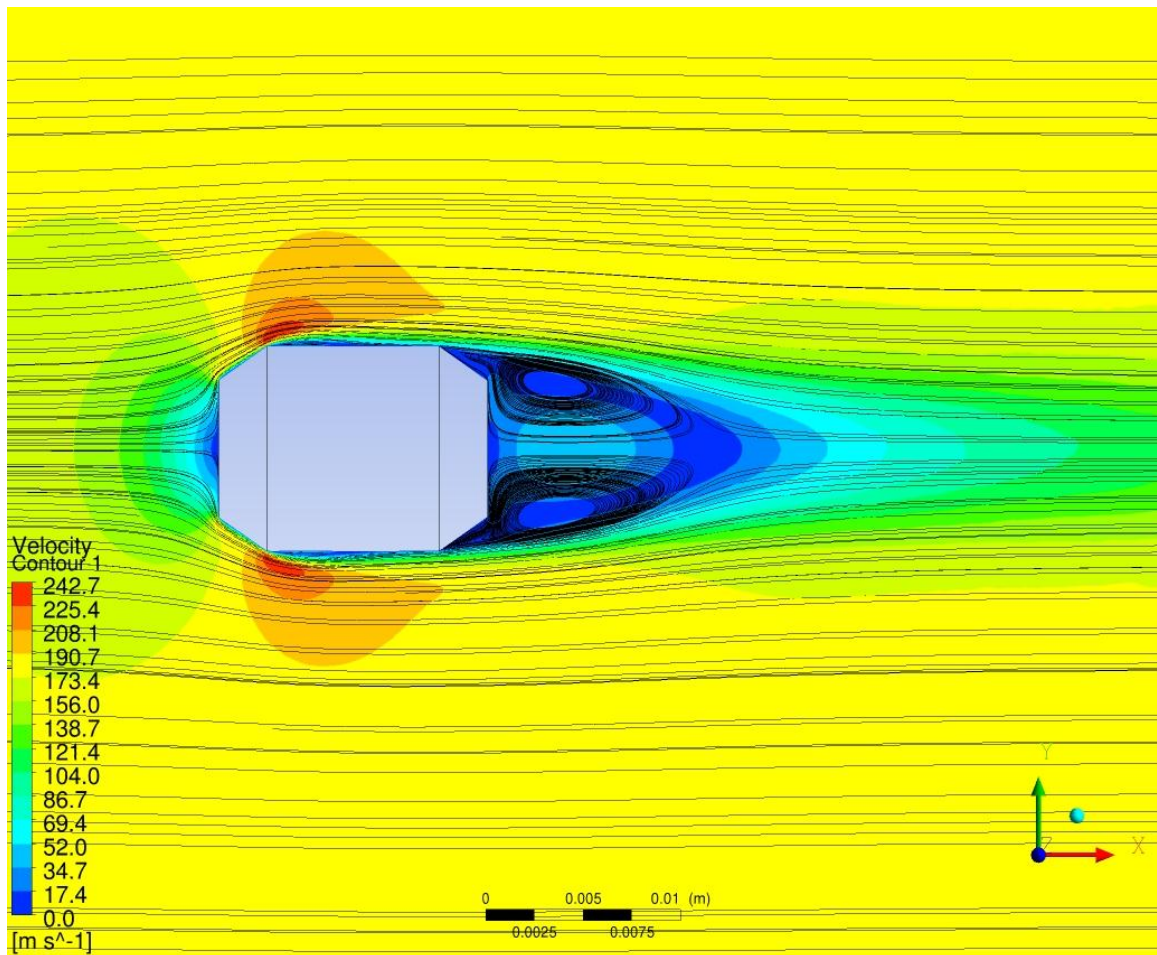


Figure 115. Velocity Contour with Streamlines on 3D, Steady-State Spinning Target in Drift Region at a Reynolds Number of 2800

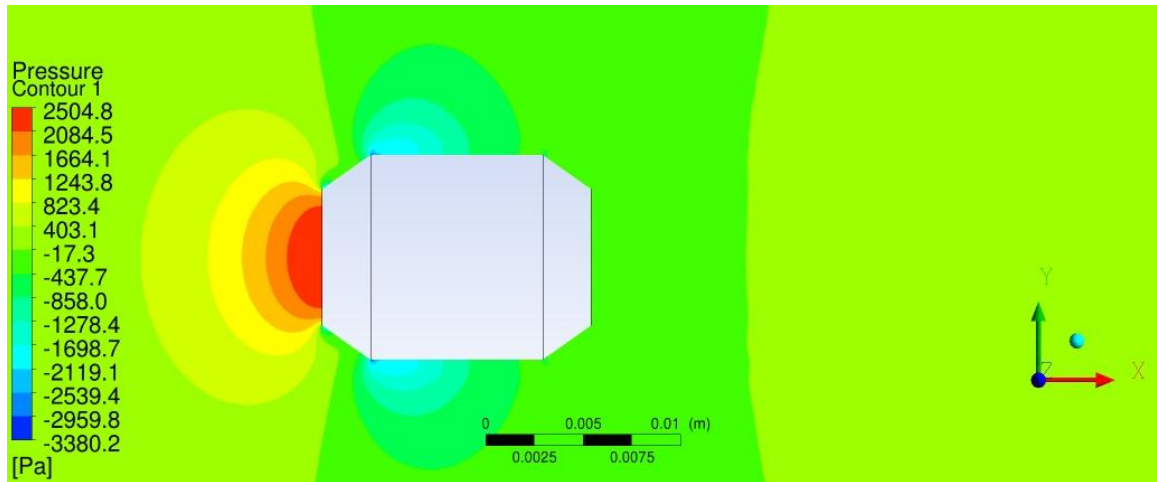


Figure 116. Pressure Contour on 3D, Steady-State Spinning Target in Drift Region at a Reynolds Number of 3200

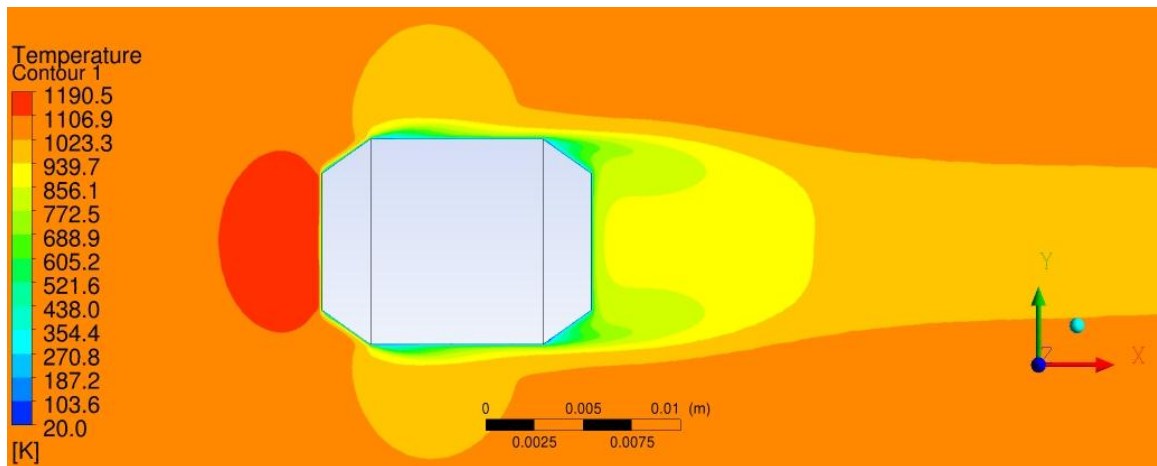


Figure 117. Temperature Contour on 3D, Steady-State Spinning Target in Drift Region at a Reynolds Number of 3200

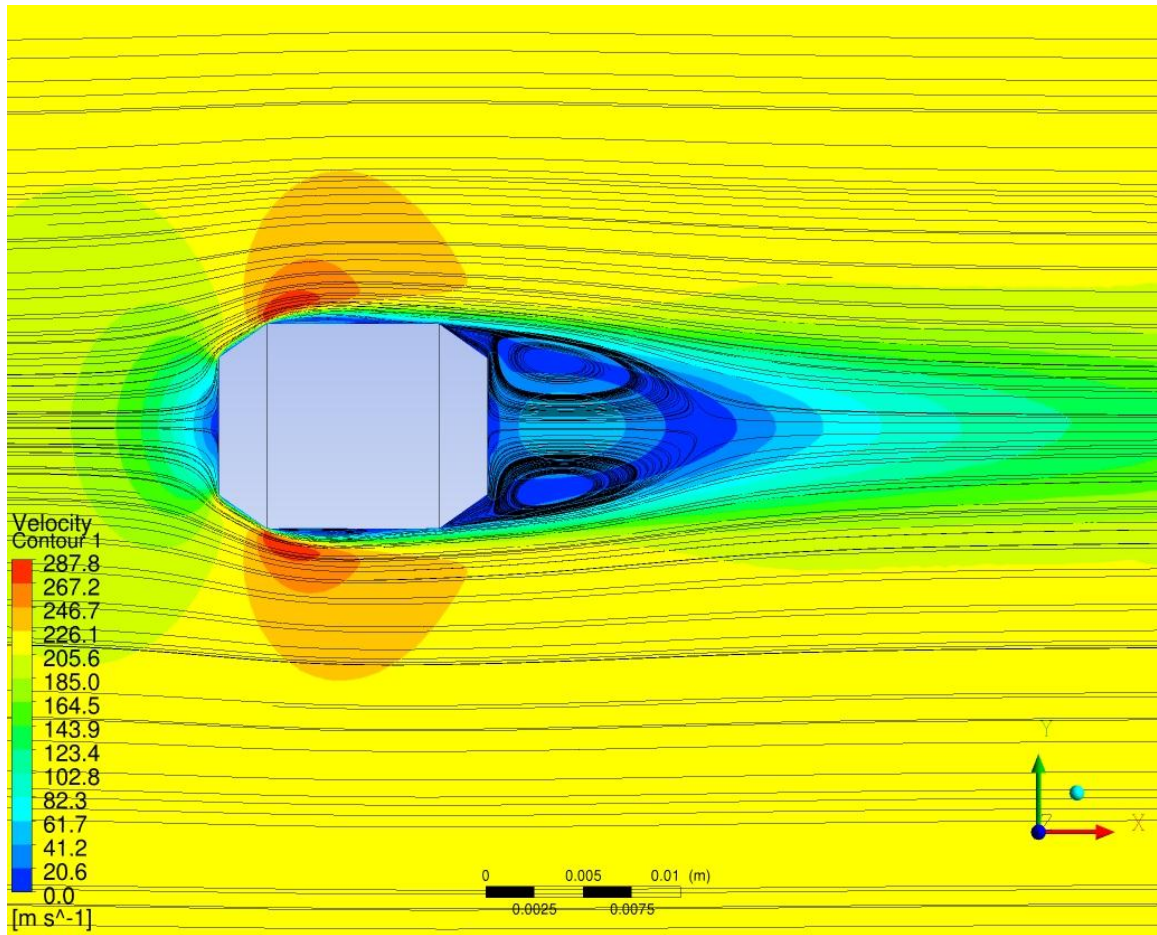


Figure 118. Velocity Contour with Streamlines on 3D, Steady-State Spinning Target in Drift Region at a Reynolds Number of 3200

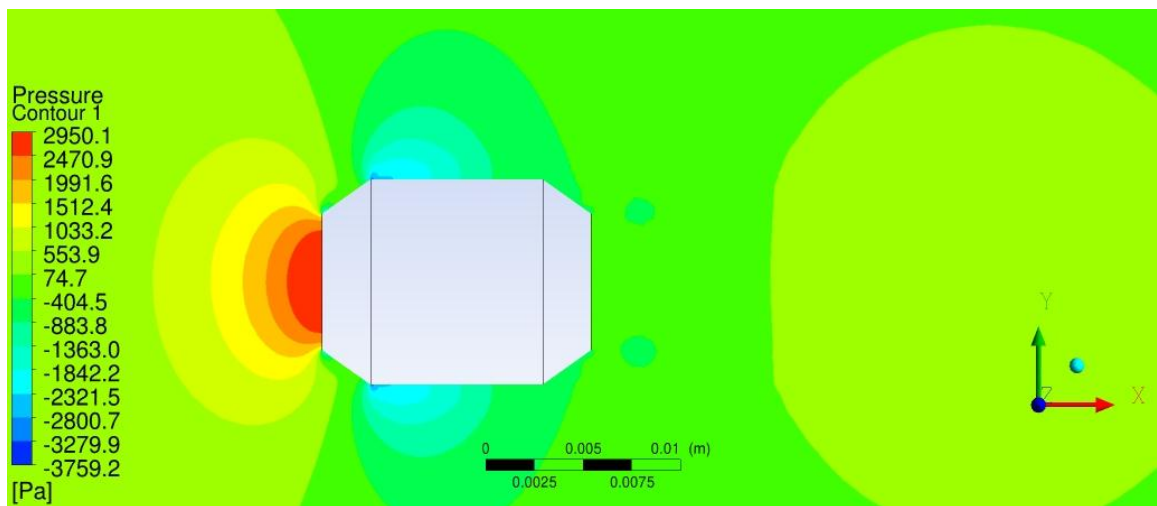


Figure 119. Pressure Contour on 3D, Steady-State Spinning Target in Drift Region at a Reynolds Number of 3600

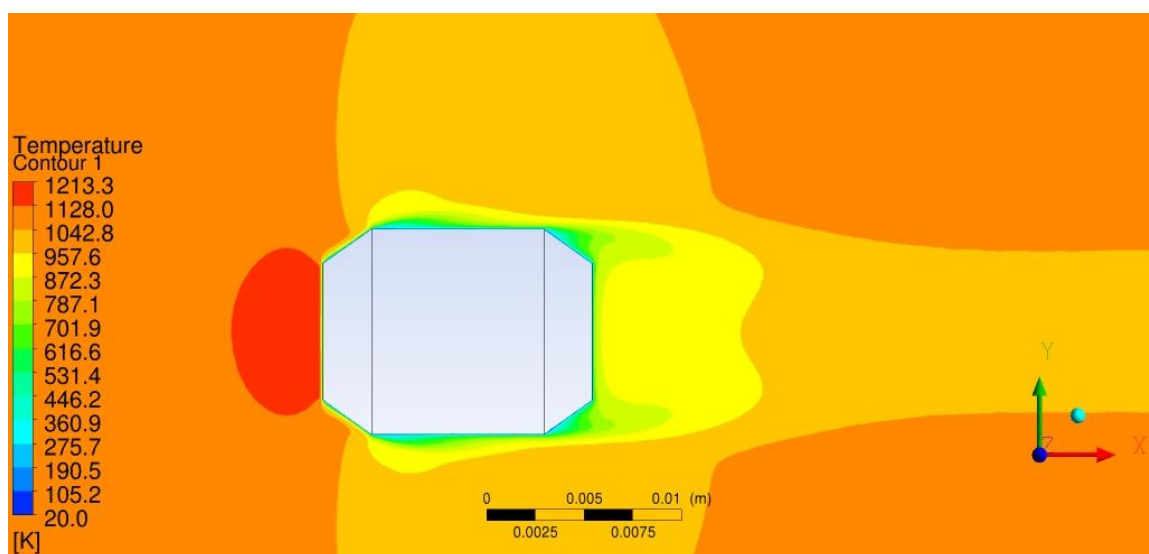


Figure 120. Temperature Contour on 3D, Steady-State Spinning Target in Drift Region at a Reynolds Number of 3600

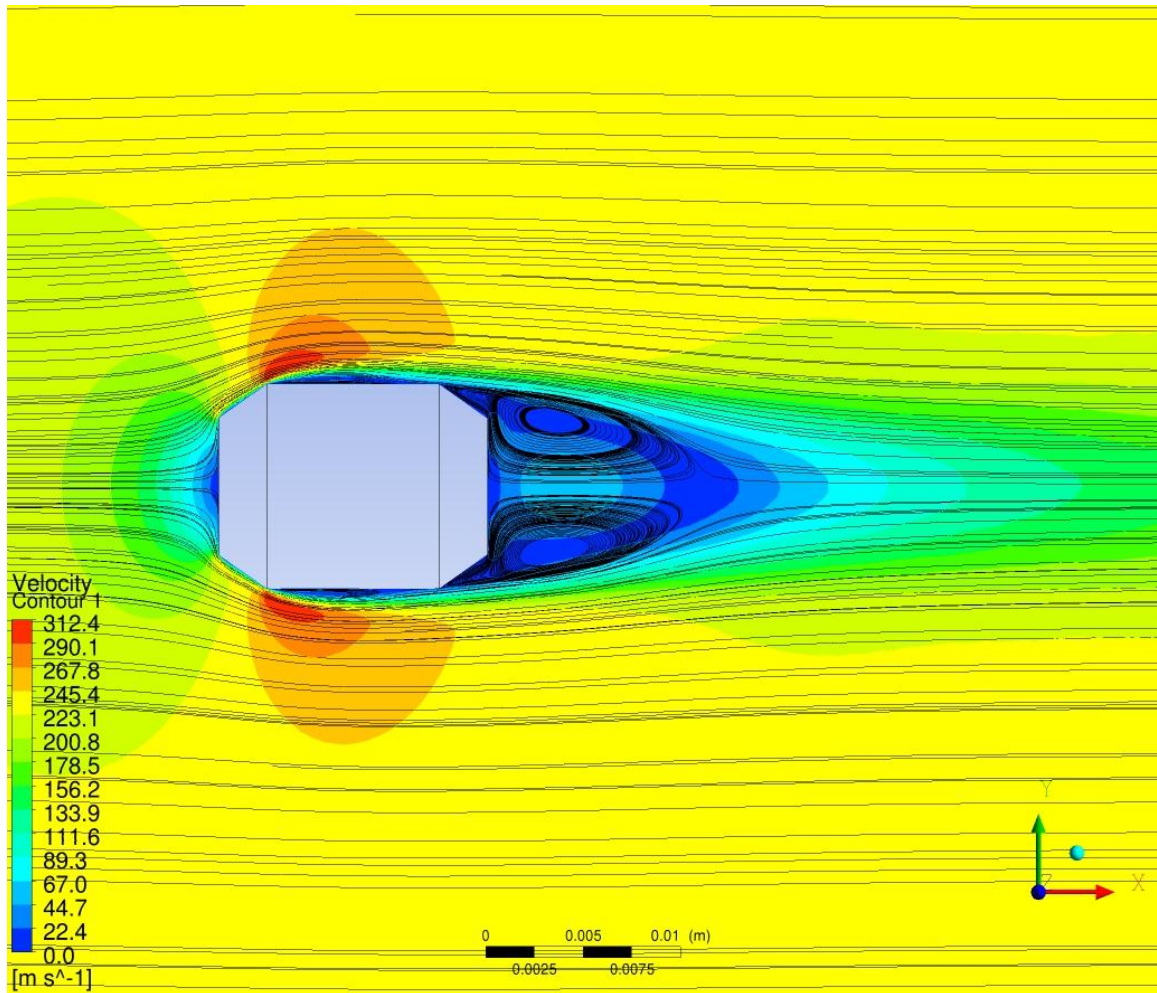


Figure 121. Velocity Contour with Streamlines on 3D, Steady-State Spinning Target in Drift Region at a Reynolds Number of 3600

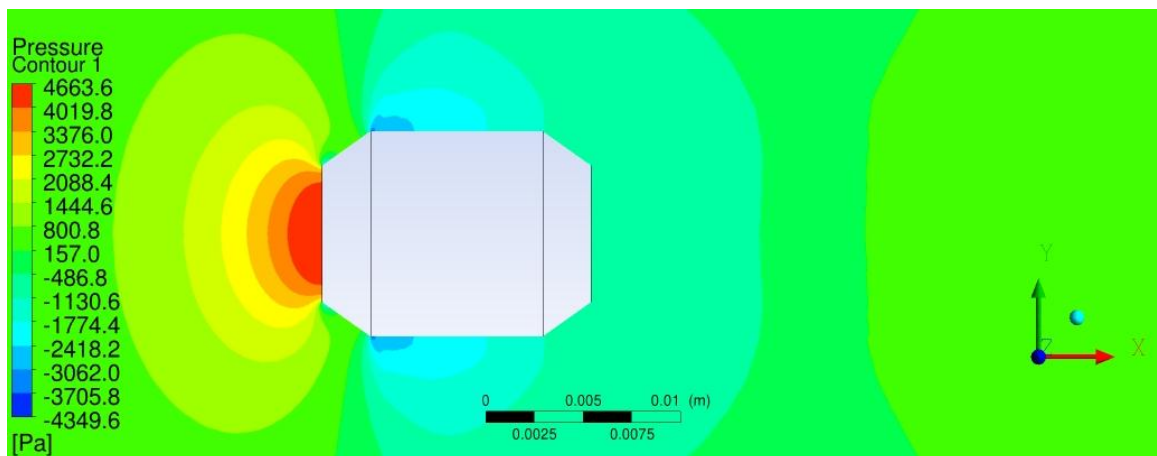


Figure 122. Pressure Contour on 3D, Steady-State Spinning Target in Drift Region at a Reynolds Number of 4400

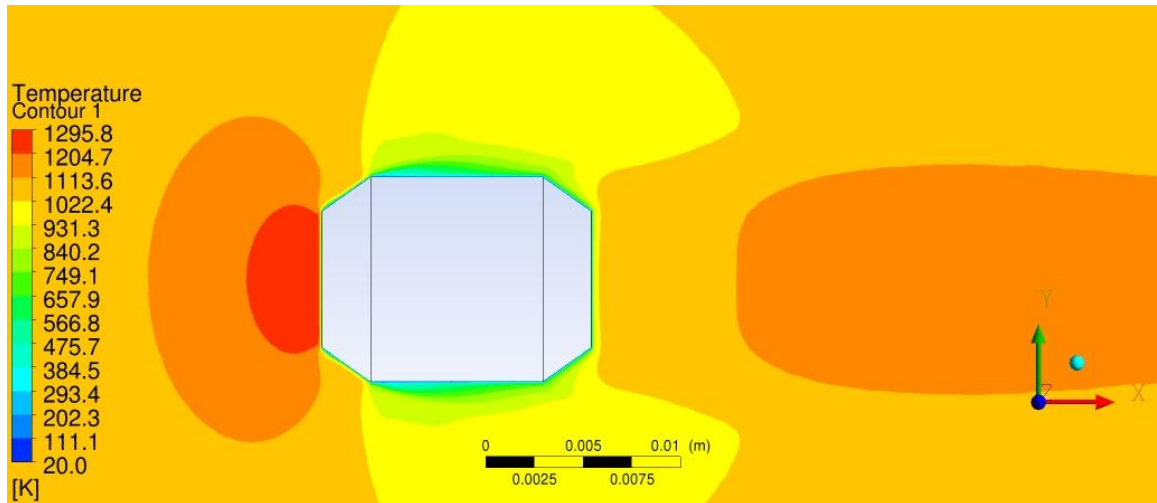


Figure 123. Temperature Contour on 3D, Steady-State Spinning Target in Drift Region at a Reynolds Number of 4400

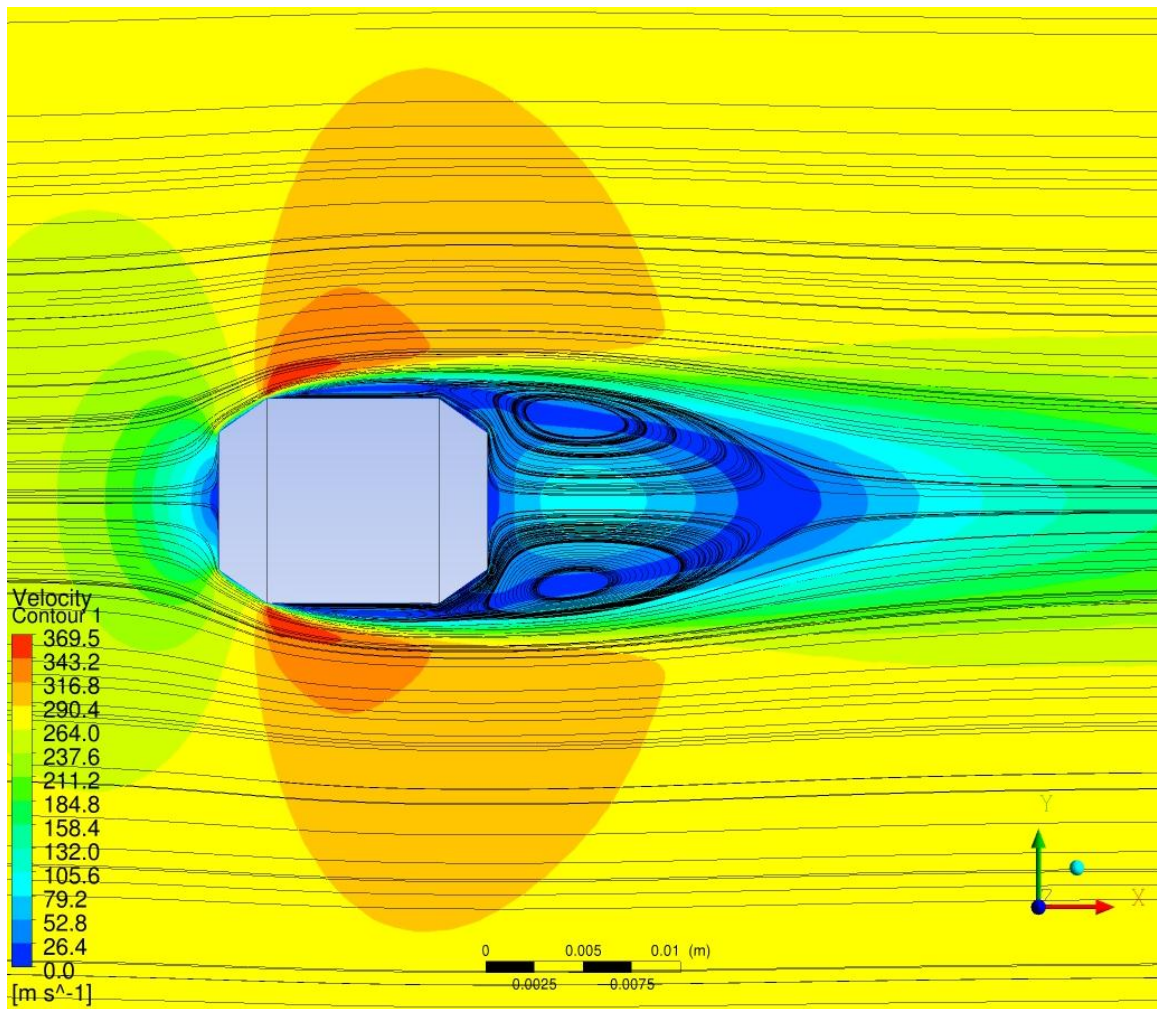


Figure 124. Velocity Contour with Streamlines on 3D, Steady-State Spinning Target in Drift Region at a Reynolds Number of 4400

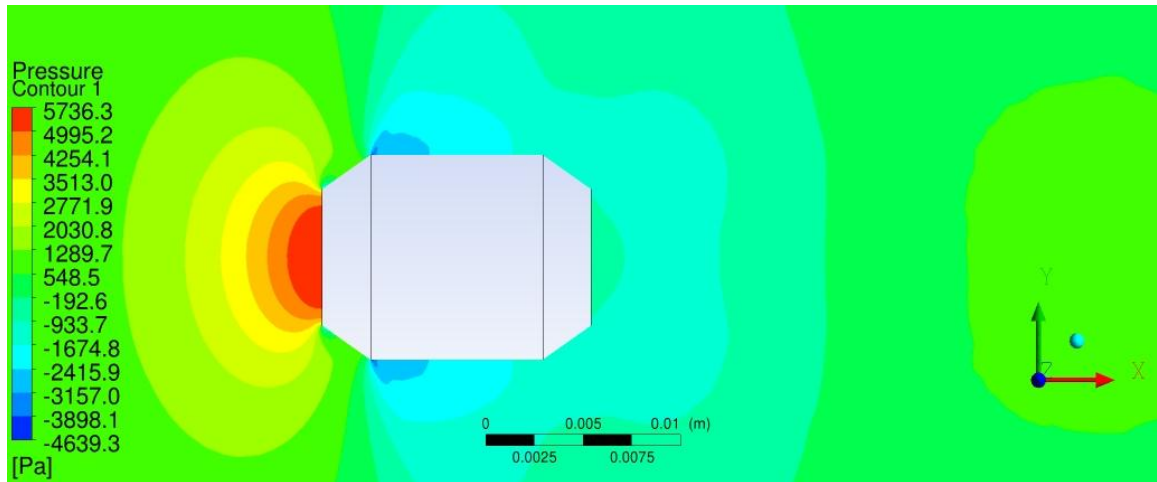


Figure 125. Pressure Contour on 3D, Steady-State Spinning Target in Drift Region at a Reynolds Number of 4800

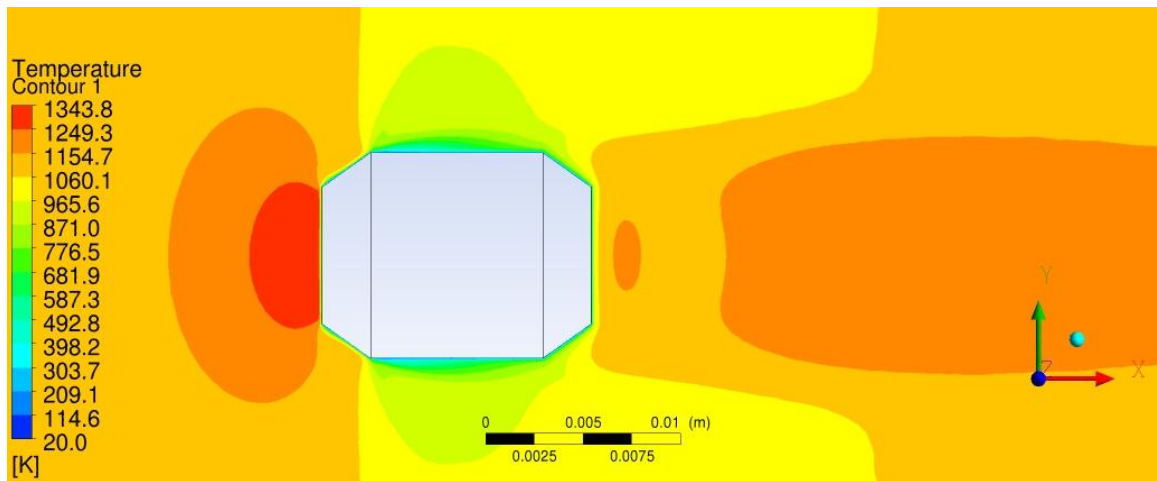


Figure 126. Temperature Contour on 3D, Steady-State Spinning Target in Drift Region at a Reynolds Number of 4800

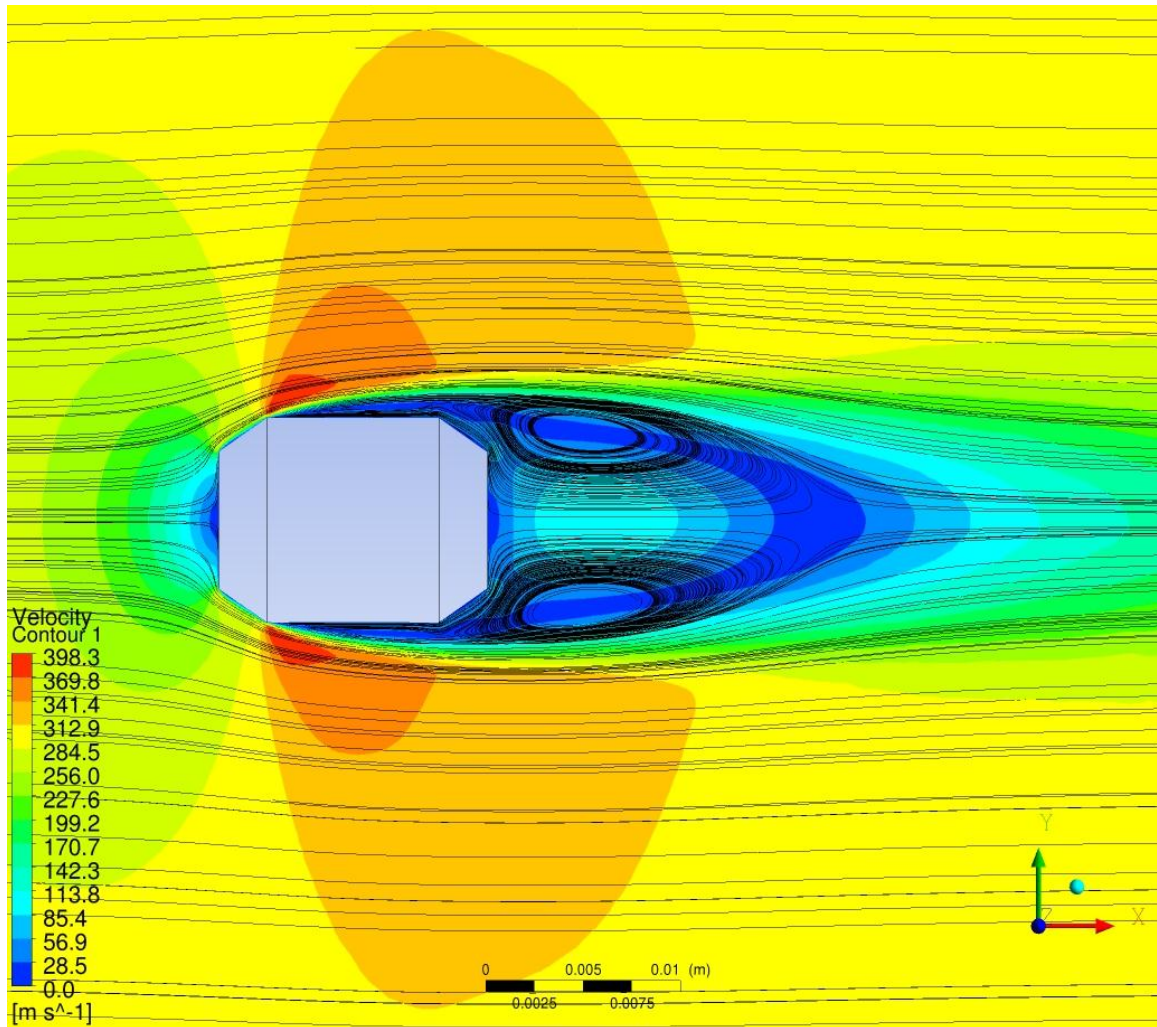


Figure 127. Velocity Contour with Streamlines on 3D, Steady-State Spinning Target in Drift Region at a Reynolds Number of 4800

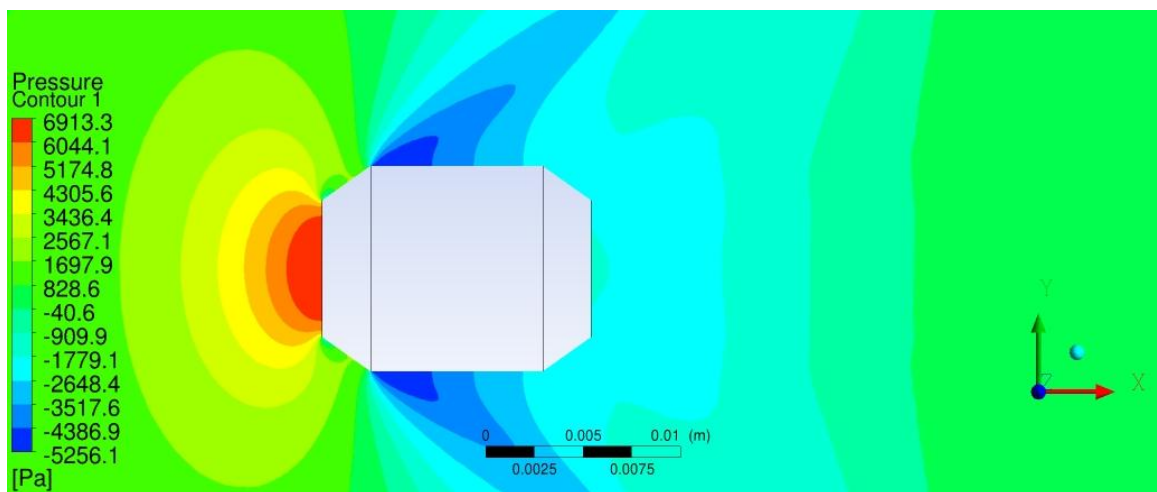


Figure 128. Pressure Contour on 3D, Steady-State Spinning Target in Drift Region at a Reynolds Number of 5200

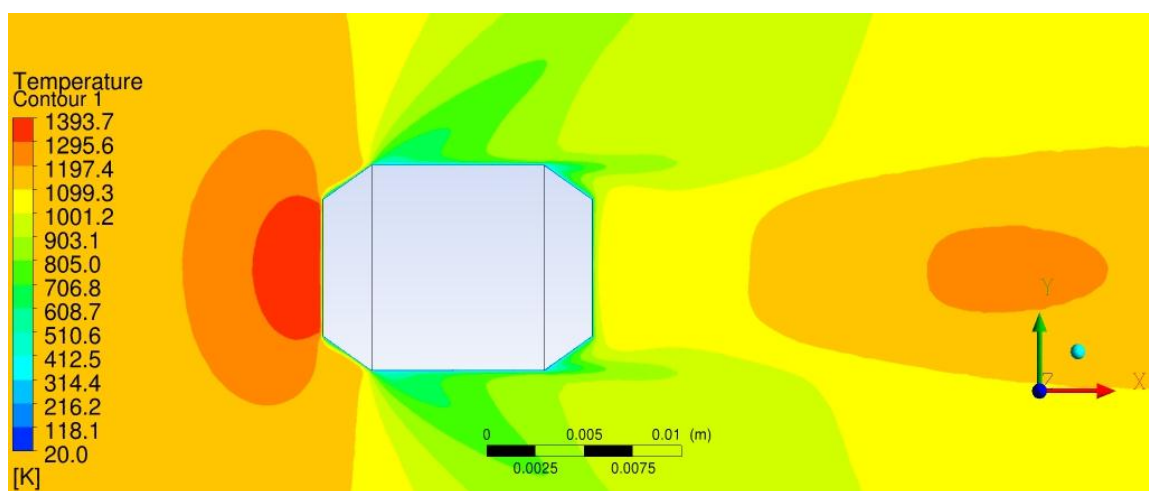


Figure 129. Temperature Contour on 3D, Steady-State Spinning Target in Drift Region at a Reynolds Number of 5200

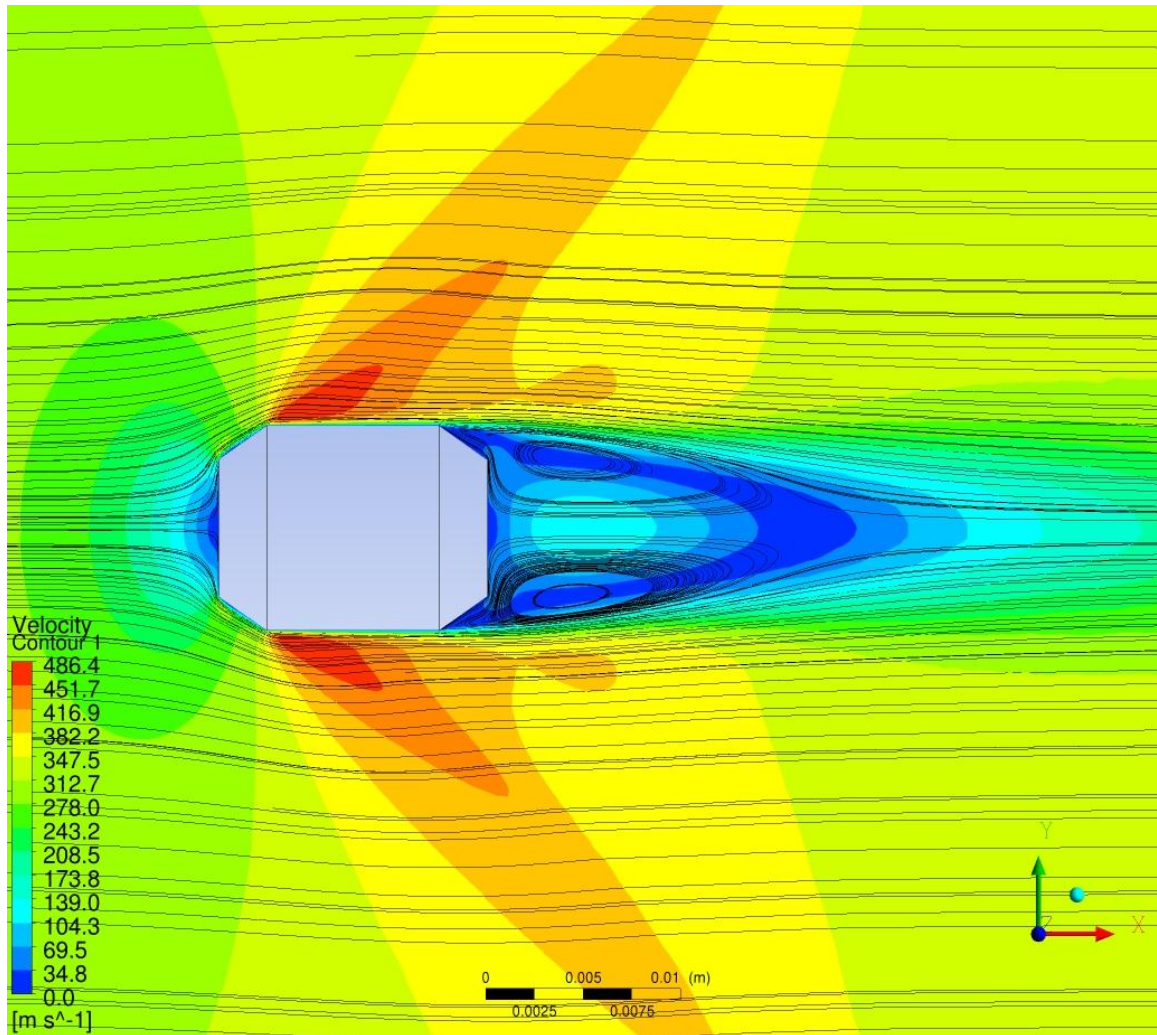


Figure 130. Velocity Contour with Streamlines on 3D, Steady-State Spinning Target in Drift Region at a Reynolds Number of 5200

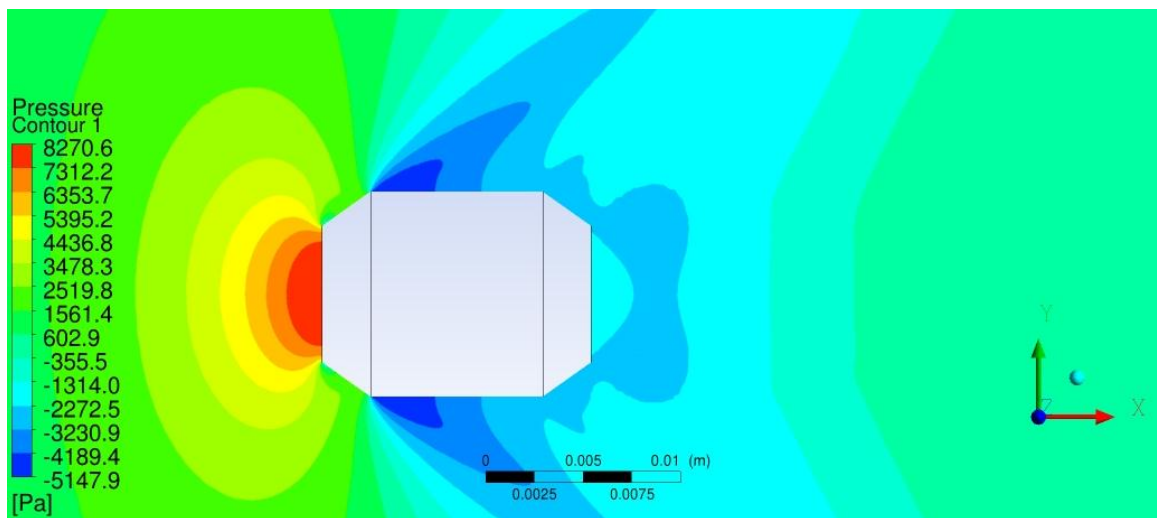


Figure 131. Pressure Contour on 3D, Steady-State Spinning Target in Drift Region at a Reynolds Number of 5600

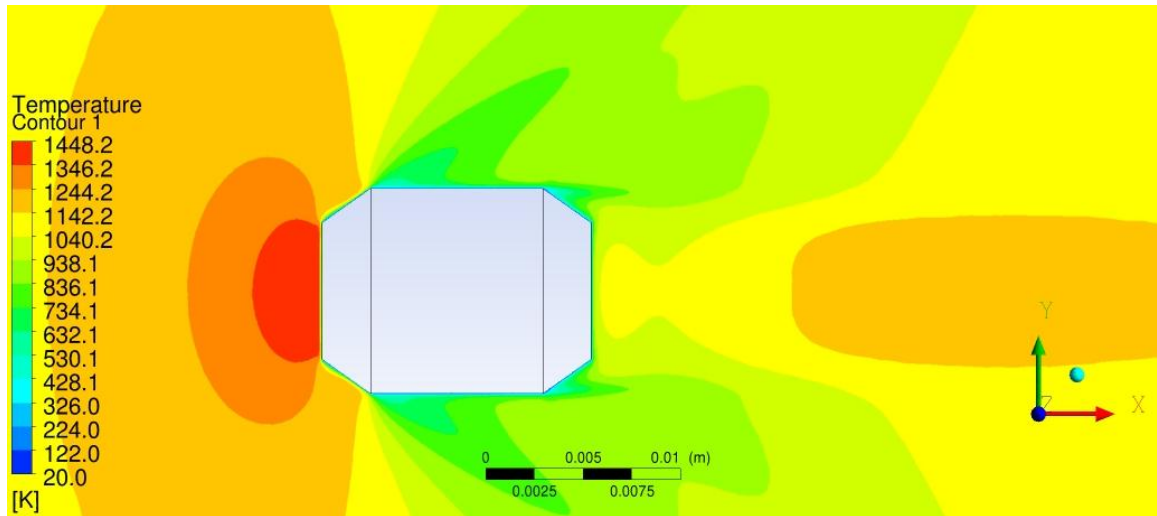


Figure 132. Temperature Contour on 3D, Steady-State Spinning Target in Drift Region at a Reynolds Number of 5600

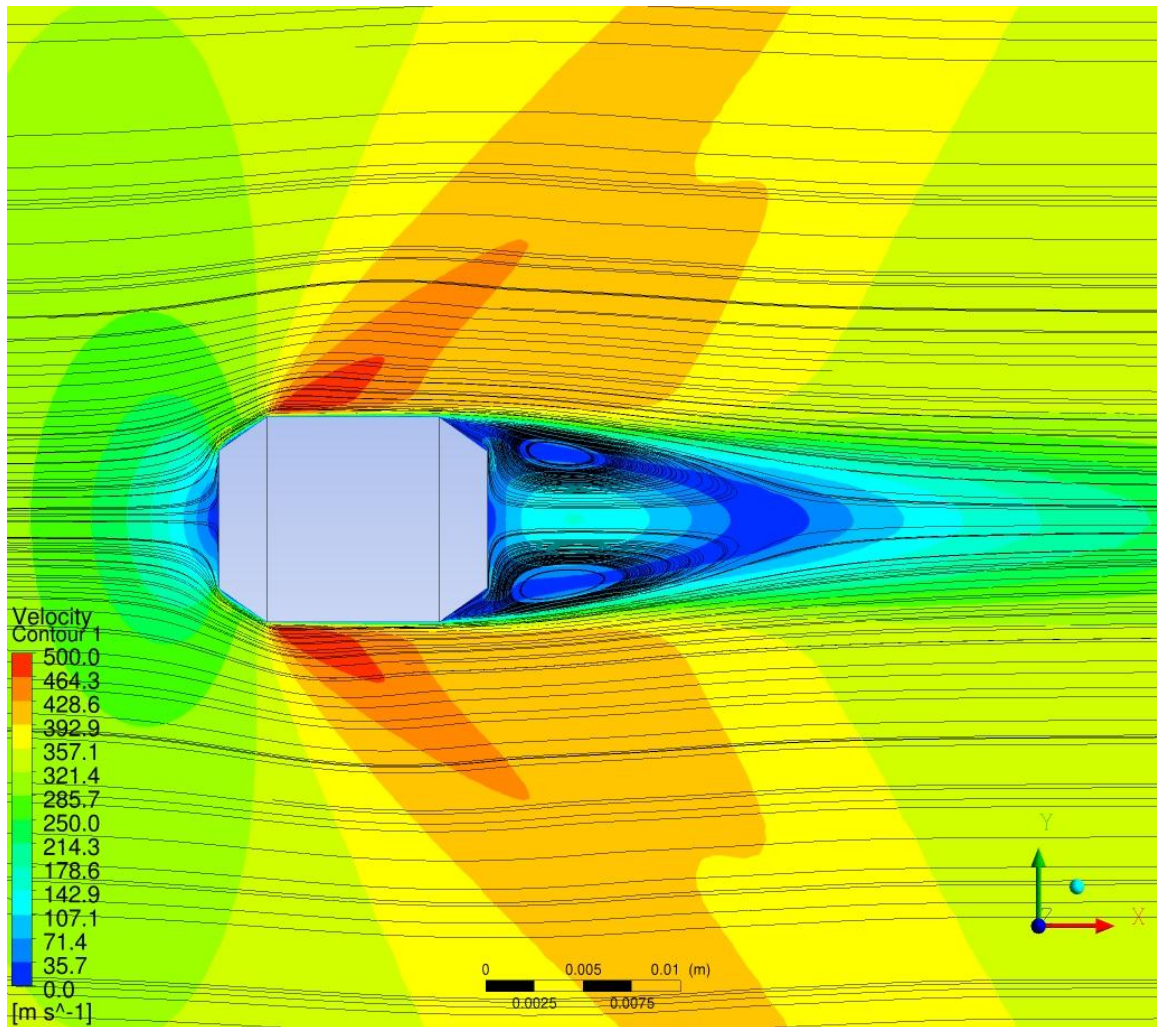


Figure 133. Velocity Contour with Streamlines on 3D, Steady-State Spinning Target in Drift Region at a Reynolds Number of 5600

Appendix D: Angle of Attack MATLAB Code and Plots

The MATLAB code used to determine the target's angle of attack over time was:

```
clear all;
clc;

thetad=15; %Initial angle of attack in degrees
theta=thetad*pi/180; %Initial angle of attack in radians
omega=0; %Initial angular velocity about z-
axis in rad/s
alpha=0; %Initial angular acceleration about
z-axis in rad/s^2
inertia=8.6e-8; %Mass moment of inertia in kgm^2
dt=.0000001; %Timestep in seconds
t=1.0; %Total simulated time in seconds
steps=t/dt; %Number of timesteps
steps=round(steps);
thetad_vec=zeros(1,steps);

for n=1:1:steps
    if theta<0
        %Overturning moment equation from best-fit polynomial from
        angle of
        %attack study
        moment=(5.265e-8)*(abs(thetad))^3-(2.510e-
6)*(abs(thetad))^2+(2.584e-5)*(abs(thetad))+3.290e-6;
        %Positive moment to decrease magnitude of angle of attack for
        negative theta
    else
        moment=-1*((5.265e-8)*(thetad)^3-(2.510e-6)*(thetad)^2+(2.584e-
5)*(thetad)+3.290e-6);
        %Negative moment to decrease magnitude of angle of attack for
        positive theta
    end
    %Assume constant angular acceleration over small time interval
    alpha=moment/inertia; %Kinematic equation from
    Meriam [19]
    omega=omega+alpha*dt; %Kinematic equation from
    Meriam [19]
    theta=theta+omega*dt+0.5*alpha*(dt^2); %Kinematic equation from
    Meriam [19]
    thetad=theta*180/pi; %Transform back to degrees
    thetad_vec(1,n)=thetad;
end

time=dt:dt:t;

figure
plot(time,thetad_vec)
xlabel('Time (s)')
ylabel('Angle of Attack (deg)')
```

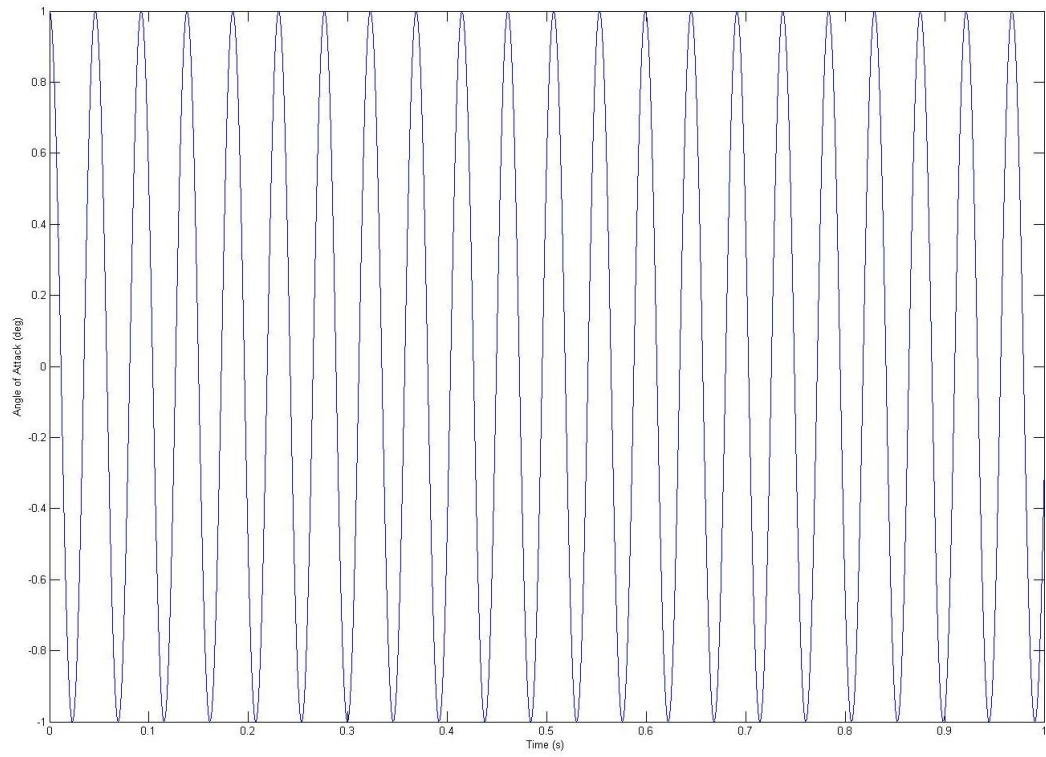


Figure 134. Angle of Attack over Time for Target with Initial Angle of Attack of 1°

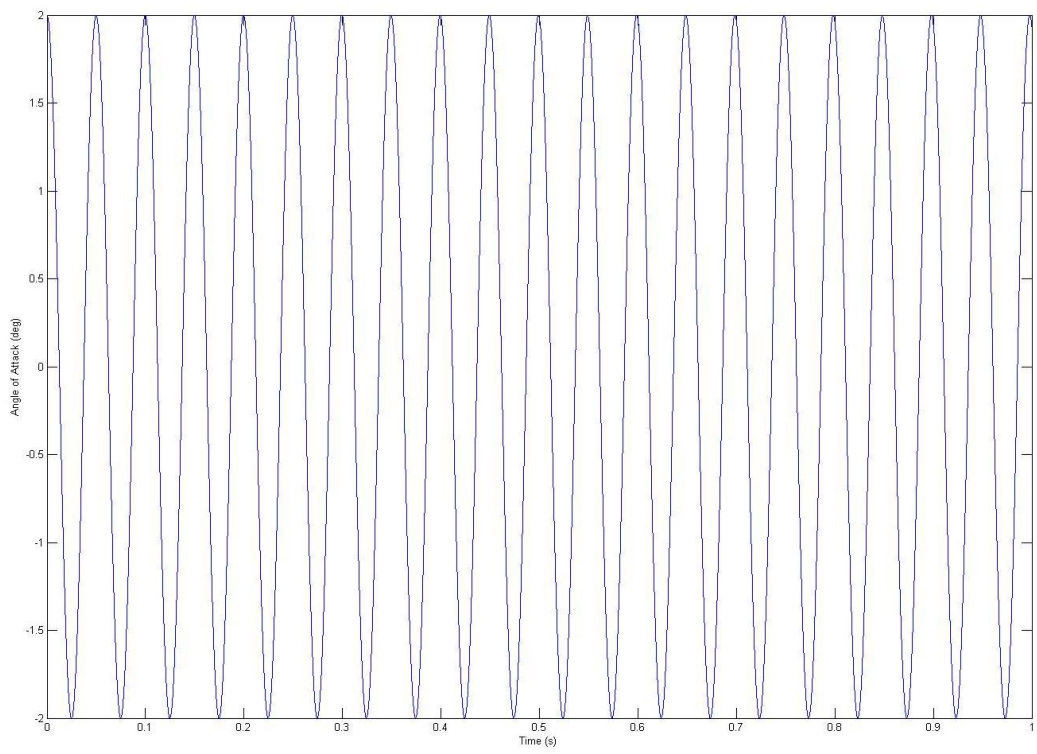


Figure 135. Angle of Attack over Time for Target with Initial Angle of Attack of 2°

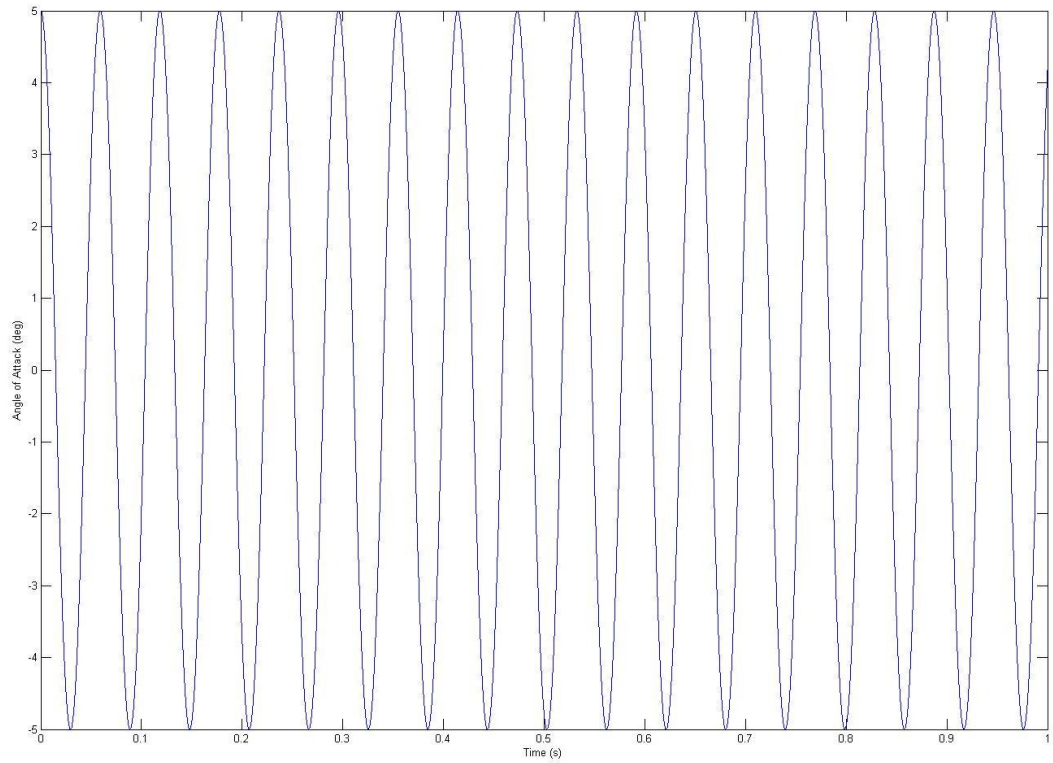


Figure 136. Angle of Attack over Time for Target with Initial Angle of Attack of 5°

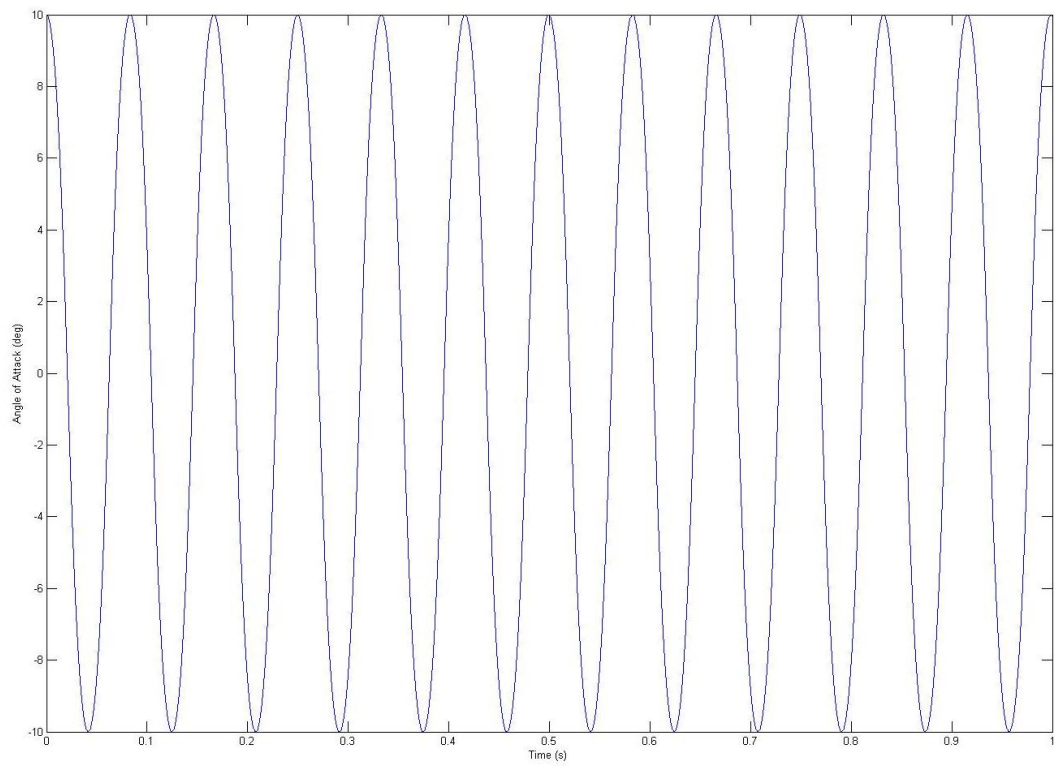


Figure 137. Angle of Attack over Time for Target with Initial Angle of Attack of 10°

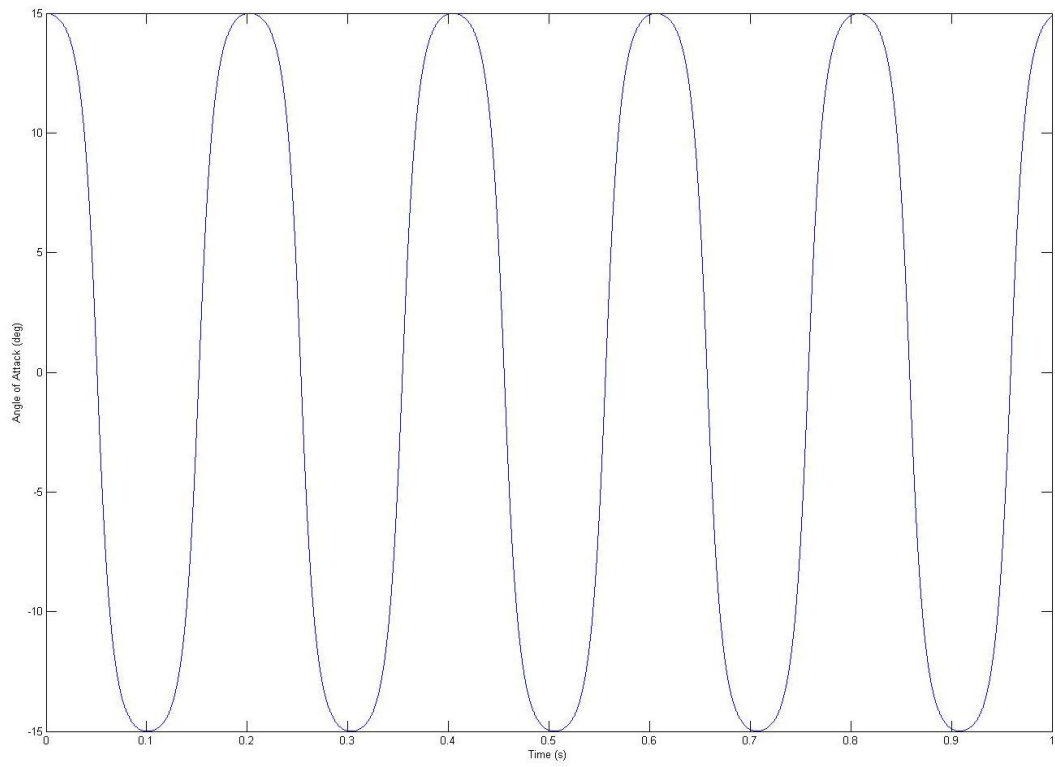


Figure 138. Angle of Attack over Time for Target with Initial Angle of Attack of 15°